Optical spectroscopy of mono- and multilayered semiconductors

Shivangi Shree

To cite this version:

Shivangi Shree. Optical spectroscopy of mono- and multilayered semiconductors. Physics [physics]. INSA de Toulouse, 2020. English. NNT : 2020ISAT0027 . tel-03471434

HAL Id: tel-03471434
https://theses.hal.science/tel-03471434

Submitted on 8 Dec 2021

THÈSE

En vue de l'obtention du

DOCTORAT DE L'UNIVERSITÉ DE TOULOUSE

Délivré par l'Institut National des Sciences Appliquées de Toulouse

---

Présentée et soutenue par

Shivangi SHREE

Le 14 décembre 2020

Spectroscopie optique des monocouches et multicouches de semi-conducteurs

Ecole doctorale : **SDM - SCIENCES DE LA MATIERE - Toulouse**

Spécialité : **Nanophysique**

Unité de recherche :
LPCNO-IRSAMC - Laboratoire de Physique et Chimie des Nano-Objets

Thèse dirigée par
Bernhard URBASZEK et Andrea BALOCCHI

Jury
Mme Maria Vladimirova, Rapporteure
M. George Kioseoglou, Rapporteur
M. Stefano Sanguinetti, Examinateur
M. Lionel Calmels, Examinateur
M. Bernhard URBASZEK, Directeur de thèse
M. Andrea Balocchi, Co-directeur de thèse

Abstract

Two-dimensional (2D) materials have attracted great research interest since the breakthrough of graphene, revealing exceptional mechanical, electrical and optical properties. The 2D material graphene has demonstrated excellent electrical properties. However, the absence of a bandgap is an obstacle for its interaction with light and therefore limits applications in optics. In this aspect, atomically thin of transition metal dichalcogenides (TMDs) semiconductors appear to be a promising platform for optoelectronics, as they possess a direct bandgap at the K-points of the Brillouin zone in the visible range. Despite being only three atoms thick, these semiconductors show exceptionally large light absorption, efficient light emission, and strong light matter interaction as summarized in Chapter 3. Their light matter interaction is governed by Coulomb bound electron-hole pairs (excitons).

In addition to the impact of optical quality on several parameters, in Chapter 4 we highlight a key issue for efficient energy relaxation channels which directly influence the exciton formation process, namely the exciton-phonon interaction in $MoSe_2$ monolayers both in absorption and emission. This experimental observation was possible due to the narrow exciton linewidth which was masked by mainly inhomogeneous broadening in earlier investigated samples.

Another striking feature of 2D materials is their unique ability to be combined in stacks. The weak van der Waals force between adjoining layers in vertical homo- or heterolayers results in strong with electrical coupling between layers. The light-matter interaction is strongly modified when going from mono- to multilayers. The modified electronic bandstructure in multilayer TMDs especially in bilayers enable completely new excitonic properties and phenomena, which do not exist in the monolayer. Homobilayers host new type of excitons named 'interlayer excitons' (IEs) where electrons are localized in a single layer while holes are delocalized over both layers. The main features of homobilayer such as MoS_2 are : strong absorption of IEs which have an in-built static electric dipole.

In Chapter 5 we show in homo-multilayer systems that IE transitions with strong absorption are visible up to room temperature. Chapter 6 is devoted to gated multilayer MoS_2. There we measure a giant IE Stark splitting and a widely tunable energy shift in applied electric fields due to the in-built static electric dipole. We show strong coupling between intra- and interlayer excitons when they are energetically tuned into resonance. In trilayer MoS_2, we uncover two distinct types of IEs in magneto-optics with very different in-built static electric dipoles.

In this thesis, we show the impact of the local dielectric environment on the optical transitions and how we can largely suppress the dielectric disorder in chemical vapor deposition (CVD)-grown MoS_2 monolayers by hexagonal boron nitride encapsulation in Chapter 7. The considerably improved optical sample quality allows us to observe interlayer excitons and interlayer coupling in CVD-grown multilayers.

We determine a correlation between the stacking order and interlayer coupling in artificially stacked and as-grown CVD layers shown in Chapter 8. We show that hole delocalization over the bilayer is only allowed in *2H* stacking and results in strong interlayer exciton absorption and also in a modified valence band spin splitting as compared to *3R* bilayers.

On the way to the realization of practical new photonic applications, this thesis studies the fundamental aspects of rich optical properties : (a.) high optical quality of large-area CVD-grown layer, (b.) tuning of interlayer exciton energy over a wide energy range in electric and magnetic fields and (c.) strong interaction of interlayer exciton with standard intralayer excitons.

Résumé

Les matériaux bidimensionnels (2D) ont suscité un grand intérêt pour la recherche depuis la percée du graphène, révélant des propriétés mécaniques, électriques et optiques exceptionnelles. Le graphène a des propriétés remarquables. Cependant, l'absence de bande interdite est un obstacle à son interaction avec la lumiére et limite donc les applications en optique. Dans ce contexte, les semi-conducteurs TMD atomiquement minces semblent être une plate-forme prometteuse pour l'optoélectronique, car ils possèdent une bande interdite directe aux points K de la zone Brillouin dans le domaine du visible. Bien qu'ils n'aient que trois atomes d'épaisseur, ces semi-conducteurs présentent une forte interaction lumière-matière comme résumé au chapitre 3. Leur interaction lumière-matière est régie par des paires électron-trou (excitons) liées par attraction de Coulomb.

En plus de l'impact de la qualité optique sur plusieurs paramètres, dans le chapitre 4, nous soulignons un problème clé pour des canaux de relaxation d'énergie efficaces qui influencent directement le processus de formation des excitons, à savoir l'interaction exciton-phonon dans les monocouches $MoSe_2$ à la fois en absorption et en émission. Cette observation expérimentale a été possible en raison de la largeur de raie d'exciton étroite qui a été masquée par un élargissement principalement inhomogène dans les échantillons étudiés précédemment.

Une autre caractéristique frappante des matériaux 2D est leur capacité unique à être combinés en piles. La force de van der Waals entre les couches adjacentes dans les couches homo- ou hétérogènes verticales se traduit par un couplage électrique fort entre les couches. L'interaction lumière-matière est fortement modifiée lors du passage de monocouches à multicouches. La structure de bande électronique modifiée dans les TMD multicouches, en particulier dans les bicouches, permet des propriétés et des phénomènes excitoniques complètement nouveaux, qui n'existent pas dans la monocouche. Les homobicouches hébergent un nouveau type d'excitons appelés «excitons intercouches» (IE) où les électrons sont localisés dans une seule couche tandis que les trous sont délocalisés sur les deux couches. Les principales caractéristiques d'une homobicouches tel que MoS_2 sont : une forte absorption des IE qui ont un dipôle électrique statique.

Au chapitre 5, nous montrons dans les systèmes homo-multicouches que les transitions IE à forte absorption sont visibles jusqu'à la température ambiante. Le chapitre 6 est consacré aux MoS_2 multicouches avec contact électrique. Là, nous mesurons une clivage géante de Stark pour les IEs et un changement d'énergie réglable dans les champs électriques appliqués en raison du dipôle électrique sta-

tique intégré des IEs. Nous montrons un fort couplage entre les excitons intra- et intercouches lorsqu'ils sont énergiquement accordés en résonance. Pour les tricouches MoS_2, nous découvrons deux types distincts d'IEs en magnéto-optique avec des dipôles électriques statiques intégrés très différents.

Dans cette thèse, nous montrons l'impact de l'environnement diélectrique local sur les transitions optiques et comment nous pouvons supprimer en grande partie le désordre diélectrique par encapsulation de nitrure de bore hexagonal dans les monocouches MoS_2 élaborés par dépôt chimique en phase vapeur (CVD) au chapitre 7. Une qualité optique considérablement améliorée nous permet d'observer les excitons intercouches et le couplage intercouche dans les multicouches développées par CVD.

Nous déterminons une corrélation entre l'ordre d'empilement et le couplage intercouche dans les couches CVD empilées artificiellement que nous montrons au chapitre 8. Nous montrons que la délocalisation des trous sur la bicouche n'est autorisée que dans l'empilement *2H* et entraîne une forte absorption d'exciton intercouche et aussi dans un clivage spin-orbite de la bande de valence modifiée par rapport aux bicouches *3R*.

Sur le chemin de la réalisation de nouvelles applications photoniques pratiques, cette thèse étudie les aspects fondamentaux des propriétés optiques riches : (a.) Haute qualité optique de la couche à croissance CVD de grande surface, (b.) Réglage de l'énergie d'exciton intercouche sur un large gamme d'énergie dans les champs électriques et magnétiques et (c.) forte interaction de l'exciton intercouche avec les excitons intra- couche.

Acknowledgements

I wish to extend my heartfelt thanks to the people I had the opportunity to meet during my work in three years as a PhD student at the LPCNO (Laboratoire de Physique et Chimie des Nano-Objects). Firstly, it is difficult to express in words my gratitude to my supervisor Bernhard Urbaszek for his trust for accepting me as a PhD student, and from whom I have learned almost everything I know about optics and beyond. Bernhard is a wonderful scientist and skilled research manager providing his invaluable support, constant inspiration and enthusiasm to several PhD students and postdocs at the same time. He always sets well defined short term and long term goals of different research projects for everyone. He taught me the basics of transition metal dichalcogenides layers and optical spectroscopy techniques through extensive hands-on training. He explained me the working principle of each components and its use in optical set-ups to probe and manipulate these layers. His continuous guidance and unstinting help at every step of my work have contributed most significantly in the development of this thesis. He provided me with ample freedom to explore and patiently corrected my mistakes on numerous occasions. I am also thankful for his support and accompanying me to participate in several international conferences and meetings during these three years. My association with him has not only enhanced my scientific training and knowledge but also enriched me on the personal level (human dimensions, swimming, cycling and many more).

I would like to give my sincere thanks to Delphine Lagarde for designing and building the magneto-optics setup, guiding me through it and for her indispensable support and trust during my PhD period. Like other members of the team, she is also very enthusiastic and helpful. She continuously keeps track on the experimental set-ups making sure that they are operational. She improved them regularly in making our experiments simple and efficient both in spectroscopy and fabrication set-up.

Andrea Balocchi always remain very kind and motivating wherever I had to seek any suggestions either about interesting physics or any other help I asked for. It was my pleasure to work with you. Your feedbacks and questions were very important Andrea to improve my scientific as well as presentation skills. I also like your passion for swimming which inspires me to swim regularly!

I am also grateful to Cedric Robert for his full of patience and dedication to train me. He has shown me how to fabricate van der Waals heterostructures and characterize our samples. I am thankful to him for giving me instant support and advice in continuing the research without delay whenever I needed.

My sincere thanks to Xavier Marie for his help and co-operation in several stages of my doctoral research. It was a great opportunity to work with you on TMD monolayers. I am also fortunate to attend your series of lectures at LPCNO, in the winter school on “Frontier research in 2D materials" in Cargese, and during Covid19 confined period.

I am also grateful to Thierry Amand for several discussions. He is always very keen to talk about Physics. Your passion for Physics and its mathematical tools is motivating for me. Thank you for your time, Thierry. I also loves our non-scientific discussion. I wish your good health and time.

I would like to thank to Pierre Renucci, Lombez Laurent and Hélène Carrere for their constant encouragement. I will remember your strong interest and dedication for education and research.

I will also remain indebted to all the members of the team, the postdoctoral researchers : Ioannis Paradeisanos, Hans Tornatzky, Honghua Fang, Joshya Shyamala Rajagopal, Maher Nafouti, and the PhD students : Marco Manca, Emmanuel Courtade, Bo Han, Ren Le, Maxime Mauguet and Sawsen Azaizia.

I have been extremely fortunate to work with Ioannis. He is an excellent scientist and passionate towards science and sports. Thanks a lot for your great support and making me understanding all questions very patiently. We have shared many ups and downs. I have learned varied things from you on scientific as well as in human level. I enjoyed our time together in Toulouse. Good luck in all that comes your way in the future.

Thanks a lot Emmanuel for working with me and sharing your experience on spectroscopy experiments and fabrication during my PhD work. We discussed together repeatedly and had several interesting conversations. In addition to a person with excellent scientific skills, you were always kind and cheerful. I like our time in experiments, office, outings and of course our CNRS canteen! I hope your future will fulfill your expectations. When I arrived, I had chance to work with Marco. I will remember your excellent scientific skills. I wish you a bright future.

Bo and me spent almost three years together in LPCNO so we overcame a lot of similar obstacles! It was reassuring to work with you as you are a nice, calm person and skillful researcher. I will also remembered our cheerful time we spent in Cargese! I wish you good luck for your future life and work. Thank you for having been so welcoming!

I also met Joshya, Hans and Lei Ren in the team. They are very friendly and excellent researchers. My warm thanks to you for being a joyful person and always supportive. I wish you all the best for the project and bright future!

Though we could not spend much time together but it was a pleasure knowing

Honghua. I wish you good luck to you and your family for your life in Beijing.

I fondly remember several interaction with Maxime, Maher and Sawsen at LPCNO. It was a pleasure to discuss with you about everything.

Besides our Quantum Optoelectronics team, there were several other people helped me to pursue my research work. At LPCNO there are strong collaborations among several teams. Each team has developed expertise in different subjects. I also have to express my sincere gratitude to Iann Gerber who regularly bring to us his theoretical expertise (for example performing advanced DFT calculations). I also want to thank Benjamin Lassagne and Alexandre Pierrot without whom I could not have performed all AFM measurements on our van der Waals heterostructures.

At LPCNO we also collaborated with department of Chemistry for some of our works. Many thanks to Angélique Gillet for your help, time, being very welcoming and giving access to the laboratory to clean our substrate for high-quality van der Waals heterostructures as well as to Lise-Marie Lacroix and Deborah De Masi for providing us Au - nanoparticles for our quantum emitter in TMDs project.

I extend my warmest thanks to many people outside of LPCNO. First, Mathieu Pierre from LNCMI who helped me (for example, to do bonding on our devices). This was quite helpful for controlled tuning of electric field in our device which result in important observation of intrerlayer exciton which can be tuned in wide energy range. Thank you Mathieu for having been so available.

I am also grateful to our colleagues from CEMES and extend my warm thanks to Vincent Paillard, Jean-Marie Poumirol, Aurélien Cuche and Gonzague Agez, and from LAAS : Guilhem Larrieu, Nicolas Mallet and Peter R. Wiecha for making an interesting collaboration with Bernhard. It was great experience to be part of the project on to couple TMD monolayers with nano-resonators.

I had opportunity to work with excellent scientists of the field from outside Toulouse : Richard J. Warburton from Basel, Scott Crooker from Los Alamos, Khaled Karrai from Munich, 4-PHOTON teams and partners, Takashi Taniguchi and Kenji Watanabe from NIMS in Japan among many others! In particular, I express my sincere appreciation for Mikhail Glazov and Marina Semina from Ioffe Institute for their constant help and support.

I would also like to mention here great experiences that I gained during my work with the local teams at the University of Basel and Attocube. My sincere gratitude to my PhD supervisor Bernhard, Richard J. Warburton from the University of Basel and Khaled Karrai from Attocube without their support both secondments would not have happened. Thank you for fruitful discussions and progressive thoughts.

Special acknowledgment to Nadine Leisgang and Lukas Sponfeldner. It was my pleasure working with both of you. In addition of our productive collborative work, we also shared some cheerful time in Basel specially in the departmental Aperó, table tennis and Jonas's defense. I also thank you my friends : Daniel Najer, Liang Zhai, Natasha Tomm, Jonas G. Roch and all others for accompanying me in the team.

It was exciting for me also to work in Attocube which was new experience for me. Thank you my colleagues : Meryem Benelajla, Jessica Lindlau and the team. During my time in Toulouse, I have made and maintained friends that have become my family here an incredible, infinite source of support and inspiration, thank you Bernhard and the team. I will remain grateful to all you people!

My sincere thanks to the non-academic staffs of our department and the Institute for their help on numerous occasions : Brice Altman, Elisabeth Lance, Assia Khodja among many others.

I am immensely fortunate to be a part of 4PHOTON ITN network. Thanks a lot to Stefano Sanguinetti, Sandrine Soubes, Sergio Bietti for organizing several scientific and social activities that helped me a lot in enriching my skills and thoughts. I am also very happy to thanks my colleagues in the 4PHOTON team : Adonai Rodrigues da Cruz, Dimosthenis Toliopoulos, Liang Zhai among others.

I am immensely fortunate to have incredible support of my brother and sister-in law Amal Kumar and Sweta Kumari. I am also thankful to my fiancé Swetamber Das who stood by me these years. None of this would have been possible without the affectionate support, and guidance of my father Shailendra Kumar Sinha as well as for the love, affection and inspiration from my mother Lalita Kumari. I dedicate this thesis to them.

Contents

Chapter 1

Introduction to transition metal dichalcogenides

Richard Feynman's famous lecture [1] entitled "There is plenty of room at the bottom" in the 1959 APS meeting is often regarded as an inspiration for the field of Nanotechnology. This term was first introduced 15 years later by Norio Taniguchi in a conference in Tokyo to explain a highly controlled processing of semiconductors. However, it received worldwide attention a few years later through the 1981 paper by K. Eric Drexler followed by his book named "Engines of Creation : The Coming Era of Nanotechnology" in 1986. The era was indeed ushered and the field has witnessed a rapid development ever since.

The properties of materials derive from their intrinsic atomic arrangement and bonds. Metals, insulators, and semiconductors are made of atoms, however, they differ in their electronic bandstructure. These properties can be modified as the spatial dimensions of the crystal are changed. When thinned down to atomic monolayers thickness, materials reveal fascinating and unique properties. In 2004, two scientists at the University of Manchester, Andrei Geim and Kostya Novoselov, isolated a single layer of graphite. This two dimensional (2D) layered material is named graphene, an extremely versatile semi-metal. After Novoselov's paper, many techniques for producing, characterizing, and manipulating atomically thin flakes were developed, which in turn lead to the rapid growth of the field.

There are more than thousands of 2D materials available with diverse functionality as shown in Fig. 1.1 with a broad bandgap energy range from 0 eV (graphene) conducting to 6 eV (hBN) insulating materials. This offers possibilities to use these materials for a wide range of applications. For example, optoelectronic devices such as light emitting diodes (LEDs), photovoltaics, photodetectors in addition to transistors, fiber communications, thermal imaging among many others see Fig. 1.2.

Among 2D materials, transition metal dichalcogenides (TMDs) are particularly interesting for their optical properties. These materials exhibit a crossover from an indirect to direct bandgap by reducing the thickness to a single monolayer. The most common method to obtain a thin film typically a few to tens of micrometers in the lateral dimension is micro-mechanical cleavage (commonly referred to as exfoliation or 'scotch-tape technique') illustrated in Fig. 1.3. The weak van der Waals force between the adjoining layers, compared to covalent bond that forms the monolayer, make it possible to stack layers from different layered materials

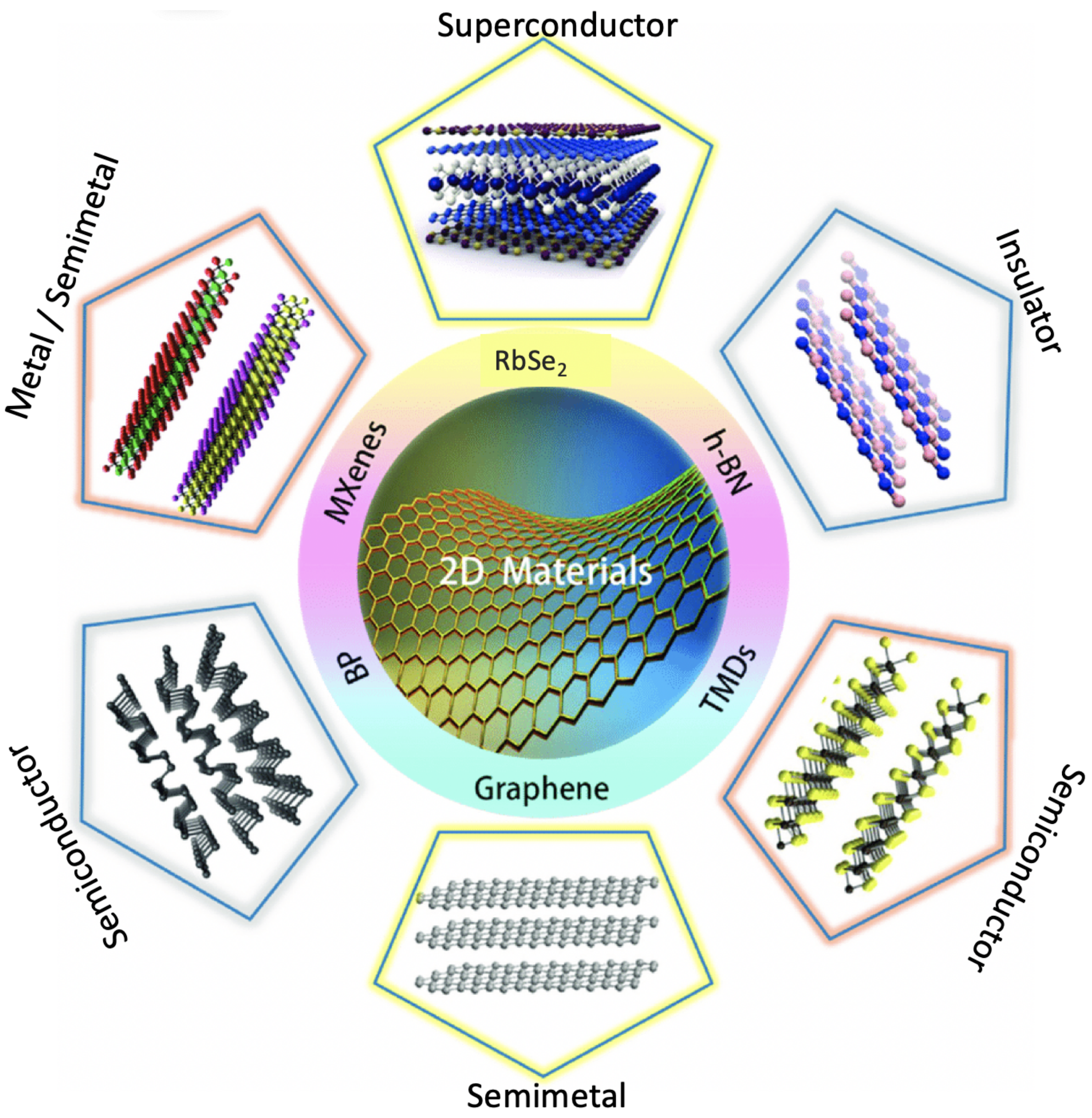

Figure 1.1: The main family of 2D materials. The figure is extracted from [2].

to get van der Waals heterostructures with new physical properties, see Fig. 1.4. This technique is very simple and cost efficient compared to molecular beam epitaxy (MBE) where lattice matching with the substrate material is a necessary ingredient. However, this method is not useful for wafer scale production of 2D layers because of its low yield and randomness in getting a monolayer on a substrate. But, this technique is extremely useful at the fundamental research level for working on the interesting physical properties of high quality, artificially stacked heterostructures. Another fabrication technique that is also making progress to have a wafer scale thin films is chemical vapor depositon (CVD). The detail optical spectroscopy studies of atomic layer thick TMDs fabricated using exfoliation and CVD are discussed in the following Chapters. In this Chapter, we will introduce very briefly the main properties of TMD material family. From the next Chapter onward, we will mainly discuss optical properties of monolayers $MoSe_2$ and multilayers MoS_2.

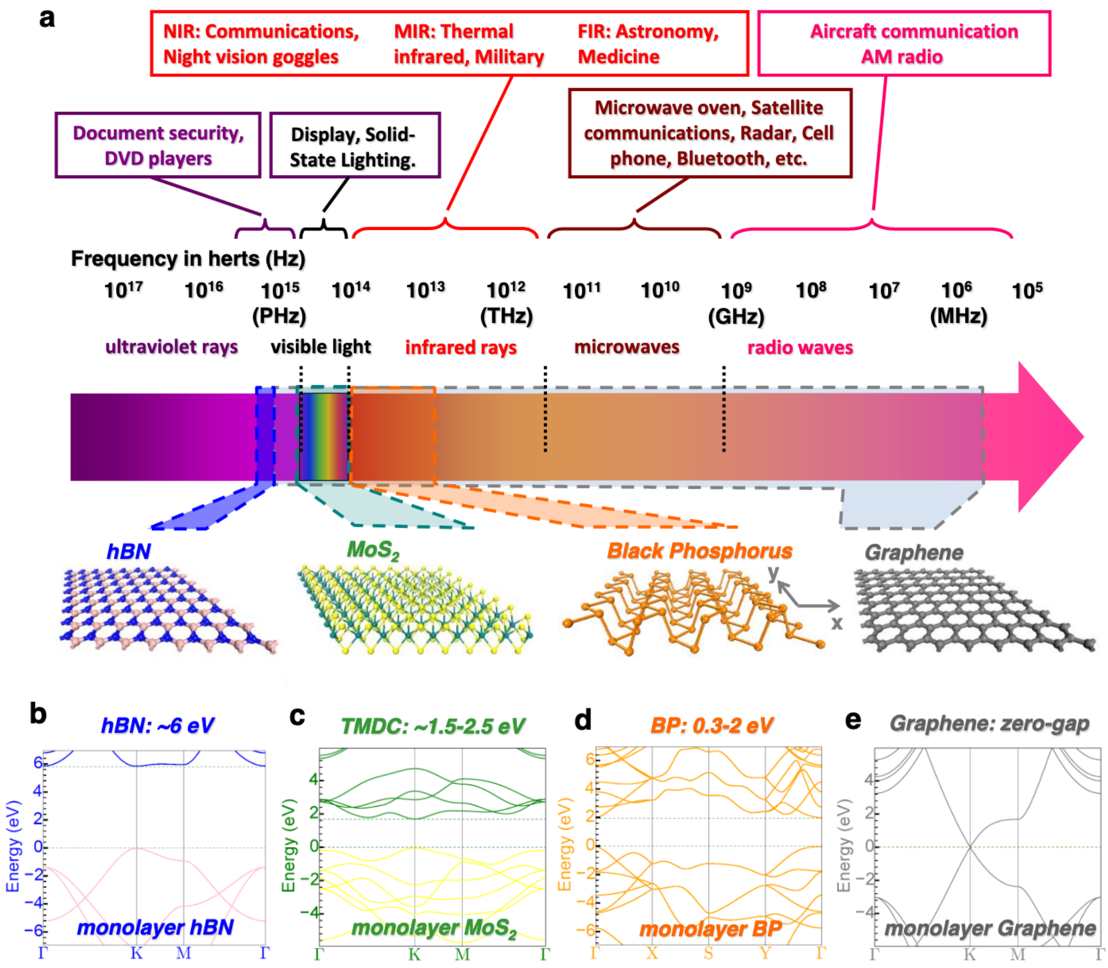

Figure 1.2: **(a)** Wavelength range and energy bandgap covered by different 2D materials. **(b)**, **(c)**, **(d)** and **(e)**, respectively. The electronic band structure of 2D materials. The figure is reproduced from [3] .

1.1 Transition metal dichalcogenides

TMDs are an extremely promising class of materials in the field of 2D materials. The TMD family consists of about 60 materials, most of them are layered structures in their bulk form with a weak van der Waals interaction between the layers.

1.1.1 Crystal structure

TMDs layered materials are represented as MX_2. Here M stands for metal atoms (Mo, W) sandwiched on either side by chalcogen atoms X (S, Se, Te). The properties of the MX_2 materials are dependent on the choice of metal, chalcogen atom, and the atomic configuration. Fig. 1.5 is an artistic representation of a monolayer MX_2 made of a honeycomb sheet of metal atoms covalently sandwiched between two honeycomb sheets of chalcogen atoms. Layers of TMD monolayer can be stacked to form multilayer or bulk. The height of the monolayer is approximately 0.6 - 0.7 nm and can be measured by atomic force microscopy (AFM). In the MX_2 structures, each metal atom covalently bonds to 6 chalcogen atoms (3 on either side), and each

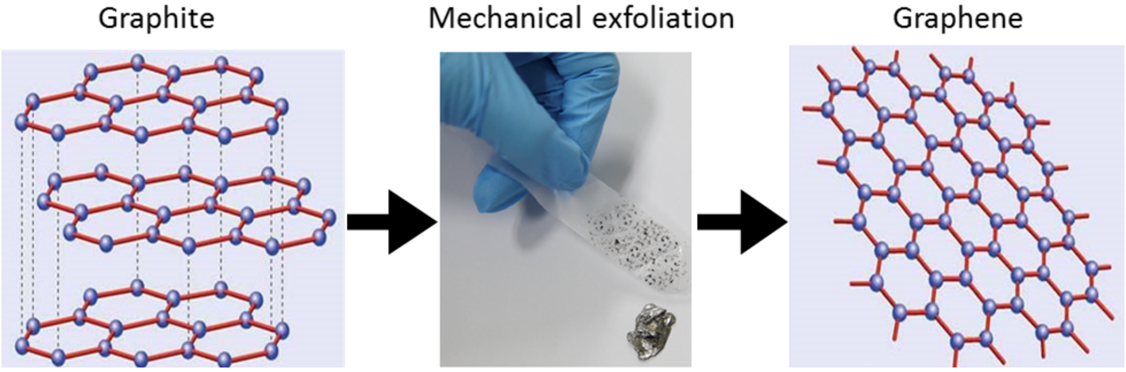

Figure 1.3: A schematic showing graphene exfoliated from graphite. The figure is taken from [4] .

chalcogen atom bonds respectively to 3 metal atoms. When Mo or W are combined with S or Se monolayers are semiconductors. Whereas when Mo atoms combine with Te the monolayer can be switched between semiconducting and metallic phase by tuning strain or carrier concentration [5].

Moreover, TMDs monolayer can have two different phases : octahedral and trigonal prismatic shown in Fig. 1.5. Octahedral is not as stable as the trigonal prismatic phase. Hence, trigonal prismatic phase is the most likely to be found in nature and also in the grown bulk material. In addition, the monolayers with this phase are stable enough under ambient conditions to perform optical and electrical characterization.

TMD bulk crystals and monolayer have different crystal symmetry. This can be understood by considering the stacking order of TMD layers. Beyond monolayers, several types of stackings are possible. We will discuss mainly the two different stackings in TMDs layers : *2H* (hexagonal) and *3R* (rhombohedral). The digit represents the numbers of layers in the crystallographic unit cell. In *2H* stacking, the adjacent layers are rotated by 180 degree and stack directly upon one another. Hence, *2H* bulk preserves crystal inversion symmetry while for a monolayer inversion symmetry is broken. In general, crystal inversion symmetry is present with an even number of layers while absent in samples with odd layer numbers. In contrast, when the adjacent layers are displaced slightly from each other without any rotation we obtain *3R* stacking, see Fig. 1.5 (c). This type of stacking retains crystal symmetry for repetitive building blocks of TMD layers. Therefore the stacking order that changes the symmetry of the crystal plays a significant role in light-matter interaction, leading to a different optical response in TMDs. Details are discussed further in Chapter 8.

1.1.2 Bandstructure

TMDs exhibit one of the most interesting properties when thinned down to a single monolayer limit, they show switching from indirect bandgap to direct bandgap in theory and experiment as shown in Fig. 1.6.

In TMDs, the bandstructure changes between multilayers compared to monolayers due to two main effects : quantum confinement and the change in orbital

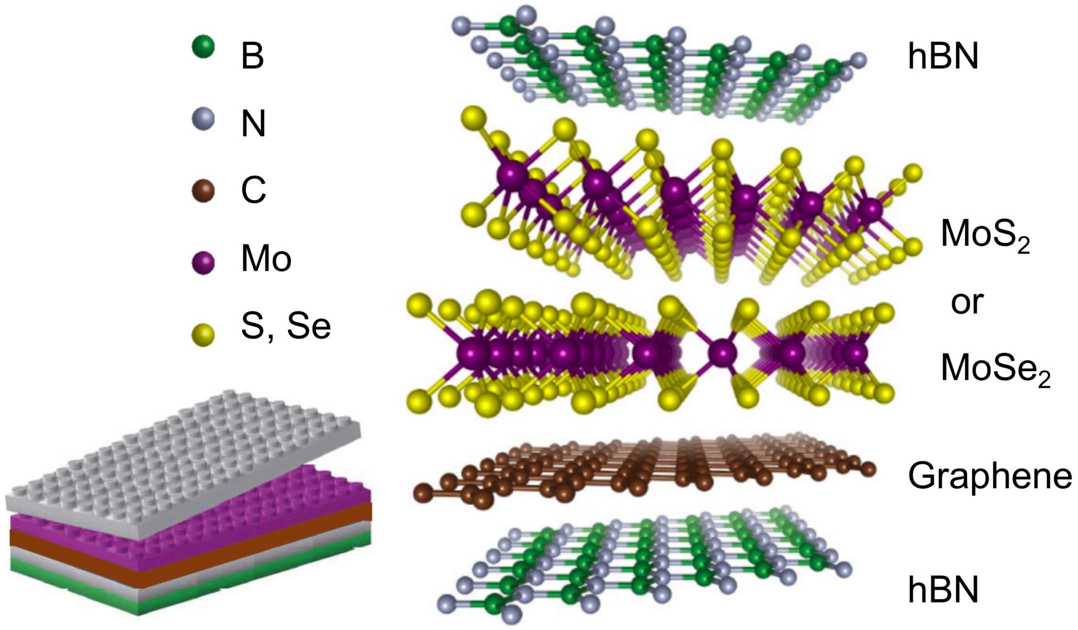

Figure 1.4: A schematic of layered materials for a van der Waals heterostructure, also represented in a very simple view as the assembly of building blocks. The figure is taken from [3] .

hybridization. In bulk MoS_2, for example, the valence band maximum (VBM) are situated at the center of the hexagonal Brillouin zone referred to as Γ-point while the conduction band minimum (CBM) are located nearly halfway along the $\Gamma - K$ direction [7, 8]. However, in monolayers, the CBM and the VBM both are located at the corners of the first Brillouin zone Fig. 1.6 (b). The hexagonal Brillouin zone looks similar to the one of graphene, but a bandgap is present at the K-points of the Brillouin zone. Furthermore, in TMD monolayers, the six corners of the Brillouin zone belong to two different groups represented by K^+ and K^--point respectively. Each group has three equivalent corners mutually related by reciprocal lattice vectors. The energetically degenerate but non-equivalent states at the band extrema K^+ and K^- transform into each other under the time-reversal operation. States at K^+ is attributed to a valley index of $+1$, and states at K^- have a valley index of -1. In addition to the spin, valley index quantum number can be initialized in optical experiments and manipulated in electric and magnetic fields, see the details below.

In TMD monolayers, the conduction band and the valence band states (K_c and K_v) at K-point are mainly due to d-orbitals from the transition metal atoms M which are sandwiched between the two layers of chalcogen atoms. In contrast, one of the local minimum of the conduction band Q_c and the local maximum of the valence band Γ_v have a major contribution from P_z chalcogen atoms shown in Fig. 1.6 (b) [9]. These orbitals are spatially more influenced by the interlayer coupling compared to the d-orbitals because P_z is closer to the neighboring layers which can lead to interlayer hopping. So by increasing the layer number from monolayer to bulk, the energy of Γ_v is raised and that of Q_c is lowered significantly, while the energies of K_c and K_v do not change much. As a consequence, the bandgap crosses over to an indirect one between $Q_c \leftrightarrow \Gamma_v$ in the Brillouin zone at the bilayer, and further

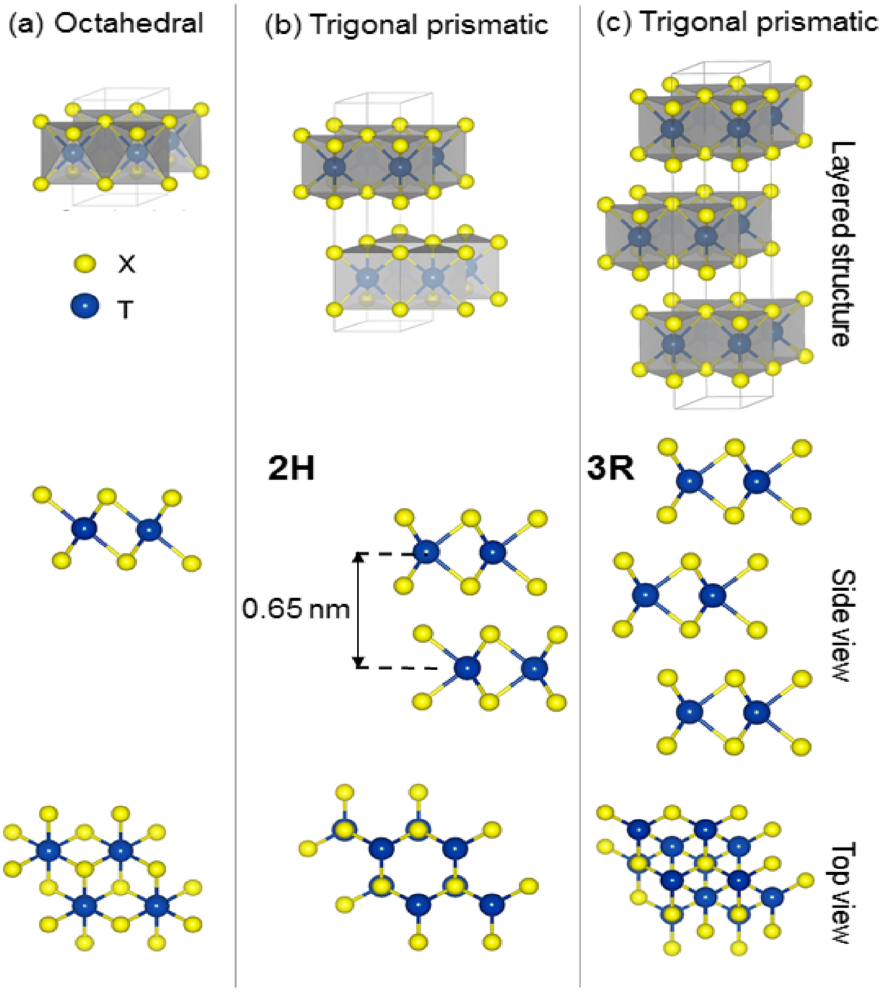

Figure 1.5: Structural representation of different phases of TMD polytype (**(a)** octahedral, **(b)**-**(c)** trigonal prismatic) and their corresponding metal atoms coordination. Dissimilar stacking sequences of trigonal prismatic single layers with a different rotation angle of layers corresponding to each other can give different stacking : hexagonal symmetry *2H* and rhombohedral symmetry *3R*. The figure is taken from [3] .

decreases with the increase of thickness [10, 11, 12], see Fig. 1.6 (b).

1.1.3 Excitons in TMD monolayers

In typical semiconductors, an electron can be excited to the unoccupied conduction band leaving an empty electron state in a sea of other electrons in the valence band. This many-particle system can be reduced to the two-body problem of the negatively charged conduction electron interacting by the strong Coulomb attraction with a positively charged valence hole and give rise to a bound state called "exciton". In semiconductors, the two main types of excitons can be formed : Frenkel and Wannier-Mott excitons. A Frenkel exciton possesses a very strong Coulomb attraction between the electron and hole. Their radius is of the order of 0.1 nm, they are tightly-bound excitons. These excitons have a very large binding energy of the order of 1.0 eV. Frenkel excitons are usually found in insulators, alkali halides, and organic molecular crystals. In contrast, Wannier-Mott excitons due to weak

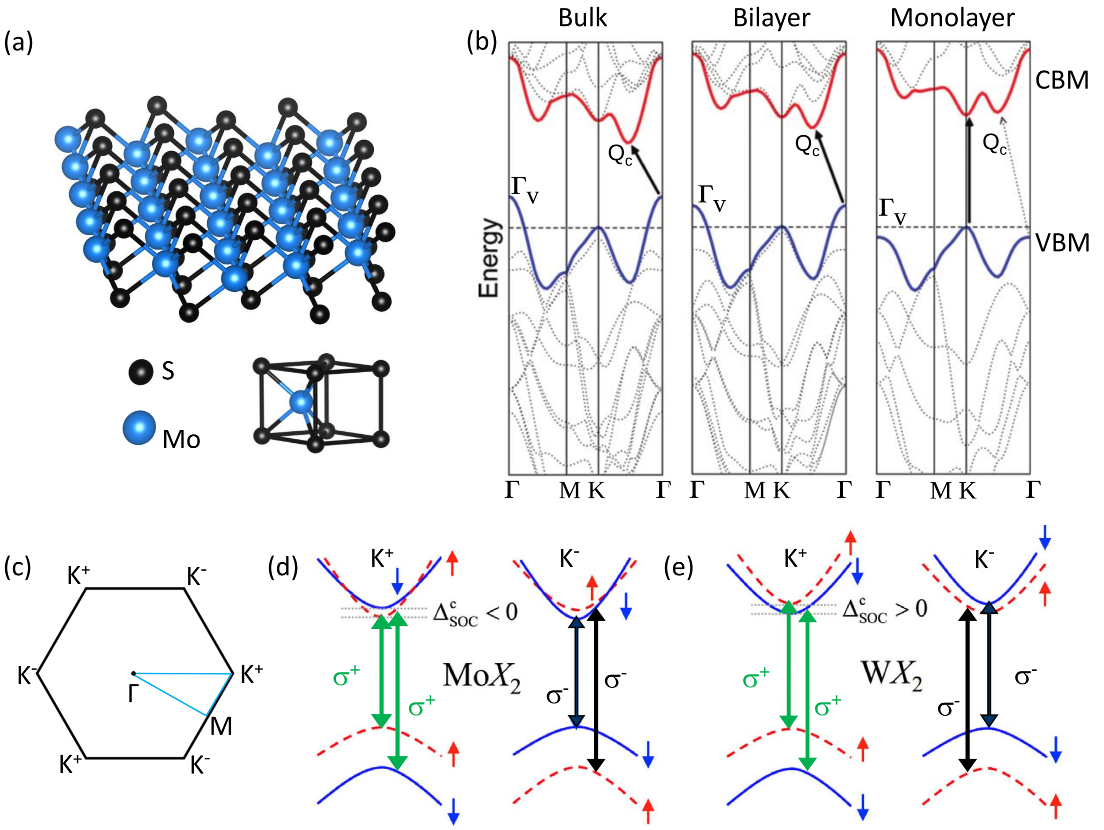

Figure 1.6: **(a)** 3D model of the structure of a TMD monolayer and corresponding unit cell. **(b)** Calculated bandstructure of bulk, bilayer and monolayer MoS_2. The three panels show the transition from indirect to direct bandgap semiconductor. The figure is taken from reference [6]. **(c)** Sketch of the hexagonal Brillouin zone where the K, Γ, M points are located. The light blue lines indicate the directions along which the bandstructure in panel **(b)** is calculated. **(d)**-**(e)** Schematic shows that the conduction bands are opposite in MoX_2 and WX_2 monolayers. The arrow represent spin allowed A-exciton transition given by the optical selection rules.

Coulomb interaction between the carriers are free excitons delocalized over many lattice sites. The binding energy is typically the order of tens of meV. Hence these excitons are found in semiconductors with smaller energy bandgaps and higher values of dielectric constant as compared to materials that host Frenkel excitons. In TMD monolayers, the exciton Bohr radius is about a few nanometers and the correlation between an electron and a hole extends over several lattice periods. Hence, the exciton can have an intermediate nature between the so-called Wannier-Mott or large-radius-type (similar to classical semiconductors such as GaAs and CuO_2) and the Frenkel exciton.

The excitonic transition can be observed in the optical spectra : if the Coulomb interaction is strong, it can be seen at lower energy compared to the free carrier bandgap E_g. This energy difference is the exciton binding energy E_B, see a schematic in Fig. 1.7.

In a 2D TMD crystal, the electron and the hole which form the exciton have relative motions which are strongly coordinated as demonstrated in Fig. 1.7. The

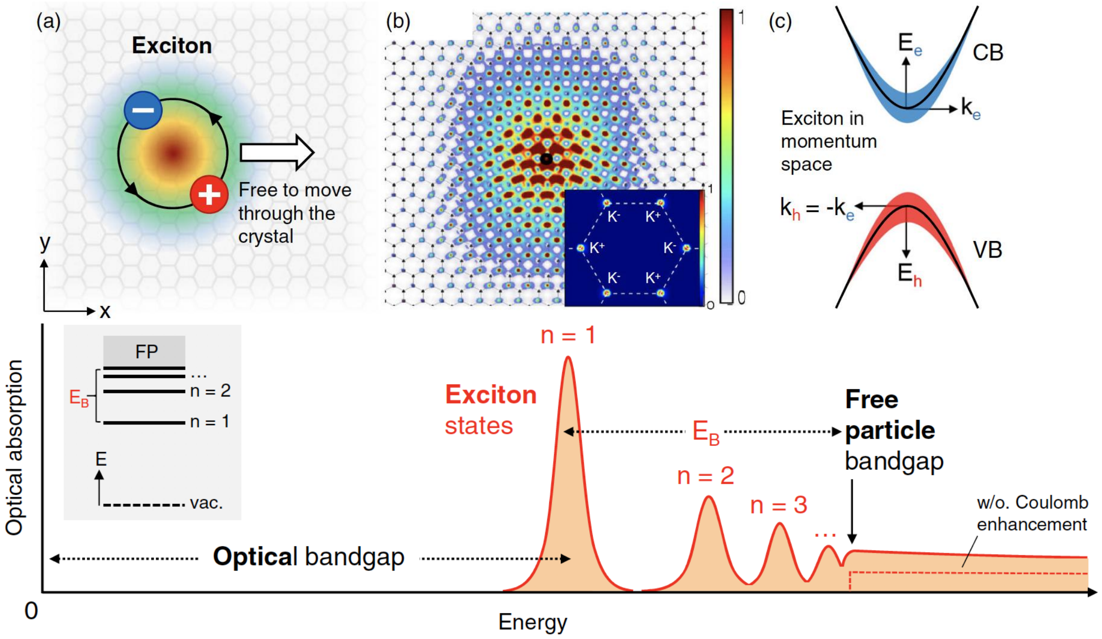

Figure 1.7: The picture schematically shows the optical absorption of an ideal 2D semiconductor including the exciton and its series of excited states at lower energy than the electronic bandgap. The inset shows an energy level scheme of the exciton states, in analogy with the hydrogen atom. Principal quantum numbers identify the excited states. The energy difference between the lowest energy exciton state ($n = 1$) and the free-particle bandgap is the exciton binding energy E_B. The figure is taken from Wang et al. [13]

. .

exciton center-of-mass with a wavevector $\vec{K}_{exc}$ can move freely in the plane of the material, in accordance with the Bloch theorem. As a result of the large binding energy of excitons and their small Bohr radius in real-space ($a_B \simeq 1$ nm), the exciton spreads in the k-space significantly. Hence, states at a larger distance from the K-point are included in the exciton wavefunction as indicated in Fig. 1.7 (c).

We can analytically derive a numerical expression for the exciton energy considering the two-dimensional case in an effective mass approximation. The motion of the electron and hole are confined to a monolayer plane so $\vec{K}_{exc} = \vec{K}_x + \vec{K}_y$. As a consequence the total energy of exciton states is given by [14]:

$$E^{2D}_{\mathrm{exc}}(n, \vec{K}_{\mathrm{exc}}) = E_g - R^*_y \frac{1}{(n - \frac{1}{2})^2} + \frac{\hbar^2 |\vec{K}_{\mathrm{exc}}|^2}{2M_{\mathrm{exc}}} \tag{1.1}$$

where E_g the free carrier bandgap, exciton mass $M_{exc} = m_e + m_h$ and n is the principal quantum number. When $n \rightarrow \infty$, energies tend to the continuum which corresponds to the free carrier bandgap : unbound electron-hole pairs. R^*_y is the exciton Rydberg energy given by :

$$R^*_y = \frac{13.6\mu}{m_0 \varepsilon^2}(eV) \tag{1.2}$$

ε is the dielectric constant of the medium and μ is the reduced mass of the electron-hole system :

$$\mu = \frac{m_e m_h}{m_e + m_e}$$

The evolution of exciton binding energy and Bohr radius as a function of principal quantum number n are different for 2D and 3D excitons. In a first approximation for 3D excitons, the binding energy can be given by :

$$E_B^{3D} = R_y^* \frac{1}{n^2} \tag{1.3}$$

Therefore, we expect the different energy levels for $n = 1, 2, 3..$, give corresponding transitions in optical spectroscopy experiments. The signal amplitude of these transitions can be assessed through a dimensionless parameter called oscillator strength f_n. The oscillator strength decreases with increasing n as :

$$f_n^{3D} \propto n^{-3} \tag{1.4}$$

Now we discuss about 2D excitonic properties. The binding energy of the exciton E_B which is defined earlier $E_B = E_g - E_{\text{exc}}^{2D}$, decreases when n increases. The binding energies of 2D excitons in terms of the principal quantum number can be written as [14, 15]:

$$E_B^{2D} = R_y^* \frac{1}{(n - \frac{1}{2})^2} \tag{1.5}$$

and the oscillator strength of an excitonic state is different in the 2D case compared to 3D :

$$f_n^{2D} \propto (n - \frac{1}{2})^{-3} \tag{1.6}$$

Comparing relations 1.3 and 1.5 shows the binding energies can change significantly while going from 3D exciton to 2D exciton. We can further understand this with an example for $n = 1$, in 3D we get a binding energy equal to R_y^* however in 2D case, it is $4R_y^*$. By considering relations 1.4 and 1.6, we conclude that the oscillator strength which depends on the principal quantum number are different for 2D and 3D excitons. These two parameters play a very important role in fundamental properties of TMD monolayers.

The binding energy depends on several factors, for example when the dimensionalities of exciton are reduced from 3D to 2D, the electron and hole are confined in the 2D plane. In this case, both carriers are spatially much closer which leads to strong Coulomb interaction. It can be also affected by the local dielectric environment experienced by 2D exciton because electric field lines between the electron and the hole extend outside the monolayer. The local environment (vacuum, SiO_2, hBN, etc...) with a smaller dielectric constant compared to TMDs is used for experiments which reduce dielectric screening for a 2D exciton compared to a 3D exciton in a bulk TMD.

Furthermore, by considering the simple hydrogenic model 2D excitons in TMDs have a large reduced mass $\mu \approx 0.25\ m_0$. This value of μ is very large compared to the case of GaAs for which $\mu \approx 0.06\ m_0$. The binding energy increases with reduced mass, see Equ. 1.2. The binding energy of excitons in TMD monolayers is of the order of several hundreds of meV, which is considerably larger than for other typical semiconductors such as GaAs ($\sim$ 10 meV) or ZnO ($\sim$ 60 meV [16, 17, 18, 19, 20].

The binding energy E_B can be determined experimentally using techniques such as linear reflectance, scanning tunneling spectroscopy (STS), 2-photon (PLE), second harmonic generation. But in reality, it is difficult to measure the free carriers bandgap because it merges with higher energy excitonic states Fig. 1.7. Hence we could not determine the binding energy directly from experiments. However, it is possible to extract the binding energy using simple optical spectroscopy experiments such as photoluminescence (PL) or reflectivity when $n_B \longrightarrow \infty$. The energy, when $n_B \longrightarrow \infty$ corresponds to the free particle bandgap. By measuring the energies for different excitonic states ($n = 1s, 2s, 2p, 3s...,$) and extrapolating, the value of E_g can be deduced. The binding energy E_B can be extracted by taking a difference between the free carriers bandgap E_g and the optical bandgap E^{2D}_{exc}. In an ideal 2D system, the binding energy is given by : $R^*_y \frac{1}{(n-\frac{1}{2})^2}$ from the relation 1.1 in a hydrogenic series with $n = 1, 2, 3, \ldots$. In fact, samples show deviation from the relation 1.1. Therefore, we must take in account the Coulomb interaction which is very sensitive to the local dielectric environment. The Coulomb interaction varies from the $(\dfrac{1}{r})$ law caused by the nonlocal dielectric screening associated with a spatially inhomogeneous environment [13, 21]. Hence, the electron and hole separation variation strongly affects the energy spacing of the $n = 1, 2, 3, ..,$ exciton states leading to large deviations from the 2D hydrogen model. Theoretical calculations of excitonic states and binding energies in TMD MLs have been performed using several approaches, including effective mass methods, atomistic tight-binding, and density functional theory (DFT). In the effective medium approximation, the dielectric constant of the TMD monolayer is larger compared to the dielectric constants of the surroundings. As a consequence, an effective interaction potential varies differently for large and small relative electron-hole separation in TMD ML [13]. The resulting overall form of the effective potential, called Rytova-Keldysh potential [22, 23, 24], is given by :

$$V(r) = \frac{-e^2}{8\epsilon_0 r_0}\left(H_0\left(\frac{\kappa r}{r_0}\right) - Y_0\left(\frac{\kappa r}{r_0}\right)\right) \tag{1.7}$$

where e is electric charge, ϵ_0 is the vacuum permittivity, H_0 and Y_0 are the Struve and Neumann functions and r_0 is the effective screening length, κ is an average dielectric constant $\kappa = \dfrac{\epsilon_{top} + \epsilon_{bottom}}{2}$ with ϵ_{top} and ϵ_{bottom} are the dielectric constants of the top and bottom layers surrounding the monolayer. The screening length is given by $r_0 = 2\pi\chi_{2D}$ with χ_{2D} the 2D polarizability of the monolayer. Numerical fits of spectroscopic data in MLs WS_2, MoS_2, $MoSe_2$ and $MoTe_2$ showing $n = 1$ and excited states ($n > 1$) can be performed using Equ. 1.7, see for example [25].

1.1.4 Spin valley coupling and optical selection rules

Spin orbit effects play a significant role in the TMD bandstructure. The spin-orbit interaction is much stronger in TMDs than in graphene because TMDs consist of relatively heavier elements. This leads to large spin splitting Δ^{VB}_{SO}, especially in valence band at the K-point about 200 meV (Mo-based) and 400 meV (W-based) [11, 16, 26, 27, 28]. However, the spin-orbit splitting in the CB in these TMDs is one order of magnitude smaller (about tens of meV) than in the VB splitting [12, 26, 29, 30, 31, 32]. The smaller spin-orbit splitting at the CBM is ascribed to partial compensation of the chalcogen p- and metal d-states contributions. Interestingly, the conduction band splitting sign differs depending on the metal atom (Mo or W). Therefore, the spin degeneracy of both the conduction and valence bands is fully lifted at the K-point contrary to a typical GaAs or CdTe quantum well structures where the CBM and the VBM remain spin degenerate at the Γ-point of the Brillouin zone in a quasi particle picture.

The valence band at the K-point is split by the spin-orbit interaction in A and B-branches. Both A and B valence states can be involved in optical transitions. The optical transition from the first top valence band to the lower conduction band is called as A-exciton. Similarly, the optical transition that happen from lower the valence band to other conduction band is named as B-exciton. The energy difference between these two excitonic transitions is approximately equal to the spin-orbit splitting of the valence band Δ_{SO}^{VB}.

By choosing a suitable laser energy, we can address B or A-exciton which will be discussed in the section 3.2 of Chapter 3. In addition, by choosing σ^+ and σ^- polarized laser excitation, we can address optical transitions in the K^+ and K^- valley respectively. The valley selective optical selection rules for interband transitions in the K^+ and K^- valleys are given by the symmetry of the system. The orbital Bloch functions of the valence band states at K-points are invariant, while the conduction band states transform like the states with angular momentum components of $+1$ or -1. Therefore the optical selection rules for interband transitions at K-points are chiral, electrons can move VB ↔ CB transitions between states with the same spin orientation [26, 33, 34, 35, 36, 37]. As a consequence, the K^+ valley can be excited with a σ^+ polarized laser while K^- valley using a σ^- polarized laser see Fig. 1.6. These features of TMDs is important for studying the valley degree of freedom in a very simple fashion. The degree of polarization can be measured in PL and is given by :
$P_c = \dfrac{I_{\sigma^+} - I_{\sigma^-}}{I_{\sigma^+} + I_{\sigma^-}}$, where I_{σ^+} or I_{σ^-} are the intensity of the right (σ^+) and left (σ^-) circularly polarized emission. The circular polarization in time-integrated experiments depend on the exact ratio of PL emission time versus depolarization time (τ_{depol}) : $P_c = \dfrac{P_0}{(1+\frac{\tau_{PL}}{\tau_{depol}})}$, where P_0 is the initially generated polarization, τ_{PL} is the exciton lifetime. Extrinsic parameters such as short PL emission times due to nonradiative channels can strongly affect this value, therefore a detailed analysis of steady-state experiments is challenging. The polarization decay time (τ_{depol}) for exciton of the order of *ps* has been measured [38, 39]. Spin conserving intervalley scattering is generally energetically unfavorable as electron or hole either has to change spin to go from one valley to the other. In another circumstance, if it preserves its spin but has to overcome the spin-orbit splitting especially large in the valence band. Therefore, spins- and valleys are coupled, one demands changing valley state while other requires flipping spin. Moreover, the valley dynamics in TMD MLs is strongly influenced by the Coulomb interaction between the charge

carriers [40]. The long-range Coulomb exchange interaction between the electron and hole forming an exciton gives rise to efficient decay mechanism for the exciton polarization. This mechanism is efficient only for bright exciton states and the dark states which are spin forbidden transition remain unaffected. This we can understand by assuming a bright exciton propagating in the ML plane with the center-of-mass wave vector K_{exc} as a linear combination of eigenstates active in the $\sigma+$ and $\sigma-$ circular polarization. One eigenstate has a dipole moment oscillating along the wavevector K_{exc}, called longitudinal exciton while the other one has the dipole moment oscillating perpendicular to the K_{exc} named as the transverse exciton. The splitting between these two states (the longitudinal-transverse splitting), acts as an effective magnetic field and mixes the $\sigma+$ and $\sigma-$ polarized excitons. As a result of this, the circular polarization of the emitted light decays in time. In TMD MLs the longitudinal-transverse splitting is 1 to 2 orders of magnitude larger than 2D exciton in GaAs or CdTe quantum wells due to the stronger Coulomb interaction. This results in comparatively faster exciton polarization relaxation on ps timescales, see also section 3.2 in Chapter 3.

As excitation with circularly polarized light can induce valley polarization in a TMD monolayer. Similarly, excitation with linearly polarized light can generate a coherent superposition of K^+ and K^- valley states called valley coherence [41]. The linear PL polarization degree P_{lin} is defined as $P_{lin} = \dfrac{I_X - I_Y}{I_X + I_Y}$, where I_X (I_Y) denotes the intensity of the X and Y linearly polarized emission, respectively.

So far we have discussed mainly about the A-exciton which is optically active in our TMD monolayers (see Fig. 1.6 d-e). The A-excitons result in the lowest energy optical transition in the monolayer referred to as optical bandgap. The A-excitons show large oscillator strength in absorption and strong emission in PL, also detailed in the section 3.2 of Chapter 3.

For the light-matter interaction involving excitonic effects, optical transitions have to obey the following rules [13, 43]. First, they have to conserve energy. It means, the energy of the initial state should be equal to the final state. In another words, the valence band energy should be equal to the difference between the conduction band energy and the photon energy. Second, they have to preserve its momentum. For TMDs monolayer, exciton dispersion in two-particle representation is shown in Fig. 1.8 (b). The photon wavevector $(q_{||})$ should be equal to the exciton wavevector which is given by : $\vec{K}_{exc} = \vec{k}_e + \vec{k}_h$. Both wavevectors are almost zero inside the light cone where bright exciton transitions happen, shown in yellow color in Fig. 1.8 (b). Therefore, the exciton composed of an electron at the K^+-point and a hole at K^--point recombines at the center of the exciton Brillouin zone Γ. The bright excitons transition in electronic bandstructure is represented by yellow color in Fig. 1.8 (a). In TMDs, all optical transitions that happen at $K \leftrightarrow K$ valley correspond to bright excitons. In addition to energy and momentum conservation, optical transitions have another restriction. The initial and final states should have the same spin. The bright exciton transitions have the same spin states which are pure either oriented up or down. However, in addition to the bright excitons, we see additional optical transitions at lower energies compared to the bright excitons in PL emission. There are two possibilities which could allow these transitions : (i) Electrons have to mix their spin states in order to conserve

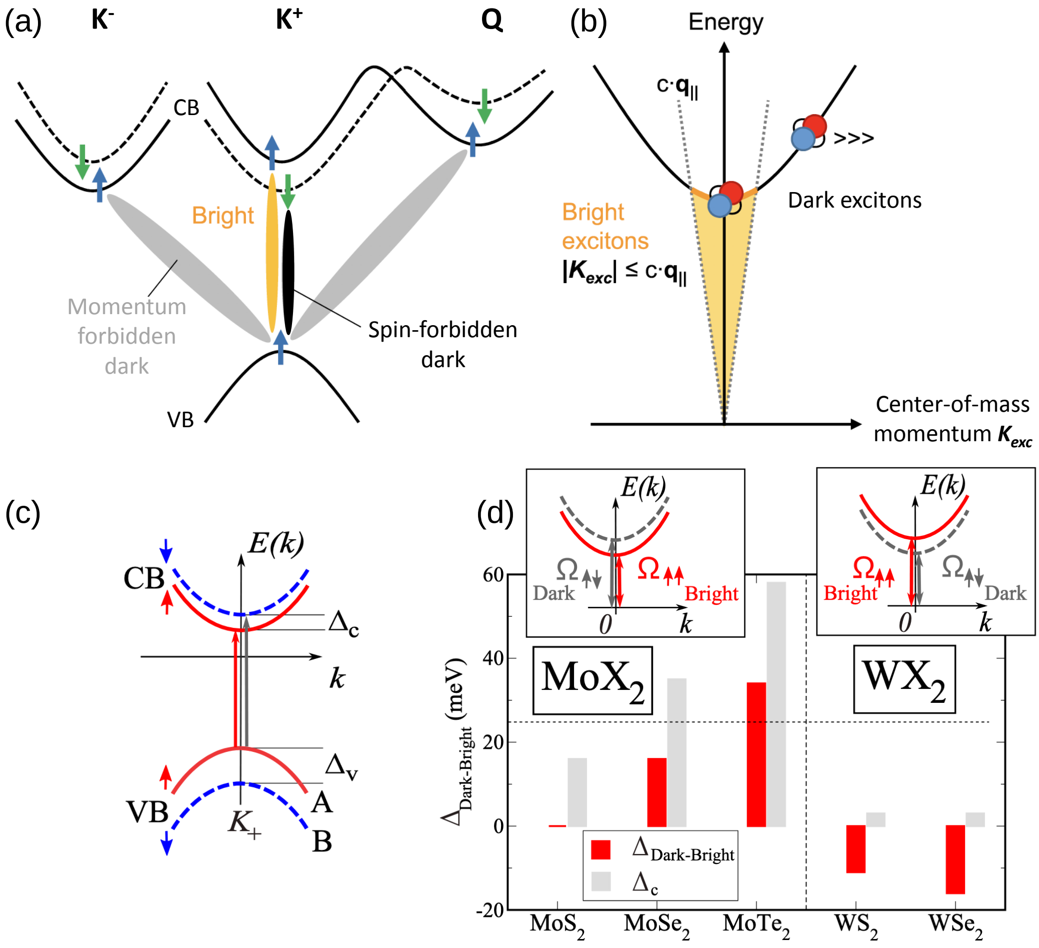

Figure 1.8: **(a)** A schematic of typical optical transitions for the bright and dark exciton states. For simplicity, we have shown only transitions evolving between the upper valence band at K-points and the high-symmetry points K and Q in the conduction band in W-based monolayers. **(b)** A pictorial illustration of the exciton ground-state dispersion in the two-particle representation. The light cone for bright excitons is marked by the free-space photon dispersion $c.q_{||}$, where c is the speed of light and the excitons outside of the cone are dark. The figure is reproduced from [13]. **(c)** Schematics of the one-particle bandstructure of systems for MoX$_2$ ML in the K^+ valley. The spin-orbit induced splittings for valence (VB) and conduction bands (CB) are shown. **(d)** Dark-bright energy splittings of the A-excitons in the MoX$_2$ and WX$_2$ ML from $G_0W_0 + BSE$ theory, the bright exciton energy is set to be 0, in comparison with the conduction band splitting induced by spin-orbit coupling. Insets are the corresponding qualitative bandstructure of the excitons in Mo-(left) and W- based TMDs (right), with bright and dark excitons in red and dotted gray, respectively. The figure is taken from [42].

spin, are so-called spin-forbidden dark excitons shown in black color in Fig. 1.8 (a), and (ii) The electrons with the same spin states are in two different valleys, so they have to change the valley which is possible via interacting with phonons to conserve its momentum. They are momentum forbidden dark excitons, shown in gray color in Fig. 1.8 (a). In TMDs, there are several types of phonons which provides sufficient energy and momentum to exciton for relaxation. Some phonons have energy with zero momentum. Hence, depending on the required energy and momentum for the optical transitions, phonons take part in the optical processes. In general, all optical transitions are consequences of an interplay between exciton and photon, in some cases phonons.

We will now discuss about the important differences between the two main types of excitons: bright excitons and spin-forbidden dark excitons. The bright excitons have larger oscillator strength than the dark exciton, therefore, its intrinsic radiative lifetime is shorter than for the dark state [44, 45]. The spin-forbidden dark excitons have out-of monolayer-plane optical dipole moment (which comes from symmetry) in contrary to bright exciton where optical dipole lies in the monolayer plane. Therefore, it is possible to observe the dark exciton emission by exciting with a laser in-plane to the monolayer. It can not be detected at all if light propagates normal to the monolayer-plane. However, in our PL experiments, we observe dark excitons transition in WSe_2 and WS_2 monolayers by exciting with a laser which is perpendicular to the monolayer-plane. The main reason is that we use a large numerical aperture microscope objective in excitation and detection because our samples are of few μm in lateral size. Therefore, the electric field vector at the focal tail has a significant out-of-plane component which enables excitation/detection of the dark transition even at the normal incidence, see detail in Chapter 3. Also, local strain or ripples can lower the symmetry of the 2D crystal induces a small mixing between bright and dark excitons, yielding the observation of the dark component. In W-based TMDs, the dark exciton existence can also be indirectly demonstrated in temperature-dependent PL experiments showing an increased PL yield at higher temperatures. In WS_2 and WSe_2 MLs, the dark excitons are present at lower energy than the bright excitons. Here, most excitons thermalize in these dark states, which drastically reduces the efficiency of light emission. As temperature increases, more excitons occupy the energetically higher bright states within the light cone resulting increased PL emission. Moreover, brightening of these states can also be observed in low-temperature magneto-PL experiments by applying strong in-plane magnetic fields. This increases the mixing of the spin-states and softens the spin-selection rule [46, 47, 48, 49]. As a result, dark excitons appear about 50 meV below the bright exciton resonance in magneto-PL spectra of W-based TMDs.

We have discussed above the main differences between the bright and dark excitons including the possible optical transitions in W-based TMDs. We will now highlight the main differences in optical transitions for W- and Mo-based TMDs. Before going in detail we first underline fundamental differences between these materials. The spin-orbit interaction that lifts the spin degeneracy of the CB has a opposite sign for W- and Mo-based TMDs. This is why the dark excitons transition is at lower energy than the bright excitons. According to first DFT prediction [50], the conduction band splitting in W-based TMDs is larger compared to MoS_2 and $MoSe_2$, where CBs crosses at the K-point of the exciton Brillouin zone, see Fig. 1.6

(d-e) [29, 31].

For an example, we consider the transitions involving between the highest VB and the two lowest CBs in a single-particle picture of a typical TMDs ML as shown in Fig. 1.8 (c-d). Here $\Omega_{\uparrow\downarrow}$ represents spin-forbidden dark excitons transition and $\Omega_{\uparrow\uparrow}$ shows bright exciton transition. In a simple approximation, the energy splitting between bright and dark excitons is $\Delta_{dark-bright} = \Omega_{\uparrow\downarrow} - \Omega_{\uparrow\uparrow}$ mainly due to the CB splitting (Δ_c) induced by spin-orbit coupling. Hence, it appears that Δ_c can either be negative for WX_2 or positive for MoX_2 systems. But for the accurate determination of the dark-bright exciton splitting, we need to consider the short-range part of the e-h Coulomb exchange interaction for the exciton [42]. Therefore the dark-bright exciton splitting is given by : $\Delta_{dark-bright} = \Delta_{exch} + \Delta_c$. This splitting is positive for A- excitons in the cases of $MoSe_2$ and $MoTe_2$ MLs. These results are in agreement with the measured dependence of the photoluminescence intensity with respect to the temperature. In these materials, PL intensity goes down drastically by increasing temperature from $T = 4\ K$ to $300\ K$ [46, 51]. Similar observation has been shown in MoS_2 MLs and therefore is considered to be the bright excitons transition is at lower energy than the dark excitons. In MoS_2 ML, this is not conclusive yet as the CB spin-orbit splitting and the exciton exchange term almost cancel each other yielding very small bright-dark exciton separations. Recent magneto-optics results indicates that the spin-forbidden dark exciton in MoS_2 MLs encapsulated in hBN is about 15 meV below the spin-allowed bright exciton [52]. So an unified explanation for temperature dependent, magnetic-field dependent and optical dipole dependent spectroscopy still merits further investigation.

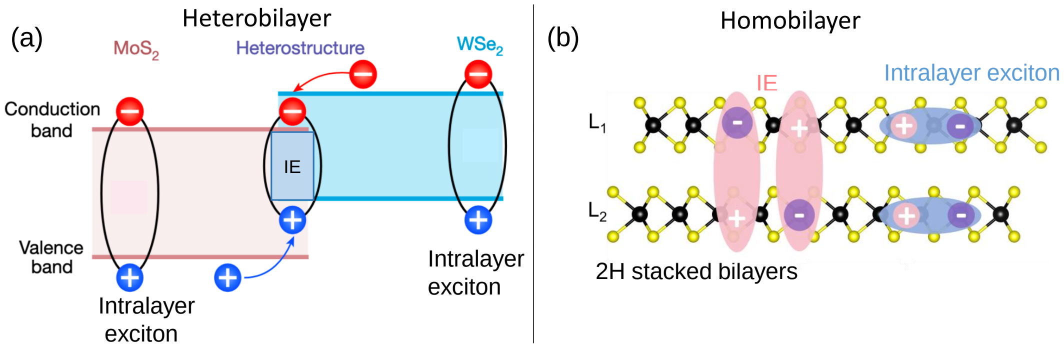

Figure 1.9: **(a)** Schematic of type-II band alignment in the WSe_2 - MoS_2 heterostructure with intralayer (A:1s) and interlayer (IE) excitons. The red and blue areas represent corresponding bands in the two individual materials and the heterobilayer. Holes and electrons are represented in positive and negative symbols, respectively. The figure is taken from [53]. **(b)** Interlayer excitons formation while a hole is delocalized over two different layers is represented in red area and intralayer excitons can be created when the electrons and holes are in the same layer.

In TMDs, there could be other possible optical transitions which are different than free excitons. For example : in the presence of impurities or strain in TMD samples, electrons and holes can be trapped in potentials resulting in localized excitons [54, 55, 56]. It can be determine as a spectrally narrow resonances appears below the bright A-excitons in PL spectra at low temperature, see also section 3.1.1 in Chapter 3. These resonances can be ascribed to excitons trapped in local potential wells. They disappear at higher temperatures, where the thermal energy is sufficient to overcome the trapping potential. Localized excitons which bind to impurities or defects give important information about the materials purity and the nature of the impurities. It has been shown in the past that these impurity analysis are of a great importance to reach an effective and controlled doping of the material in some case as a source of single photons.

In addition to the large variety of neutral excitons, other exciton complexes such as charged excitons (trions) or biexcitons can be observed [57, 58, 59]. All these different excitonic transitions make the optical spectra rich, and sometimes difficult to interpret like in the case of tungsten-compounds with still many open questions. The study of exciton species and their identification is very important both fundamentally and for future applications.

1.1.5 Bilayer TMDs

The physics of excitons in monolayer TMDs is well developed. Excitons in multilayer van der Waals (vdW) structures is currently rapidly a growing research field because if offers new excitonic features for light-matter interaction. When going from monolayer to bilayer structures the electronic bandstructure changes which significantly can lead to new tunable optical properties compared to a monolayer.

The van der Waals TMDs heterostructures switch from a direct to indirect bandgap material by adding one atomic layer on monolayers. We have seen in Fig. 1.6 (b), that the band extrema K_v, Γ_v and Q_c(which is located between M and Γ) shifts significantly while going from bulk to bilayer. The interlayer hopping between the P_z orbitals of the nearest neighbor chalcogen atom is larger compared to other orbitals which are more localized within each layer. It means that the interlayer hopping at K_v is much weaker than Γ_v and Q_c because K_v does not have a contribution from P_z orbital like Γ_v and Q_c [9, 13]. These effects considerably modify the light-matter interaction in a bilayer. This results in the formation of new exciton complexes where the electron and hole residing in different layers see Fig. 1.9 (a). These spatially separated particles can form a so-called interlayer exciton. Note that in this thesis, the interlayer exciton is labelled as (IE).

In contrary to monolayer, bilayer or multilayer offers a new degree of freedom i.e twist angle. The *2H* stacking is the most stable configuration for homobilayer TMDs where the upper layer is rotated by 180 degree with respect to the bottom layer [60]. Due to the restoration of inversion symmetry in *2H* bilayers the valley dependent physical properties of each monolayer such as the valley optical circular polarization and valley Hall effect on average are zero. However, a perpendicular electric field can break the inversion symmetry which can make these materials useful for valley circular dichroism [61] and a valley Hall effect experiments [62]. Hence it possible to tune valley physical properties by changing the symmetry of the system with a perpendicular electric field [9].

Interlayer exciton have been investigated experimentally in TMD heterobilayers by aligning two different TMDs layers on each other in type-II band alignment. This means that the conduction band and valence band of the second semiconductor are both lower than the band extrema of the first semiconductor, see Fig. 1.9 (a) [63]. The most commonly used combination is $MoSe_2/WSe_2$. The lattice mismatch in vertically stacked twisted bilayers assists the formation of moiré patterns which offers the possibility to manipulate their electronic properties [53, 64, 65], see also Chapter 3. The interlayer exciton in heterobilayers can be detected in photoluminescence. However, it has much smaller oscillator strength compared to the intralayer excitons which give rise to long recombination times measured for interlayer excitons which exceed *ns*, an order of magnitude longer than the intralayer excitons *ps*. In heterobilayer system, electron and hole are in opposite layers, interlayer excitons have a permanent electric dipole in the out-of-plane direction. This enables a large Stark shift (transition energy shift) of interlayer exciton by the application of out-of-plane electric field in a gated device. The electron is located in either the top or bottom layers decided by the initial stacking [63]. Heterobilayers composed of a monolayer with a hole is located on top of another monolayer carrying an electron in type II band alignment. Hence, by applying a negative gate voltage, we can increase the relative band-offset lead to a blue shift in PL. However, in an inverted system, where the stacking order of the two different layers is reversed, shows a red-shifted [63]. Subsequently, the direction of its permanent dipole can be determined from the electrical control of the energy of IE.

The interlayer exciton can also be formed in homobilayers [9, 60, 66, 67]. The fundamental difference between interlayer excitons in hetero- and homobilayers is that in heterobilayers the interlayer excitons are indirect in both real and reciprocal space while interlayer excitons in homobilayers are indirect in real space but direct in reciprocal space [68, 69]. An important point to note is that because of large oscillator strength in homobilayers the interlayer exciton transitions are visible in absorption whereas in heterobilayers this feature appears in emission only [60, 66, 68] discussed further in Chapter 5. In MoS_2 homobilayers investigated in this thesis, the interlayer exciton form when an electron is localized in one layer while the hole is delocalized over both layers for $K-K$ transitions. Interlayer excitons in MoS_2 bilayers have a permanent built-in electric dipole oriented out-of the bilayer plane and have degenerate states at zero electric field. Therefore, we can lift the degeneracy of two IE states by applying a perpendicular electric field. This effect enables us to achieve an exciton energy separation of two IEs by as much as 120 meV (more than 10 times of their linewidth). There are two main characteristics of interlayer excitons which are useful to identify them experimentally. First, the interlayer excitons show large Stark shift compared to intralayer excitons by applying out-of-plane electric field. In addition, the interlayer character of the transitions in an applied magnetic field shows large Zeeman splittings with opposite signs compared to intralayer transitions. The detail results are shown in Chapter 6.

In homobilayers, interlayer exciton formation strongly depends on the stacking order of the layers. In *2H*-bilayers, the interlayer coupling of valence states is nonzero which leads to the formation of interlayer excitonic states. However, interlayer exciton can not form in *3R*-bilayers because of the absence of interlayer coupling. These are illustrated in detail in Chapter 8.

In this chapter, we have underlined the fundamental properties of TMDs, the monolayers are direct bandgap semiconductors. We have also described the strong excitonic effects in TMDs monolayers which dominate in the optical spectra of TMD monolayers. The binding energy of 2D excitons is extremely large up to several hundred meV, one to two orders of magnitude larger than the excitons in III-V quantum wells. In TMDs, chiral selection rules allow us to create carriers in two different valleys (K^+ and K^-) of the momentum space by means of light of different circular polarization. We have also discussed that the electronic bandstructure changes while increasing TMD layer thickness. This leads to new excitonic features IEs appearing in TMD bilayers. We can tune the transition energy of the interlayer excitons by applying out-of-plane electric as well as magnetic fields. The detail studies on optical properties of MoS_2 and $MoSe_2$ monolayers, bilayers and trilayers will be presented in the following Chapters. We will also present the high optical quality of van der Waals heterostructures assembled using CVD-grown monolayers.

Chapter 2

Sample Fabrication

In the previous chapter, we have studied optical properties of TMDs layers. These properties very much rely on the sample quality. Hence it is important to discuss some technical details about sample fabrication, which is the goal of this chapter. The deterministic transfer methods developed at LPCNO is implemented to fabricate all samples which are used throughout this PhD thesis.

2.1 Monolayer isolation

As described in the previous chapter, most of the attractive optical and electronic properties of 2D materials appears when TMDs are an atomic layer thick. The most common examples are electron transport physics in graphene, or rich spin-valley physics in TMDs with broken inversion symmetry and direct bandgap. Monolayers of 2D materials could be obtained in two different ways : (i) "top-down" methods i.e. exfoliation from the bulk material, and (ii) "bottom-up" methods of single-layer growth. In this thesis, we have used two methods for sample fabrication : mechanical exfoliation (LPCNO) and CVD growth of high quality crystals (performed by collaborators). We will present both of these methods in the next sections.

2.1.1 Mechanical exfoliation

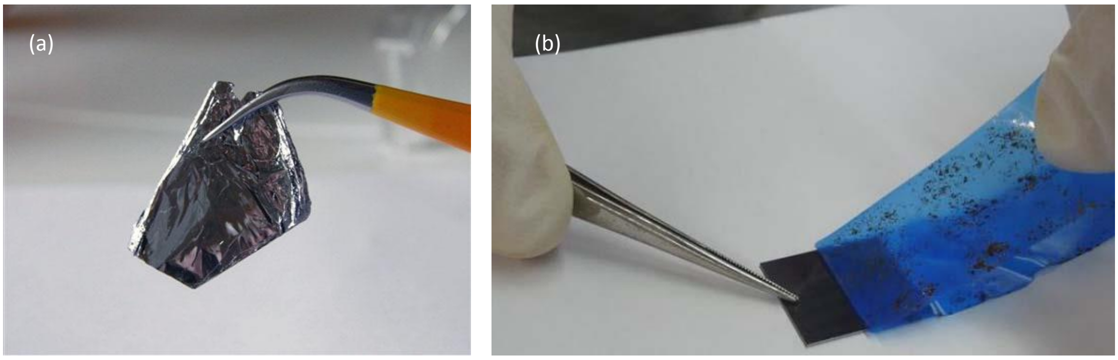

Figure 2.1: **Mechanical exfoliation**. **(a)** MoS_2 bulk crystal are used for mechanical exfoliation. **(b)** Final step is peeling off sticky tape with the crystals from the substrate.

This technique became famous after pioneering works in graphene and MoS_2 [70, 71] and since then it has been greatly improved. Mechanical exfoliation is a relatively simple technique that exploits weak van der Waals interaction between several number of layers of 2D materials. To start exfoliation, the first step is to select a high-quality bulk crystal shown in Fig. 2.1 (a), that will serve as source of exfoliated monolayers. The TMD bulk materials can be purchased from commercial suppliers such as 2D semiconductors. The bulk crystals are brought in contact with a piece of sticky tape in order to cleave and peal-off some pieces of the crystals. The pieces of the crystals which are now stuck on the scotch tape are further cleaved on the clean part of the same tape. This step is then gently repeated about 3-4 times to "open" the bulk crystals so that a major part of the tape surface is covered. In the next step, the side of tape with freshly cleaved crystals is applied on a SiO_2/Si substrate. Before this, for a better interface between the TMD layer and SiO_2/Si substrate, the substrate is cleaned with acetone and isopropanol using ultrasonication for 10 minutes. The substrate is then dried with a nitrogen (N_2) gun and exposed to 10 W oxygen/N_2 plasma for 2 minutes (we are using plasma treatment machine (NanoETCH SCI 1094). This pretreatment activates the surface, which significantly improves monolayer yield on SiO_2/Si substrate. All of these steps are performed in a chemistry laboratory and not necessarily in a clean room. The final step of exfoliation, shown in Fig. 2.1 (b) is to slowly peel-off the scotch tape from the substrate, leaving thin flakes including monolayers on the surface. Alternatively, crystals can be exfoliated on a piece of polydimethylsiloxane (PDMS) polymer stamp for further transfers which will be discussed in the next section.

2.1.2 Deterministic exfoliation

To fabricate van der Waals heterostructures, i.e. to stack different layered materials on top of each other, it is essential to deposit layers at precise locations on a substrate in a controlled way. However, the basic mechanical exfoliation process described in the previous section transfers the layers at random locations onto the substrate. To overcome this issue, we will introduce a method which relies on the use of a PDMS viscoelastic stamp [72]. In this approach, instead of transferring the layers directly from the scotch onto a substrate, we transfer the flakes from the scotch tape onto a PDMS stamp supported by a glass slide. In the next step, we look for a monolayer by looking at the optical contrast under an optical microscope. The PDMS stamp on a glass slide is carefully fixed on a mechanical stage which can move in the XYZ directions using micro-manipulators under an optical microscope, see Fig. 2.2 (b)-(c). The whole PDMS surface with several TMD flakes of random thickness is thus scanned with an optical microscope with a long working distance objective. We use an Olympus objective MPLFLN x 10 with a working distance of 11 mm. Once the monolayer is found on the PDMS stamp, it can be carefully aligned with respect to the target substrate. In the next step, by slowly approaching this stamp on a desired location of a target substrate and removing it steadily, the layers can be transferred from the stamp onto the substrate. In the final step, a thermal annealing at 150 °C in air is generally performed to enhance the adhesion of the monolayer onto the substrate. The different steps of the technique are demonstrated in Fig. 2.2 (a). It is important to mention that due to the strong light-matter interaction, TMD monolayers can be simply identified by optical contrast using an optical microscope with a high quality imaging camera. An image of a TMD monolayer on PDMS is shown in Fig. 2.3 (b). Our exfoliation setup allows us to measure the room temperature micro-photoluminescence of a flake. TMD bilayers or the multilayers have an indirect bandgap and their PL is thus strongly quenched. Therefore, the detection of a PL signal at $T = 300\ K$ is a clear indication of the single layer TMD flake. Note that Raman spectroscopy can also be used to discriminate between bulk and monolayer as E^1_{2g} and A^1_g mode shifts while going from multilayer to a single layer [73]. Atomic force microscopy (AFM) is another way to measure precise thickness of the layer precisely. However, in general, for the main members of TMD family (MoS_2, WS_2, $MoSe_2$, WSe_2, $MoTe_2$), I have gained enough experience to be able to simply identify monolayers by optical contrast. Identifying TMD bilayers and trilayers by optical contrast is more challenging. Hence we perform AFM to confirm the layer thickness [60].

2.1.3 Van der Waals hetersostructures

We have briefly discussed a deterministic exfoliation method for isolating a single layer of TMDs on a substrate like SiO_2/Si. We will now describe a technique for fabricating van der Waals hetersostructures. As mentioned in the previous chapter, in 2D crystals weak van der Waals forces between layers offer the possibility to combine layers of different materials. In van der Waals heterostructures, a single building block is held together by the covalent bonds in the atomic plane, while the van der Waals force provides the stability of the stack. Hence it is possible to combine several layered crystals not found together in nature for different heterostructures. However, it is important to note that not all layered crystals are stable under ambient condition, for instance CrI_3 and black phosphorus are extremely fragile. A problem for monolayers (that do not oxidize or degrade quickly) is the possible accumulation of adsorbents on the top surface. These contaminants are usually squeezed into micron sized bubbles by the van der Waals force itself, thus creating several clean regions on the monolayer flake. We can remove some bubbles by thermal annealing. As temperature increases to about 150 °C, adsorbent starts to move and eventually agglomerate in larger bubbles.

There are different approaches for fabricating van der Waals heterostructures. The most desirable method for fabricating these heterostructures would be van der Waals epitaxy[74], in which individual layers are grown on top of each other. But the weak van der Waals force compared to the covalent bonds in monolayer makes this method very challenging [75]. Moreover in order to avoid lattice distortion in the crystal, this method requires the lattice of the top layer to be similar (in terms of flatness and lattice constant) to that of the bottom layer. These issues are currently addressed by ongoing research projects on growing heterostructures using molecular beam epitaxy (MBE) [76]. For fundamental research, exfoliation is a practical method due to its simplicity and cost efficiency.

The most common heterostructures fabricated in our laboratory are encapsulated samples. In these heterostructures, a TMD monolayer is placed between hexagonal boron nitride (hBN) flakes, which is an insulator with a wide bandgap

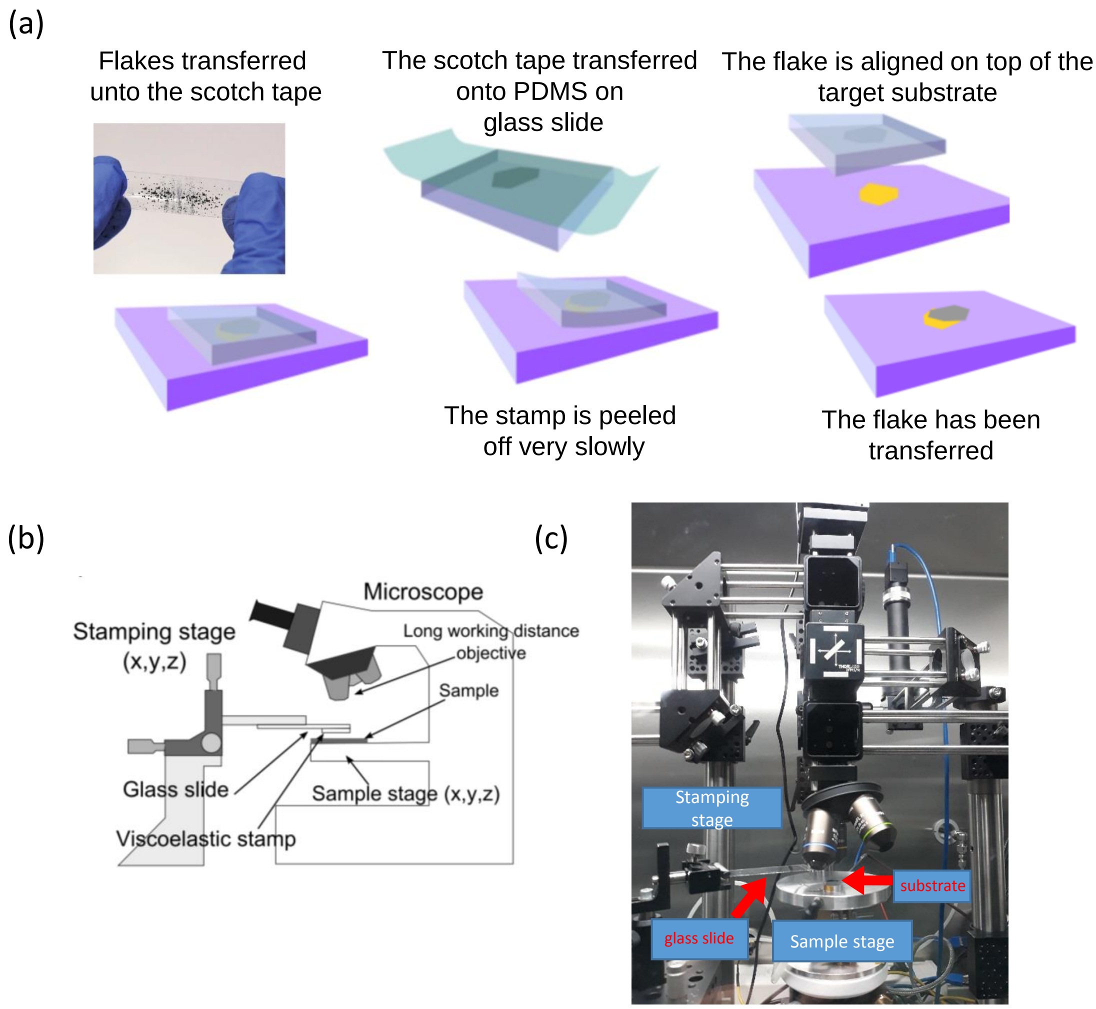

Figure 2.2: **(a)** Schematic of dry exfoliation method [72]. Stepwise procedure for the deterministic transfer of think flakes from bulk crystals. **(b)-(c)** schematic and a photograph of our exfoliation setup in which the main components are a stamping and a sample stages and a confocal optical microscope for high quality imaging and room temperature photoluminescence.

(≈ 6 eV). The bulk crystals of hBN employed in our structures are highly pure (i.e. have a considerably lower defect density than commercially available hBN), synthesized from Ba-BN solvent at the NIMS Tsukuba, Japan [77]. hBN is also a layered material and can therefore be exfoliated to obtain flakes of different thicknesses. The purpose of using a bottom hBN layer is to protect the TMD layer from the detrimental impact of the substrate, for example, surface roughness and charge fluctuations. A top hBN layer protects the monolayer from laser damage or contamination [78]. Therefore encapsulated TMD layers show considerably improved optical quality as compared to unencapsulated samples [51, 79, 80], see also section 3.1 in Chapter 3 and section 7.2 in Chapter 7 for exfoliated and CVD-grown monolayers. To prepare such heterostuctures shown in Fig. 2.3 (a), we first take high quality bulk hBN crystals on a scotch tape and fold it repeatedly so that some of these crystals spread over a large area of the tape. Employing a deterministic exfoliation method, we can transfer hundreds of flakes on the PDMS from the scotch tape. Then, using the optical microscope we look for hBN layers which should have a smooth surface and suitable thickness. We choose a particular thickness for the bottom layer of hBN because the PL emission intensity and oscillator strength of the exciton resonances are strongly influenced by the hBN thickness due to thin film interference effects [81, 82]. The flake is then transferred to a substrate, and annealed at 150 °C in air for 10 minutes. An image of a hBN flake exfoliated on a SiO_2 substrate is shown in 2.3 (b). Once the hBN bottom layer is transferred on the substrate, we repeat the same procedure for transferring a TMD monolayer. Finally, a second thinner (about 10 nm) hBN flake is used to cap the TMD monolayer. The optical micrographs of a sample at different stages are shown in Fig. 2.3 (b). Annealing is performed after transferring each layer during the fabrication process. In a similar way, we can also encapsulate TMDs bilayer and trilayer in hBN to investigate new exciton states. It will be discussed briefly in Chapters 5, 6 and 8.

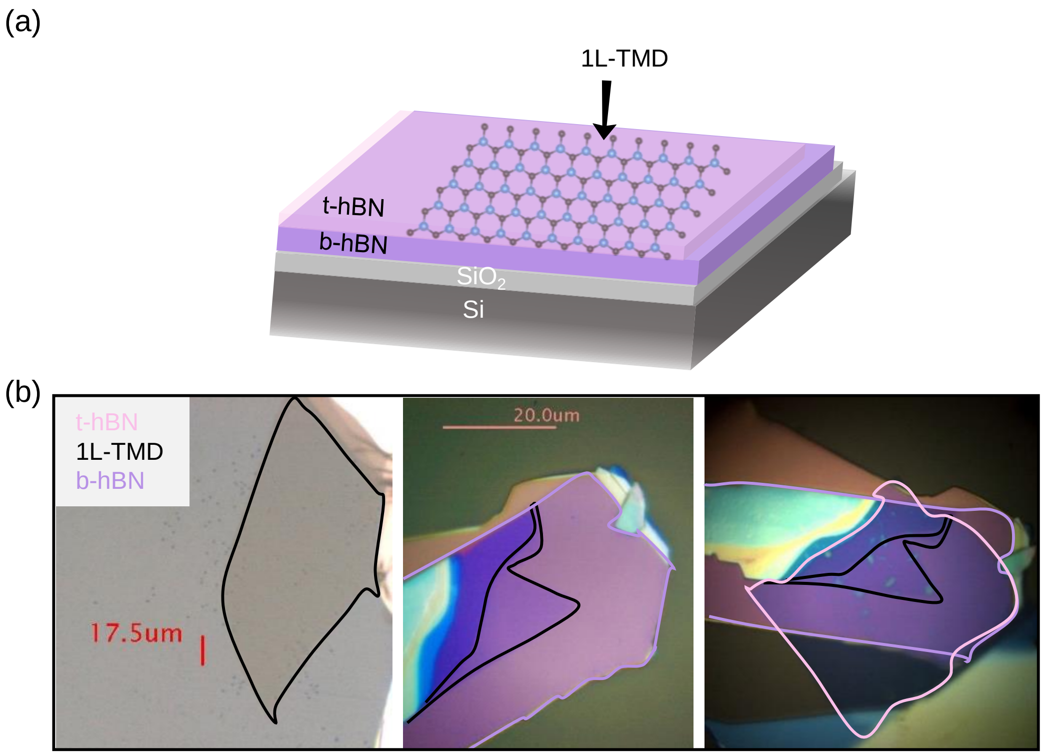

1L-TMD/PDMS 1L-TMD/b- hBN/SiO_2 t-hBN/1L-TMD/b- hBN/SiO_2

Figure 2.3: **(a)** Schematic of sample structure, where t-hBN stands for top layer and b-hBN for bottom layer hBN. **(b)** Optical microscope images at different stages of the sample fabrication : TMD monolayer looks transparent on PDMS, it is shown in black area in left panel, TMD monolayer transferred onto bottom hBN, see middle panel and the right panel shows a complete van der Waals hetersostructures on SiO_2.

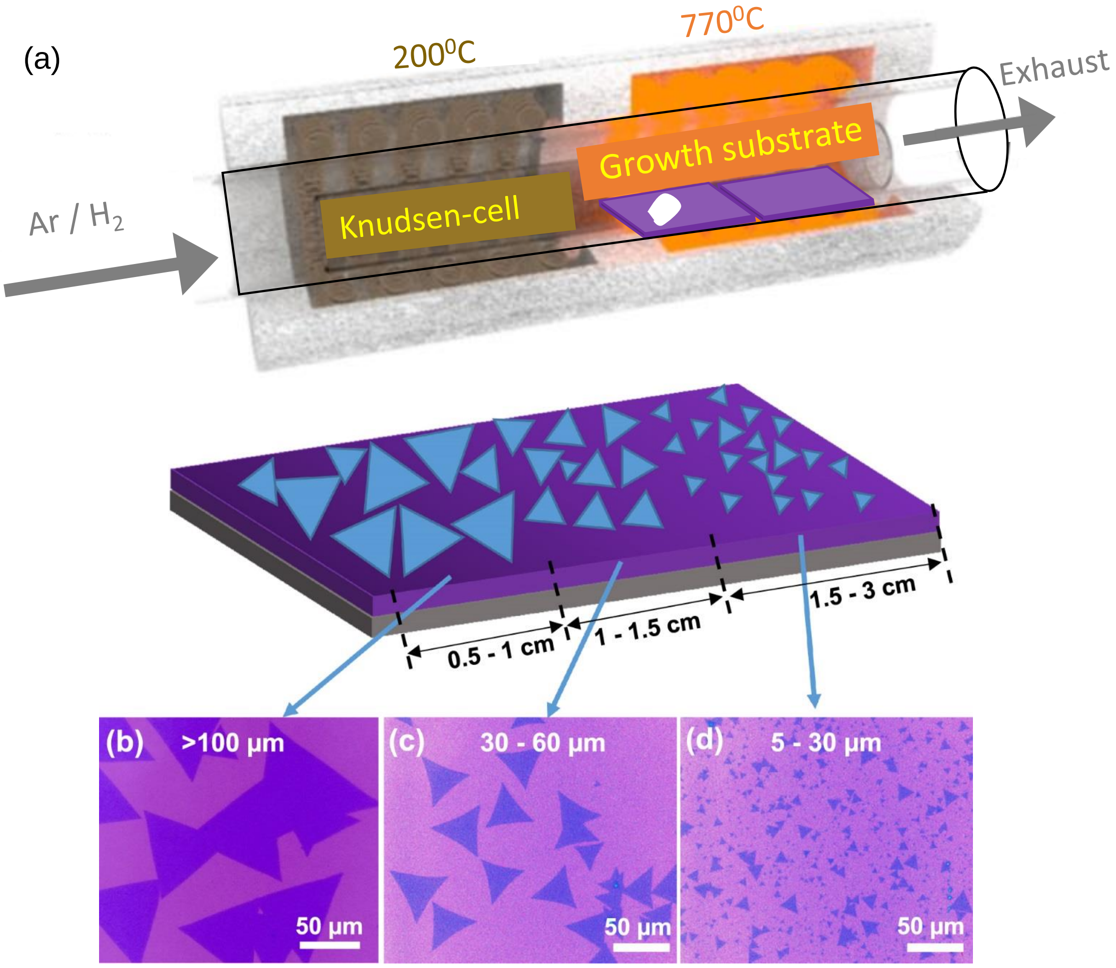

Figure 2.4: **(a)** Schematic representation of CVD set-up for the growth of MoS_2 monolayers using a Knudsen-cell. The figure is taken from [83]. **(b)-(d)** Optical microscope images of MoS_2 monolayers grown by CVD. The grown crystals have a size distribution depending on the source MoO_3 distance. As the distance increases the crystal size decreases.

2.2 Large area CVD growth

In the previous section we have detailed exfoliation methods. In this section we will describe another method for fabricating TMD monolayers. So far exfoliated TMD crystals from high quality bulk show the lowest defect density (The flux technique achieves a large reduction in defect density to below 10^{11} cm^{-2} [84]) and hence better optical response compared to crystals grown by chemical vapor deposition and molecular beam epitaxy [83, 84]. Exfoliation is very useful to fabricate high quality samples for fundamental research. There are several limitations that prevent exfoliation from being industrially viable : (a) to get a single monolayer is random (i.e. we have to systematically scan the PDMS surface for getting monolayers under an optical microscope), (b) it is time consuming, (c) the size of monolayers is relatively small with an average lateral size of tens of micrometer, and (d) the yield for finding monolayers per unit of surface area is very low.

In my typical experiments, I obtained one TMD monolayer per PDMS stamp surface area of 1 cm^2. A variety of growth methods have made possible to increase the number of monolayer flakes and control the layer size and thickness. Among them CVD is an important method used for the growth of graphene crystals [85, 86]. Moreover, CVD based synthesis is the most simple and cost effective for the growth of single crystalline TMD monolayers. CVD has already given several promising results for the growth of TMDs: MoS_2 [83, 87], WS_2 [88], $MoSe_2$ [89], and $MoTe_2$ [90]. Hence, it is an alternative approach to the mechanical exfoliation for TMD monolayers and multilayers. In contrast, to the bottom-up approach described in the previous section, this is a top-down technique which results in a controllable growth of large single-crystalline flakes [91, 92, 93]. Growth of high quality CVD samples investigated during this thesis is performed in the group of Andrey Turchanin at FSU Jena, Germany. I do spectroscopy and encapsulation of CVD-grown TMD layers, not CVD growth in Toulouse. For the growth, they use 83 nm thick silicon oxide (SiO_2) on top of silicon (Si) as a growth substrate. The thickness of the oxide layer is optimized to yield the highest optical contrast (defined by light interference [94]) for monolayer TMDs so that ultrathin layers deposited on the substrate could be identified. In this method, desirable powders of metal oxides (e.g. MoO_3 or WO_3) and chalcogens (e.g. S, Se) are used as precursors. These precursors are kept inside a reaction tube, heated to appropriate temperatures to be evaporated in an inert gas atmosphere which transports them to the target substrate, see Fig. 2.4 (a). Eventually the precursors are thermally activated to react and subsequently form the desired TMD monolayers. An important challenge for the 2D TMD high quality crystal growth is to control the flow rates of the precursors for the nucleation and growth in the reaction zone. This is achieved by using a Knudsen-type effusion cell for the chalcogen precursor instead of the most commonly used open crucible [83]. The monolayer size (lateral dimension) depends on the source (MoO_3) distance, which typically is about 100 μm.

Once the TMD monolayers are grown on the SiO_2 substrate, they are transferred onto PDMS from the substrate by a water assisted pick-up method for encapsulating the monolayers in hBN for better optical response. The detailed optical spectroscopy measurements of CVD-grown monolayer and bilayer are shown in Chapters 7 and 8. In this thesis, we will investigate and compare in detail excitonic features in monolayers and bilayers fabricated by dry exfoliation and using CVD-grown monolayers.

2.2.1 Water assisted pick-up technique

MoS_2 monolayers grown by CVD on SiO_2 will adhere ('stick') to the sample more strongly than an MoS_2 monolayer flake deposited by exfoliation on SiO_2. CVD-grown monolayers are usually released by wet etching from their growth substrate followed by polymer-assisted wet- or dry-transfer [95, 96]. These processes involve chemical etching of the growth substrates due to strong substrate interactions of the CVD films compared to exfoliated flakes. Moreover, removal of the polymer requires processing such as chemical dissolution and annealing. These processes further contaminate or degrade the 2D material which is detrimental to optical quality and eventually device performance. Therefore, to address these limitations, we fab-

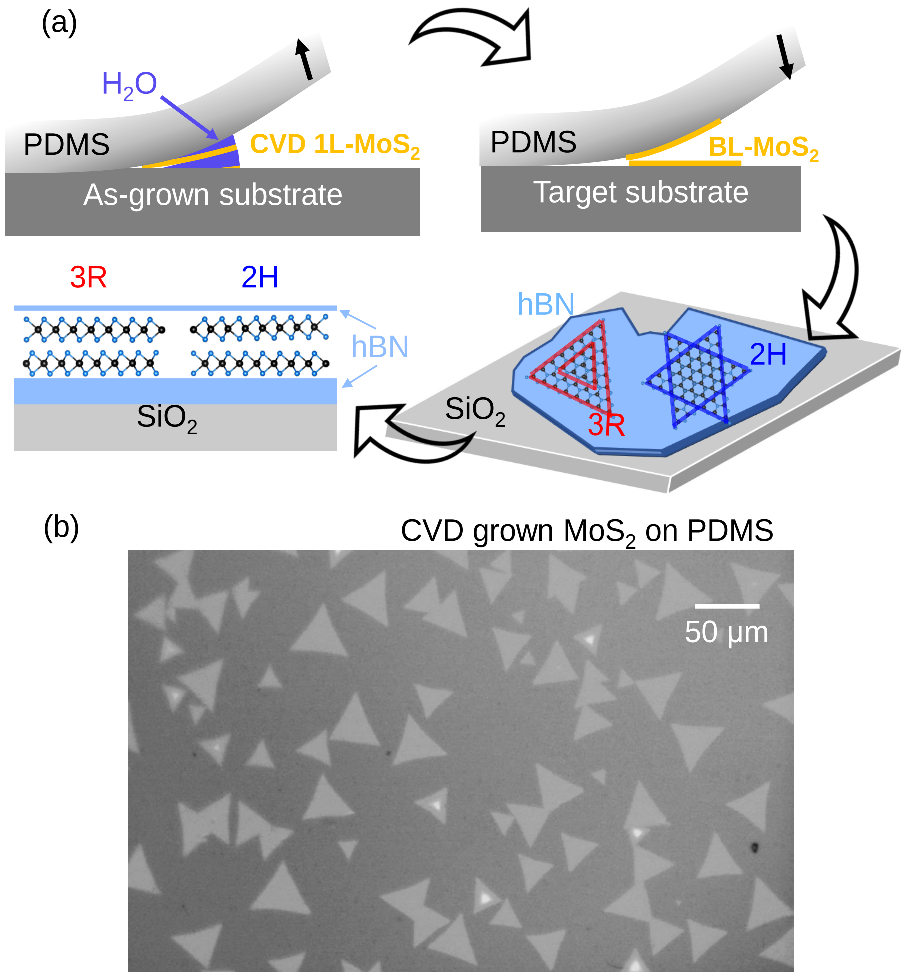

Figure 2.5: **(a)** Schematic of water assisted pick-up techniques for CVD-grown MoS_2 monolayers for assembling bilayers for optics. **(b)** Optical micrograph of CVD-grown MoS_2 monolayers and a few homobilayers, transferred to the PDMS stamp following water assisted pick-up from the growth substrate.

ricate van der Waals heterostructures with CVD-grown monolayers employing a PDMS-based water assisted lift-off process [97]. The PDMS stamp is hydrophobic in contrast to hydrophilic SiO_2/Si growth substrate when in contact with droplets of deionized (DI) water. Hence, by simply wetting the interface between the PDMS stamp and 2D thin films grown on SiO_2 substrates, monolayers can be released and transferred onto the PDMS stamp prepared on a glass slide. We can therefore assemble, for example, *2H* and *3R* stacked MoS_2 bilayers by employing water assisted lift-off and PDMS-based dry transfer, see Fig. 2.5 (a) and also Chapter 8. This transfer starts by gently pressing the substrate containing CVD-grown MoS_2 flakes onto a PDMS stamp supported by a glass slide and locking the glass slide, stamp and substrate in place by means of a scotch tape. Subsequently, DI water droplets are injected at the perimeter of the substrate, see Fig. 2.5 (a). It is crucial to allow water to penetrate into the $SiO_2\backslash MoS_2\backslash$PDMS interfaces while preventing the substrate from sliding during lift-off. The MoS_2 film would not be transferred on the PDMS stamp if the growth substrate and PDMS film are pressed together so firmly that water cannot wet the interface. Detaching the growth substrate after 1-2 minutes releases the MoS_2 material reliably and over a large area onto the PDMS stamp as shown in Fig. 2.5 (b). Thereafter, drying of the PDMS stamp with nitrogen gas prior to the final transfer step ensures that no solution trapping can occur. The risk of 2D crystal degradation and damage is minimized. Subsequently we can use deterministic dry transfer to encapsulate the lifted-off, CVD-grown monolayers in hBN. The whole process is facile, rapid, and potentially applicable to a wide range 2D materials.

We have highlighted different methods to obtain TMDs thin films. Now we will explain briefly the selection of hBN thickness which impacts the optical quality. All TMDs heterostructures that we will discuss in this thesis are encapsulated in hBN. The hBN thickness plays an important role in the optical response of the samples, see Fig. 3.2 (b) in Chapter 3. It is therefore important to acquire a certain control on the hBN flakes that we use to fabricate samples. We scan the PDMS stamp to find hBN layers and select them following the main criteria : their flatness, lateral dimensions and thickness. We use hBN as a substrate and also for capping the TMD layer. The bottom hBN layer as a substrate (thick bottom layer order of 100 nm) must be atomically flat to avoid creating strain in the TMD monolayer. It must be thick enough to avoid any impact of the roughness of the underlying substrate SiO_2 and protecting the monolayer from charge fluctuations from SiO_2. The hBN flake for capping the TMD layer should be homogeneous and thin enough (about 10 nm).

A basic way to evaluate the thickness of a hBN flake, instead of performing each time AFM, is by optical color contrast. We have developed an understanding of optical contrast variation on hBN thickness. Indeed, due to interference, hBN thin films exhibit different colors depending on their thickness. To make the identification easier, we simulate hBN colors as a function of thickness using a transfer matrix approach. Optimizing hBN thickness is very important for optical spectra to enhance the visibility of exciton resonances in reflectivity spectra of the TMD monolayer [81] and even for controlling the exciton lifetime [82]. In addition to using optical color contrast, we can measure reflectivity of an hBN flake and compare this spectrum with the simulated reflectivity to know the thickness.

2.3 Interferences in van der Waals heterostructures

In this section, we will discuss a way to select a suitable thickness of hBN for our samples. We use transfer matrix approach to model the full optical response of the multilayer structure. The shape and visibility of the excitonic resonances vary not just due to differences in oscillator strength but also because of interference effects [81]. In this section, we use this method developed with our collaborators M. Glazov and M. Semina (Ioffe Institute, St-Petersburg) to calculate reflectance of our van der Waals heterostructures.

We consider a multilayer system : hBN\ MoS_2 monolayer\ hBN\ SiO_2(83 nm)\Si, see Fig. 2.6. We calculate the following matrices :

- Matrices at the interfaces : $T_{vacuum} \rightarrow T_{t-hBN}$, $T_{b-hBN} \rightarrow$ SiO_2, $T_{SiO2} \rightarrow$ Si
- Matrices accounting for the phase shifts of each medium acquired by the wave propagating to the right and to the left : T_{SiO_2}, T_{b-hBN}, T_{MoS_2} and T_{t-hBN}.

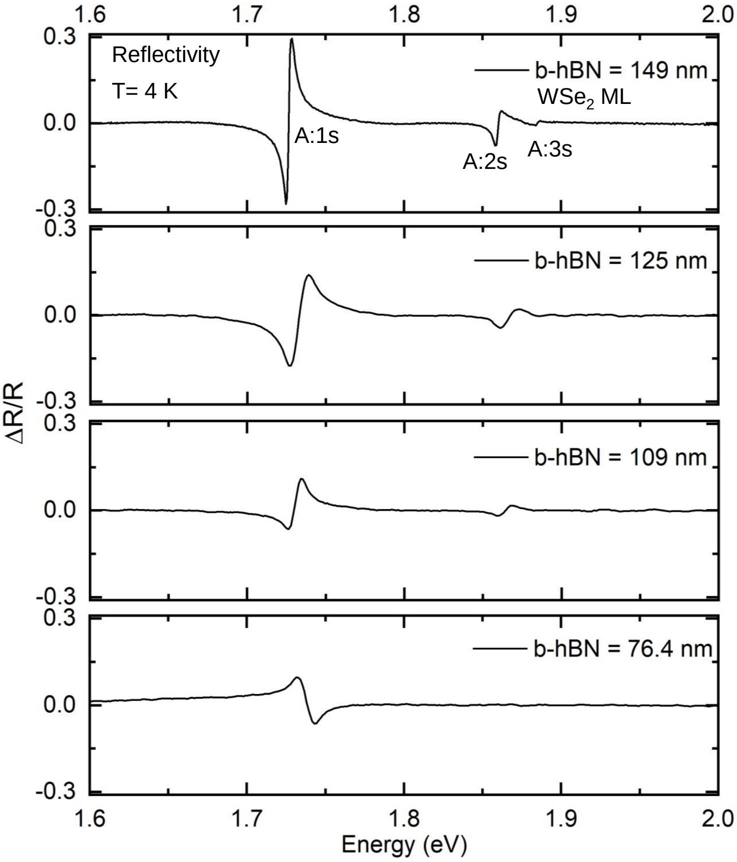

Figure 2.6: The differential reflectivity spectra (the experimental technique is detailed in Chapter 3) in black are plotted for a van der Waal heterostructure: t-hBN\WSe_2 monolayer\ b-hBN\ SiO_2(83 nm)\Si varying the bottom hBN thickness. The strong transition at lower energy is due to the A-exciton (A:1s) ground state absorption. At higher energies, two more transitions are clearly visible in the top panel, these transition are ascribed to be the higher energy excited states of the A-exciton: A:2s and A:3s respectively. The hBN thicknesses are determined by AFM. The reflectivity contrast visiblity and the shape of the exciton resonances varies significantly on bottom hBN thickness, while the thickness of other layer are fixed.

In each layer, the solution of the wave equation can be written as :

$$E(z) = E_+ e^{ikL} + E_- e^{-ikL}$$

The matrix T accounting for the phase shift in a medium with each layer thickness L :

$$T = \begin{pmatrix} e^{ikL} & 0 \\ 0 & e^{-ikL} \end{pmatrix}$$

The white light used for reflectivity propagates from the layer with the refractive index n_1 to the layer with the refractive index n_2.

The transfer matrix at an interface between the layers :

$$T_{n_1 \to n_2} = \frac{1}{2n_1} \begin{pmatrix} n_1 + n_2 & n_2 - n_1 \\ n_2 - n_1 & n_2 + n_1 \end{pmatrix}$$

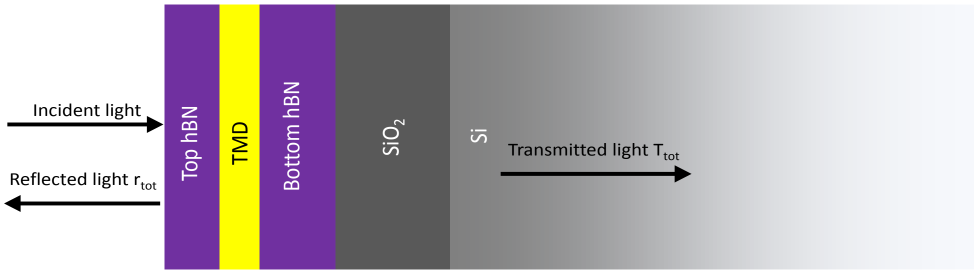

Figure 2.7: A schematic of van der Waal heterostructure for transfer matrix simulation. Light is propagating perpendicular to the monolayer plane. We numerically simulate the transfer matrix of each interface layers for calculating the reflection coefficient r_{tot}.

where, the wave vector $k = n\frac{\omega}{c}$, ω is the angular frequency of light, n is the refractive index of the medium and c is the speed of light in vacuum. Finally, we calculate the matrix accounting for the TMD monolayer :

$$T_{n_1 \to n_2} = \frac{1}{t}\begin{pmatrix} t^2 - r^2 & r \\ -r & 1 \end{pmatrix}$$

with t the transmission coefficient ($t = 1 + r$) and r the reflection coefficient.

We can express the coefficient r for the MoS_2 monolayer as [81]:

$$r(\hbar\omega) = \sum_{n=1}^{3} \frac{i\Gamma_{0,A:ns}}{E_{A:ns} - \hbar\omega - i(\Gamma_{0,A:ns} + \Gamma_A)} + \frac{i\Gamma_{0,B:1s}}{E_{B:1s} - \hbar\omega - i(\Gamma_{0,B:1s} + \Gamma_B)}.$$

It includes independent contributions of the A-exciton with principal quantum number $n = 1, 2,$ and 3 as well as that of the B-exciton, $E_{A:ns}$, $E_{B:1s}$ are the corresponding energies, and Γ_0 and Γ are the radiative and nonradiative damping of the excitons. The total transfer matrix for the whole structure is thus given by :

$$T_{tot} = T_{SiO_2} \to_{Si} T_{SiO_2} T_{\text{b-hBN}} \to_{SiO_2} T_{\text{b-hBN}} T_{\text{MoS}_2} T_{\text{t-hBN}} T_{\text{air}} \to \text{t-hBN} \qquad (2.1)$$

The transfer matrix provides the following relation between r_{tot} and t_{tot} which are the amplitude reflection and transmission coefficients respectively through the structure :

$$T_{tot}\begin{pmatrix} 1 \\ r_{tot} \end{pmatrix} = \begin{pmatrix} t_{tot} \\ 0 \end{pmatrix}. \qquad (2.2)$$

Equation 2.2 allows us to obtain r_{tot} from the transfer matrix 2.1 by simply multiplying matrices of each medium at interfaces. By keeping L_{SiO_2} = 83 nm, L_{t-hBN} = 15 nm and varying the bottom hBN thickness (L_{SiO_2}) in the matrix 2.1, we evaluate the shape and relative intensities of the exciton transitions in the reflectivity spectra. Using this approach in our heterostructures, we choose appropriate bottom hBN thickness for the enhanced visibility of excitonic resonances. We note in Fig. 2.6 for example that for an encapsulated WSe_2 monolayer in hBN the visibility of the exciton features is much better for a bottom hBN thickness of 149 nm as compared to 76.4 nm.

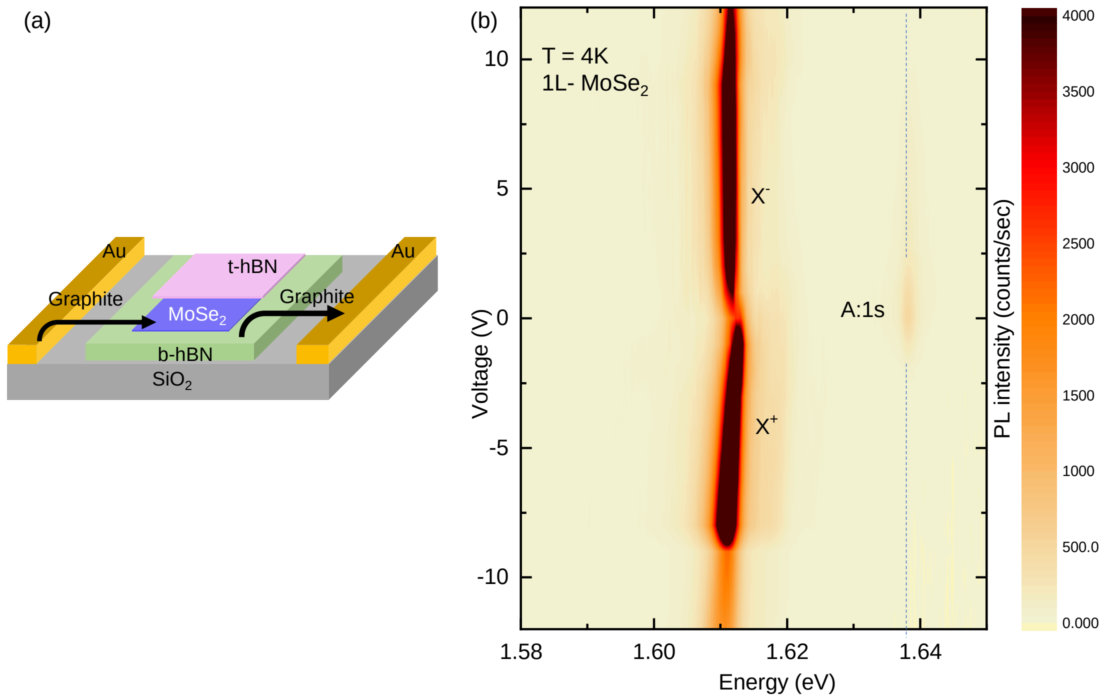

Figure 2.8: **(a)** Schematic of encapsulated $MoSe_2$ monolayer charge tunable device. **(b)** Colormap of photoluminescence spectra as a function of applied voltages at $T = 4\ K$. Holes are injected in the monolayer at positive voltages whereas electrons are injected at negative voltages. Two transitions associated to charged excitons (X^+ and X^-) appear while comparatively weak A:1s emission disappears by application of external voltage.

2.4 Heterostructure device

It is also possible to fabricate heterostructure devices using the same approach as mentioned above for controlling the charge density or for tuning electric field inside a TMD monolayer. The silicon substrate is connected to a source meter and acts as a back gate while the top surface is patterned with gold electrodes. The bottom hBN flake is exfoliated close to one electrode and, after the deposition of the monolayer, a thin graphite flake is used to connect with the gold electrodes, see Fig. 2.8 (a). Note that we position the graphite flake with the same technique as used for TMDs and hBN, namely with a PDMS stamp. A capping hBN layer is used on the top of the stack to protect the TMD layer. In this scheme, applying a voltage between the top and the back gate will modify the charge density of the monolayer, thus allows to explore effective p- and n-doping regimes (X^+ and X^-), see Fig. 2.8 (b). If the doping is significant, charged excitons (or trions) can be formed and become dominant over the main neutral transition (A-1s) in the optical spectra, see Fig. 2.8 (b). These three particles complexes consist of a charge (an electron or a hole, depending on the type of doping) bound to a neutral exciton. Note that with little variation on charge tunable structure it would be possible to build a device in which we can apply different electric fields to the material without changing the doping level, for studying the variation of its optical response (in a double gated structures). The detailed optical spectroscopy results on new exciton features in MoS_2 bilayers and trilayers in applied electric field will be given in Chapter 6. Using different 2D materials in desired configuration with certain stacking orders allows to build devices with different functionalities such as light emitting diodes (LEDs) [49].

In this chapter, overview of different fabrication techniques has been discussed. Among them, mechanical exfoliation is described as it is the most popular in the scientific community working on TMD monolayers. However, researchers are also developing another methods for high quality wafer scale production of TMDs for future industrial applications. In our laboratory, the deterministic transfer technique with PDMS has been used extensively for fabricating high quality van der Waals heterostructures. It remains a technique with many attractive aspects : low cost, applicable to many materials and resulting in high optical quality compared to other methods. We have also developed an understanding of the impact of interference effects in multilayer systems which significantly changes the visibility of exciton resonances. In all our heterostructures, the bottom hBN thickness is carefully chosen based on transfer matrix simulations to have a better optical response. We have shown that electric field tunable and change tunable device can also be fabricated using deterministic exfoliation methods. We have developed a water assisted pick-up method to assemble CVD-grown TMD layers with clean interfaces, as will be detailed in Chapter 8. This approach will be useful for fabricating large area TMD heterostructures with different stackings (i.e. twist angles), combining TMD layers on hybrid structures to engineer optical and electric properties.

Chapter 3

Optical spectroscopy techniques

In this chapter I give an introduction to optical spectroscopy for layered materials as a powerful, non-invasive tool to access details of the electronic bandstructure and crystal quality which have been discussed in the previous chapters. Potential applications in photonics and optoelectronics are based on our understanding of the light-matter interaction on an atomic monolayer scale. Here atomically thin transition metal dichalcogenides, such as MoS_2 and WSe_2, are model systems for layered semiconductors with a bandgap in the visible region of the optical spectrum. They can be assembled to form heterostructures and combine the unique properties of the constituent monolayers. I will summarize the working principles of micro-photoluminescence spectroscopy and optical absorption experiments. I will discuss the physical origin of the main absorption and emission features in the optical spectra and how they can be tuned. I explain key-aspects of practical set-ups for performing experiments in different conditions such as variable temperatures or in applied magnetic fields and how parameters such as detection spot size and excitation laser wavelength impact the optical spectra. I will describe the important influence of the direct sample environment, such as substrates and encapsulation layers, on the emission and absorption mechanisms. A survey of optical techniques that probe the coupling between layers and analyze carrier polarization dynamics for spin- and valleytronics is provided. The work corresponding to this chapter is a submitted review article [98] that I wrote during my PhD thesis.

3.1 Measuring optical absorption and luminescence in layered semiconductors

The fundamental optical transitions in TMDs lie in the energy range from ≈ 1.1 eV (monolayer $MoTe_2$) up to ≈ 2.1 eV (monolayer WS_2). Ferromagnetic semiconductors, such as $CrBr_3$ and CrI_3 cover similar transition energies [99, 100]. Interlayer excitons in heterostructures such as MoS_2/WSe_2 can reach emission wavelengths above 1100 nm (<1.1 eV), approaching the telecommunication bands [101]. Black phosphorous is a layered semiconducting material with a direct bandgap that strongly varies with the number of layers and covers the visible (monolayer) to mid-infrared (bulk) spectral region [102]. The same evolution of bandgap change versus thickness occurs in $PtSe_2$ [103], but here the bandgap is indirect as for Si, so applications for detectors are possible. At the opposite end of the spectrum layered hexagonal boron nitride (hBN) has a bandgap in the deep ultraviolet at 6 eV (200 nm). Below we describe the working principles of experiments to study absorption and emission of the optical transitions in layered semiconductors.

3.1.1 Optical spectroscopy equipment

A typical spectroscopy set-up contains a light source and several optical components to guide the excitation light to the sample and the signal to the spectrometer (monochromator) and detector. A charged-coupled device (CCD) or a complementary metal–oxide–semiconductor (CMOS) camera is also essential for the sample imaging. In this section we outline the characteristics of the main components and explain in Fig. 3.1 the working principle of a versatile micro-spectroscopy set-up, widely used in commercial and also home-built systems. A typical microscope set-up shown in Fig. 3.1 can be used to perform with similar equipment photoluminescence, reflectance, photoluminescence excitation (PLE), Raman scattering and second harmonic generation (SHG) spectroscopy experiments.

Light sources.- The main parameters for the laser excitation depend on the application and the sample's bandstructure : (i) the wavelength is selected in accordance to the investigated optical transitions (ii) the laser can be continuous-wave (CW) or pulsed. Pulsed lasers are more suitable for time-resolved experiments. For femtosecond (fs) or picosecond (ps) pulse duration the spectral width should be taken into account when investigating transitions close in energy. At the same time, the laser peak power should be calculated to avoid sample damage. High beam quality (aiming for perfect collimation, i.e. low M^2 factor) lasers are preferable for focusing the beam tightly to a diffraction limited spot, considering the small lateral dimensions of many exfoliated samples. For CW excitation, laser diodes can be typically selected between 375 nm and 2000 nm. For experiments requiring tunable wavelength excitation, convenient solutions for the 700-1000 nm range include Titanium Sapphire (Ti:sapphire) lasers, which can be either pulsed (ps/fs) or continuous. To cover the wavelength range between 500-700 nm and 1000-1600 nm, an optical parametric oscillator can be coupled to the Ti:sapphire laser combined with a doubling crystal. Dye lasers can also be used, where the choice of dye and its solvent allows for the selection of the emission range. Absorption or reflection measurements are performed using a broadband white-light source to cover the full visible wavelength range. Often a simple halogen lamp suffices. When only one specific optical transition is investigated, a monochromatic LED or SLED with 10-20 nm spectral bandwidth can be used. This enables a good compromise between a small spot size and sufficient excitation power. Other solutions include laser driven light-sources or super continuum white lasers that allow to select a broad or narrow wavelength range for excitation, which makes them versatile for photoluminescence but also for broad band absorption experiments. All the experimental data presented in this thesis were performed using HeNe laser (632.82 nm), green laser (532.83 nm), Ti:sapphire laser (700-1000 nm) and white halogen lamp as a light source.

Optical components.- The optical components used in the set-up are selected for a specific wavelength range depending on both the excitation source and the

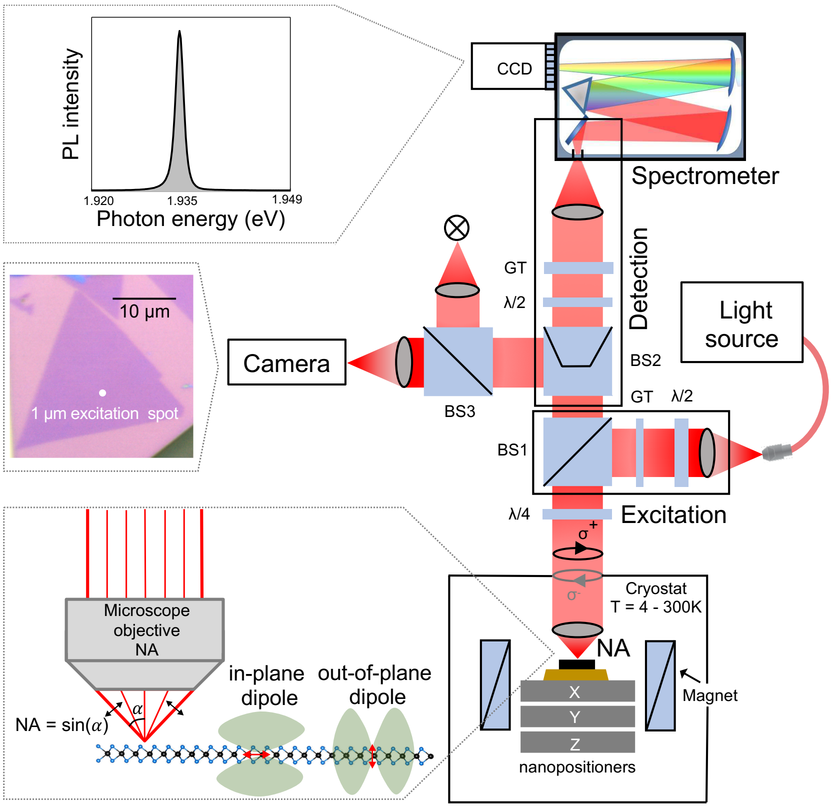

Figure 3.1: **A typical microscope for optical spectroscopy compatible for temperatures** $T = 4 - 300\ K$: Micro-photoluminescence and reflectivity set-ups have to fulfill several key criteria : High spatial resolution for sample mapping and accessing specific sample areas, high detection efficiency for example for quantum emitters in layered materials, combination of two detectors (one CCD/CMOS camera for sample imaging to guide the experiment and another camera to accumulate the emission signal as a function of wavelength). All this can be combined in a microscope, where excitation and detection pass through the same objective (epi-fluorescence geometry). Excitons in layered materials can have an optical dipole either in-plane or out-of-plane, see inset representing emitters with in-plane and out-of-plane optical dipoles. Objectives with high numerical aperture (NA) also collect part of the emission from an out-of-plane optical dipole. The samples are placed on nonmagnetic nanopositioners (travel distance several millimetres). An objective located inside a cryostat is more stable for long signal integration times. The other microscope components remain at room temperature. The microscope design has several modules : The excitation light propagates through an optical fiber via the lower horizontal arm. The upper horizontal arm consists of a camera and broad-band light source for sample imaging. The vertical arm is used for detection. The signal is collected by a spectrometer with a diffraction grating coupled to a highly sensitive Si-CCD camera. The fiber transports the signal from the microscope to the spectrometer entrance and also acts as a spatial pin-hole, making this a confocal arrangement for increased lateral (xy) and depth (z) resolution [104]. Both linear polarization and circular polarization analysis can be achieved for studying layered materials such as TMDs for spintronics and valleytronics.

emission wavelength. These include the polarization components, microscope objectives, and lenses (ideally achromatic doublets) shown in Fig. 3.1. Homogeneous areas (flat surface, no charge fluctuations) in typical exfoliated sample have lateral dimensions down to a few micrometers. Therefore small excitation/detection spots close to the diffraction limit are crucial to record spectra with transition linewidths limited by the homogeneous, not inhomogeneous, broadening. A diffraction limited spot diameter can be achieved by using high numerical aperture (NA) objectives. The spatial resolution is given by the diameter Δ of the detection spot. This depends on the NA of the objective and the wavelength λ through the Rayleigh criterion as $\Delta = \frac{0.61\lambda}{NA}$ [105], where $NA > 0.8$ is common in commercial objectives. For linear polarization, in the excitation part a Glan-Taylor (GT) polarizer and a halfwave plate ($\lambda/2$) can be inserted. It is important to take into account the impact of the beamsplitters (BS) on the polarization state. Circular polarization can be achieved by adding a quarter wave plate ($\lambda/4$) that transforms the linear into circular polarization and vice versa. A liquid crystal retarder (where a precise retardance of $\lambda/2$, $\lambda/4$ etc. can be adjusted by the applied bias) is used in the detection path to avoids a macroscopic beam movement which can occur during rotation of a typical waveplate as the retardance/polarization is changed, see Fig. 3.1. The performance of all optical set-up components is wavelength dependent, such as limited bandwidth of reflection coatings, chromatic aberrations of the objective or optical retardance for specific wavelength.

Detection.- The final target is to detect the intensity as a function of wavelength of the light emitted from/scattered by the sample. The signal is focused onto the entrance slit of a spectrometer. The collected signal is then dispersed by a monochromator, which can host different diffraction gratings, where a small (large) number of lines/mm allows studying a broad (narrow) spectral range (here we show a Czerny-Turner geometry), see Fig. 3.1. The signal can then be detected by a CCD or high quality CMOS chips. Alternatively, the monochromator can be left out and a simple combination of filters can be used in front of the detector.

Experimental conditions.- Control of the ambient conditions is crucial. Many experiments are carried out at room temperature but low temperature experiments are necessary to access particular optical transitions. In simple bath cryostats the sample is kept in thermal contact with a liquid helium bath at $T = 4\ K$, either via helium exchange gas or a cold finger. The main drawback is that the bath needs to be periodically refilled with liquid helium. Alternatively, closed-cycle cryostats liquify the helium gas using external compressors and allow continuous operation. The external compressor needs to be mechanically decoupled from the sample space to minimise vibrations. A piezo-based 3-axis stage with nanometer step-size is used to place a specific area of the layer of interest in the focal point of the objective. For high mechanical stability of the set-up, a low-temperature compatible microscope objective can be placed inside the cryostat, see Fig. 3.1.

The sample holder can also be placed inside the bore of a superconducting coil to apply magnetic fields. In this case the nanopositioners, as well as the objective lens must be made of non-magnetic materials such as titanium and beryllium copper. The sample needs to be placed at the centre of the coil which limits in practice the sample size and also the optical access (beam diameter). The motivation for magneto-optics is manifold such as extracting the valley Zeeman splitting, and hence identifying the origin of new excitonic transitions including interlayer excitons in TMD homo- and heterobilayers, trilayers and bulk [68, 106]. Furthermore, it is possible to investigate valley polarization dynamics and 'brightening' of otherwise spin forbidden-transitions [107]. Attention should be given to undesired Faraday effects in certain optical components. Magnetic ions in the glass result in an undesired rotation of the linear polarization in the presence of magnetic fields. This needs to be compensated by other polarization control elements.

3.1.2 Absorption spectroscopy

Strictly speaking, measuring absorption (A) requires to measure both transmittance (T) and reflectance (R) where $A = 1 - R - T$. Transmission measurements require a transparent substrate and a detection path different from the excitation path, for example a separate microscope objective on each side of the sample or alternatively one objective combined with a fiber on the other side of the sample [25]. In practice often reflectivity is measured as it is the simplest experiment for samples on substrates like SiO_2/Si that are not transparent. To get a quantity independent of the optical response of the set-up, one generally measures the reflectivity contrast defined as $(R_{\mathrm{sam}} - R_{\mathrm{sub}})/R_{\mathrm{sub}}$, where R_{sam} is the intensity reflection coefficient of the sample with the TMD layer and R_{sub} comes from the same structure without the TMD layer. The multiple reflection caused by the samples and substrate interfaces can affcet the lineshape of the spectra and also real absorption. The absolute absorption can be obtained from the reflectivity contrast using Kramers-Kronig relation [14].

The optical properties of a material can be seen in a simple classical picture as the interaction between light (electromagnetic radiation), and various types of oscillators [14]. In TMD monolayers, the dominating oscillators are exciton resonances. Therefore, in reflectivity different exciton resonances are accessible up to room temperature as they possess strong oscillator strength and high density of states (DOS). This allows to observe the Rydberg series of the A-exciton : $1s$, $2s$, $3s$...(see Fig. 3.2 (b) bottom panel), thus giving a measure of the exciton binding energy and the quasi particle bandgap [19, 25] Other optical transitions related to defect states in the gap or other exciton complexes which posses weaker oscillator strength and/or comparatively lower density of states are difficult to trace in absorption, although they might appear in photoluminescence emission, as discussed below.

Monolayers.- The energy of the A-exciton transition in TMD monolayers is given by the difference of the quasi particle bandgap (of unbound electrons and holes) and the exciton binding energy. Engineering the dielectric environment (and hence all energy scales linked to the Coulomb interaction) results in significant changes in the quasi particle bandgap [109] and the exciton binding energy of TMD monolayers. But the shift in the global A-exciton transition energy is rather small, as changes in quasi particle bandgap and the exciton binding energies partially compensate each other. Compare Fig. 3.2 (c) for monolayer $MoSe_2$ transition energies with and without hBN encapsulation, which are very close in value. However, the linewidth in absorption is significantly impacted by dielectric disorder [79]. For instance, bubbles, wrinkles, polymer residues and hBN have different dielectric con-

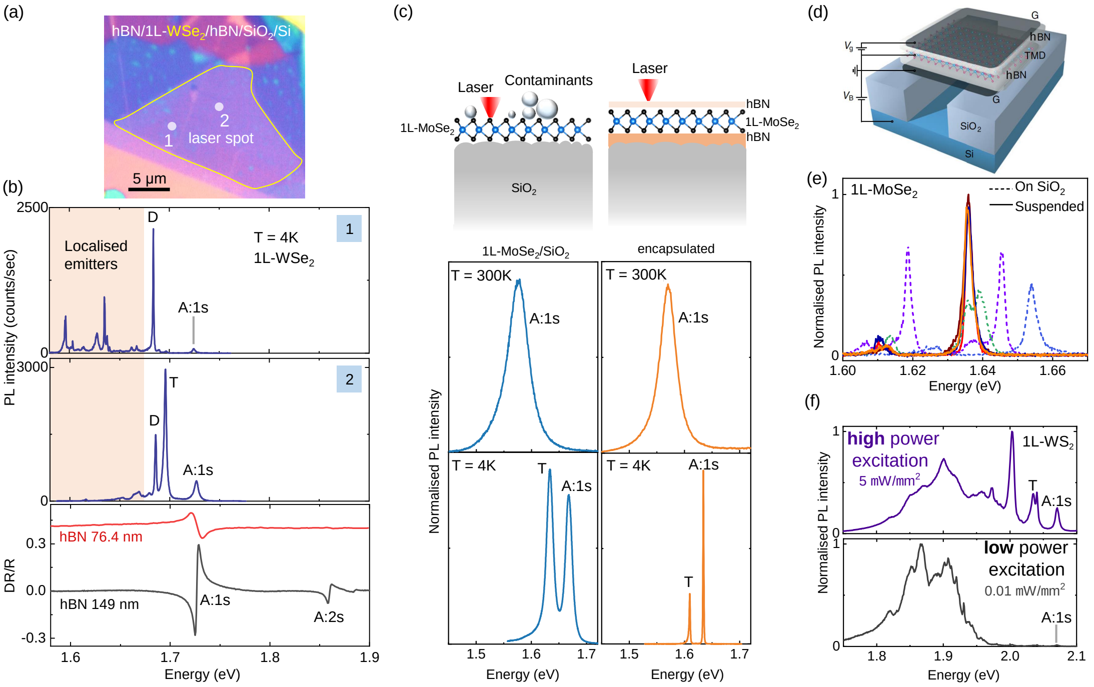

Figure 3.2: **Variation in photoluminescence (PL) response for different experimental conditions**. **(a)** Optical micrograph of a typical van der Waals heterostructure sample containing a WSe_2 monolayer between hBN top and bottom encapsulation layer, sample homogeneity and sample imperfections (bubbles and wrinkles) can be seen. The homogeneous and non-homogeneous regions of the sample are labelled 1 and 2 in white, respectively. **(b)** Typical PL spectra at $T = 4\ K$ recorded at two different locations 1 and 2 of the sample shown in **(a)**. The main exciton transitions (neutral excitons (A:1s), charged excitons (T) and spin-forbidden dark exciton (D) are quenched and localized emitters appear when PL is recorded on the bubbles or on wrinkles. However, strong PL emission corresponding to the main excitons from WSe_2 monolayers is recorded on the flat region of the sample. **(c)** Sketch of $MoSe_2$ monolayer sample structures in different dielectric environment. The left panel is the sample structure of a non-encapsulated TMD monolayer on SiO_2 and the TMD monolayer encapsulated in hBN is on the right panel. Typical PL spectra recorded at $T = 300\ K$ and $4\ K$ on the encapsulated and the non-encapsulated sample are shown in the bottom panel. The linewidth reduces significantly for the encapsulated sample at $T = 4\ K$ compared to non-encapsulated sample. **(d)** hBN encapsulated $MoSe_2$ layer suspended over a trench [108] and corresponding spectra are shown in **(e)**. The PL emission energy remains constant on suspended samples on different locations on the monolayer showing sample homogeneity [108]. **(f)** WS_2 monolayer encapsulated in hBN on a SiO_2/Si substrate, WS_2 layer plasma treated to generate optically active defects. Typical PL emission spectra for CW laser (532 nm) excitation at $0.01\ \mu W$ and $5\ \mu W$ at $T = 4\ K$. The PL emission intensity of the main excitons are clearly visible at high power density, whereas these features are almost not detectable at low laser power density. PL spectra at low laser power density reveal that carriers can be trapped efficiently by defect sites and recombine by emitting photons at lower energy. Therefore at low laser power the PL emission of defects is considerably stronger than the free exciton emission.

stants. Therefore, a non-uniform dielectric environment affects the energy of the exciton transitions and the overall shape of reflectivity spectra. Uniform dielectric slabs such as thick (tens to hundreds of nm) hBN layers can be exploited to steer the absorption. The visibility of exciton resonances in absorption is mainly influenced by the thickness of hBN and SiO_2, see Fig. 3.2 (b). This is due to thin-film interference effects, the bottom hBN thickness determines how far the monolayer is from the Si/SiO_2 interface, which acts as a mirror. The choice of hBN thickness of the heterostructure can be optimized using a transfer matrix approach to increase the visibility of the targeted transitions [81]. In this process, the particular energy of the excitonic resonance of the layered semiconductor should be taken into account [81] also described in the previous chapter. Recent results in TMD materials placed in front of mirrors show a modulation in the absorption strength of up to 100% due to interference/cavity effects [110]. The strong influence of the dielectric environment on the light-matter interaction of atomically thin semiconducting membranes motivates a great potential for sensing applications including novel device architectures with precisely tunable optical properties.

Multilayers.- In general the nature (direct or indirect) and the energy of the bandgap evolves as a function of the layer number for a given material. In addition, the absorption of layered semiconductors such as black phosphorous [102] and $ReSe_2$ [111, 112] reveals information on the crystal structure of these particular materials as it is highly anisotropic in the layer plane, as a direct result of a highly anisotropic lattice structure. In TMD multilayers and even bulk strong excitonic features are reported even at room-temperature in early studies [113]. In addition to these features typically attributed to the intralayer A- and B-exciton, more recently the observation of interlayer excitons (formed by carriers in two adjacent layers) has been reported in absorption of bulk samples [68, 114]. Absorption of interlayer excitons is also reported in homobilayers and homotrilayers of MoS_2 [60, 67]. In these systems the transition energy of the absorption can be tuned through the application of an electric field perpendicular to the layers (Stark shift) over 120 meV and the interaction between interlayer and intralayer excitons can be investigated [106, 115].

3.1.3 Photoluminescence spectroscopy

Luminescence experiments are widely used for studying the macroscopic optical properties of materials as well as their microscopic electronic excitation, for the evaluation of crystalline quality (presence of defects) and for testing novel optoelectronic devices [121, 122]. Luminescence is defined as a surplus of the electromagnetic radiation (light) emitted by a solid, in addition to its equilibrium radiation described by Planck's law. This surplus energy is transformed into detectable luminescence radiation. During the process of luminescence the electrons are excited to higher energy states (by a *light*-source in the case of *photo*-luminescence). Subsequently the carriers relax in energy for example through phonon emission, followed by photon emission. The succession of all involved relaxation and recombination events lasts a relatively long time, which is a main difference compared to other types of so-called secondary radiation : reflected light and scattered light (for example Raman). Once the material is excited with a light pulse, the luminescence continues to

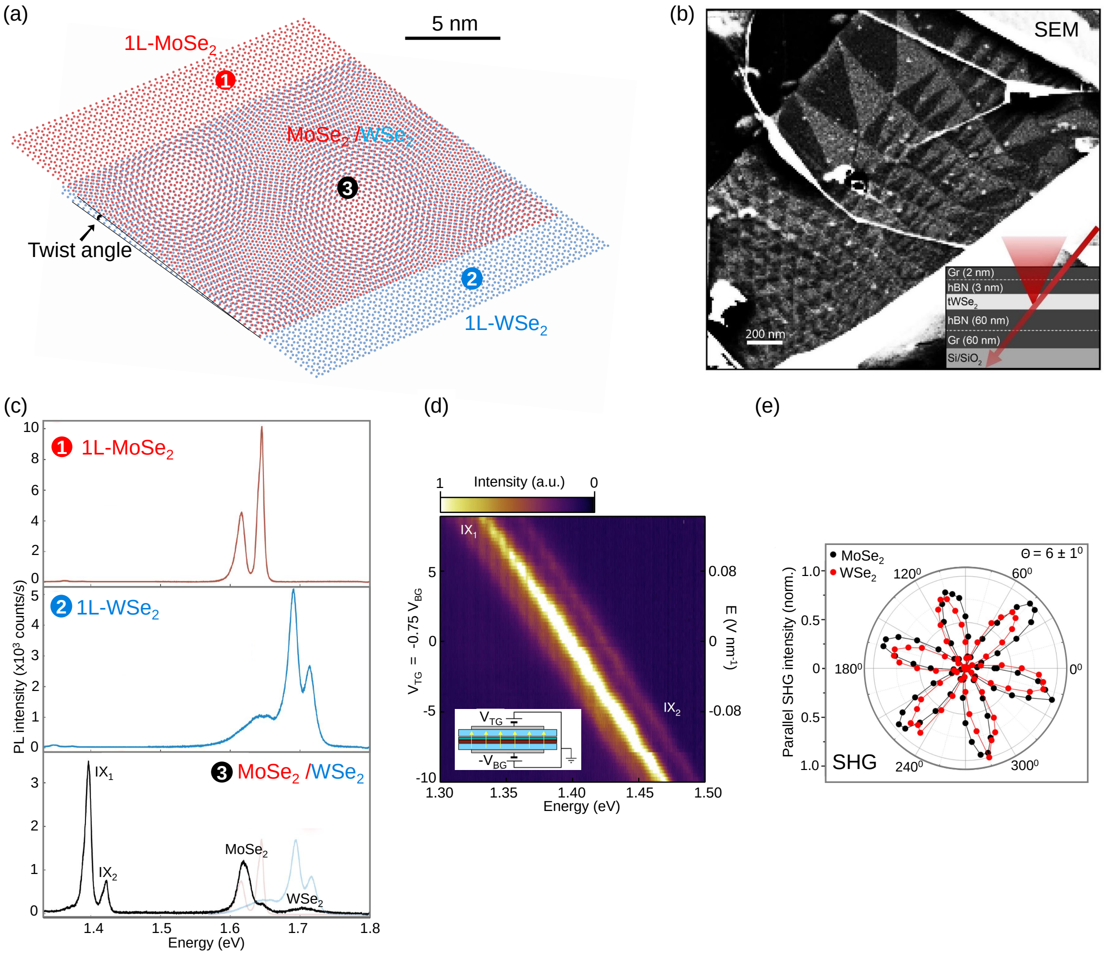

Figure 3.3: **Moiré interlayer excitons in heterobilayers.** **(a)** Two different monolayer materials stacked vertically that display a moiré pattern due to slight lattice mismatch and twist angle. Different local atomic alignments in the heterostructure show different optical properties [116, 117]. Three spots labelled 1, 2 and 3 are chosen for PL measurements on MoSe$_2$ monolayer, WSe$_2$ monolayer and MoSe$_2$/WSe$_2$ heterostructure, respectively, and corresponding spectra are shown in **(c)**. **(b)** SEM imaging of hBN-encapsulated twisted WSe$_2$ bilayers with a spatially varying reconstruction pattern due to the interaction between the respective layers after stacking [118]. **(c)** Example of photoluminescence spectrum from an hBN-encapsulated MoSe$_2$ monolayer (solid red curve), MoSe$_2$/WSe$_2$ heterostructure (solid black curve) and WSe$_2$ monolayer (solid blue curve) [119]. Intralayer exciton emission is observed from the MoSe$_2$ and WSe$_2$ monolayers. The interlayer exciton emission (IX$_1$ and IX$_2$) appear in energy below the intralayer resonances from the heterostructure. **(d)** Electrical control of interlayer excitons in MoSe$_2$/WSe$_2$ heterobilayer. Colormap of PL emission spectra as a function of applied gate voltages V_{TG} and V_{BG} when sweeping at constant doping. Stark shift of the interlayer excitons in applied electric fields perpendicular to the layers showing out-of-plane electric dipole [119]. **(e)** Polarization-resolved second harmonic generation (SHG) intensity of the individual monolayers from a different publication compared to panels **(c)**-**(d)**, indicating the armchair directions of the monolayers which determine the twist angle (θ) between the WSe$_2$ and MoSe$_2$ layers [120].

decay for some time and can be recorded in time-resolved photoluminescence [121]. These experiments give information on carrier relaxation and recombination times. In addition to time-resolved photoluminescence (an incoherent technique), also important information can be gleaned from coherent spectroscopy such as four-wave mixing and two-color pump-probe experiments [123].

In absorption spectra optical transitions with large oscillator strength and high density of states dominate. In contrast, the emission spectrum given in photoluminescence experiments can be dominated by other transitions as these experiments probe the population of a state. Typically, optical transitions at lower energies are detected in PL as carriers relax towards these lower energy states before radiative recombination. It is therefore instructive to compare emission with absorption spectra (measured in reflection geometry) as in Fig. 3.2 (b). For the material investigated, monolayer WSe_2, the main bright exciton transition (A:1s) that dominates in absorption is not generally the strongest feature in PL emission, as electron-hole pairs can relax towards states lying at lower energy to recombine [43].

Sample temperature.- At room temperature, the main transitions such as the A- and B-excitons in TMDs will be broadened due to scattering with phonons, compare spectra at $T = 4\ K$ and 300 K in Fig. 3.2 (c). Carriers or excitons are mobile at high temperature and defect potentials in the lattice with only shallow confinement energy will not act as efficient trapping sites. At low temperature phonon absorption is reduced and the linewidth reveals the sample quality (inhomogeneous broadening versus homogeneous broadening [82]). This is illustrated in Fig. 3.2 (c). Spectral lineshape and main emission energy can change compared to high temperature. Carriers can get trapped at sufficiently deep defect potentials. Also excitonic complexes with lower binding energy, such as trions, are now stable and contribute to the PL signal, see Figs. 3.2 (b), (c), (f) for three different materials [45, 51, 123, 124].

Excitation power.- Laser power plays an important role as it controls the number of photoexcited carriers. Strictly speaking, the power density (defined as the average power per unit area) is directly related to the photogenerated exciton density in layered semiconductors. It is inversely proportional to the square of the focused beam radius, thus it is directly related to the numerical aperture of the objective lens and laser wavelength. Let us take an example of a sample with a finite value of defect density : for a tightly focused beam (spot size $\approx 1\ \mu$m), at low laser power (typically hundreds of nW) all carriers can be trapped at defect sites and the PL signal of free excitons is not visible, as in Fig. 3.2 (f), lower panel. Increasing laser power (few μW) fills all defect sites and free exciton PL can be measured in addition to defect emission, see Fig. 3.2 (f) upper panel. Further increase in power (tens to hundreds μW) will lead to such a high concentration of excitons that exciton-exciton interactions start to play a role. At high excitation density very different phenomena such as biexciton formation and exciton-exciton annihilation can be studied depending on the material [125, 126]. Understanding emission for high exciton (carrier) concentrations is crucial for applications such as lasing and for investigating collective states such as condensates [127].

Sample quality and dielectric environment.- Two monolayer samples exfoliated from the same quality bulk crystal but placed on different substrates can exhibit very different PL characteristics, see Fig. 3.2 (c) for a comparison of $MoSe_2$

on SiO_2 and on hBN, respectively. The total line broadening comes both from homogeneous contributions given by ≈ 1 ps lifetime (below 1 meV linewidth) and inhomogenous contribution from sample imperfections (impurities, defects, interface, substrate, etc) [128]. The key role of high quality hBN buffers with low defect density is to provide atomic flatness [77] for monolayer deposition and a very clean, homogeneous dielectric environment. The hBN bulk bandgap of 6 eV [129] is high enough to use it as an essentially transparent encapsulation layer for many materials, providing an ideal environment to address intrinsic properties of 2D-TMDs and preserving good optical quality of air-sensitive materials such as CrI_3 or black phosphorous. As the inhomogenous broadening is largely suppressed in high quality samples of TMD monolayers, the linewidth starts to be an indication of the exciton lifetime (homogeneous broadening) and can be tuned by carefully choosing the encapsulating hBN thickness - placing the monolayer on a node or anti-node of the electromagnetic field in the multilayer structure [82].

PL emission is sensitive to the presence of wrinkles or bubbles which induce strain and localization potentials in encapsulated monolayers. Small strain (1%) in monolayer induces a rather significant (about 50 meV) shift in bandgap energy [38] which can explain shifts in absolute emission energy from sample to sample and for different areas of the same sample. Therefore, in practice PL emission intensity as well as linewidth varies on different location of TMD monolayers, see Fig. 3.2 (b) when the detection spot (1 μm diameter) is scanned across a WSe_2 monolayer. Remarkably, exciton emission energy that does *not* vary as a function of the detection spot position has been observed in hBN-encapsulated $MoSe_2$ monolayers, suspended over a trench, see Fig. 3.2 (d), (e) [108], indicating a stable, inert environment.

The general study of the dielectric environment, surface quality, flatness, charging events and their impact on optical properties is very important also for other nanostructures such as carbon nanotubes [130, 131] and layered perovskites [132] which show strong excitonic effects.

Interference effects.- Layered materials are usually placed on a substrate such as Si with an SiO_2 layer of typically 85 nm. As discussed earlier for white light absorption experiments, optical interference will also be important for the laser excitation beam and the PL emission as a function of the SiO_2 thickness and possibly the encapsulation layer thickness. Reversely, for constant SiO_2 thickness absorption and emission intensities and directivity will depend on the wavelength, as detailed in [133, 134]. In practice the thickness of the SiO_2 layer on top of Si is chosen to maximize optical contrast of monolayers already during sample fabrication, as discussed in detail for graphene on SiO_2 [135].

Emission dynamics.- The detected luminescence signal from a layered semiconductor is the result of an intricate interplay between radiative and non-radiative energy relaxation. Time-resolved PL can be performed using a pulsed laser excitation and measuring the recombination (emission) time. In clean TMD samples the strong exciton oscillator strength leads to an intrinsic radiative lifetime of the order of 1 ps at low temperature [39]. Localized emitters recombine considerably slower and also dark excitons have a lifetime up to 3 orders of magnitude longer. In the time domain, low temperature measurements on high quality samples allow spectrally isolating each transition (either with bandpass filters or with a spectrometer) and then studying the emission dynamics of each optical transition separately [44, 45, 82].

Optical dipole orientation.- In TMD monolayers the main optical transitions have an in-plane optical dipole, they therefore emit light normal to the monolayer plane. However, in addition to these bright (spin-allowed) transitions also excitons that have an out-of-plane optical dipole emit light [43]. Out-of-plane dipole transitions are also prominent in InSe [136]. Due to the small sample dimensions most experiments are carried out in a microscope using an objective with high (>0.8) NA, see inset on microscope objective in Fig. 3.1. As a result, PL emission containing out-of-plane and also in-plane components in the monolayer are detected. In WSe_2 and WS_2 monolayers, dark excitons are prominent, see Fig. 3.2 (b) and lead to exotic, higher order complexes (such as biexcitons made up of a dark and a bright exciton and so-called dark trions [125]), that can be identified by monitoring the orientation of the exciton dipole. The role of out-of-plane dipole emission is also investigated for quantum emitters in WSe_2 [137]. Brightening of (spin-) dark states due to an increased mixing of the spin-states in WSe_2, WS_2, $MoSe_2$ and MoS_2 monolayers can be observed in low-temperature magneto-PL experiments by applying strong (ideally several tens of T) in-plane magnetic fields [45, 52].

Multilayers.- PL spectroscopy is useful also in TMD heterobilayers with type II alignement for the examination of spatially indirect interlayer exciton (see Fig. 3.3 (c)) with large binding energies ($\approx$ 150 meV) [63, 138]. A long period moiré pattern (see sketch in Fig. 3.3 (a)) offers new directions to explore and control exciton arrays in twisted TMD heterobilayers from potentials that trap individual excitons to the formation of minibands. This allows physics related to the Mott-insulator [117], for potential applications in quantum optoelectronic devices [115]. Some key characteristics of interlayer excitons include a long-lifetime (ns), a wide transition energy tunability that ranges over several hundreds of meV via applied electric fields, see Fig. 3.3 (d) and a characteristic Zeeman splitting when compared to intralayer excitons [114].

3.1.4 Photoluminescence excitation spectroscopy

In photoluminescence excitation spectroscopy (PLE) the PL emission intensity for a chosen energy is recorded for different photon excitation energies. Tunable lasers or powerful white light sources are used as an excitation source. The linewidth and tuning step of the source will determine the spectral resolution of the PLE experiment. The measured PL intensity will depend on two factors (i) the absorption strength at the excitation energy and (ii) the efficiency of energy relaxation followed by radiative recombination (in competition with non-radiative channels). This combined dependence on both absorption and energy relaxation (often through phonon emission) make PLE spectroscopy a very interesting tool for several investigations :

Interlayer excitons.- A PL signal enhancement of interlayer excitons is observed when the laser excitation energy is resonant with intralayer states in one of the layers, confirming that interlayer excitons form via charge transfer processes between the layers [119, 63, 139], see Fig. 3.3 (c). In general electronic coupling or charge transfer between layers can be investigated by tuning a laser in resonance with an electronic transition in one layer and monitoring PL emission at an energy corresponding to the adjacent layer or to the heterostructure.

Measuring excited exciton states.- PLE can be also used to establish a link between optical transitions with similar microscopic origin within the same monolayer. In MoS_2 monolayers, B-exciton states energetically overlap with the excited A-exciton states (A:2s, A:3s..,). PLE spectroscopy allows to distinguish the excited states by collecting the emission intensity of the ground state, A:1s, as a function of the excitation laser energy, scanned over the energy of A:2s, A:3s, etc. Besides states with s-symmetry, also p-states can be examined. To access p-states, two-photon absorption processes are necessary and therefore the laser energy needs to be tuned to half of the transition energy [129]. The identification of high-excited exciton states in one and two-photon-PLE is a powerful method to evaluate the impact of different dielectric environments on the energy evolution of the exciton states. Furthermore, it is possible to extract the exciton binding energies [140] and investigate predictions of splittings of the p-exciton states [141]. However, one should note that the crystal symmetry or disorder effects can mix s and p exciton states [142].

Identification of dominant phonon modes for energy relaxation.- In addition to key information on absorption, PLE is used to identify efficient relaxation channels. In PLE experiments on $MoSe_2$ monolayers a periodic oscillation in energy is observed over an energy range without any expected exciton resonance (roughly constant absorption [143]). These maxima are all equally spaced in energy by longitudinal acoustic phonons at the M point of the Brillouin zone, LA(M), revealing the efficient energy relaxation of excitons through emission of LA(M) phonons [144, 124]. This experimental observation was possible due to the spectrally narrow excitation source, resolving fine separations between different peaks related to phonon emission [124].

3.2 Accessing spin-valley polarization in optical spectroscopy

The symmetry of the electronic states in monolayers and multilayer crystals governs the optical selection rules for light polarization in emission and absorption [116], as studied since several decades for semiconductor nanostructures [145]. For polarization analysis, linear polarizers and waveplates can be inserted in the detection and excitation path of the set-up, see Fig. 3.1 for practical details. Exciting a system with polarized light can address a specific spin or valley state, see Fig. 1.6 (d) and (e) in Chapter 1. The emitted light gives information on spin and valley dynamics in time-integrated PL experiments. The circular polarization in time-integrated experiments depends on the exact ratio of PL emission time τ_{PL} versus depolarization time (τ_{depol}) as $P_c = P_0/(1+\frac{\tau_{PL}}{\tau_{depol}})$, where P_0 is the initially generated polarization which could depend on the excitation energy [146].

TMD monolayers.- The interband transitions in monolayer materials such as MoS_2 are governed by chiral selection rules as optical transitions in the K^+ (K^-) valley are σ^+ (σ^-) polarized. For neutral, bright excitons the intrinsic lifetime is of the order of 1 ps, so from time-integrated PL experiments that report P_c values in the order of 50% one can infer that τ_{depol} is at least of this order of magnitude. In practice more sophisticated pump-probe measurements reveal very short valley lifetimes for neutral excitons [128]. The ratio $\frac{\tau_{PL}}{\tau_{depol}}$ can be tuned by placing monolayers in optical microcavities [147]. Longer valley lifetimes in monolayers are reported for resident carriers [148] not excitons, measured with pump-probe techniques such as Kerr rotation employed for probing polarization in semiconducting or metallic nanostructures [149].

TMD heterobilayers.- Optical spectroscopy can be used to probe the local atomic registry, i.e. how metal and chalcogen atoms are aligned in the top with respect to the bottom layer [116, 119, 150]. Here information can be gleaned on the formation of nano-scale, periodic moiré potentials, see sample sketch in Fig. 3.3 (a). But similar to bilayer graphene, reconstruction can occur when two TMD layers are brought in contact, which can be visualized using imaging techniques such as transmission electron microscopy (TEM) or scanning electron microscopy (SEM). Recently Sushko et al. [118] reported SEM imaging of hBN-encapsulated twisted WSe_2 bilayers showing that a spatially varying reconstruction pattern develops due to the interaction between the respective layers after stacking, see Fig. 3.3 (b). Polarization selection rules probed in PL also carry information on different stackings (H-type or R-type for 60° or 0° twist angle, respectively) [151]. Therefore, polarization-resolved optical spectroscopy together with direct atomic-resolution imaging of the lattice is a very powerful combination for analyzing the formation of moiré potentials [152]. The PL experiment samples over a spot diameter of 1 μm, whereas moiré potentials can occur with a periodicity of nanometers, see Fig. 3.3 (a), which leads to averaging effects. The intrinsic lifetime of interlayer excitons is of the order of ns at low temperature and not ps as in monolayers, which allows for imaging exciton and polarization spatial diffusion in PL maps [153, 154]. The physics of both intralayer and interlayer excitons can be accessed in the monolayer and bilayer regions of the same sample, as in Fig. 3.3 (a) and (c).

Experiments in applied magnetic fields.- The circular polarization can be manipulated by applying external magnetic fields [155]. Interesting examples are heterobilayers, where a giant Zeeman splitting of 26 meV at B = 30 T for interlayer excitons induces near-unity valley polarization measured in PL emission [120]. In monolayer $MoSe_2$ a field of 7 T results in near unity polarization of electrons probed in absorption and emission [156].

3.3 Optical techniques for accessing crystal quality and orientation

Raman spectroscopy is based on the analysis of laser light scattered by a material. During this process the crystal typically absorbs (or emits) energy in the form of lattice vibrations - phonons. The analysis of the scattered light's energy and polarization reveals information on the crystal symmetry and quality, doping and where applicable alloying and stacking in multilayers. A typical PL set-up (shown in Fig. 3.1) can be conveniently adapted to collect the Raman spectra by selecting a suitable set of filters according to the wavelength of the excitation laser. Typically, filters for Raman spectroscopy reject the excitation laser with a cut-off frequency of few tens of cm^{-1} ($\approx$ 10 meV from the single mode energy). The selection of laser wavelength λ has an important impact on the spectral sensitivity as the intensity of the Raman signal is proportional to λ^{-4}. Key parameters of the excitation laser include spectral linewidth ($\leq$1 GHz) for high spectral resolution systems, frequency and power stability, spectral purity ($\geq$65 dB side-mode suppression ratio), beam quality (close to Gaussian) and output power. The excitation wavelength in the Raman scattering of TMDs is also important because of the presence of excitonic states. When the photon energy matches the transition energy of a real state it gives rise to a strong signal enhancement and appearance of new features, associated to symmetry dependent electron-phonon interactions (resonant Raman scattering) [157, 158].

Information on the structural phase and composition of materials can be obtained by means of Raman spectroscopy [159]. This allows for example investigating currently debated link between ferromagnetic ordering and structural phase transitions in CrI_3 [160] as a function of temperature. Raman spectroscopy can reveal anisotropy in the crystal structure of, for example, $ReSe_2$, which can be directly linked to measurements of anisotropic optical absorption in the same material [161]. Electron-phonon interactions can have significant effects on the Raman frequencies. As a result, doping effects can be effectively monitored in TMD monolayers for example with the out-of-plane phonon, A_1', due to its strong electron-phonon coupling [162]. It is also possible to extract quantitative information about the presence of uniaxial strain since the in-plane phonon energy, E', decreases with applying tensile strain and a splitting occurs (degeneracy is lifted) [163]. An estimation of the monolayer crystal quality and presence of defects can be realized due to the activation of defect-induced zone-edge phonon modes, such as the LA(M). Furthermore, disorder and interference effects originating from the substrate impact the intensity and spectral shape of the optical phonons in the monolayer. A powerful and reliable means to determine the number of TMD layers with atomic-level precision is to measure the energy difference between the two main vibrational modes (E and A phonons), affected by interlayer interactions. Apart from the high-frequency ($\geq$ 80 cm^{-1}) spectral range, the number of layers can be identified by collecting optical signatures of the rigid layer vibrations (breathing and shear modes) in the ultra-low frequency range [164]. In this case, important information on the interlayer interaction and determination of the stacking order in multilayers can be obtained. In TMD multilayers resonant Raman spectroscopy can also provide a fingerprint of the extension of excitons over several layers, as otherwise symmetry forbidden modes are activated for the so-called C-exciton region in energy above the A- and B-exciton. Raman spectroscopy can also be used to investigate the competition between formation of periodic moiré potentials and local reconstruction (compare Figs. 3.3 (a) and (b)) in artificially stacked $WSe_2/MoSe_2$ and bilayer MoS_2 as a function of twist angle [165].

Second-harmonic generation (SHG) is a nonlinear optical process that converts two photons of the same frequency into one photon of twice the original frequency. It is a powerful technique to analyze the orientation and symmetry properties of 2D materials. For SHG experiments, the optical set-up is typically coupled to a pulsed laser that is capable of generating sufficient peak power for this nonlinear optical process. The SHG signal depends on the elements of the second-order susceptibility tensor $\chi^{(2)}$ [14], which are non-vanishing for non-centrosymmetric media (i.e. odd number of TMD layers) along the armchair direction of TMDs. This crystalographic direction can thus be directly determined by rotating the linear polarization in the experiment. The resulting polar plot of the SHG intensity reveals the crystallographic orientation of the material, useful to precisely measure the relative twist angles (stacking) of homo- and heterobilayers [166], see Fig. 3.3 (e). Novel techniques exploit this effect to map with high spatial resolution (≈ 400 nm) the armchair orientation in twisted bilayers, as well as in large ($> 10^4\ \mu\mathrm{m}^2$) monolayer areas and evaluate their crystal quality since dislocations and grain boundaries can affect the armchair orientation i.e. change the lattice vector [167]. Also the presence of uniaxial strain can be quantified by measuring the SHG intensity along different polarization directions [168].

The SHG response of a material does not only reflect the crystal structure but also depends on the electronic excitations. The efficiency of the SHG signal can be enhanced by several orders of magnitude by selecting the excitation energy to be in resonance with excitonic states of the investigated materials. This opens the way for investigating in general the role of electronic excitations (exciton resonances) on the SHG response of a material [169]. Using the sensitive SHG response to detect the energy position of electronic transitions is termed 'SHG spectroscopy'. In bilayer $\mathrm{CrI_3}$ SHG has been shown to originate from the layered antiferromagnetic order, which breaks both the spatial inversion symmetry and the time-reversal symmetry [170] of this centro-symmetric crystal. This makes SHG a highly sensitive probe also for magnetic ordering in layered materials.

3.4 Conclusions

We dedicated this chapter to the description of the experimental set-ups and techniques we used for studying layered materials. We underlined technical challenges that can be resolved by careful considering different variables. We highlighted key-parameters of practical set-ups for performing optical experiments in different temperatures or in applied magnetic fields and the influence of parameters such as detection spot size, excitation laser wavelength, excitation power and also the direct sample environment on the optical spectra. We also described the main optical techniques which will be extensively used in the next chapters for investing optical transition not only in stander monolayer but also for discovering new optical transitions and its optical properties in TMD multilayers. These techniques are our main tool for investigating the samples and understanding the physics which govern these atomically thin layered crystals.

Chapter 4

Observation of exciton-phonon coupling in $MoSe_2$ monolayers

In this chapter we study experimentally the exciton-phonon interaction in $MoSe_2$ monolayers (MLs) encapsulated in hexagonal boron nitride (hBN), which has an important impact on both optical absorption and emission processes. The exciton transition linewidth down to 1 meV at low temperatures makes it possible to observe high energy tails in absorption and emission extending over several meV, not masked by inhomogeneous broadening. To fit and interpret our spectra, our collaborators Marina Semina and Mikhail Glazov (Ioffe Institute, St. Petersburg, Russia) have developed an analytical theory of the exciton-phonon interaction accounting for the deformation potential induced by the longitudinal acoustic phonons, which plays an important role in exciton formation. Their theory allows fitting absorption and emission spectra that I have measured using the experimental techniques described in Chapter 3. This reveals information about the deformation potential in $MoSe_2$ monolayers. The importance of exciton-phonon interactions is further highlighted by the observation of a multitude of Raman features in the photoluminescence excitation (PLE) experiments. The work corresponding to this chapter is published as Shree *et al* [124].

4.1 Introduction to exciton-phonon coupling

The interaction of excitons with phonons governs many important aspects of the optical properties of 2D materials [171, 172, 173, 174] and semiconductor nanostructures in general [175, 176, 177] including energy relaxation, dephasing and transition linewidth broadening with temperature. Under non-resonant optical excitation high energy excitons are generated that subsequently loose energy by phonon emission, as recently discussed for $MoSe_2$ MLs [144]. Interactions of carriers with phonons play a key role in the exciton formation process [178, 179, 180]. Other important signatures of the exciton-phonon interaction are single resonant and double resonant Raman scattering processes [157, 181, 182, 183]. Also the possible impact of polarons, electrons dressed by a phonon-cloud, on the optical properties has been discussed [184] for TMD MLs.

There is a multitude of neutral and charged excitons in ML TMDs that give rise to complex photoluminescence (PL) spectra [185]. Here phonons provide the necessary energy and in certain cases momentum for transitions between states in different valleys [186, 187]. Knowing details about the interaction of excitons with phonons is therefore important for exciton dynamics that dominates light-matter interaction in TMD MLs.

The deformation potential is a key parameter which describes the interaction of the charge carriers and excitons with phonons. It controls a plethora of effects including momentum and energy relaxation processes, linewidth broadening, as well as the photoelastic properties of nanosystems relevant for optomechanical applications. The direct determination of the deformation potential, e.g., by shifts of the exciton line as a function of the elastic strain or deformation as in Refs. [188, 189] is difficult due to the necessity of applying homogeneous uniaxial strain and requires substantial deformations in order to provide a measurable line shift. That is why determination of the deformation potential values from other effects, like thermal broadening of the exciton emission lines and asymmetric shapes of the exciton absorption lines are of high importance, as we discuss in this chapter.

Recently encapsulation in hBN of TMD monolayers has resulted in considerable narrowing of the exciton transition linewidth, down to about 1 meV [182, 190, 51], as mentioned in the previous chapters. This gives now access to interesting details of the exciton spectra. Here we show in photoluminescence excitation spectroscopy on monolayer $MoSe_2$ encapsulated in hBN at $T = 4$ K a strong absorption tail at energies as high as 15 meV above the neutral exciton peak, well outside the transition linewidth. We demonstrate in resonant absorption experiments with a tunable laser that this high-energy tail is a very prominent feature in several samples investigated, underlining the importance of phonon-assisted exciton formation. In temperature dependent PL experiments we show a high energy emission tail appearing as the temperature is raised from 9 K to 70 K. We argue that the efficient interaction between excitons and acoustic phonons is responsible for both the broadening in absorption and the unusual evolution of the PL line with temperature observed on the same sample. For comparison with results from other groups, phonon sidebands in absorption spectra of ML $MoSe_2$ are discussed in [184]. Here we provide evidence for this coupling at low temperature, previously masked by inhomogenous broadening, and introduce exciton-acoustic phonon coupling as an important ingredient also for emission lineshape analysis. Based on the model calculations developed by M. Semina and M. Glazov within an analytical approach and taking into account the deformation potential interaction between excitons and acoustic phonons we obtain compact expressions for the absorption spectrum and phonon-assisted emission. This allows for a numerical fit of our absorption and emission experiments. We discuss the role of phonons in exciton formation and compare our findings to exciton-phonon interactions in quasi-2D quantum well structures.

The chapter is organized as follows: In Sec. 4.2 we report on experimental methods and results. Sec. 4.3 presents the model and analytical results. In Sec. 4.4 we compare the experiment and theory and estimate the exciton – acoustic phonon coupling strength. Conclusions are given in Sec. 4.5.

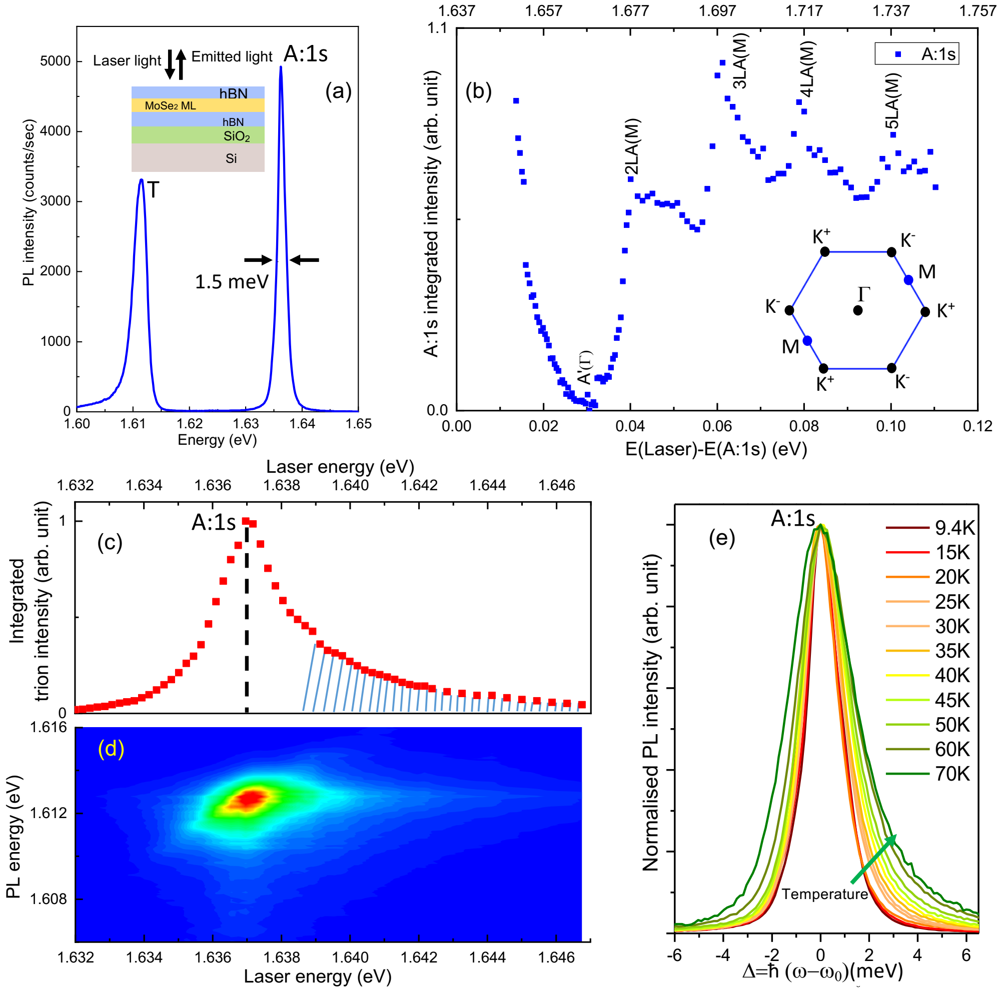

Figure 4.1: **Optical spectroscopy results. ML MoSe$_2$ encapsulated in hBN - Sample 1** **(a)** Typical PL emission spectrum at $T = 4$ K. Emission peaks at energy 1.613 eV and 1.637 eV are due to the charged (T) and the neutral exciton A:1s. Inset of panel **(a)**: Schematics of sample structure: MoSe$_2$ ML encapsulated in hBN, the bottom hBN layer is $(140 \pm 5$ nm) thick as determined by AFM, the SiO$_2$ layer is 80 nm thick. **(b)** PLE experiments : Integrated A:1s PL intensity plotted in terms of excess energy (bottom axis), defined as the difference between the laser energy (top axis) and the A:1s resonance. The average oscillation period corresponds to the M-point longitudinal acoustic phonon LA(M). Inset of panel **(b)**: Schematics of 2D Brillouin zone with K, M and Γ-points. **(c)** Integrated trion PL intensity as a function of excitation energy scanning laser across A:1s resonance. **(d)** Contour plot of trion PL intensity scanning laser across A:1s resonance at $T = 4$ K. **(e)** Temperature dependent PL emission at A:1s resonance. For better comparison of emission shape, the A:1s PL intensity is normalized to the maximum value and the energy shifted to compensate the temperature evolution of the bandgap.

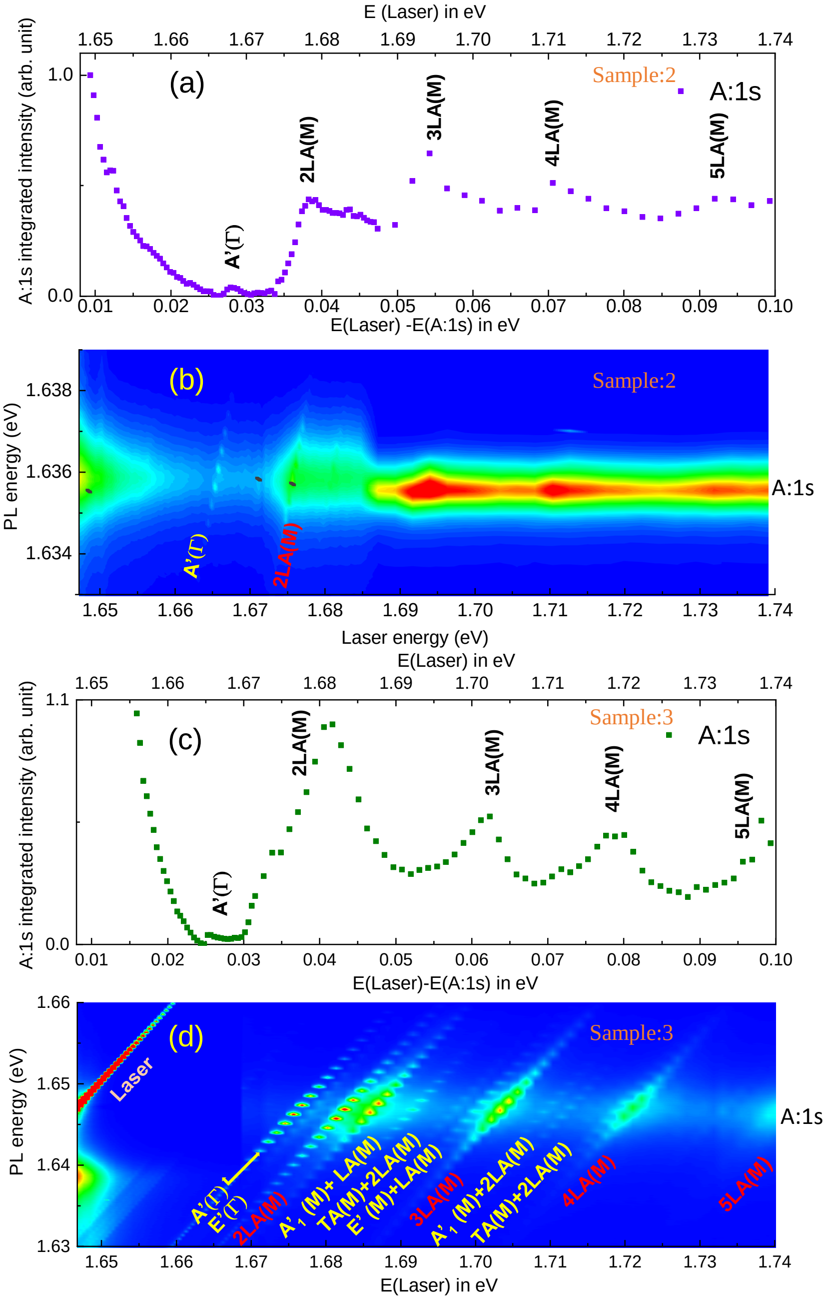

Figure 4.2: **Sample 2.** **(a)** PLE spectra of $MoSe_2$ ML plotted in terms of excess energy (bottom axis), defined as the difference between the laser energy (top axis) and the A:1s resonance. **(b)** Contour plot of the same data, where sharp Raman features are superimposed on broad exciton absorption features. **Sample 3.** **(c)** Same as **(a)** but for different sample. **(d)** same as **(b)** but for different sample. Phonons are labelled according to [183]. In samples with more disorder and stronger localization, Raman features are more prominent as momentum conservation is relaxed [183], which leads to rich features in panel **(d)**. In addition to PL emission, the integrated signal in panels **(a)** and **(c)** also contains contributions from Raman scattered photons if the laser energy is a multiple of a prominent phonon energy above the A:1s transitions. In panels **(b)** and **(d)** the Raman features are spectrally very narrow due to the narrow linewidth of the excitation laser used.

4.2 Optical Spectroscopy Results

4.2.1 Experimental methods

The samples are fabricated by mechanical exfoliation of bulk $MoSe_2$ (commercially available from 2D semiconductors) and very high quality hBN crystals [77] on 80 nm-thick SiO_2 on a Si substrate, as described in detail in Chapter 2. Details on the optical spectroscopy set-up are given in Chapter 3. The experiments are carried out in a confocal microscope built in a vibration free, closed cycle cryostat with variable temperature $T = 4 - 300$ K. The excitation/detection spot diameter is $\sim 1\ \mu m$. The monolayer is excited by continuous wave (cw) Ti-Sa laser (Msquared solstis) with sub-μeV linewidth. The photoluminescence signal is dispersed in a spectrometer and detected with a Si-CCD camera. The typical laser excitation power is $3\ \mu W$.

4.2.2 Experimental results

In PL experiments shown in Fig. 4.1 (a) we observe well-separated (≈ 25 meV) emission lines for neutral (A:1s at ≈ 1.637 eV) and charged excitons (trions, T, at ≈ 1.613 eV) [58, 191]. The transitions at low temperature in encapsulated $MoSe_2$ MLs show very narrow lines with a linewidth down to 1.2 meV [51]. This gives access to physical processes previously masked by inhomogeneous contributions to the linewidth. We study now in detail quasi-resonant and resonant laser excitation of the A:1s transition. We start by discussing PL excitation experiments detecting the A:1s PL emission intensity as function of excitation laser energy. The integrated intensity of the A:1s transition is plotted in Fig. 4.1 (b). We tune the laser (cw Ti-Sa laser from Msquared) from 1.651 eV to 1.747 eV in 2.5 meV steps (wavelength is incremented by $\Delta\lambda = 0.5$ nm). We observe oscillations of the PL intensity as a function of excitation energy, see also Fig. 4.2 (a), (c) for different samples. Please note that the laser power was kept constant for these measurements. The period of the oscillation is ~ 20 meV and exactly matches the longitudinal acoustic phonon energy at the M-point of the 2D hexagonal Brillouin zone, LA(M), as discussed in detail [144]. As the excitation laser energy approaches the A:1s transition, we make an important observation : in Fig. 4.1 (b) the PL emission intensity starts to increase considerably for excitation energies below 1.653 eV, even though the A:1s resonance is still ~ 15 meV away and the A:1s PL emission line is spectrally very narrow. We verified this surprising result by performing PLE measurements on several other samples of $MoSe_2$ MLs encapsulated in hBN, compared in Fig. 4.2.

As we approach the A:1s transition with the laser, scattered laser light starts to obscure the PL signal on the CCD. In order to avoid this complication, we change detection scheme : We approach the A:1s resonance further with our laser but we detect the trion emission and assume that it is a reasonable measure of A:1s absorption. The excitation energy is tuned from 1.632 eV to 1.647 eV. The integrated trion emission intensity as a function of laser energy is recorded in Fig. 4.1 (c). This A:1s absorption spectrum strongly deviates from a symmetric Lorentzian lineshape, with a pronounced tail on the high-energy side of the main resonance. We have repeated this experiments for different laser powers (kept constant during the individual measurement cycle) and have reproduced each time this highly asymmetric lineshape. Note that instead of monitoring the trion emission when scanning across the neutral exciton transition, also upconversion emission of the B-exciton and the excited A-exciton states can be monitored. I have carried out the upconversion measurements on several $MoSe_2$ samples and have confirmed the pronounced high energy tail in absorption. These upconversion results are published together with the work of my fellow PhD students Bo Han and Emmanuel Courtade on $MoTe_2$ MLs in Han *et al* [192], where the reader can find further details.

In addition to this high energy tail in absorption, we also obtain a surprising result when studying emission at different temperature. In temperature dependent PL from 10 K to 70 K of the A:1s, shown in Fig. 4.1 (d), we observe an asymmetric broadening, with stronger broadening on the high energy side, a clear deviation from a standard Lorentzian emission lineshape.

In the following section we will explain the observed asymmetry in absorption and emission due to the efficient coupling of excitons to acoustic phonons. Especially the strong dependence on temperature of the asymmetry observed in emission is a strong indication that phonon related processes are important. Our theoretical investigation is further motivated by the efficient exciton-phonon coupling observed for two additional samples in Fig. 4.2. Also for these sample we confirm the strong absorption tail at higher energy, well above the A:1s resonance. In Figs. 4.2 (a) and 4.2 (c) for samples 2 and 3, respectively, this absorption tails is clearly observable up to 25 meV above the A:1s resonance. At higher excitation energy also for these samples we observe the multi-phonon LA(M) resonances as for sample 1 in Fig. 4.1 (b). In addition samples 2 and 3 show strong resonant Raman signals, involving different phonons and their multiples, as indicated in Fig. 4.2 (b) and (d).

4.3 Theory of exciton-phonon interaction

The aim of this section is to develop a simplified but analytical approach to exciton-phonon interaction in TMD monolayers. Here we argue that taking into account emission and absorption of acoustic phonons the broadening of the exciton line both in absorption at low temperature shown in Fig. 4.1 (c) and in emission at higher temperature shown in Fig. 4.1 (e) can be explained. The final target is to fit the experiments to demonstrate order of magnitude agreement between our model and the measurements. For a complementary, self-consistent approach the reader is referred to [184], where a polaron framework was used and the link between dark (momentum-forbidden) excitons and phonon-side band formation is discussed in detail.

4.3.1 Deformation potential interaction

In semiconductors usually two types of interaction between excitons and acoustic phonons are discussed : the deformation potential interaction and the piezoelectric interaction [193, 194]. Although the latter is typically dominant for individual charge carriers [193, 194, 195], the piezoelectric coupling is expected to be strongly suppressed for excitons in transition metal dichalcogenides for mainly two reasons : (i) Due to close values of effective masses of electrons and holes, the wavefunction overlap is nearly perfect (i.e. the exciton is charge neutral). Note that the exact effective mass values are still debated, our argument is based on predictions by theory [196]. (ii) The exciton has a small Bohr radius.

Since the width of the a semiconductor bandgap depends on the lattice constant and on the arrangement of the atoms in the basis, a change of these quantities will influence the bandstructure. In this context a phonon can be considered as a periodic deformation of the arrangement of atoms, and the carriers "feel" the resulting modulation of the bands. The resulting interaction between carriers and phonons is called deformation-potential scattering [14]. The deformation potential interaction involves, in the axially symmetric approximation, longitudinal acoustic phonons. This is because the energy shift of the charge carriers dispersion is, within the axial approximation, proportional to the divergence of the lattice displacements $\boldsymbol{u}(\boldsymbol{r})$: $\mathcal{U} \propto \boldsymbol{\nabla} \cdot \boldsymbol{u}(\boldsymbol{r})$. Thus, $\mathcal{U} \neq 0$ for the longitudinal phonons only, where the displacements of atoms are parallel to the phonon wavevector. Hereafter we consider only the phonons from the MoSe$_2$ monolayer because the electron-phonon deformation potential interaction occurs in general at short range. The van der Waals interaction between the monolayer and surrounding is relatively weak and, unlike ionic or covalent bonding, is not expected to efficiently transfer deformation from one layer (or material) to another. The exciton perturbation due to the deformation potential reads

$$\mathcal{U}_{\boldsymbol{q}} = \sqrt{\frac{\hbar}{2\rho\Omega_q S}} q b_q^\dagger [e^{-\mathrm{i}\boldsymbol{q}\boldsymbol{r}_e} D_c - e^{-\mathrm{i}\boldsymbol{q}\boldsymbol{r}_h} D_v] + \text{c.c.}\ . \tag{4.1}$$

Here $\boldsymbol{q}$ is the phonon wavevector, $b_{\boldsymbol{q}}^\dagger$ ($b_{\boldsymbol{q}}$) is the phonon creation (annihilation) operator, ρ is the two-dimensional density of mass of the TMD ML, $\Omega_q = sq$ is the phonon frequency, s is the (longitudinal) sound velocity, S is the normalization area, D_c (D_v) are the deformation potential constants for the conduction (valence) band, c.c. stands for the complex conjugate. The matrix element describing the exciton scattering from the state with the center of mass wavevector $\boldsymbol{k}$ to the state with the center of mass wavevector $\boldsymbol{k}'$ accompanied by the phonon emission is derived from Eq. 4.1 with the result

$$\boxed{M_{\boldsymbol{k}'\boldsymbol{k}}^{\boldsymbol{q}} = \sqrt{\frac{\hbar}{2\rho\Omega_q S}} q (D_c - D_v) \mathcal{F}(q) \delta_{\boldsymbol{k},\boldsymbol{k}'+\boldsymbol{q}}}, \tag{4.2}$$

where the form-factor

$$\mathcal{F}(q) = \int e^{-\mathrm{i}\boldsymbol{q}\boldsymbol{\rho}/2} \varphi^2(\rho) d\boldsymbol{\rho} = \frac{1}{\left[1 + \left(\frac{qa_B}{4}\right)^2\right]^{3/2}}, \tag{4.3}$$

is introduced. Here and in what follows we assume equal electron and hole effective masses, $\varphi(\rho) = \sqrt{2/(\pi a_B^2)} \exp(-\rho/a_B)$ is the ground state envelope function (taken in the hydrogenic form), a_B is the effective exciton Bohr radius. For relatively small phonon wavevectors $qa_B \ll 1$ the form-factor is not sensitive to the shape of the envelope function.

4.3.2 Exciton-phonon scattering

In this subsection we study the phonon-induced broadening of exciton resonance in the simplest possible approach based on the Fermi golden rule. This broadening can be related to temperature dependent measurements I performed, which allow determining the PL linewidth as a function of temperature plotted in Fig. 4.3. First we introduce the out-scattering rate $\frac{1}{\tau_k}$ from the exciton state with the wavevector $\boldsymbol{k}$ and kinetic energy $E_k = \hbar^2 k^2/2M$, where M is the translational mass of the exciton $M = m_e + m_h$, due to emission of the acoustic phonons:

$$\frac{1}{\tau_k} = \frac{2\pi}{\hbar} \sum_{\boldsymbol{k}'\boldsymbol{q}} |M^{\boldsymbol{q}}_{\boldsymbol{k}'\boldsymbol{k}}|^2 \delta(E_k - E_{k'} - \hbar\Omega_q). \tag{4.4}$$

For $E_k, E_{k'} \gg E_s$, where $E_s = Ms^2$, the exciton-phonon scattering is quasi-elastic [193] (this point is discussed in detail below in Sec. 4.3.3), thus we can omit the phonon energy, $\hbar\Omega_q$, in the energy conservation δ-function. The calculation of the sum ($\sum_{\boldsymbol{k}} \ldots = S/(2\pi)^2 \int d\boldsymbol{k} \ldots$) in Eq. 4.4 is trivial assuming that typical phonon and exciton wavevectors are smaller than the inverse of Bohr radius $k, k' \ll a_B^{-1}$ (this condition is fulfilled at all realistic temperatures). We put the form-factor $\mathcal{F} \equiv 1$ and obtain from Eq. 4.4 and Eq. 4.2:

$$\frac{1}{\tau_k} = \frac{M(D_c - D_v)^2}{4\pi\hbar^2 \rho s} \int d\phi_{\boldsymbol{k}'} \sqrt{2 - 2\cos\phi_{\boldsymbol{k}'}} = \frac{8}{\hbar} \sqrt{2(Ms^2)^3 E_k} \frac{(D_c - D_v)^2}{4\pi\hbar^2 \rho s^4}. \tag{4.5}$$

$$\boxed{\mathcal{E}^{-1} = \frac{(D_c - D_v)^2}{4\pi\hbar^2 \rho s^4}, \quad E_s = Ms^2}. \tag{4.6}$$

Eq. 4.5 thus reads

$$\frac{1}{\tau_k} = 8\frac{\sqrt{2E_s^3 E_k}}{\hbar\mathcal{E}}.$$

Since exciton-phonon scattering is quasi-elastic both absorption and emission processes are possible because the phonon energy $\hbar\Omega_q$ is typically much smaller than $k_B T$ with T being the temperature and k_B the Boltzmann constant. Thus, for a thermalized exciton gas one has

$$\frac{1}{\tau_T} = \frac{2\pi}{\hbar} \sum_{\boldsymbol{k}'\boldsymbol{q}} |M^{\boldsymbol{q}}_{\boldsymbol{k}'\boldsymbol{k}}|^2 (1 + 2n_q) \delta(E_k - E_{k'}), \tag{4.7}$$

where

$$n_q = \frac{1}{\exp\left(\frac{\hbar\Omega_q}{k_B T}\right) - 1}$$

is the phonon occupation number. For $\hbar\Omega_q \ll E_k, E_{k'} \sim k_B T$ we have $n_q = k_B T/\hbar\Omega_q \gg 1$ and, as it follows from Eq. 4.7 [1]

$$\frac{1}{\tau_T} = \frac{4\pi}{\hbar} \frac{E_s k_B T}{\mathcal{E}}. \tag{4.8}$$

---

[1] In Ref. [197] analogous expression, Eq. (25), was derived for the electron-phonon scattering.

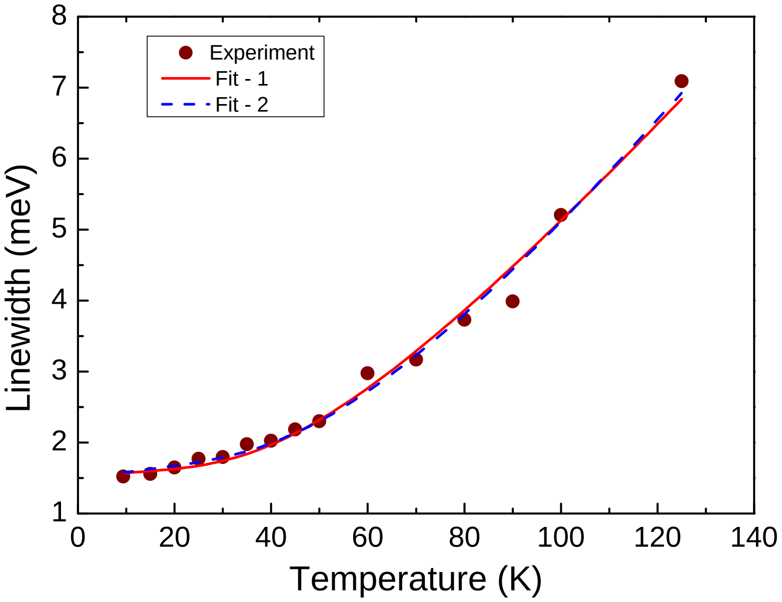

Figure 4.3: **Measured Exciton linewidth** (2× half width at half maximum at *low* energy side) as a function of temperature extracted from the PL data in Fig. 4.1 **(e)** (points). Fit - 1 (red solid curve) is performed by Eq. 4.10 with the parameter set $\gamma(0) = 1.52$ meV, $c_1 = 52\ \mu\text{eV/K}$, $c_2 = 11.52$ meV and $\hbar\Omega_0 = 13.4$ meV. Fit - 2 (blue dashed curve) is performed by Eq. 4.10 with the parameter set $\gamma(0) = 1.49$ meV, $c_1 = 88\ \mu\text{eV/K}$, $c_2 = 14.9$ meV and $\hbar\Omega_0 = 15.5$ meV.

The phonon-induced exciton linewidth can be roughly estimated making use of Eqs. 4.7 and 4.8 with the result :

$$\boxed{\frac{\hbar}{\tau_T} = c_1 T, \quad c_1 = 4\pi \frac{E_s k_B T}{\mathcal{E}}}. \tag{4.9}$$

This is an important result as we can link now theory to experimental findings. The parameter c_1 can be accessed in experiments [51, 198] and I have measured it here : Fig. 4.3 presents the dependence of the exciton linewidth in photoluminescence (measured as full width at half maximum) on the sample temperature. Two fits are performed with very close values of parameters according to the general expression [198, 199]

$$\boxed{\gamma(T) \equiv \frac{\hbar}{\tau_T} = \gamma(0) + c_1 T + \frac{c_2}{\exp\left(\frac{\hbar\Omega_0}{k_B T}\right) - 1}}. \tag{4.10}$$

Here $\gamma(0)$ is the zero-temperature linewidth not related to the exciton-phonon interaction, the T-linear term is due to the exciton-acoustic phonon scattering, Eq. 4.9, and the last term describes the interaction of excitons with optical phonons or acoustic phonons at the Brillouin zone edges, $\hbar\Omega_0$ is the effective phonon energy. Reasonable fit quality can be achieved for the values of c_1 which differ by a factor of 2, compare Fit - 1 and Fit - 2 parameter sets in the figure caption.

Since the material parameters and the speed of sound are known to a large extent, the experimentally determined value of c_1^{exper} allows us to estimate the strength of the exciton-phonon interaction. This can be done by combining Eq. 4.9 and 4.6 with the relevant parameters of the exciton-phonon interaction summarized in Tab. 4.1. Analysis above demonstrates that the accuracy of determination of c_1 parameter is not extremely high because at moderate to high temperatures the broadening can be dominated by the optical phonons and acoustic phonons at the Brillouin zone edge. Therefore the values c_1^{exper} and the deduced deformation potentials can be considered as order-of-magnitudes estimates only. So using $c_1^{exper} = 52\ldots88$ μeV/K we find for our MoSe$_2$ monolayer a difference in valence and conduction band deformation potential of $|D_c - D_v| = 5\ldots6.5$ eV.

Table 4.1: Material parameters

Property	MoSe$_2$	MoS$_2$	WSe$_2$	WS$_2$
s ($10^5\times$cm/s)[a]	4.1	6.6	3.3	4.3
ρ ($10^{-7}\times$g/cm^2)[b]	4.46	3.11[c]	6.04	4.32
c_1^{exper} (μeV/K)	91[d], 52…88[e]	45[f], 70[g]	60[h]	28[d]
$\vert D_c - D_v\vert^{\text{fit}}$ (eV)[i]	5…6.5	5.5[f] , 7.7[g], 10.5[j]	5.4[k]	3.5

[a] From Ref. [200].

[b] Calculated from the data on bulk crystals as $\rho = \rho_{\text{bulk}} c/2$, where c is the lattice constant for the 2H polytype.

[c] From Ref. [197].

[d] From Ref. [198].

[e] This work.

[f] From Ref. [199].

[g] From Ref. [51].

[h] From Ref. [123].

[i] Fit to experimental data on c_1 (thermal broadening of exciton resonance) after Eq. (4.9).

[j] From experimental data in Ref. [188] on strain tuning of optical resonances.

[k] From experimental data in Ref. [189] on strain tuning of optical resonances.

4.3.3 Phonon-assisted absorption and high-energy tail: Perturbative derivation

In this paragraph we aim to discuss exciton formation, assisted by phonons, for laser excitation energies below the first LA(M) resonance i.e. closer than 19 meV to the neutral exciton resonance. In absence of exciton-phonon interaction the absorbance of the transition metal dichalcogenide monolayer at the normal incidence of radiation in the spectral vicinity of exciton resonance is described by the Lorentzian profile

$$\mathcal{A}_0(\omega) = \frac{2\Gamma_0\Gamma}{(\hbar\omega - \hbar\omega_0)^2 + (\Gamma + \Gamma_0)^2}. \tag{4.11}$$

Here ω is the incident light frequency, ω_0 is the exciton resonance frequency, Γ_0 is the exciton radiative decay rate, Γ is the non-radiative decay rate of the exciton. This expression can be derived within the non-local dielectric response theory [40, 201] by calculating the amplitude reflection $r(\omega)$ and transmission $t(\omega) = 1 + r(\omega)$ coefficients of the monolayer and evaluating the absorbance as

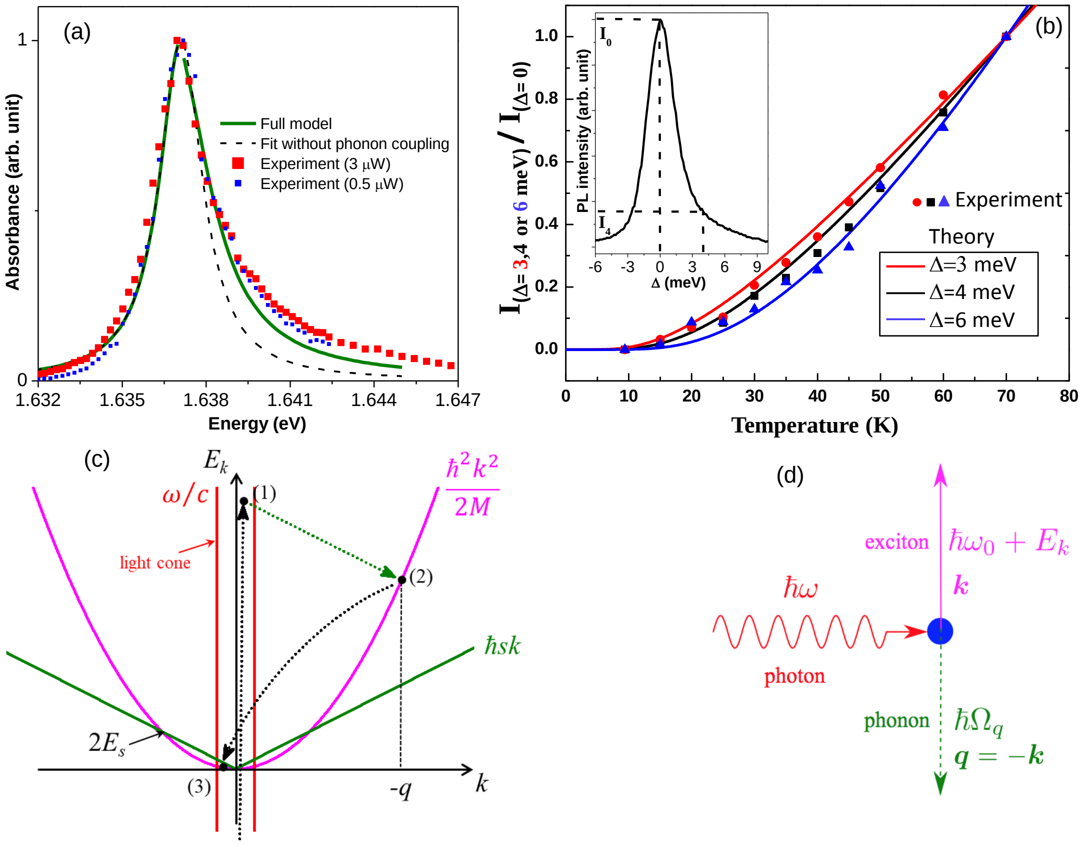

Figure 4.4: **(a)** Absorbance at the A:1s exciton in MoSe$_2$ monolayer. Experimental data same as Fig. 4.1 **(c)** - red squares, data at lower laser excitation power shown as small blue squares, full theory by solid green curve, Eqs. 4.18 and Eq. (4.19), black dashed curve shows the result in the absence of phonon-assisted transitions. $\Gamma_0 = \Gamma = 0.47$ meV, $|D_c - D_v| = 11$ eV, other parameters are from the Tab. 4.1. in the calculation $T = 4\ K$. **(b)** Normalized to the value at $T = 70\ K$ with the $T \to 0$ offset subtracted intensity of PL emission measured (symbols) and calculated after Eq. 4.21 (solid lines) as a function of temperature at a fixed detunings of $\Delta = 3$ (red), 4 (black), and 6 meV (blue). The parameters of the calculation are the same as in **(a)**. **(c)** Schematics illustrating exciton and phonon dispersion, the intersection gives the energy scale $2Ms^2$, for $E_k \gg Ms^2$ the exciton-phonon interaction is quasi-elastic. Steps (1), (2), and (3) describe, respectively, photon absorption with exciton formation in a virtual state, exciton-phonon scattering resulting in a real final state for exciton (on the exciton dispersion, 2), and relaxation toward the radiative states inside the light cone (3). **(d)** Sketch of the photon absorption accompanied by the phonon emission. Exciton and phonon wavevectors have same absolute value but opposite directions.

$\mathcal{A}_0(\omega) = 1 - |r(\omega)|^2 - |t(\omega)|^2$. Hereafter we disregard the effects related with the light propagation in the van der Waals heterostructure [81]. The estimates performed for our structures show that the asymmetry in the shape of the $\mathcal{A}_0(\omega)$ related to the light propagation effects is negligible. Also, we observe this asymmetry in absorption for 3 different samples with different hBN top and bottom layer thicknesses, see Figs. 4.1 and 4.2.

Our target now is to obtain an expression for absorption similar to (Eq. 4.11) but that takes in addition phonon-assisted absorption into account. To look ahead, the final result of the derivations below will result in Eqs. 4.18 and 4.19 which will allow to fit the experimental spectra I recorded, see Fig. 4.4 (a).

To simplify derivations we consider in a first approach in what follows the limit of $\Gamma_0 \ll \Gamma$, which allows us to take into account the light-matter interaction perturbatively. In this limit we can arrive at Eq. 4.11 making use of the Fermi's golden rule and evaluating the rate of the transitions to the excitonic state with the in-plane wavevector $\boldsymbol{k} = 0$ as

$$\mathcal{A}_0 = \frac{2\pi}{\hbar}|M_{opt}|^2\delta(\hbar\omega - \hbar\omega_0).$$

Here $|M_{opt}|^2$ is the squared matrix element of the optical transition to the $\boldsymbol{k} = 0$ state normalized per flux of the incident photons. The δ-function ensuring the energy conservation is broadened by non-radiative processes

$$\delta(\hbar\omega - \hbar\omega_0) = \frac{1}{\pi}\frac{\Gamma}{(\hbar\omega - \hbar\omega_0)^2 + \Gamma^2}.$$

The radiative broadening of the exciton resonance can be introduced as $\Gamma_0 = |M_{opt}|^2/\hbar$. Within second-order perturbation theory the phonon-assisted absorption [schematically shown in Fig. 4.4, panels (c) and (d)] is possible for $\hbar\omega > \hbar\omega_0$ via a two step process: First the exciton is created in the intermediate (virtual) state with $\boldsymbol{k} \simeq 0$ and the emission of the phonon takes place as a second step. Correspondingly, the contribution to absorbance due to this two-step process reads

$$\mathcal{A}_1 = \frac{2\pi}{\hbar}\sum_{\boldsymbol{k},\boldsymbol{q}}\left|\frac{M^{\boldsymbol{q}}_{\boldsymbol{k},\boldsymbol{0}}M_{opt}}{\Delta}\right|^2\delta(\Delta - E_{\boldsymbol{k}} - \hbar\Omega_{\boldsymbol{q}}). \tag{4.12}$$

Here

$$\Delta = \hbar\omega - \hbar\omega_0, \tag{4.13}$$

is the detuning between the photon energy and the exciton resonance energy.

It follows from the momentum conservation law that the phonon wavevector $\boldsymbol{q} = -\boldsymbol{k}$ as the total linear momentum of the electron-hole pair is equal to the in-plane photon momentum, that is close to zero at the normal incidence of radiation. The energy conservation law therefore reads

$$\frac{\hbar^2k^2}{2M} + \hbar sk = \Delta. \tag{4.14}$$

Eq. 4.14 can be readily solved to obtain the phonon energy in the form $(q = k)$

$$\hbar\Omega_k = E_s\left(\sqrt{1 + \frac{2\Delta}{E_s}} - 1\right) \approx \begin{cases}\Delta, & \Delta \ll E_s,\\ \sqrt{2\Delta E_s}, & \Delta \gg E_s.\end{cases} \tag{4.15}$$

For typical parameters $E_s \sim 100$ μeV$\ll \Delta$ all energy is transferred to the recoil exciton, leaving the phonon with a small energy $\sqrt{2\Delta E_s} \ll \Delta$. An illustration of the exciton and phonon dispersions is shown in Fig. 4.4 (c). Summation over $\boldsymbol{k}$ in Eq. 4.12 can be performed for any ratio of Δ to E_s with the result

$$\mathcal{A}_1 = 2\pi\Gamma_0 \frac{\mathcal{F}^2(\Omega_k/s)}{\mathcal{E}} \mathcal{P}\left(\frac{\Delta}{E_s}\right) \Theta(\Delta), \tag{4.16}$$

where $\Theta(\Delta)$ is the Heaviside Θ-function and the function $\mathcal{P}(x)$ is defined as

$$\mathcal{P}(x) = \frac{1}{\sqrt{1+2x}} \left(\frac{\sqrt{1+2x}-1}{x}\right)^2 \approx \begin{cases} 1, & x \ll 1, \\ \sqrt{2/x^3}, & x \gg 1. \end{cases}$$

For the experimentally relevant situation where $x = \Delta/E_s \gg 1$ the function $\mathcal{P}(x) \approx \sqrt{2}/x^{3/2}$ and $\mathcal{A}_1$ in Eq. 4.16 reduces to

$$\mathcal{A}_2 = 2\sqrt{2}\pi\Gamma_0 \frac{\mathcal{F}^2(\Omega_k/s)}{\mathcal{E}} \left(\frac{E_s}{\Delta}\right)^{3/2} \Theta(\Delta). \tag{4.17}$$

Eq. 4.17 describes the tail of absorption at $\hbar\omega - \hbar\omega_0 \equiv \Delta \gg \Gamma, \Gamma_0, E_s$, Ω_k is given by Eq. 4.15, similarly to predicted and observed in Ref. [184]. Accounting for both the phonon emission and absorption processes gives rise to an additional factor of $(1 + 2n_k)$ in Eq. 4.17.

For the purpose of direct comparison with experiment, it is convenient to obtain a model expression for the absorption spectrum which accounts for both the (no-phonon) direct and indirect (phonon-assisted) processes. To that end we employ the self-consistent Born approximation [202] for the exciton-phonon interaction, see [124] for details, and arrive at

$$\boxed{\mathcal{A}(\hbar\omega) = \frac{2\Gamma_0[\Gamma + \gamma_{ph}(\Delta)]}{\Delta^2 + [\Gamma + \Gamma_0 + \gamma_{ph}(\Delta)]^2}}, \tag{4.18}$$

where the acoustic phonon scattering rate is:

$$\gamma_{ph}(\Delta) = \coth\left(\frac{\hbar\Omega_k}{2k_BT}\right) \frac{\pi\mathcal{F}^2(\Omega_k/s)\Delta^2}{\mathcal{E}} \mathcal{P}\left(\frac{\Delta}{E_s}\right) \Theta(\Delta). \tag{4.19}$$

In Eqs. 4.18 and 4.19 both phonon absorption and emission processes are included. The results of calculation of $\mathcal{A}(\hbar\omega)$ are shown in Fig. 4.4 (a) and fit very well the measured absorption spectra, they are discussed further in Sec. 4.4.

4.3.4 Temperature-dependent photoluminescence

In the photoluminescence process the exciton formed non-resonantly relaxes in energy towards small k-states. For a monolayer in free space the light cone is defined as $q_{phot} = \omega/c$, c is the speed of light, and when $k(\omega) \leqslant q_{phot}$ the exciton can recombine by emitting a photon. In the absence of exciton-phonon interaction the photoluminescence spectrum has a simple Lorentzian form, cf. Eq. 4.11. The exciton-phonon interaction makes states outside the light cone optically active as well. For example, an exciton with the wavevector $\boldsymbol{k}$ can decay by emitting a phonon with wavevector $\boldsymbol{q} = \boldsymbol{k}$ and in addition a photon along the monolayer normal i.e. $q_{phot} = 0$. For experiments at finite temperature not only the phonon emission, but also phonon absorption processes become important.

In general the calculation of the photoluminescence spectrum requires detailed analysis of the exciton energy relaxation and recombination processes [203, 204]. Here, to simplify the consideration as we aim for a qualitative comparison with our experimental data, we assume that the excitons are thermalized and their occupation numbers are described by the Boltzmann distribution

$$f_k = \exp\left(\frac{\mu - E_k}{k_B T}\right),$$

where $\mu < 0$ is the chemical potential of the exciton gas. The **increase** in temperature mainly results in occupation of **higher energy** excitonic states, which due to the quasi-elastic character of the exciton-phonon interaction gives rise to the **high-energy** wing in the photoluminescence which is so striking for the experiments shown in Fig. 4.1 (e). Denoting, as in Sec. 4.3.3, by $\hbar\omega$ the energy of the emitted photon, by $\hbar\omega_0$ the energy of the exciton at $k = 0$, and by Δ the detuning, Eq. 4.13, we arrive at the photon emission rate in the form [cf. Eq. (4.12)]

$$I(\omega) \propto \sum_{\boldsymbol{k},\boldsymbol{q}} f_k(1 + 2n_q) \left| \frac{M^{\boldsymbol{q}}_{\boldsymbol{0},\boldsymbol{k}} M_{opt}}{\Delta} \right|^2 \delta(\Delta - E_{\boldsymbol{k}}). \tag{4.20}$$

Eq. 4.20 holds for $\Delta \gg \Gamma$, in the energy conservation δ-function the phonon energy is omitted. The calculation shows that the photoluminescence spectrum at the positive detunings related to the phonon-assisted emission takes the form

$$\boxed{I(\omega) \propto e^{-\Delta/k_B T} \frac{k_B T E_s}{\Delta^2} \mathcal{F}^2 \left(\frac{\sqrt{2\Delta E_s}}{\hbar s}\right), \quad \Delta \gg \Gamma}. \tag{4.21}$$

The coefficient in Eq. 4.21 is temperature and detuning independent. For given detuning $\Delta > 0$ the relative photoluminescence intensity drastically increases with temperature mainly due to the presence of excitons with higher energies.

At the same time, the photoluminescence spectrum at $\omega < \omega_0$ (negative detuning $\Delta < 0$) is practically unaffected by the temperature increase. Indeed, to emit a photon with energy significantly (by more that $\hbar\Gamma$) lower than $\hbar\omega_0$ a phonon with the energy $\hbar\Omega_q \geqslant |\Delta|$ should be emitted as well. The rate of this process is given by

$$I(\omega) \propto \sum_{\boldsymbol{k},\boldsymbol{q}} f_k(1 + n_q) \left| \frac{M^{\boldsymbol{q}}_{\boldsymbol{0},\boldsymbol{k}} M_{opt}}{\Delta} \right|^2 \delta(\Delta - E_{\boldsymbol{k}} + \hbar\Omega_q).$$

Due to the energy conservation law the process is allowed for small absolute values of detunings only $|\Delta| \leqslant E_s/2$, see Fig. 4.4. **Thus, for the experimentally relevant parameters the photoluminescence increase at *negative* detunings is not expected in the theory, in agreement with the observation of an asymmetric lineshape in Fig. 4.1 (e).**

4.4 Discussion

Fig. 4.4 (a) (same data as Fig. 4.1 (c)) shows the A:1s absorption measured via the integrated trion PL intensity with a very prominent high energy tail. The results of our model calculations using Eqs. 4.18 and 4.19 for the best fit parameters (given in the caption) are shown by the red solid line. For comparison, blue dashed curve shows the symmetric Lorentzian which describes the low-energy wing of the absorption ($\hbar\omega < \hbar\omega_0$), but does not reproduce the high energy wing. In contrast, the full calculation fits the spectrum and reproduces the observed absorption asymmetry very well, giving a strong indication that including exciton-phonon coupling is important for describing the absorption process.

The free parameters in our fit are the radiative, Γ_0, and nonradiative, Γ damping of the exciton as well as the difference of the deformation potentials for the electron and hole, $|D_c - D_v|$. The values used for $\Gamma_0 = \Gamma \simeq 0.5$ meV is in order of magnitude agreement with results from time resolved spectroscopy reporting hundreds of fs to few ps lifetimes [205, 128, 44]. The best fit value of $|D_c - D_v|$ of 11 eV is somewhat larger than the literature and experimental data summarized in Tab. 4.1, but within the same order of magnitude. The discrepancy can originate from the simplification of the model, particularly, the absence of the coupling with optical phonons as well as with phonons at the Brillouin zone edge. Another potential source of error can be related to the inaccuracy in determination of the deformation potentials through fitting of the temperature-induced broadening, as discussed above for the data shown in Fig. 4.4. Additionally, the presence of free charge carriers may also provide a contribution to the high-energy wing in absorption due to the possibility to relax the momentum conservation law. We also stress that the absorption (Figs. 4.1 (c) and 4.4 (a)) is detected via the photoluminescence of the trion, therefore, efficiency of the relaxation pathway may play a role as well. Recent A:1s absorption experiments in our group based on detecting upconversion PL, which I performed on $MoSe_2$ MLs, have confirmed the high energy absorption tail [192]. So the experimental observation for these absorption experiments is independent of the detection method.

Similarly to the high energy tail in the absorption, the calculations predict the same asymmetry in the photoluminescence emission spectrum. As described in Sec. 4.3.4 this is because the excitons with wavevectors $k \gtrsim q_{phot} = \omega/c$ become optically active due to the phonon-assisted processes. The increase in the temperature gives rise to the increase of the occupancy of excitonic states at larger wavevectors. This is exactly what is observed in Fig. 4.1 (e). Fig. 4.4 (b) shows the intensity of photoluminescence at three values of the positive detuning $\Delta = 3$, 4, and 6 meV (all on the high energy wing) as a function of temperature. The experimental data are in reasonable agreement with the calculation after Eq. 4.21 and indeed confirm the importance of the phonons in the photoluminescence emission.

4.5 Conclusion

Our combined experimental and theoretical study sheds light on the strong impact of the exciton-acoustic phonon interaction in TMD monolayers on exciton formation and recombination. We interpret strong absorption above the exciton resonance in terms of phonon-assisted exciton formation. Asymmetric lineshapes with high-energy tails in emission are observed in temperature dependent experiments. Also this unusual emission lineshape is due to deformation potential exciton-acoustic phonon coupling and can be fitted by our simplified analytical theory. The developed analysis shows that exciton-phonon interaction is quite strong in transition metal dichalcogenide MLs as compared with conventional GaAs-based quantum wells. We have to keep in mind an important difference: in a $MoSe_2$ ML, which is a 2D crystal, the exciton will interact with phonons that have a 2D density of states. In contrast, in GaAs quantum wells the 2D exciton will interact with 3D phonons in the crystal. For example the parameter c_1 in GaAs quantum wells [206] is an order of magnitude smaller than in $MoSe_2$ despite higher values of deformation potential and the fact that exciton interacts with bulk (3D) phonons in GaAs-case. Qualitatively, the enhanced exciton-phonon interaction in atom-thin crystals is due to the fact that for small wavevectors the phonon density of states is larger in 2D than in 3D. This is because the density of states of 2D phonons $\propto q$ is greatly enhanced compared to that of the bulk (3D) phonons $\propto q^2$. This results in about an order of magnitude enhancement (see [124] for further details) and accounts for the observation of the high-energy tails in exciton absorption in TMD monolayers.

Chapter 5

Interlayer excitons in bilayer MoS_2 with strong oscillator strength up to room temperature

Coulomb bound electron-hole pairs, excitons, govern the optical properties of semiconducting transition metal dichalcogenides like MoS_2 and WSe_2. In this chapter we study optical transitions at the K-point for *2H* homobilayer MoS_2 in reflectivity measurements in high quality samples encapsulated in hexagonal boron nitrite (hBN) and compare with Density Functional Theory (DFT) calculations performed by Iann Gerber (LPCNO) including excitonic effects (GW-BSE). In both calculated and measured spectra we find a strong interlayer exciton transition in energy between A- and B-intralayer excitons, observable for $T = 4 - 300\ K$, whereas no such transition is observed for the monolayer in the same structure in this energy range. The interlayer excitons consist of an electron localized in one layer and a hole state delocalized over the bilayer, which results in the unusual combination of high oscillator strength and a static dipole moment. We also find signatures of interlayer excitons involving the second highest valence band (VB) and compare absorption calculations for different bilayer stackings. For homotrilayer (TL) MoS_2 we also observe interlayer excitons and an energy splitting between different intralayer A-excitons originating from the middle and outer layers, respectively. The work described in this chapter corresponds to the publication [60].

5.1 Introduction to multi-layers

Van der Waals materials have in-plane covalent bonding and the individual layers are held together by the so-called dispersion forces [75, 207]. A fascinating aspect of this class of materials is the drastic change of physical properties by changing the sample thickness by just one atomic monolayer. A prominent example is the striking difference between mono- and bilayer graphene [208]. For the van der Waals semiconductor MoS_2 the transition from indirect to direct bandgap material occurs when going from bilayers to a monolayer [6, 71]. These dramatic changes are very different from classical semiconductors like GaAs for example, where the optical properties change gradually with thickness [209].

The light-matter interaction in monolayer (ML) transition-metal dichalcogenides

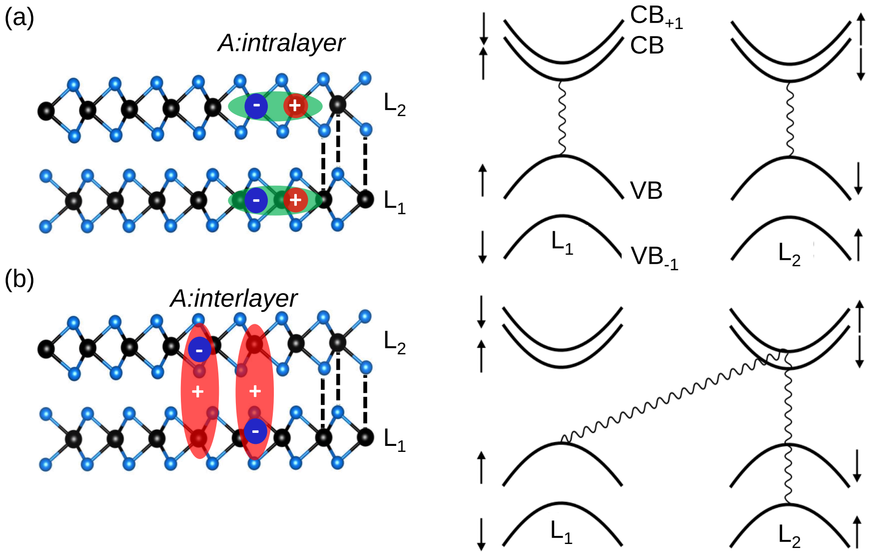

Figure 5.1: **Schematics of intralayer and interlayer excitons in *2H* MoS_2 homobilayers. (a)** Intralayer excitons consist of an electron (red) and a hole (blue) in the same layer while in **(b)** an electron localized on one layer interacts with a hybridized hole state to form an interlayer exciton. Optical selection rules, represented by wavy lines, for intralayer and interlayer transitions in k-space are also given for K-points, respecting spin conservation. For clarity only one interlayer exciton (spin up) is shown, there is also the spin down state with the same energy.

is governed by Coulomb bound electron-hole pairs, excitons [19, 210]. As a second layer is added, the light-matter interaction is strongly modified since new exciton complexes can form, with electron and hole residing in different layers [139, 211, 212, 213, 214], as sketched in Fig. 5.1 (b). These interlayer excitons show interesting properties [66], also for thicker layers [68, 215] and more sophisticated van der Waals structures [216]. A very active branch of research investigates spatially indirect interlayer excitons in TMD heterobilayers of with great prospects for spin-valley physics and nano-scale moiré potentials [116, 120, 150, 153, 217]

In this chapter I will discuss interlayer excitons in homobilayers of MoS_2. Contrary to interlayer excitons in TMD heterobilayers, which are indirect both in real and reciprocal space, we find strong signatures in absorption of the interlayer exciton, about 20% of the oscillator strength of the intralayer exciton. The DFT-*GW* calculations solving the Bethe-Salpeter equation uncover a strong, spin allowed interlayer exciton peak about 80 meV above the A:1s transition. We find a 20% reduction of exciton binding energy of the interlayer exciton compared to the intralayer exciton. The calculated absorption also predicts an interlayer transition involving the B-valence band located in energy above the B:1s intralayer transition. We compare several bilayer stackings in our calculations of optical absorption spectra [211, 218]. Our experiments on high quality bilayer and trilayer MoS_2 in hBN show prominent signatures of interlayer excitons up to room temperature in absorption, signalling strong oscillator strength. The clear manifestation of interlayer excitons opens the way for electric field control of the optical transitions based on

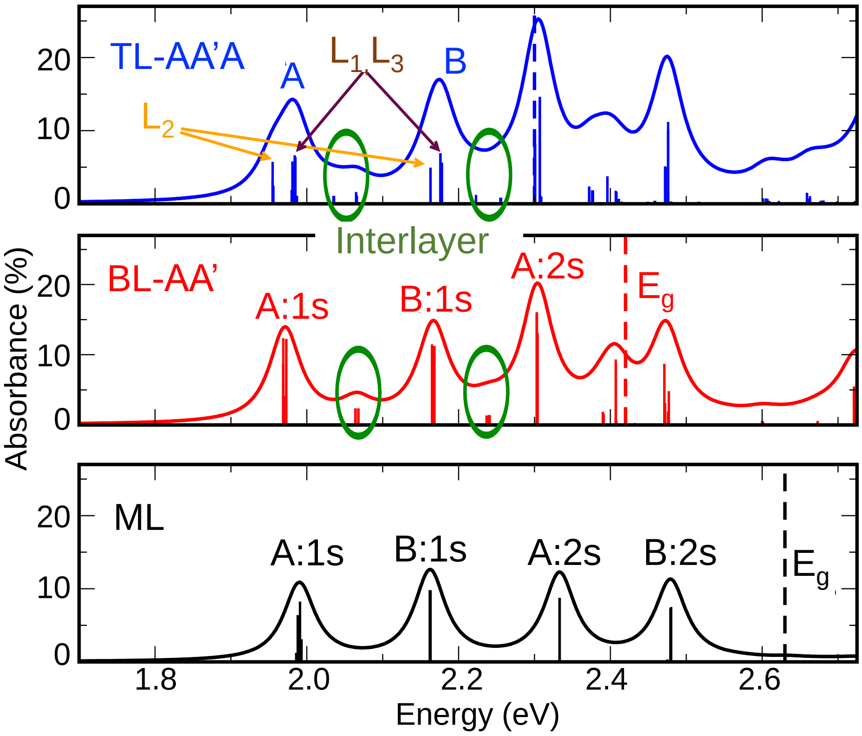

Figure 5.2: **Calculated absorption spectra for a single mono-, bi and trilayer (*2H*).** Interlayer exciton transitions are marked by green circles. Orange arrows for the TL case indicate intralayer transitions involving only the middle layer (L_2) of the three layers, while the marroon ones stress the L_1, L_3 intralayer transitions.

their out-of-plane electric dipole [212], as discussed in detail in Chapter 6. Their strong oscillator strength makes this in addition an interesting system for efficient, tunable coupling to optical microcavities and plasmons [219, 220, 221, 222, 223]. Our work shows directly the stronger interlayer coupling for the hole states in MoS_2 as compared to much weaker coupling expected for K-excitons in WSe_2 homobilayers due to the larger A-B valence band separation [224, 225].

5.2 Bandstructure and absorption spectra calculations

The calculations of bandstructures and optical absorption by Iann Gerber (LPCNO) have been crucial for the analysis of the optical spectroscopy that I have performed. Here I summarize the main results of these calculations : The natural MoS_2 bilayer (BL) stacking is AA', see Fig. 5.3 (a) for atomic stacking representation, corresponding to the *2H* bulklike symmetry. This is thermodynamically the most stable configuration. When using the DFT-D3 exchange-correlation functional scheme of Grimme *et al* [226], the AB-stacking, prototypical of the *3R*-structure [218], has the same binding energy as *2H* within meV accuracy, i.e 117 meV/formula unit.

In other words, both monolayers gain 117 meV (per elementary cell) by forming a bilayer as compared to staying at infinite distance. AA-stacking is much less favorable : 82 meV per formula unit. The interlayer distance d_{inter} found is similar for *2H* and *3R* stacking order, being 6.17 Å, in good agreement with previous studies [227, 228].

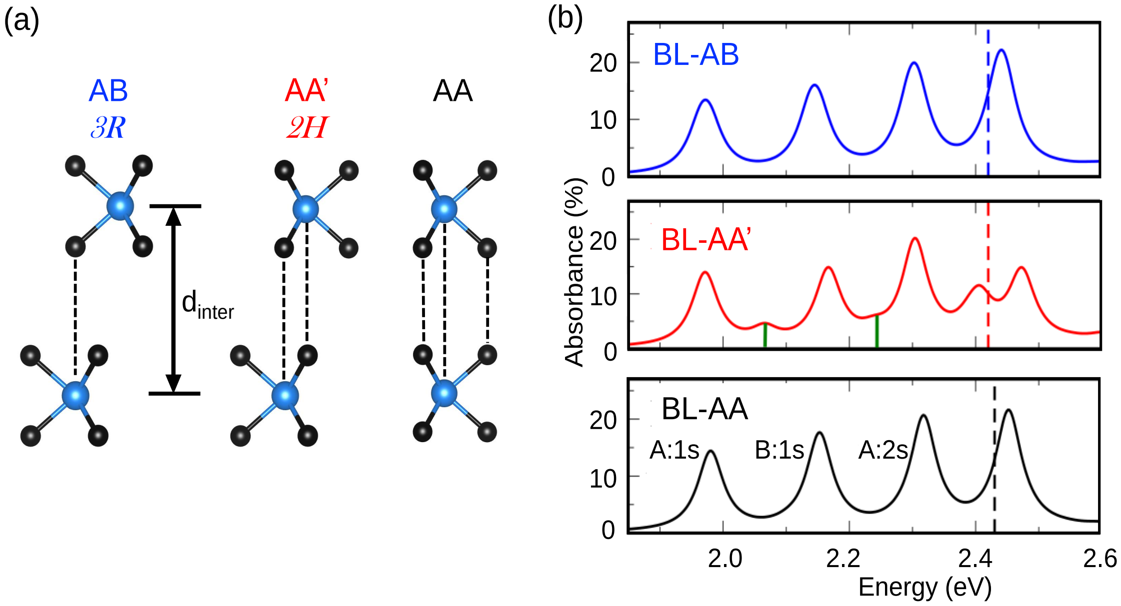

Figure 5.3: **Calculated absorption spectra for a bilayer, using three different stackings.** The green lines mark interlayer transitions for AA' stackings (*2H*).

In Fig. 5.2, we show absorption spectra calculated from the imaginary part of the complex dielectric function extracted from *GW*+BSE procedure, for free-standing ML, BL-AA' and trilayer (TL) in *2H*-like stacking systems, which are the most relevant for samples exfoliated from naturally occurring MoS_2 [229]. The calculations for the absorbance are based on a precise determination of the band-structure and then including the strong excitonic effects. In order to validate the computational approach and precision, which is of the order of few tens of meV for excitonic peak positions, we perform calculations for monolayer MoS_2 in vacuum and we identify and reproduce the peak positions of the different spectral features as in the work of Qiu *et al.* [18, 230]. Note that the 2s feature oscillator strengths are overestimated due to limited number of k-points used in the response function calculations in the BSE step of the calculations. Using a higher number of k-points is not practical for this study as already the calculations presented here took several weeks to perform. The accurate monolayer results give us confidence for the bilayer system where comparison with experimental data was so far not possible in detail because of the poor optical quality of the structures. As expected, when the number of layers is increased the fundamental gap E_g at the K-point is decreased : 2.62, 2.43 and 2.30 eV for ML, BL and TL respectively, when the multilayered systems become globally indirect in the $\Gamma - K$ direction, as it can be seen in Fig. 5.6.

In the calculated *2H*-BL absorption spectrum we can see an additional transition between the A- and B-intralayer exciton 1s states, 0.09 eV above the A- and B-peaks, see Fig. 5.2. Considering only the spin up transitions in the K valley as proposed in Fig. 5.1 (b), it has 19 % of the oscillator strength of the corresponding A:1s intralayer transition. Its main contributions come from states corresponding to the valence band spin up : VB of L_1 and VB_{-1} of L_2 partially hybridized, and a well-localized electron lying in the second lowest conduction band (CB_{+1}) states of L_2. Here the hole states delocalized over the bilayer are important, as the transition we call for brevity interlayer has an intralayer contribution, sketched in Fig. 5.1 (b): the intralayer (L_2) VB_{-1} to CB_{+1} oscillator strength is roughly 18% of the spatially indirect VB to CB_{+1} one. We recall that the symmetry of the first VBs in K are mainly of $d_{x^2-y^2}$ and d_{xy} characters, mixed with $p_{x,y}$ orbitals of S, when the first CBs are made of d_{z^2} orbitals. Interlayer hopping (hybridization) are thus possible in the VBs, helped by the $S-p_z$ orbital contributions in Γ, but remains impossible for electrons in the CBs [12, 211, 218]. We experimentally control interlayer excitons formation by choosing different stackings as shown in Chapter 8.

Quantitative analysis of the optical transitions in the related system of $MoSe_2$ bilayers in hBN using the Dirac-Bloch equations also predicts an oscillator strength of 20% of the interlayer A-exciton compared to the intralayer exciton [66]. In their work the encapsulation in hBN is taken explicitly taken into account, whereas our calculations are performed in vacuum to avoid high computational cost. The general target was to see what type of new exciton absorption feature emerges as we go from monolayer to bilayer material - the exact energy position of the transition will be sensitive to screening by the dielectric environment [231, 232]. We extract in BL MoS_2 the exciton binding energies for the intralayer excitons of about 0.45 eV compared to 0.36 eV for interlayer excitons. This relative comparison shows strong binding for interlayer excitons with carriers residing in different layers, although the absolute values will be smaller in encapsulated samples in hBN principally due to the globally higher dielectric constant, see measurements for encapsulated monolayers in [25].

For the trilayer case shown in Fig. 5.2, several interesting features are observed : The A:1s state is split, with the intralayer exciton of the central layer (L_2) having the largest binding energy and followed in energy by intralayer excitons from the two outside layers (L_1, L_3). In our calculations we also see clear signatures of interlayer excitons in TLs. A set of interlayer transitions is present 0.05 eV above the A-peak and again split by 0.03 eV due to the possibility for the carriers to reside either in the central or outside layers. The interlayer exciton oscillator strengths are relatively large as in the bilayer case, around 20% of the intralayer transitions.

Interlayer coupling of VBs and CBs is governed by symmetry and also the spin-orbit splitting between spin-up and spin-down bands, as revealed in very early work in bulk samples [215]. Whereas interlayer coupling for electrons is suppressed by symmetry also for *2H* stacking [211], the interlayer coupling for hole states depends on both symmetry (and more specifically on atomic arrangement between layers) and, if allowed, also on the amplitude of the spin-orbit splitting [211, 218]. In that respect *2H* stacking in bilayer MoS_2 provides favorable conditions for the observation of interlayer excitons, as the interlayer coupling of VBs is allowed and the spin-orbit splitting is smaller than in $MoSe_2$, $MoTe_2$, WSe_2 and WS_2. So

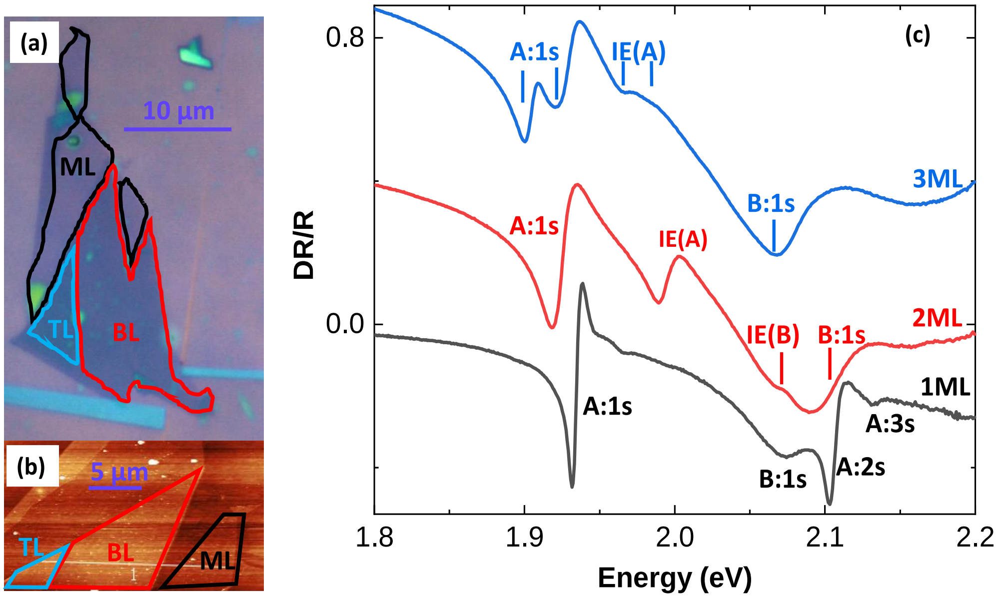

Figure 5.4: **Monolayer (ML), bilayer (BL) and trilayer (TL) MoS$_2$ encapsulated in hBN**. **(a)** Optical microscope image of the hBN/MoS$_2$/hBN heterostructure. **(b)** AFM measurements confirms atomic steps. **(c)** Differential reflectivity of the three different thicknesses (ML, BL and TL) at a sample temperature of $T = 4\ K$. Spectra have been shifted for clarity. The intralayer A- and B-excitons (A:1s, A:2s, A:3s and B:1s) and the two interlayer resonances IE(A) and IE(B) are labelled.

for sake of completeness, we also calculated the absorption spectra for AA and AB stacking (corresponding to *3R* symmetry in bulk), for which we observe no signature interlayer exciton transitions as shown in the comparison in Fig. 5.3. More detailed theory and experiment on MoS$_2$ bilayers in *2H* versus *3R* stacking will be presented later in this thesis.

5.3 Optical Spectroscopy on MoS$_2$ mono-,bi- and trilayers in hBN

Bilayer MoS$_2$ is a fascinating system with tunable properties, explored in a large spectrum of theoretical work [16, 211, 212] and also experiments [228, 233, 61, 234]. So far experimental studies of optical properties concentrated on the intralayer exciton. As bilayer MoS$_2$ has an indirect gap, the technique of choice is absorption spectroscopy, either in transmission or reflection geometry, emission in photoluminescence on the other hand is strongly quenched compared to the monolayer [6, 71]. Further progress was hampered until recently by the very broad optical transition linewidth in MoS$_2$ based nanostructures of the order of 50 meV. Encapsulation in hexagonal boron nitride (hBN) of MoS$_2$ monolayers (MLs) has resulted in considerable narrowing of the exciton transition linewidth down to 1 meV [51, 235] and allowed identification of excited exciton states [81]. This gives access to fine features of the exciton spectra and considerably clearer comparison with theory.

We fabricated a sample with monolayer steps (ML, BL, TL) encapsulated in hBN by exfoliating MoS_2 bulk crystals, see Chapter 2 for details, so we compare all 3 different thicknesses in identical conditions, see Fig. 5.4. Atomic force microscopy (AFM) measurements have been performed in tapping mode, before deposition of the top hBN layer. The topography of Fig. 5.4 (b) shows height steps corresponding to monolayer, bilayer and trilayer MoS_2. The extremely different white light reflectivity spectra in Fig. 5.4 (c) are so striking, they can be used for thickness identification, as discussed below. As this sample is exfoliated from *2H* bulk, the bilayer stacking is the thermodynamically most stable *2H* configuration, analyzed in detail by DFT in the previous section.

5.3.1 Low temperature differential reflectivity

First we discuss the measurements at low temperature $T = 4\ K$. We measure differential reflectivity $(R_{\mathrm{ML}} - R_{\mathrm{sub}})/R_{\mathrm{sub}}$, where R_{ML} is the intensity reflection coefficient of the sample with the MoS_2 layer and R_{sub} is the reflection coefficient of the hBN/SiO_2 stack. Please note that the overall shape of the differential reflectivity depends on cavity effects (thin layer interference) given by top/bottom hBN and SiO_2 thickness. This leads to exciton transition lineshape variations in amplitude and sign in the presented spectra, see section 2.3 in Chapter 2 and also section 3.1 in Chapter 3 for a detailed discussion and comparison with transfer matrix simulations [81].

Monolayer. As for theory, also for experiment the monolayer sample allows us to validate our approach : the spectra are very similar to the exciton states identified for hBN encapsulated MoS_2 in previous work [81], with a clear signature of the A:2s exciton state superimposed on B:1s, where we find a typical A-B exciton separation of 150 meV in energy [12]. Here cavity effects determined by the top and bottom hBN thickness used for encapsulation need to be taken into account to analyze the oscillator strength [81]. The identification of the A:2s and A:3s as excited A-excitons is confirmed by analyzing the diamagnetic shift in magneto-absorption [25] and using photoluminescence excitation experiments [81]. Note that for the monolayer A:1s to A:2s separation we find an energy of about 170 meV. This is less than the 1s to 2s exciton state separation measured for the B-exciton in uncapped monolayer MoS_2 on hBN/SiO_2 of about 225 meV [140]. This follows the general trend of finding lower exciton binding energies in hBN encapsulated samples as compared to non-encapsulated ones, underlining the importance of the dielectric environment for the strength of the Coulomb interaction [231, 21].

Bilayer. The difference between ML and BL absorption is striking : there is an additional transition in Fig. 5.4 (c) right between A:1s and B:1s. We attribute this transition 70 meV above the A:1s to the interlayer exciton IE(A), with both carriers at the K-point but in different layers. The energy position between A:1s and B:1s fits well with the predictions from our DFT calculations, compare with Fig. 5.2. In the region of the B-excitons we find 2 transitions. In addition to B:1s the second peak is the interlayer exciton IE(B) involving the B-valence band. The interlayer character of peaks are confirmed by its comparatively large Stark shift and also with large amplitude and opposite Zeeman splitting to the intralayer excitons, see Chapter 6 for the details.

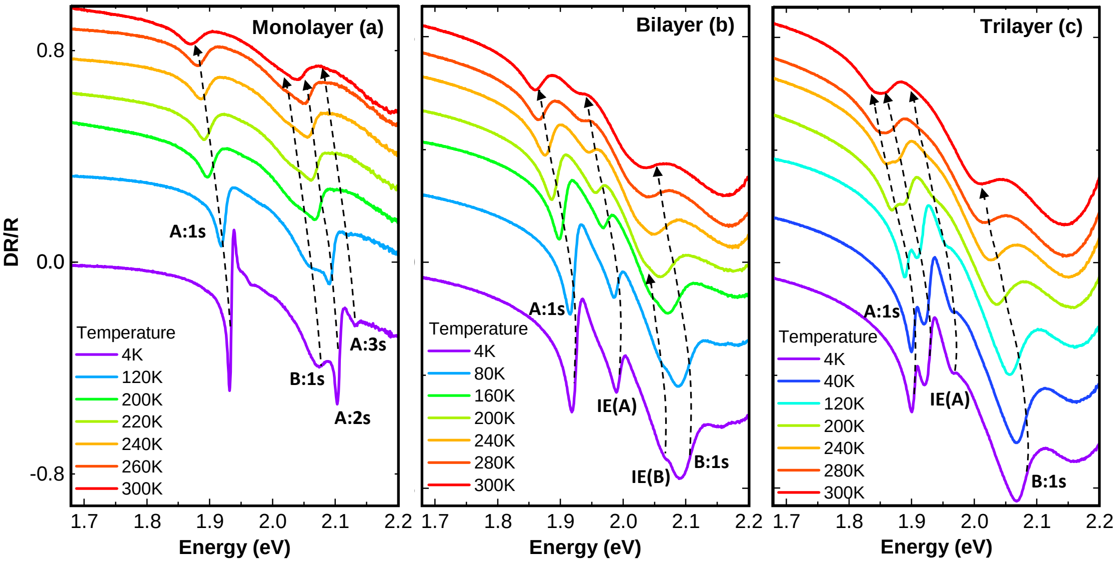

Figure 5.5: **Optical spectroscopy results:** Temperature dependent differential reflectivity spectra for monolayer **(a)**, bilayer **(b)** and trilayer **(c)** MoS_2 encapsulated in hBN.

Trilayer. Finally we investigate a homotrilayer. Here a striking aspect is the observation of not one but two features associated with the main intralayer A-exciton. Here our DFT calculations suggest, see Fig. 5.2, that the higher exciton binding energy for intralayer excitons in the middle layer (L_2) results in a lower transition energy as compared to the intralayer excitons from the two outer layers (L_1 and L_3). The measured splitting between the two transitions is about 20-25 meV. In addition, between the A- and B-intralayer excitons we observe two features which are separated by 15 meV in energy that we can attribute to interlayer excitons, as we compare our experiment in Fig. 5.4 (c) with the calculation in Fig. 5.2. From the DFT calculations and experiments in applied magnetic and electric fields (see Chapter 6 for details) we uncover two types of interlayer excitons in MoS_2 trilayer.

Both homobilayer and trilayers are indirect semiconductors. The optical transitions involving excitons direct in momentum space with carriers from the K-points can be spectrally broadened compared to the ML case due to relaxation towards the lower lying indirect bandgap.

5.3.2 Temperature evolution of absorption from $4\ K$ to room temperature

In Fig. 5.5 we analyze the temperature evolution of the differential reflectivity spectra. The evolution of the ML spectrum up to room temperature shows a standard shift of the A:1s transition with temperature. At $T = 300\ K$ at first glance two strong transitions are visible, separated by 170 meV. The B:1s absorption is very broad and its energy cannot be fitted precisely. Surprisingly, the most pronounced feature at higher energy is not the B:1s but the A:2s state. In general to observe excited exciton states also at room temperature is consistent with the high binding energy of these intralayer excitons in hBN encapsulated MoS_2 of about 220 meV

[81].

Remarkably, for the bilayer in Fig. 5.5 (b) the intralayer but also the interlayer transition are still observable at room temperature, again consistent with a high exciton binding energy, as indicated by our *ab initio* results. The good visibility of the interlayer exciton at room temperature has inspired different groups to perform strain tuning experiments, which confirmed that the transitions originate from the K-points [236, 237]. For the trilayer, the double feature for the intralayer A-exciton is visible at all temperatures. The main interlayer exciton is still discernible at 240 K.

5.4 Discussion

For simplicity, in our theory and experiment we concentrate on optical transitions with large oscillator strength, so in our optical absorption spectra we have no clear signature of possible optical transitions indirect in k-space, for example, that involve carriers from the Γ-point [8, 238]. In this work we exclusively discuss transitions involving carriers in different layers and bands, but all at the K-point. The bandstructure of TMD bilayers is rather complex at the K-point, with spin-split conduction and valence bands [31, 211, 29]. Already in a quasi particle picture this gives rise to several optical transitions. In optical spectroscopy experiments we work with excitons not band to band transitions, so all energy scales are renormalized by the Coulomb interaction, the direct and exchange terms.

We now try to analyze why the interlayer and intralayer A-excitons have different transition energies, similar arguments hold for the B-excitons. In the bilayer absorption measurements in Figs. 5.4 (c) and 5.5 (b) and also calculations in Fig. 5.2 we observe the intralayer exciton transition about $\Delta_{\text{exp}} = 70$ meV lower in energy than the interlayer exciton. Several effects can contribute to this difference :
(i) Difference in intralayer (calculated 0.45 eV) and interlayer exciton binding energy (0.36 eV). Although the calculations are for structures in vacuum and our sample is encapsulated in hBN, we see this difference is significant and will provide an important contribution to Δ_{exp}. The physical origin of the difference in binding energies can come from the different spatial extension of the exciton in the intra- and interlayer configuration. The effective mass for spin-up and spin-down conduction and valence bands that we can extract from our bandstructure calculations is another source for differences in the binding energies of different exciton species [12]. For the A-interlayer exciton the difference in mass of the two lowest lying conduction bands is relevant, and we find 0.47 m_0 for CB$_{+1}$ and 0.42 m_0 for CB, respectively, where m_0 is the free electron mass. Though significant, our calculations show this mass difference remains a smaller contribution compared to the exciton spatial extension change between the two configurations.
(ii) Due to spin-conservation in optical dipole transitions, the interlayer excitons is formed with an electron in the second lowest, not lowest conduction band, see Fig. 5.1 (b). The conduction band spin splitting is estimated to be in the meV range [31, 29], we find 13 meV in our calculations, see Fig. 5.6, in very good agreement with a recent experimental measurement [239]. So this conduction band spin splitting can contribute to Δ_{exp}, but is not the dominating term.

(iii) The exchange terms of the Coulomb interaction are also important and for the case of MoS_2 might reverse the order in energy of the spin-allowed and spin forbidden transitions [107, 42].

In a very recent preprint interlayer excitons in MoS_2 [67] are discussed in detail for bilayer and trilayers using k.p theory and comparing with magneto-optics. Although the theoretical approach is very different from our ab-initio calculations, both approaches agree on the existence and importance of interlayer K-point excitons. Predicting the exact energy positions is still challenging due to the uncertainties in amplitude and sign of the conduction band spin splitting [240], the Coulomb exchange terms and also the effective masses [239], see [67] for a complementary analysis.

5.5 Conclusions.

In this chapter we presented optical transitions at the K-point for homobilayer and trilayer MoS_2 in absorption. Interlayer excitons with high oscillator strength are found in post-DFT calculations and optical absorption measurements on MoS_2 homobilayers and trilayers. The interlayer excitons are mixed with intralayer B-excitons due to hole delocalization over two individual layers that results strong oscillator strength. The optical signatures of interlayer excitons are visible up to room temperature both in bilayer and trilayer MoS_2. The interlayer coupling for hole states in the valence bands is governed by symmetry and also the spin-orbit splitting. DFT bandstructure and absorption calculations show hole delocalization is forbidden due to symmetry in *3R* stacking and is allowed in *2H*. Therefore *2H* MoS_2 bilayers show favorable conditions to observe interlayer excitons in absorption, as hole hybridization is symmetry allowed and the valence band spin-orbit splitting is comparatively small compared to WSe_2 for example. In principle, the interlayer exciton with large oscillator strength and a large static dipole moment in bilayer and trilayer MoS_2 structures offer desirable configurations for coupling quantum tunneling with cavity photons, previously reported at cryogenic temperatures in III-V semiconductor nanostructures [241]. The evolution of the interlayer excitons in applied magnetic and electric fields will be discussed in the next chapter and coupling between intralayer and interlayer excitons will be investigated.

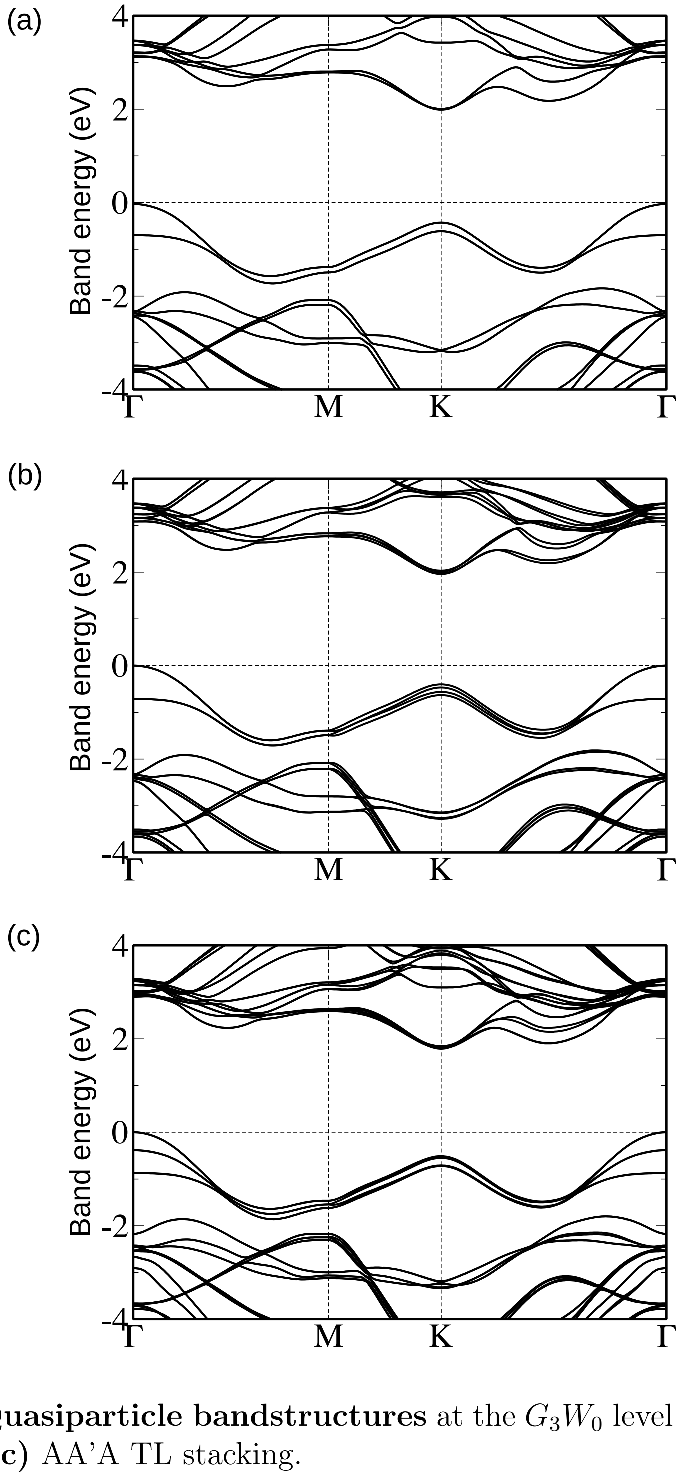

Figure 5.6: **Quasiparticle bandstructures** at the G_3W_0 level in **(a)** AA' BL, **(b)** AB BL and **(c)** AA'A TL stacking.

Chapter 6

Stark splitting of interlayer excitons in bilayer and trilayer MoS_2

In TMD monolayers optical absorption is strong, but the transition energy is not tunable as the neutral exciton has essentially no out-of-plane static electric dipole. In contrast, interlayer exciton transitions in heterobilayers are widely tunable in applied electric fields, but their coupling to light is considerably reduced. We have shown strong optical absorption of interlayer exciton in homobilayer MoS_2 in the previous chapter. In this chapter first I discuss magneto-optics results for identification of interlayer excitons. The interlayer excitons show larger Zeeman splitting with opposite sign compared to intralayler excitons [68]. Our knowledge about interlayer versus intralayer magneto-optics is crucial for the analysis and discussion of our bilayer and trilayer results. In the remaining part of this chapter I show tuning of interlayer excitons over a wide energy range in bilayer MoS_2 by application of electric fields. These energy shifts are due to the quantum confined Stark effect. We optically probe the interaction between intra- and interlayer excitons in homobilayer and trilayer MoS_2 as they are energetically tuned into resonance. Our experimental observations are supported by beyond-standard density functional theory calculations performed by Iann Gerber (LPCNO) including excitonic effects (GW-BSE). In MoS_2 trilayers, our experiments uncover two types of interlayer excitons with and without in-built electric dipoles, respectively. The results described in this chapter are based on the publication [106] also thanks to a fruitful collaboration with the group of Richard Warburton at the University of Basel (Switzerland).

6.1 Introduction.

In TMD layers the spin splittings in the two non-equivalent K^+ and K^- valleys have opposite signs. Therefore valley degree of freedom can be manipulated by applying an external magnetic field perpendicular to the 2D layer (Faraday configuration). The degeneracy of the two valleys in magnetic field can be lifted and measured as valley Zeeman splitting. This is achieved by monitoring the energy splitting between the two circularly polarized photoluminescence or reflectance. The Zeeman splitting of intralayer and interlayer excitons shows different amplitude and sign. Therefore these two criteria are used to identify the interlayer transitions in our recorded spectra.

High quality van der Waals heterostructures show close-to-unity, gate-tunable reflectivity of a single $MoSe_2$ layer [110, 242], variation of the transition energies of interlayer excitons over a broad wavelength range in heterobilayers [63, 243] and valley polarized exciton currents [154].

In this chapter, we aim to combine the strong light-matter interaction of excitons in monolayers with high tunability of interlayer excitons in external electric fields. In heterobilayers interlayer excitons are observed in photoluminescence emission [63, 154, 243] as interlayer absorption is very weak. The *2H* stacked MoS_2 homobilayers and trilayers exhibit two important properties : First, a strong interlayer exciton absorption observed up to room temperature has been observed in earlier studies on MoS_2 bilayers [60, 67, 216, 236, 237], and also discussed in the previous chapter. Second, in principle, the large in-built electric dipole of interlayer excitons as they form with the electron residing in either the top or the bottom layer [244], whereas the hole is delocalized over both layers [211]. Because of this characteristics no Stark shift is observable for the intralayer excitons A:1s and B:1s, as reported for monolayers [245, 246]. We integrate MoS_2 bilayers and trilayers in devices with Au-contacts for applying an out-of-plane electric field (F_z). The energy degeneracy of the two interlayer exciton configurations is indeed lifted, see below: In absorption, we observe two well-separated features as the amplitude of the electric field is increased. This result reveals the large in-built electric dipole and proves the interlayer character of the transition. By adjusting F_z, we tune the energy splitting between the two interlayer excitons. The blue-shifted interlayer exciton and the B-intralayer exciton exhibit a pronounced avoided crossing accompanied by a transfer of oscillator strength, two clear indications for a strong admixture of these states. In contrast, the red-shifted interlayer exciton and the strong A-intralayer exciton exhibit a weak avoided crossing, evidence that these states do not admix significantly. In MoS_2 trilayers, we discover two different interlayer excitons with very distinct Stark shifts.

6.2 Zeeman splitting and Stark effect tuning of interlayer excitons in bilayer MoS_2.

The strong oscillator strength of interlayer excitons in the homobilayers is shown in the previous chapter. I now show magneto-optics results that I have performed on the same sample. The optical reflectivity was measured at low temperature ($T = 4\ K$) using a home-built confocal microscope and a white light source. The imaginary part of the optical susceptibility $\mathrm{Im}(\chi)$, a measure of the absorption, was deduced from the differential reflectivity signal $\Delta R/R_0$, $\Delta R = R - R_0$, using the Kramers-Kronig relation, where R is the reflectivity spectrum obtained on the MoS_2 flake and R_0 is the reference spectrum (see Supplement of [247] for a detailed description).

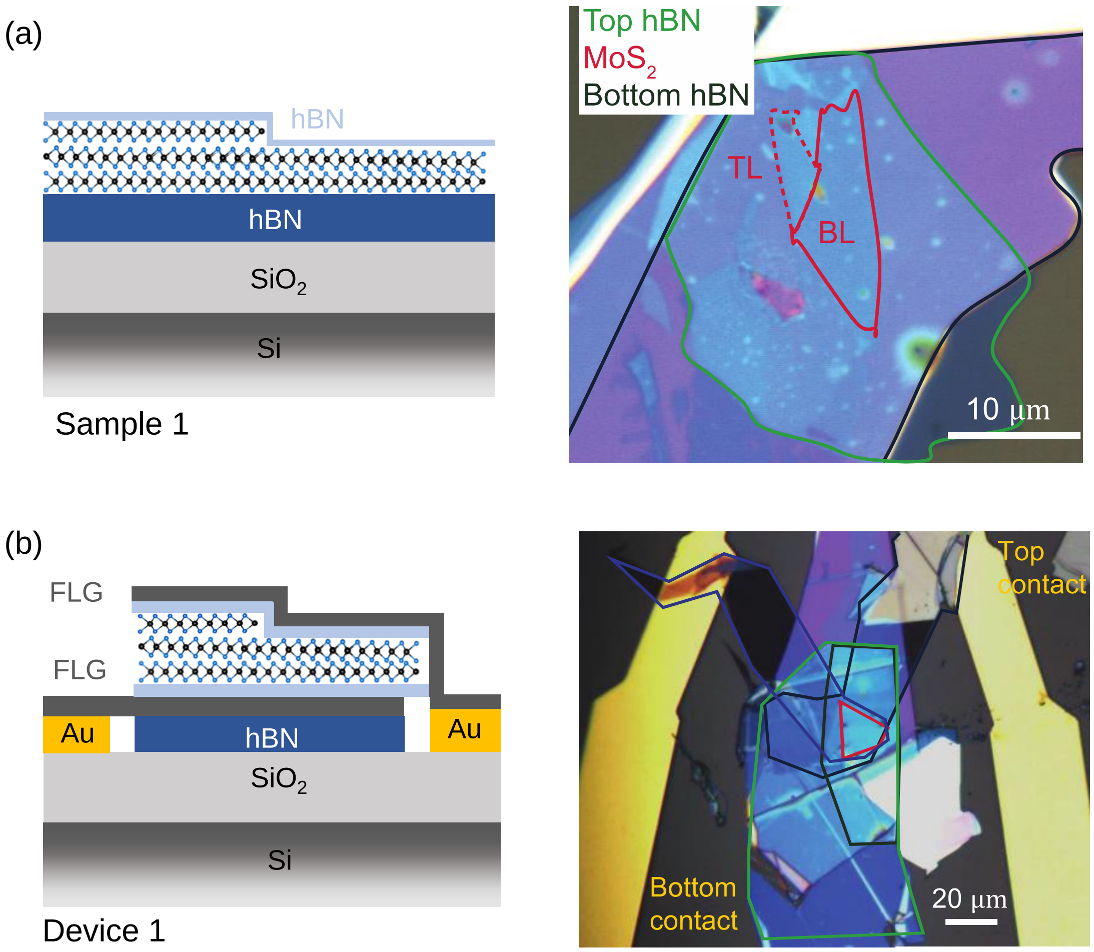

Figure 6.1: **Sample 1 and device 1 structure.** Schematics and microscope images of **(a)** sample 1 (the same as discussed in chapter 5) and **(b)** an electrical gated device 1, both consisting of bilayer (BL) and trilayer (TL) MoS_2 encapsulated in hBN.

6.2.1 Magneto-reflectance measurements for identification of interlayer excitons.

In bilayer MoS_2, each band is doubly degenerate with opposite spin configurations due to inversion and time-reversal symmetry. For the *2H* stacking, adjacent layers are rotated by 180°, which results in an inversion of the spin orientation while going from one layer to the another layer. For instance, the K^+ valley, the upper valence band VB_1 and the lower conduction band CB_1 for layer 1 (layer 2) have spin down (up) character, see Fig. 6.2 (a). The intralayer transitions are similar to the monolayer case [231]. The spin states for the σ^+ and σ^- interlayer transitions are reversed as compared to intralayer transitions. In a simple quasi particle (not exciton) picture, the spin contributions to the Zeeman splitting for an optical transition within the same layer cancel (at least partially) for intralayer excitons, whereas they are additive for interlayer excitons [68, 67]. This gives an indication why the interlayer exciton Zeeman splitting is larger.

The polarization-resolved reflectance measurements of the interlayer transitions are performed in an out-of-plane magnetic field (Faraday geometry). The optical experiments are carried out by exciting the sample 1, see Fig. 6.1 (a) with linearly polarized white light. The absorption is subsequently analyzed in a circularly polarized basis, allowing us to directly access the resulting valley-selective splitting of the transitions and quantify the Zeeman splitting. Fig. 6.2 (b) shows the absorption spectra of the interlayer excitons for both detection polarizations in magnetic fields at 0 and +9T. Two main observations are immediately apparent from the data. First, the energy degeneracy of the interlayer transitions is lifted for fields $B_z > 0$. For increasing magnetic fields, the energy of the σ^+ polarized component of interlayer exciton increases while it decreases for the σ^- polarized component opposite to the intralayer exciton characteristics. Second, the amplitude of the energy splitting in magnetic field for intralayer exciton (A:1s) is smaller compared to interlayer excitons (IE). The intralayer exciton shows a negative Zeeman splitting of about 2 meV at $B_z = +9$T, which changes sign as the magnetic field direction is reversed shown in Fig. 6.2 (b) and (c). The Zeeman splitting for the interlayer exciton IE is about 4 meV at $B_z = +9$T, and the sign is opposite compared to the intralayer case. The Zeeman splittings of the two excitonic transitions are defined as $\Delta E_A = E(\sigma^+) - E(\sigma^-) = g_A \mu_B B_z$ and $\Delta E_{IE} = g_{IE} \mu_B B_z$ with $E(\sigma^+)$ and $E(\sigma^-)$ being the transition energies for the two circular polarizations, g_A and g_{IE} are the excitonic g-factors, and $\mu_B = 58\ \mu\text{eV/T}$ is the Bohr magneton. From the data presented in Fig. 6.2 (b), we deduce a negative Landé g-factor of around -4 for the intralyer exciton A:1s and a positive g-factor of about $g_{IE} \approx 8$ for the interlayer exciton [67]. Additionally, a transition $\sim$ 145 meV above the intralayer exciton A:1s is identified as interlayer exciton, labelled as BIE in Fig. 6.2 (b) with positive g-factor and large energy tunability similar to interlayer exciton IE. To summarize these experiments, magneto-optics performed on MoS_2 bilayers allows to distinguish between intralayer and interlayer exciton transitions.

6.2.2 Stark effect tuning of interlayer excitons in bilayer MoS_2.

Our next target is to tune the interlayer transition energy in the MoS_2 bilayer absorption spectrum that carries an in-built out-of-plane electric dipole. This effect is based on the quantum confined Stark effect [248]. For bilayer MoS_2, our experiments focus on momentum-direct intralayer and interlayer excitons originating from valence and conduction bands around the K-points. The strong oscillator strength of the interlayer exciton originates from a strong admixture with the B-intralayer transition, see scheme in Fig. 6.4 (d) also detailed in the previous chapter 5 and ref. [60]. We performed experiments as a function of the out-of-plane electric field in *2H* stacked bilayer MoS_2 using devices 1, with a geometry as depicted in Fig. 6.1 (b): Two hexagonal boron nitride (hBN) flakes are used as dielectric spacers, and top and bottom few-layer graphene (FLG) act as transparent electrodes (All layers were transferred using deterministic dry exfoliation, see section 2.1 in Chapter 2 for a detail description). Applying a DC voltage to the two FLG electrodes creates an electric field in the MoS_2 (device 1), oriented perpendicular to the bilayer.

Fig. 6.3 (a) shows typical absorption spectra extracted from a colourmap of

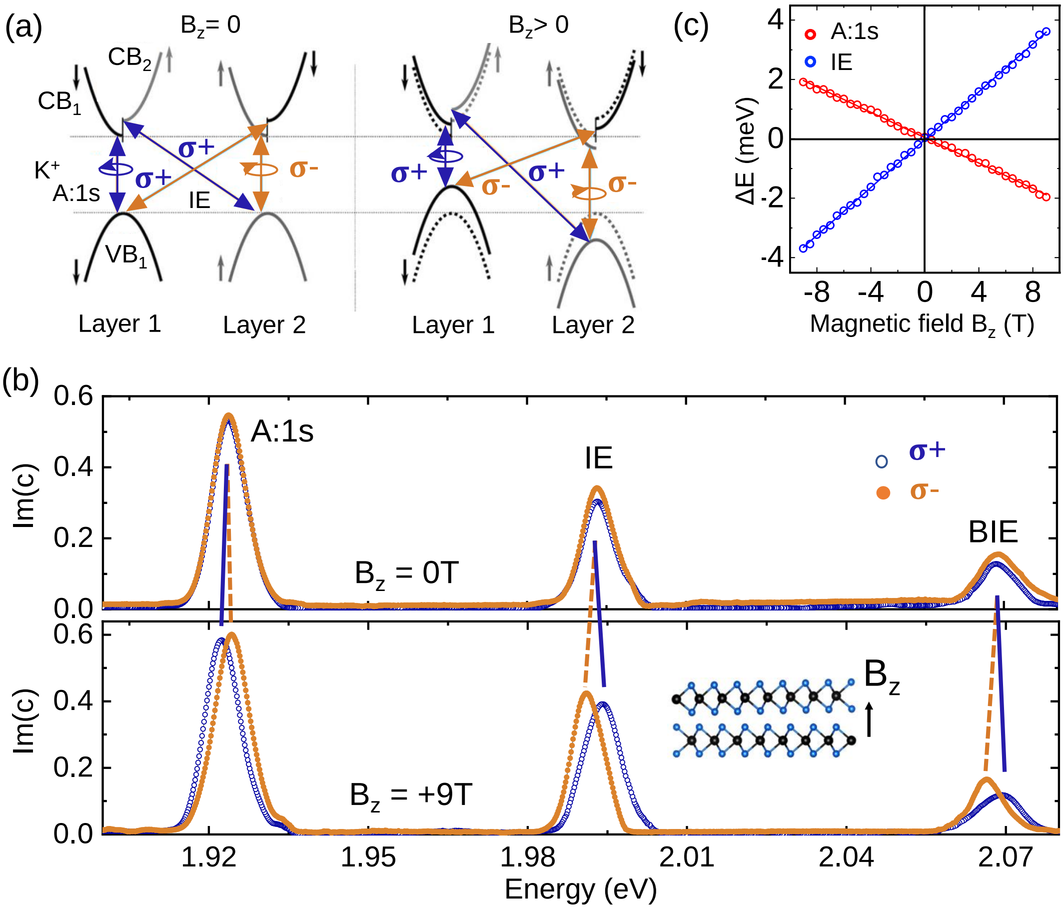

Figure 6.2: **Magneto-optics of bilayer MoS$_2$ (sample 1) at $T = 4\ K$. (a)** Optical selection rules for the intralayer and interlayer transitions at $B_z = 0$ (left) and $B_z > 0$ (right) between the valence band VB_1 and the conduction bands CB_1 and CB_2 (with carrier spins marked) bilayer or bulk MoS$_2$ in a simple quasi particle picture. The dashed lines in the right panels indicate the band positions for $B = 0$. Vertical and diagonal arrows indicate intralayer (A:1s) and interlayer transitions (IE). The schematics is taken from [68]. **(b)** Polarization-resolved absorption spectra for bilayer MoS$_2$ in magnetic fields ($B_z = 0$T and $B_z = +9$T) applied perpendicular to the layers. The orange and blue curves correspond to σ^- and σ^+ detection polarization. **(c)** Energy difference ΔE between the two circular polarization for the intralayer (red) and interlayer (blue) excitons at different magnetic fields B_z. The g-factors of the two transitions are extracted from linear fits. The intralayer A-exciton has a negative g-factor, $g_A \approx -4$, while the interlayer excitonic g-factor is approximately twice as large with opposite sign, g_{IE} and g_{BIE}.

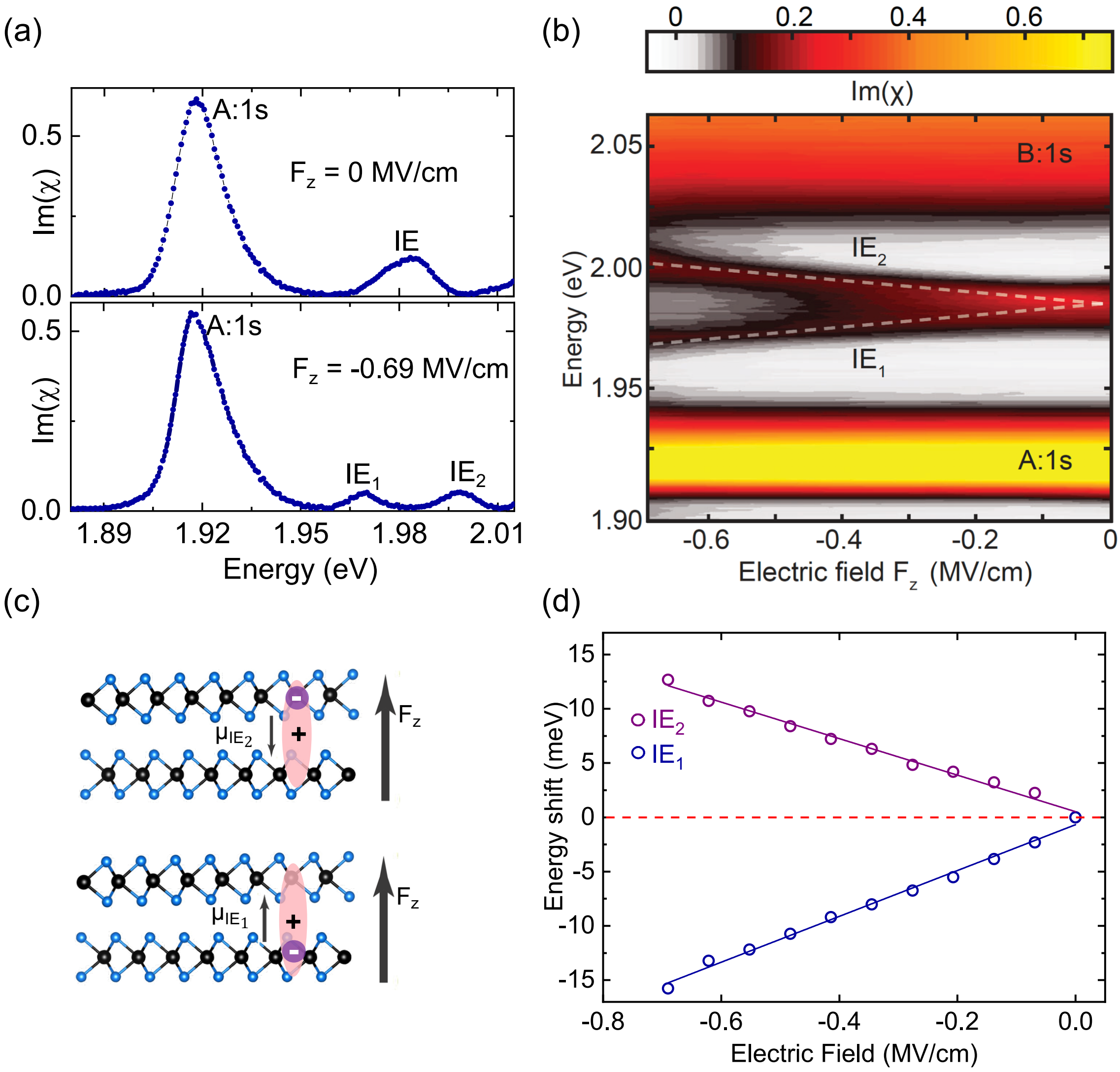

Figure 6.3: **MoS_2 bilayer van der Waals heterostructure (vdWH) in an applied electric field** at $T = 4$ K. **(a)** Typical absorption spectra recorded without ($F_z = 0$ MV/cm) and with ($F_z = -0.69$ MV/cm) an applied electric field, extracted from **(b)**. **(b)** Colourmap of the absorption spectra of bilayer MoS_2 vdWH (device 1). Stark shift of the interlayer excitons at small electric fields. The intralayer A- and B-excitons (A:1s and B:1s) and the two branches of the interlayer A-resonances (IE_1 and IE_2) are labelled. **(c)** Schematics of interlayer excitons in homobilayer MoS_2. An electron localized in one layer interacts with a hybridised hole state to form an interlayer exciton. The direction of the dipole moment depends on the location of the electron, either in the bottom (μ_{IE1}) or top (μ_{IE2}) layer. **(d)** Stark shift of the interlayer A-excitons as a function of F_z, extracted from the spectra in panel **(b)**. The solid blue and purple lines are linear fits to the experimental data points at small/moderate electric fields ($F_z = 0$ MV/cm to $F_z = -0.69$ MV/cm).

the absorption spectra as a function of the electric field F_z shown in Fig. 6.3 (b), recorded on device 1. Three prominent transitions can be clearly identified at zero electric field ($F_z = 0$ MV/cm) : The intralayer A- and B-excitons (A:1s and B:1s) near 1.918 eV and 2.09 eV, respectively, and the interlayer A-exciton (IE) at 1.98 eV [60]. On applying an external electric field F_z, the IE splits into two separate branches, as seen in Fig. 6.3 (a) for $F_z = -0.69$ MV/cm. Remarkably, at finite electric fields $F_z = -0.69$ MV/cm, the absorption strength does not vanish but remains rather strong. When the electric field F_z is increases from 0 to -0.69 MV/cm, the energy difference between the IE_1 and IE_2 states is about ~ 28 meV. So, the IEs show a wide energy splitting in contrast to the intralayer exciton (A:1s), see Fig. 6.3 (a)-(b).

For small to moderate electric fields, before significant interaction between the interlayer states and the A- and B-excitons, we observe a linear energy shift with F_z for both peaks, IE_1 and IE_2, suggesting a first-order Stark shift caused by the static electric dipole moments across the MoS_2 bilayer (Fig. 6.3 (d)). In Fig. 6.3 (d) we plot the transition energies extracted from Fig. 6.3 (b) as a function of the applied field F_z and perform a linear fit. We extract large dipole moments of μ_{IE1} and μ_{IE2} with a lower bound of about 0.3 e·nm with e being the electron charge. Applying higher electric fields in our experiment, we discover that the shifts deviate from a simple linear Stark shift, reflecting, as discussed below, very different interactions of the interlayer excitons with the A- and B-intralayer excitons. Our experiments clearly show that the absorption peak IE, initially at 1.98 eV, corresponds to interlayer exciton resonances with out-of-plane oriented electric dipoles : The carriers clearly do not reside within the same layer. For the intralayer excitons on the other hand, the energy shift with applied electric field is negligible, as in the case for excitons in monolayers [245, 246]. The magneto-optics and electric filed tuning confirm interlayer character of the $\mathrm{IE}_{1,2}$ excitons. In terms of the magnitude, the large extracted dipole moments are similar to results on interlayer excitons in $MoSe_2/WSe_2$ *heterobilayers* as determined by photoluminescence [63, 154, 243]. In the case of bilayer $MoSe_2$, K-K interlayer excitons are observed with similarities to the case of MoS_2, but with significantly lower oscillator strength [115, 66]. This is mainly due to the larger valence band spin-orbit splitting of $MoSe_2$ compared to MoS_2, which makes hole delocalization over both layers and hence the formation of interlayer excitons less favourable [211]. Signatures of interlayer excitons in bulk *2H* $MoSe_2$ have been reported, but the same study did not find K-K interlayer exciton signatures for bulk *2H* WSe_2 [114].

6.2.3 Tuning interlayer and intralayer absorption into resonance.

We have shown Stark splitting of interlayer exciton for very small electric field range because our device shown in Fig. 6.1 (b) is single gated, device 1. For small fields we confirmed Stark splitting of IEs in Fig. 6.3 (b) and also in Fig. 6.4 (a), different interactions of interlayer exciton resonances around the transition energy of intralayer excitons A:1s and B:1s. Note that the data presented in Fig. 6.4 (a) is 2^{nd} derivative of reflectivity contrast for clarity. For further quantitative understanding

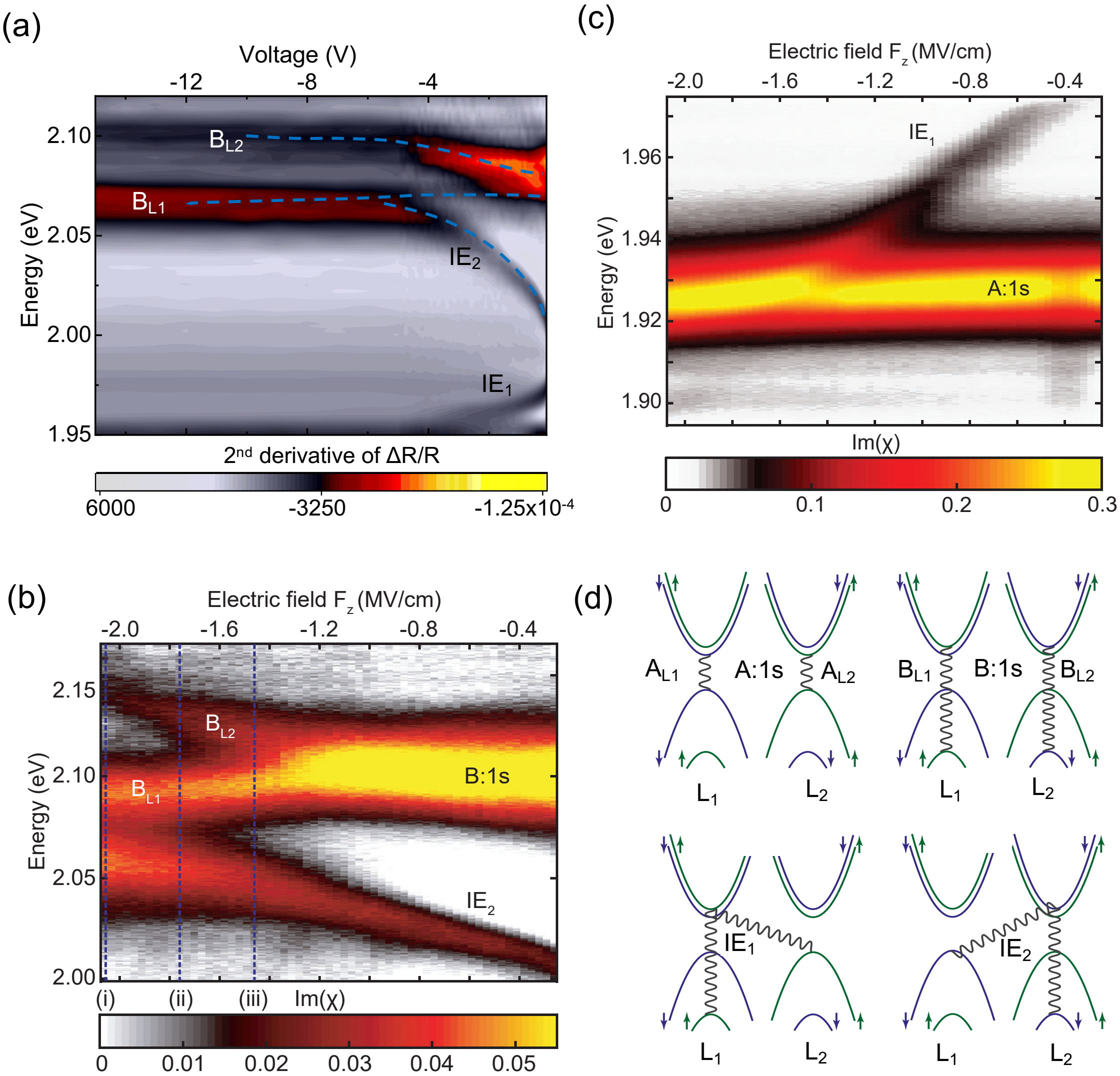

Figure 6.4: **Electric field dependence:** **(a)** Colourmap of the 2^{nd} derivative of reflectivity contrast $(\Delta R/R)$ spectra centered around the intralayer B-exciton for a single gated device 1. **(b)** Colourmap of the absorption spectra centred around the intralayer B-exciton. B_{L1} and B_{L2} are the intralayer excitons residing in layer 1 (L_1) and 2 (L_2), respectively for a double gated device, see [106] for a detail configuration. Dashed vertical lines show shift in resonance energy. **(c)** Colourmap of the absorption spectra (σ^+-polarization) centered around the intralayer A-exciton, showing a very small avoided crossing with IE_1. The data is for the same device as in **(b)**. **(d)** Band diagram and schematics of intralayer and interlayer excitons in homobilayer MoS_2 at the K-point. Intralayer resonances in the top panel A:1s and B:1s correspond to excitons where the electron and the hole reside in the same layer. Intralayer excitons can form in each of the two layers, denoted by the subscript L_1 (L_2) for layer 1 (layer 2). Interlayer excitons in the bottom panel IE_1 and IE_2 consist of an electron confined in one layer and a hole delocalized over both layers. Wavy lines connect the states involved for the formation of the different excitonic complexes at the K-point.

about the interaction of interlayer excitons with intralayer excitons resonances we collaborated with Richard Warburton's group at University of Basel. The further measurements at high electric fields were performed on a double gated device bilayer MoS_2 by Nadine Leisgans and Lukas Sponfeldner. The main advantage of a double gated device is the independent control of the applied electric field and the carrier concentration in the bilayer, here kept in the neutral regime. Due to the very large tunability shown in Fig. 6.3 (b) for the interlayer transition energy, we further tune the interlayer excitons into resonance with the A- and B-intralayer excitons while maintaining charge neutrality. Comparing Fig. 6.4 (b) ($IE_2 \leftrightarrow B$) with 6.4 (c) ($IE_1 \leftrightarrow A$) shows the interactions are very different : In Fig. 6.4 (c), the IE_1 transition merges with the A-exciton line at around -1.3 MV/cm; at the highest electric fields in these experiments. This points to a small avoided crossing of the weak IE_1 exciton with the strong A-exciton. Our estimate for the coupling of the IE–A excitons in the present sample is 5 ± 3 meV. In contrast, tuning the upper interlayer branch IE_2 energetically close to resonance with the B-exciton leads to a clear avoided crossing, see data in Fig. 6.4 (b). For the B-exciton, we can distinguish two resonances associated to intralayer excitons in the two different layers L_1 and L_2, labelled as B_{L1} and B_{L2}. The transition B_{L1} does not share any state with IE_2 as evidenced by a nearly constant transition energy, see Fig. 6.4 (b). Importantly, as IE_2 has a strong B_{L2}-intralayer component, see scheme in Fig. 6.4 (d), these states interact strongly. The pronounced avoided crossing between IE_2 and B_{L2} is accompanied by a transfer of oscillator strength from B_{L2} to IE_2, a clear indication for strong coupling. Fitting the data in Fig. 6.4 (b) with a simple coupled 2 level model for the two transitions BL_2 and IE_2, we can extract a coupling energy an interaction energy $W = 33 \pm 5$ meV, see [106] for more details.

6.3 GW+BSE modelling of excitons in MoS_2 bilayers.

The main observations of the experiments are : (i) the splitting and very large energy shifts of the IE transitions in an applied electric field, (ii) anticrossing of the IE_2 with the B-intralayer exciton, and (iii) small avoided crossing of the IE_1 with the A-intralayer exciton. In order to compare our experiential results with theory, our colleague Iann Gerber at the LPCNO performed beyond DFT calcuations including GW+BSE. The approach used here is based on the inclusion of the applied electric field as a perturbation in the band structure calculations, similar to the approach in [212] (see Supplement of [106] for computational details). Please note that we have only considered freestanding *2H* MoS_2 bilayers in our calculations, i.e. placed in vacuum, as we aim to reproduce qualitatively the main trends. When applying an electric field, we observe a global shift for L_1 of the relevant conduction and valence bands at the K-point down in energy with respect to L_2, marked as the Stark shift ΔE_{Stark} (see Fig. 6.5 (b) for the electric field configuration and Fig. 6.5 (c) for a bandstructure schematic). From the sketch in Fig. 6.5 (c), it is thus clear that the IE transitions will split in energy : Transitions involving the L_2 valence bands and the conduction bands in L_1 will lower in energy, whereas transitions

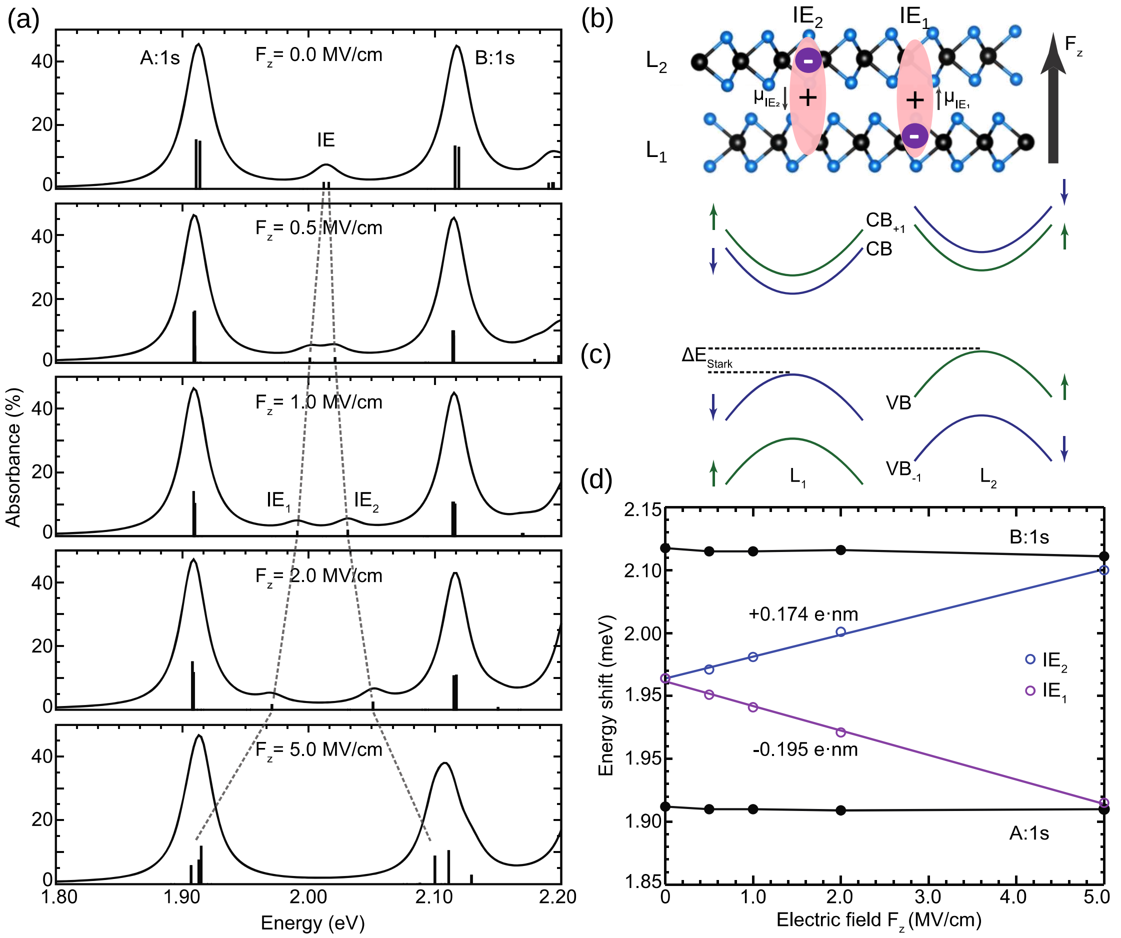

Figure 6.5: **Beyond-DFT calculations of the electric field effects on the bandstructure and excitonic properties of *2H* MoS_2 bilayer**. **(a)** Absorption spectra as a function of the applied electric field F_z. Our DFT-GW-BSE calculations determine both energy position and absorption strength corresponding to exciton transitions as shown with vertical black lines. We estimate the numerical precision of our calculations to be of the order of ±5 meV (see computational settings in Supplement) such that any splitting below this value does not have any physical significance. For comparison with the experiment, we introduce an artificial broadening of the order of 10 meV for each transition. This results in the spectra shown with solid black lines; the three main transitions A:1s (intralayer A), IE (interlayer) and B:1s (intralayer B) are labelled. **(b)** Structural model of the *2H* bilayer stacking and electric field direction. **(c)** Schematic of the bandstructure modification due to the application of F_z showing a global shift, denoted ΔE_{Stark}, between the distinct band structures of the two layers (see Supplement for detailed results on *GW* band structure calculations). **(d)** Evolution of the excitonic peak positions with respect to the electric field, and the corresponding dipole moment estimates for IE_1 and IE_2 excitons.

involving the L_1 valence bands and L_2 conduction bands will increase in energy.

The calculated absorption shown in 6.5 (a) looks very similar to our measurements at small electric fields, see Fig. 6.3 (b). Fig. 6.5 (d) demonstrates how the IE transition energy changes, roughly linearly, with the applied electric field. At large electric field values of 5 MV/cm, we see two main groups of transitions : At the low energy side, the IE_1 close to the A-exciton energy and, at the high energy side, the IE_2 close to the B-exciton. There are essentially no transitions in the energy range in-between. We refrain in our calculations to comment on any higher electric field values as our initial assumption to treat the electric field as a perturbation, in comparison with other energy splittings in the band structure, reaches its limits.

The exact nature and mixing of the absorption peaks, calculated in Fig. 6.5 (a), contain information on the evolution of the exciton states with electric field (see Supplement of [106]). Our theory indicates very little mixing between the A-intralayer exciton and the IE, consistent with the experiments in Fig. 6.4 (c). Concerning interactions with the intralayer B-exciton, the IE exciton, with a delocalized hole, is mixed with the intralayer B-exciton as they share the same valence states. This was suggested in [60] and also discussed in the previous chapter to explain the surprisingly high oscillator strength of the IE transitions. From the calculations, we see that the mixing between the higher energy IE branch and the B-exciton becomes stronger as the electric field amplitude is increased (see Supplement of [106] for a detailed description of each component). We suggest that this clear admixture of the IE-exciton with the B-exciton in our calculations is the origin of the observed avoided crossing between IE_2 and B_{L2} shown in Fig. 6.4 (a) and (b). Highly tunable excitonic transitions with large in-built dipoles and oscillator strengths will result in strong exciton-exciton interactions and therefore hold great promise for non-linear optics with polaritons.

6.4 Interlayer excitons in MoS_2 trilayers.

We apply our combined approach using experiments and theory to uncover and manipulate novel exciton species in a more complex system, namely MoS_2 homotrilayers. In contrast to inversion symmetric MoS_2 bilayers, trilayers could be advantageous in nonlinear optics due to the broken inversion symmetry that gives rise to a non-vanishing second-order nonlinear susceptibility. In the trilayer system, we uncover additional types of interlayer excitons as compared to the bilayer in our experiment : At zero electric field, two different interlayer transitions appear in absorption, labelled IE^* and IE in Fig. 6.6 (a). We show absorption measurements as a function of the electric field and make a surprising observation : Whereas IE splits into two branches (IE_1 and IE_2) as for the bilayer studies, IE^* does not show any measurable splitting and hence, a negligible or at least very small in-built electric dipole moment. Interestingly, we make the same observation in our GW+BSE calculations, shown in Fig. 6.6 (c). We can explain the different behaviour in applied electric fields by analysing the microscopic origin of IE and IE^* in our calculations, see Supplement of [106]. The schematic in Fig. 6.6 (b) shows these excitons to have very distinct characteristics : For the IE, two degenerate states form at zero electric field, i.e. IE_1 and IE_2. For IE_1, the electron is localized in the bottom layer and the hole is delocalized between the middle and bottom layers. For IE_2, the electron is localized in the top layer and the hole is delocalized between the middle and top layers. As such, IE_1 and IE_2 have a finite dipole moment, similar to the interlayer excitons in bilayers. We extract a dipole moment of $|\mu| \approx 0.15$ e·nm. This smaller value as compared to the bilayer can have its origin in the different dielectric environment and a more localized hole wavefunction. Admixture of intralayer with interlayer excitons does not change significantly over the investigated electric field range (see Supplement of [106]). For the IE^* at slightly lower energy, the situation is different compared to IE : the electron is localized in the middle layer and the hole is delocalized over all three layers. This results in a negligible in-built electric dipole moment of IE^* which translates into a non-resolvable Stark splitting of the transition in our measurements. The absence of a clear Stark shift might put the interlayer nature of IE^* into question. To answer this, I have performed magneto-optics as previously for the bilayer, shown in Fig. 6.6 (d). We observe for the intralayer excitons a Zeeman splitting of the order of 2 meV for $B_z = +9$ T and for IE and IE^*, a Zeeman splitting of the order of 4 meV, with opposite sign compared to the intralayer transitions. Therefore, we confirm the interlayer character of these peaks. These results lead to an unusual situation for interlayer excitons : We observe a strong splitting in magnetic fields for IE^*, but a very small Stark shift in electric fields.

6.5 Conclusions.

In this chapter we presented a way to clearly distinguish and identify intralayer and interlayer transitions by magneto-optics. There are two criteria : (i) The interlayer excitions transition shows larger Zeeman splitting compared to intralayer excitons and (ii) The g-factors of interlayer and intralayer excitons are opposite in sign. We further demonstrated interlayer excitons character in externally applied electric field. The transition energy of interlayer excitons with the large in-built electric dipole in bilayer MoS_2 can be tuned to A:1s and B:1s resonances. These energy shifts are due to the quantum confined Stark effect. These interlayer excitons have a large oscillator strength such that they can be detected easily in absorption. The interaction of the blue-shifted interlayer exciton with the intralayer B-exciton shows clear signatures of strong coupling. In contrast, the interaction of the red-shifted interlayer exciton with the intralayer A-exciton shows only a weak coupling. This allows us to conclude that the interlayer exciton has a strong B-exciton component in its wave function but a much smaller A-exciton component. Our observations are supported by beyond-standard density functional theory calculations including excitonic effects. We expect that at even higher fields than those in these experiments, the interlayer exciton will lie lower in energy than the A-exciton and will recover its absorption strength once it is sufficiently red-detuned from the A-exciton. This will represent an advantageous scenario for applications : the ground-state exciton is long-lived and possesses both a large in-built electric dipole moment and a strong absorption. For optoelectronics, the highly tunable excitons with an in-built dipole found here in MoS_2 bilayers are promising for exploring coupling to optical cavity modes, where excitons and photons can couple to form polaritons. In MoS_2 trilayers, we uncover different interlayer excitons with very distinct Stark shifts : Similar to the bilayer, one interlayer exciton splits into two resonances and shifts with electric field, indicating a large dipole. In contrast, a second interlayer exciton at lower energy shows a negligible Stark shift. According to our calculations, this second exciton shows a spatially symmetric charge distribution with respect to the middle layer and, hence, a negligible in-built dipole.

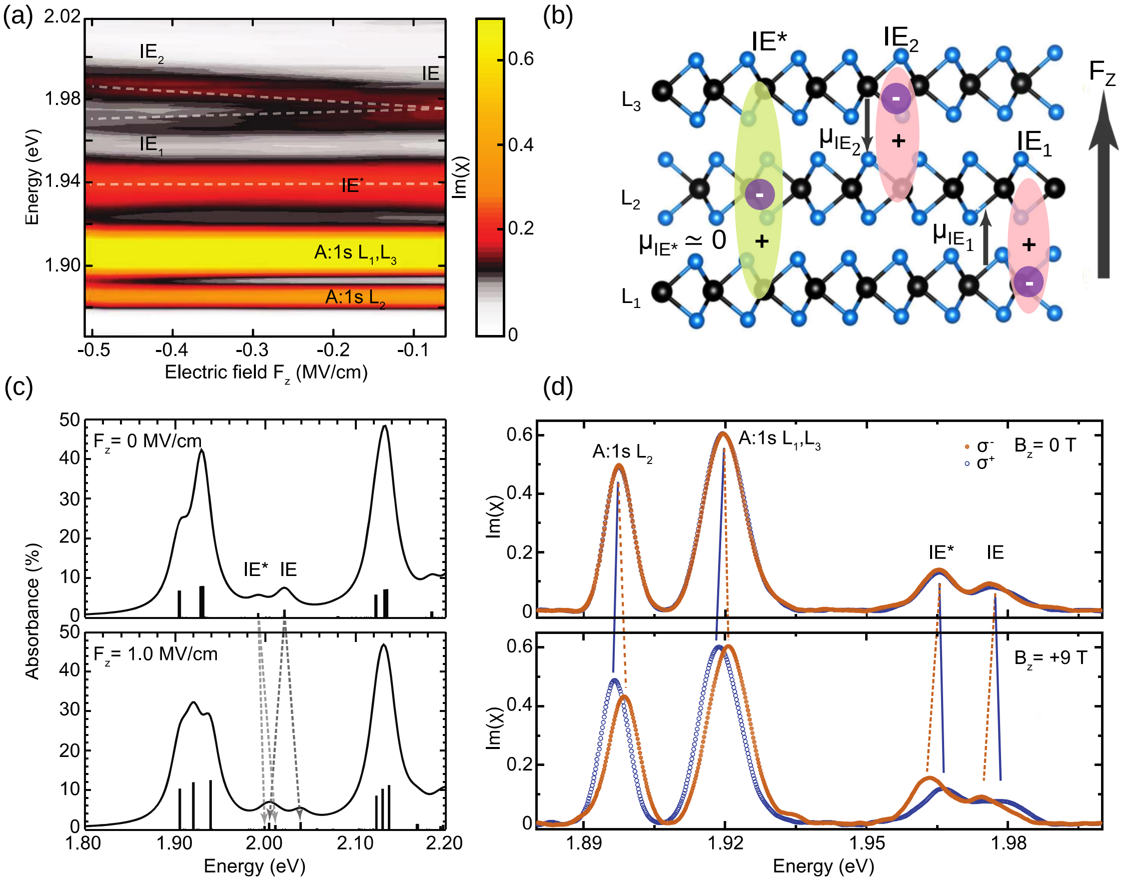

Figure 6.6: **MoS_2 trilayer in an applied electric field.** **(a)** Colourmap of the absorption spectra in device 1. **(b)** Schematic of *2H* stacked trilayer studied with scheme representing the microscopic origin of IE and IE*. **(c)** Theoretical absorption spectra of *2H* MoS_2 freestanding trilayer without (top) and with (bottom) electric field. See Supplement for a detailed discussion of the trilayer bandstructure and the effect of the electric field on it. The Stark shifts of interlayer excitons IE and IE* are indicated by arrows. **(d)** Magneto-optics on sample 1 with small Zeeman splitting for intralayer excitons (A:1s) and large Zeeman splitting for interlayer excitons IE and IE* in magnetic fields of $B_z = +9\ T$ perpendicular to the monolayer plane.

Chapter 7

High optical quality of MoS_2 monolayers grown by chemical vapor deposition

In the previous chapters, we discussed the excitonic transitions in MoS_2 monolayers (MLs) and multilayers. We showed their refectivity spectra and presented data from samples which were exfoliated using high quality bulk crystals and encapsulated in hBN. Both fundamental research and potential applications of TMD layers rely on high quality samples. The targets are to tune optical properties, achieve high emission yields and high carrier mobility in transport, for example. The optical and transport properties depend on the intrinsic quality of the TMD crystals [249, 250]. But also the surrounding dielectric environment such as the substrate used for growth or deposition [251, 239] plays an important role. It has been shown in several independent studies that using high quality hBN [77] encapsulation is crucial to access the intrinsic optical properties of the exfoliated TMD materials [51, 235, 252, 253]. In addition to high quality crystals for future applications the availability of large area TMD MLs is also critical. Individually exfoliated MLs from TMD bulk are typically only tens of micrometers in lateral size, compared to hundreds of micrometers in lateral size and a large number of flakes on the same substrate or even continuous films grown by chemical vapor deposition (CVD) [83, 87, 254, 255, 256]. However, so far the optical quality of CVD-grown MoS_2 has been considered too low for detailed optical investigations and the vast majority of work especially at low temperature is carried out on individual exfoliated flakes.

In this chapter we show that CVD growth performed in the group of our collaborators Andrey Turchanin and Antony George (FSU Jena, Germany) yields MoS_2 monolayers with high optical quality. We determine a defect concentration of 10^{13} cm^{-2} for our samples by HRTEM, comparable to defect concentrations for exfoliated MLs from naturally occurring bulk reported by several groups in the literature [257, 258, 84]. Based on this measurement we therefore expect similar optical quality to exfoliated material. However, our photoluminescence and reflectivity experiments on as-grown CVD MoS_2 MLs showed optical transitions with large inhomogeneous broadening (≈ 50 meV at $T = 4$ K), as commonly reported in the literature for this system [259, 260, 261]. To avoid detrimental effects from

ML-substrate interaction and to minimize therefore the impact of disorder [79, 84] I have removed the MLs from the SiO_2 growth substrate. I subsequently encapsulated the MoS_2 in high quality hBN [77] and have carried out optical absorption and emission experiments for temperatures between 4 K to 300 K. These hBN encapsulated CVD-grown MoS_2 MLs show very narrow optical transition linewidth with 5 meV FWHM at $T = 4$ K, similar to values for exfoliated material [51, 262] as mentioned in Chapter 3. The PL is dominated by free excitons and not by defects even at cryogenic temperatures. High optical quality of the samples is further confirmed by the observation of excited states of the Rydberg series in absorption for the A-exciton [25, 81]. Using above bandgap, polarized laser excitation, we optically generate large valley coherence and valley polarization in our CVD-grown MoS_2 layers [41]. It is therefore possible to explore spin and valley physics in these high quality CVD samples of large surface area in more detail. The results presented in this chapter are based on the publication Shree. et al [80]. This chapter focuses on improving the optical quality of CVD *monolayers*. In the next chapter we will use these large flakes with well defined shapes to build *bilayer* structures with tunable interlayer coupling.

7.1 Crystal quality from atomic resolution microscopy and optimized growth.

The defect density reported in the literature for MoS_2 is typically around 10^{13} cm^{-2}. The dominant type of point defect varies depending on the material source, as reviewed recently [84]. In naturally occurring MoS_2 and CVD-grown films, sulfur vacancies can dominate [263], whereas in synthetic crystals grown by chemical vapour transport (CVT), metal vacancies and antisites tend to dominate [250]. First, we describe how we quantitatively determine the defect density (i.e. of the dominating sulfur vacancies) in the CVD-grown monolayers and compare this data with measurements in the same set-up on an exfoliated monolayer.

The MoS_2 crystals were grown at FSU Jena by a modified CVD process in which a Knudsen-type effusion cell is used for the delivery of sulfur precursor, for details of the growth see [83]. Fig. 7.1 (a) presents an optical microscope image of a typical sample with a high density of ML MoS_2 crystals with lateral dimension of several tens of micrometers, a similar kind of sample grown under the same conditions in the same set-up investigated in optical spectroscopy experiments detailed below. To study the crystalline quality of the samples on an atomic scale we apply HRTEM at Ulm University (collaboration with the group of Ute Kaiser) with the C_c/C_s-corrected sub-Angstrom low-voltage electron microscope (SALVE) operating at 60 kV. Our collaborators in Ulm carefully optimize high resolution with respect to minimal radiation damage [264]. By this we mean that the electron beam itself can induce considerably more defects in the sample during the measurements than were initially present. The Ulm group has optimized this process during many years using low energy electron beams.

As can be seen in Fig. 7.1 (b)-(d), the CVD-grown MoS_2 MLs show an overall excellent crystallinity with a low defect density. Fig. 7.1 (d) shows an enlarged image of the area marked with a red square in Fig. 7.1 (b), where some double

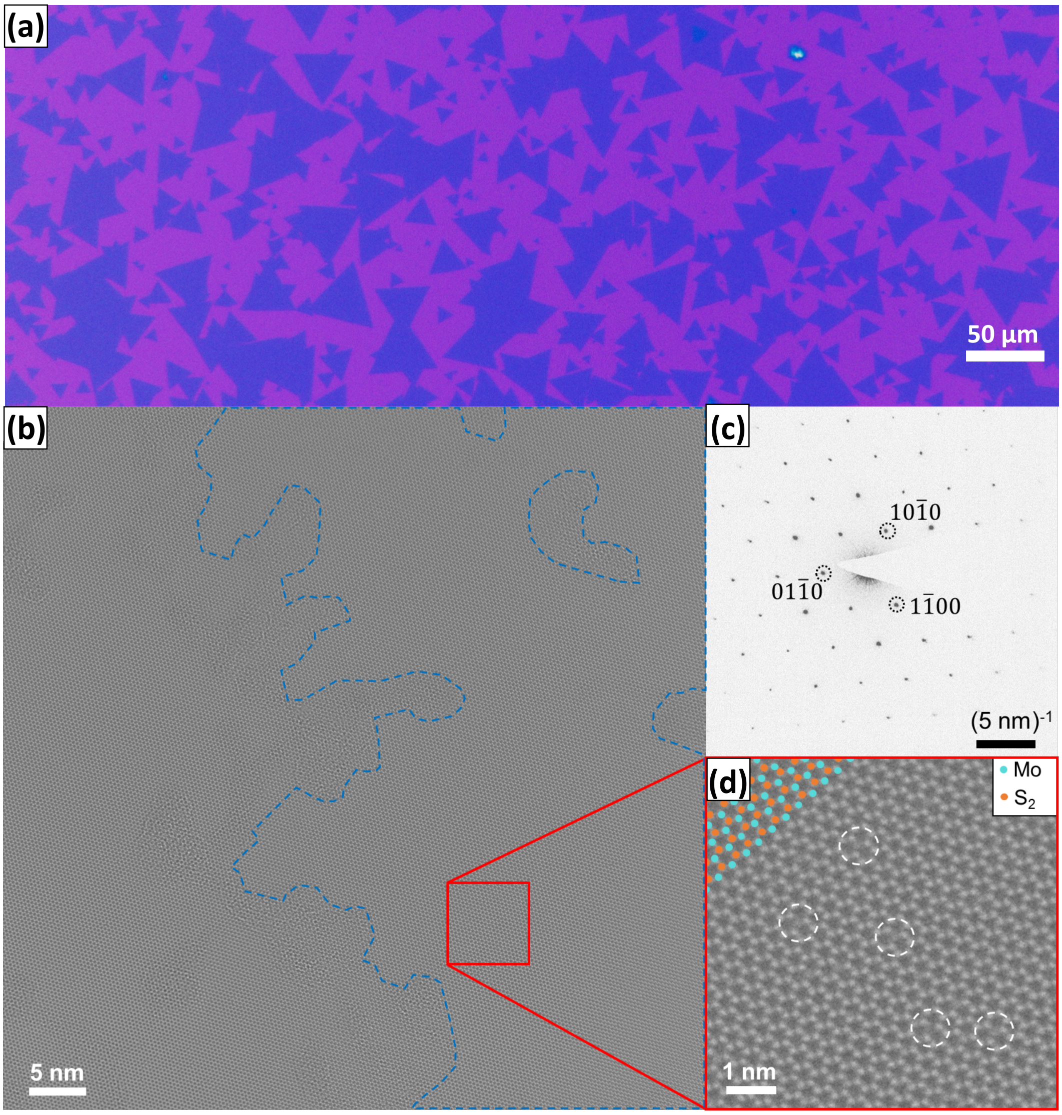

Figure 7.1: **(a)** Optical microscope image of as grown-CVD MoS_2 monolayers on SiO_2/Si wafers (300 nm of SiO_2) showing their characteristic triangular shapes. **(b)** 60 kV HRTEM image of MoS_2. Defect densities were evaluated by direct counting of vacancies on clean areas as can be seen within the blue framed area. The diffraction pattern in **(c)** shows a high crystallinity over the whole imaged area in **(b)**. The red square in **(b)** is magnified in **(d)**. For better visualization, different atoms are colored. Orange dots indicate two stacked-up S atoms (S_2) and turquoise solid dots correspond to Mo atoms. White circles mark the positions of vacancies.

sulfur vacancies typically present in the ML MoS_2 samples [83, 264, 265], can be recognized.

The double sulfur vacancies were directly counted from the HRTEM images as in Fig. 7.1 (d) to determine a quantitative value for their density $C = V/A$, where V is the number of the sulfur vacancies per area A. In the CVD-grown samples we find a density of the vacancies equal to $7.9(7) \times 10^{13}\ V/cm^2$. The value in the brackets gives the confidence intervals, see corresponding calculation in the SI of [80]. For comparison, we investigated ML samples prepared by exfoliation from bulk MoS_2 crystals. We found a vacancy density of $3.6(4) \times 10^{13}\ V/cm^2$. The measured defect density of CVD-grown ML MoS_2 is therefore roughly of the same order of magnitude as for exfoliated MLs from natural or CVT grown bulk [250, 266, 267]. Based on our HRTEM investigation we conclude that the CVD-grown ML MoS_2 possess comparatively high structural quality and therefore high optical quality in emission and absorption experiment of these samples could be expected.

7.2 Optical Spectroscopy of CVD-grown MoS_2 monolayers.

The optical transition linewidth of ML TMDs contains homogeneous and inhomogeneous contributions. As the radiative broadening is of the order of 1 meV any substantially larger linewidth at low temperature is dominated by inhomogeneous contributions due to imperfections in the ML or the direct environment [79, 123], see section 3.1 in Chapter 3 for details. I have studied the optical quality in PL and differential reflectivity experiments, using a detection and excitation spot diameter of the order of 1 μm. I have performed measurements on MoS_2 MLs in three different structures, see Fig. 7.3 (a)-(c). Large-area, as-grown MoS_2 films on SiO_2 by CVD are represented by sample 1 in Fig. 7.3 (a). To fabricate sample 2, we proceed as follows : First we deposit an hBN flake about 100 nm thick on a SiO_2/Si target substrate (different from the growth substrate). Then we remove the CVD-grown MoS_2 from the growth substrate using a water assisted pick-up method [97] and deposit this layer on top of the prepared hBN flake on the target substrate, see section 2.1 in Chapter 2 and also Chapter 8 for the technical details. Please note that separating the ML from the growth substrate can be achieved in a controlled way by water assisted pickup method [97]. In the last fabrication step, the MoS_2 layer is covered by a large hBN flake about 10 nm thick. Sample 2 has therefore the following structure: SiO_2/hBN/MoS_2 ML CVD/hBN, see Fig. 7.2 for an optical contrast image of this van der Waals heterostructure.

Sample 3 is an exfoliated MoS_2 monolayer from commercial bulk MoS_2 (from 2D Semiconductors) encapsulated in hBN, similar to exfoliated and encapsulated samples we studied previously [81, 51]. The difference between sample 2 and 3 is just the source of the MoS_2 ML using CVD-grown ML and exfoliated from bulk crystals, respectively.

First, we discuss differential white light reflectivity measurements at low temperature, $T = 4\ K$, see section 3.1 in Chapter 3 for technical descriptions of the set-up. We compare the reflectivity spectra of the CVD-grown films to those of

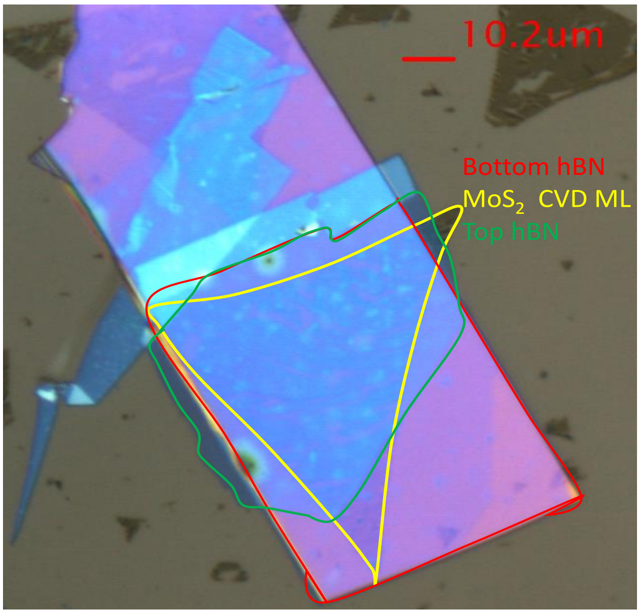

Figure 7.2: **Sample 2.** Optical microscope image of the CVD-grown MoS$_2$ monolayer (outline marked in yellow) sandwiched between an hBN bottom flake (marked in red) and a hBN top flake (marked in green). As the MoS$_2$ monolayer surface area is larger than the hBN flake area, there is also a ML part directly in contact with the SiO$_2$ substrate.

exfoliated MoS$_2$ in hBN, which represent the current state of the art in terms of linewidth close to the homogenous limit, see three panels of Fig. 7.3 (d). In differential reflectivity, the A- and B-exciton transitions are very broad (several tens of meV) in as-grown CVD monolayers (labeled A:1s, B:1s) for sample 1. However, for sample 2 the A:1s transition is considerably narrower. Near the B-exciton transition energy, two different transitions can be distinguished, namely the B:1s, much narrower than for sample 1 and in addition the excited state of the A-exciton, namely A:2s [19, 210]. The improvement in optical quality of CVD-grown MoS$_2$ in hBN is significant compared to the as-grown monolayer from the same sample. Globally the reflectivity spectrum of sample 2 and sample 3 are very similar, showing the high optical quality of our CVD-grown samples when they are encapsulated. Seeing the A:2s state in sample 2 is a sign of high optical quality [25] as with the larger Bohr radius we sample a bigger sample volume [253]. For enhanced visibility of the A:2s state also the clean dielectric environment i.e. the hBN material with very few defects is important, as excited exciton states are broadened considerably by dielectric disorder [79] and are therefore spectrally narrower in encapsulated samples [190]. The A-exciton transition A:1s is red-shifted by about 50 meV in sample 1 compared to both samples 2 and 3, which might be due to strain induced in the layer during the cool-down process after growth [260].

Now we discuss PL spectroscopy of the three samples, a technique considerably more impacted by the presence of defects compared to reflectivity, as described in the section 3.1 of Chapter 3. The PL spectrum of the as-grown MoS$_2$ monolayer on SiO$_2$ is shown as the blue curve in Fig. 7.3 (e) using a laser energy of 2.32 eV well above the emission energy. It shows a roughly 50 meV wide A-exciton emis-

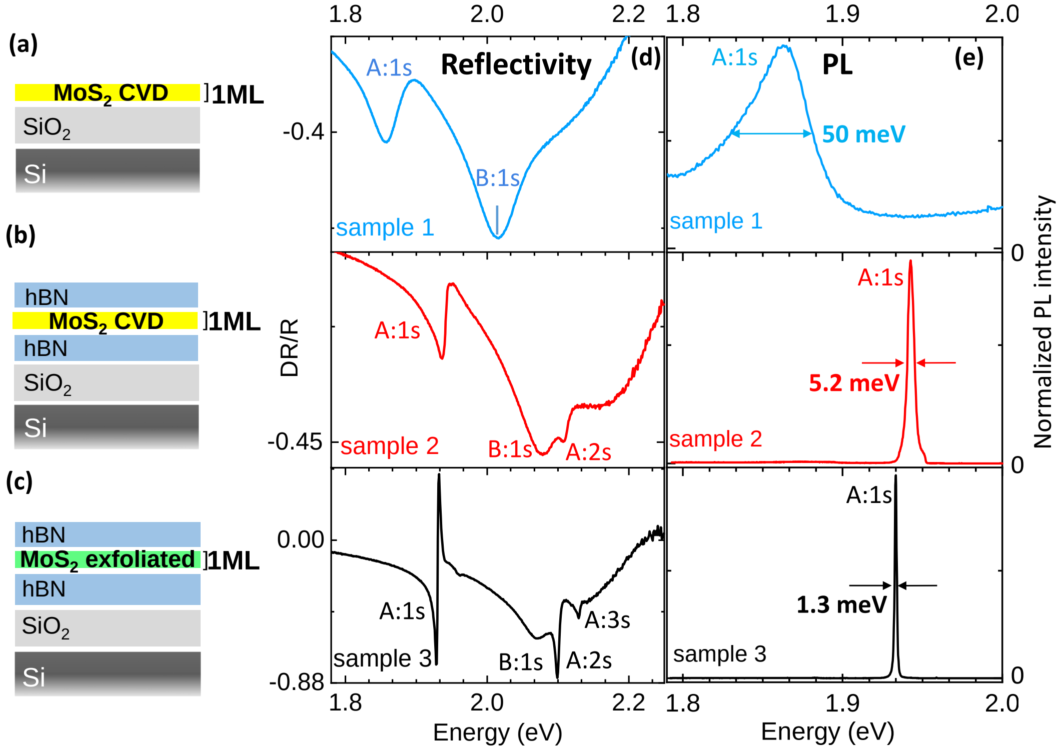

Figure 7.3: **(a)** Schematics of sample 1, as-grown CVD MoS_2 ML on SiO_2. **(b)**, **(c)** CVD-grown and exfoliated MoS_2 monolayer encapsulated in hBN layers – sample 2 and sample 3, respectively. **(d)** Differential reflectivity measurements at $T = 4\ K$ performed on different samples 1,2 and 3. A-exciton and B-exciton transitions are marked for sample 1. For samples 2 and 3 excited state of the A-exciton at higher energies are clearly visible marked A:2s, A:3s. **(e)** PL spectra of the as-grown and encapsulated MoS_2 in h-BN, respectively at $T = 4\ K$, which highlights the very different linewidth and shift in emission energy. PL excitation conditions : sample 1 ($\lambda_{\text{Laser}} = 532$ nm, $P = 5\ \mu$W), sample 2 (633 nm, 5 μW), sample 3 (633 nm, 1 μW).

sion at 1.863 eV, very similar to other spectra reported for as-grown samples in the literature [256]. We also note that the transition energy of neutral exciton A:1s is red-shifted compared to standard MoS_2 ML both in PL as observed also in reflectivity in Fig. 7.3 (d). The broad linewidth of the PL emission, similar to the broad linewidth measured in differential reflectivity, indicates large inhomogeneous broadening of the A-exciton transition. This is surprising when taking into account the high structural quality measured for this CVD-grown material, see Fig. 7.1 and hints at detrimental effects from the environment to be at the origin of this inhomogeneous broadening.

For sample 2 the PL emission linewidth is clearly reduced by a factor of 10 after encapsulating the CVD-grown MoS_2 monolayer in hBN. We also noticed a significant enhancement in PL emission intensity at the A:1s energy after encapsulation as compared to low energy defect related emission, see discussion of Fig. 7.4 below. The PL linewidth for sample 2 with 5 meV in Fig. 7.3 (e) is a typical linewidth reported also for MoS_2 exfoliated and encapsulated material at $T = 4\ K$ [51, 262].

So finally these spectra indicate that the comparable structural quality of our CVD layers to exfoliated material also results in comparable optical quality, once the detrimental impact of the substrate (surface roughness and charge fluctuations) are suppressed thanks to the hBN buffers. Sample 3 shows an even narrower PL emission linewidth with 1.3 meV and indicates that further reduction of inhomogeneous broadening for the CVD sample can be targeted in the future by tailoring growth and improving the encapsulation procedure, see discussion below. Note that for sample 3 the homogeneous contribution to the linewidth (i.e. determined by the radiative lifetime) will be important and for an exact linewidth analysis cavity effects due to different hBN layer thicknesses have to be taken into account [82] also shown in Chapter 2.

We now study the emission properties of sample 2 in more detail in Fig. 7.4. Fig. 7.4 (a) shows the PL spectrum for selected temperatures from 260 K to 4 K. The PL spectrum at $T = 4$ K exhibits a neutral exciton A:1s peak centered at 1.944 eV. The linewidth of the A:1s peak is around 5 meV and moreover the PL intensity of the defect related peaks at lower energy is significantly smaller than that of the A:1s peak, we see no clear indication of a charged exciton peak (trion) [245, 268], indicating close to charge neutrality. The fact that the PL spectrum with low laser power excitation (5 μW) is dominated by the main neutral exciton emission is a clear proof of a low defect density, in agreement with the HRTEM results shown in Fig. 7.1 (e). It is very important to note that PL spectra with spectrally narrow A:1s emission and very weak defect emission are observed throughout the sample and not just for a specific detection spot location.

PL spectra measured at different locations on sample 2 are shown in Fig. 7.5. Although there are small variations in A:1s emission energy (meV scale) our sample 2 shows narrow excitonic PL emission and only weak intensity of defect related emission for all detection spot positions.

In order to further study the main exciton transition, we measure the emission energy and linewidth as a function of temperature. Fig. 7.4 (a) shows the A:1s peak position plotted as a function of temperature. The A:1s transition energy can be fitted by the following standard expression for the temperature dependence of a semiconductor bandgap [269]:

$$E_G(T) = E_G(0) - S\langle\hbar w\rangle[\coth(\langle\hbar w\rangle/(2k_BT)) - 1]. \tag{7.1}$$

where $E_G(0)$ is the optical bandgap at $T = 0$ K, S is a dimensionless electron-phonon coupling constant, k_B is Boltzmann's constant, and $\langle\hbar w\rangle$ is an average phonon energy. Fitting the data in Fig. 7.4 (a) with Eq. 7.1 yields $E_G(0) = 1.944$ eV, $S = 1.9 \pm 0.1$ and $\langle\hbar w\rangle = 20 \pm 2$ meV. These parameters are very close to the values obtained for high quality exfoliated samples, which confirms that the narrow peak of 5 meV observed for sample 2 is indeed the main A-exciton transition (optical bandgap) of the MoS_2 monolayer [51]. This is further verified by the measurement of the same transition energy in PL and reflectivity.

The evolution of the linewidth with temperature can be phenomenologically approximated by a phonon-induced broadening [198, 199] as already studied in Chapter 4 :

$$\gamma = \gamma_0 + c_1T + \frac{c_2}{e^{\langle\hbar w\rangle/k_BT} - 1}. \tag{7.2}$$

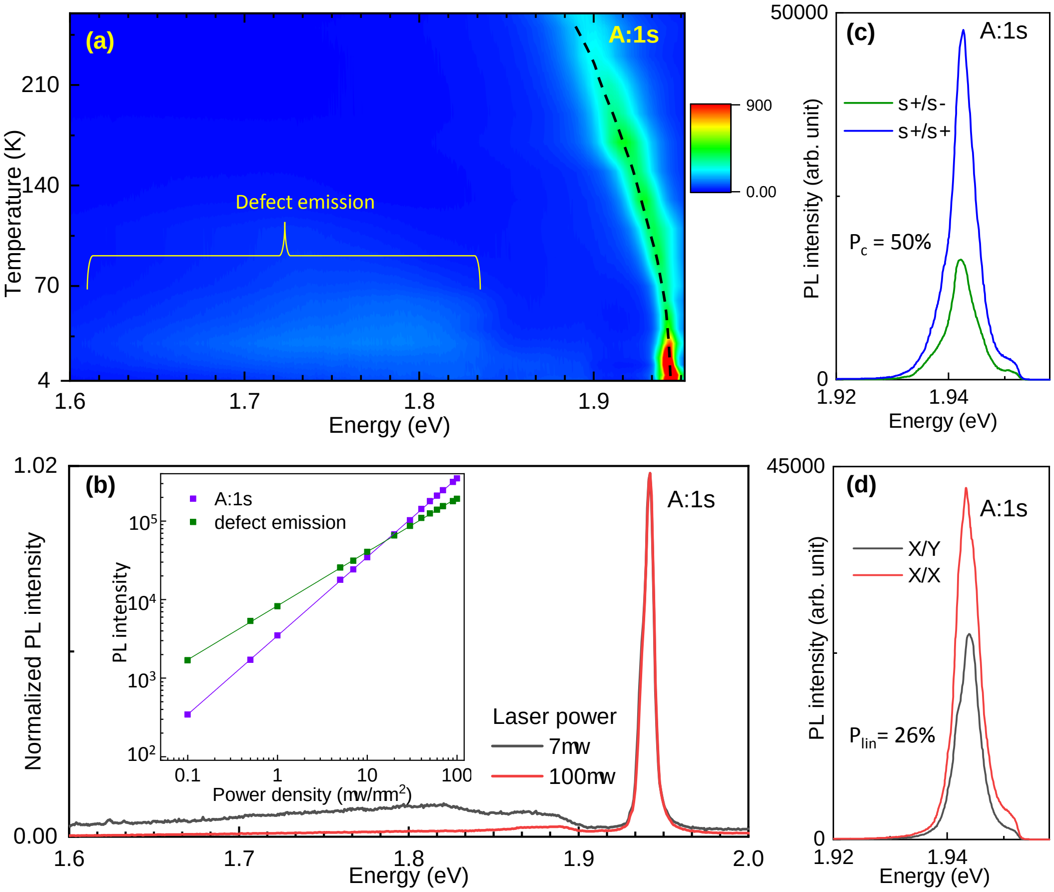

Figure 7.4: Sample 2. **(a)** A contour plot of the temperature dependence of the photoluminescence intensity using a laser excitation density 5 μW/μm^2. The dotted line tracks the evolution of the peak position of the neutral exciton (optical bandgap A:1s) with temperature according to Eq.(1). **(b)** PL spectra $T = 4\ K$ with cw laser at 2.32 eV for excitation power 7 μW and 100 μW. Low energy, spectrally broad defect emission is clearly visible at low excitation power, but not at high power. The inset shows a double logarithmic plot of the integrated PL intensity as a function of excitation power for A:1s (purple filled squares) and defect emission (green filled squares). The solid curves represent $I \propto P^{\alpha}$, a fit to PL intensity, yielding an α of 1.0 for A:1s and 0.7 for the defect state. **(c)** and **(d)** Polarization-resolved PL at $T = 4\ K$ following circularly and linearly polarized laser excitation at 2.32 eV, exhibiting efficient exciton valley polarization and valley coherence, respectively.

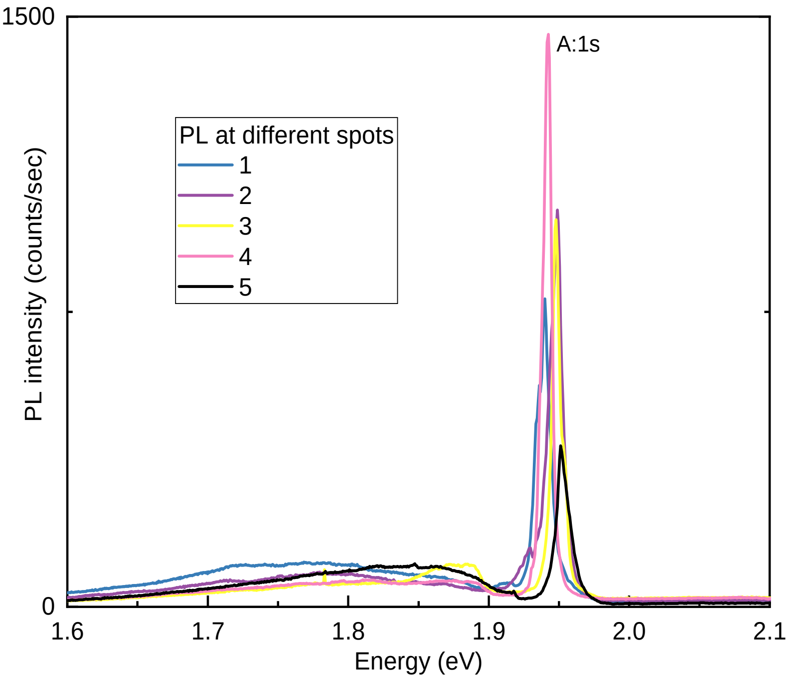

Figure 7.5: **Sample 2.** Photoluminescence emission at $T = 4\ K$ from sample 2. Spectrally narrow emission (FWHM $\approx$ 5 meV) from the A-exciton (A:1s) is dominating independent of the exact sample area investigated. So for different positions of the detection spot on the sample, the characteristics are very similar : Weak defect emission at energies below 1.9 eV and strong exciton emission at around 1.95 eV from the CVD-grown MoS_2 monolayer.

where $\gamma_0 = 5.6 \pm 0.2$ meV, $c_1 = 56 \pm 6\ \mu\text{eV/K}^{-1}$ describes the linear increase due to acoustic phonons, and $c_2 = 31 \pm 2$ meV is a measure of the strength of the exciton-phonon-coupling are determined by fitting linewidth evolution with temperature using Equ. 7.2. $\langle \hbar w \rangle = 20$ meV is the averaged energy of the relevant phonons, that we obtained by fitting the optical bandgap energy shift with Eq.(7.1) for consistency. Again these extracted values are very similar to reports on exfoliated MoS_2 MLs, indicating similar strength of the exciton-phonon interaction in our CVD-grown layers and hence no major additional broadening mechanisms [51, 198, 123, 199]. The temperature dependent PL data also shows the low energy ($<$ 1.9 eV) defect associated emission disappears above $T = 150\ K$.

Another indication for high optical quality comes from power dependent PL. The inset of Fig. 7.4 (b) displays the spectrally integrated PL intensity I, defined as the peak area, as a function of excitation power P (with $I \propto P^\alpha$) for A:1s (filled purple squares) and defect states (filled green squares). As laser power increases, more carriers are generated that fill-up gradually all available defect sites, leading to a gradual saturation of the defect assisted emission. This leads to a sublinear behavior when defect emission is plotted as a function of laser power for the defect peak reaching $\alpha = 0.68$. The power dependence of defect emission follows a nonlinear curve, while A:1s is linear with fitted $\alpha \approx 1$. Only at higher excitation powers when exciton-exciton scattering processes become important also the neutral exciton emission will saturate with power, for example due to exciton-exciton

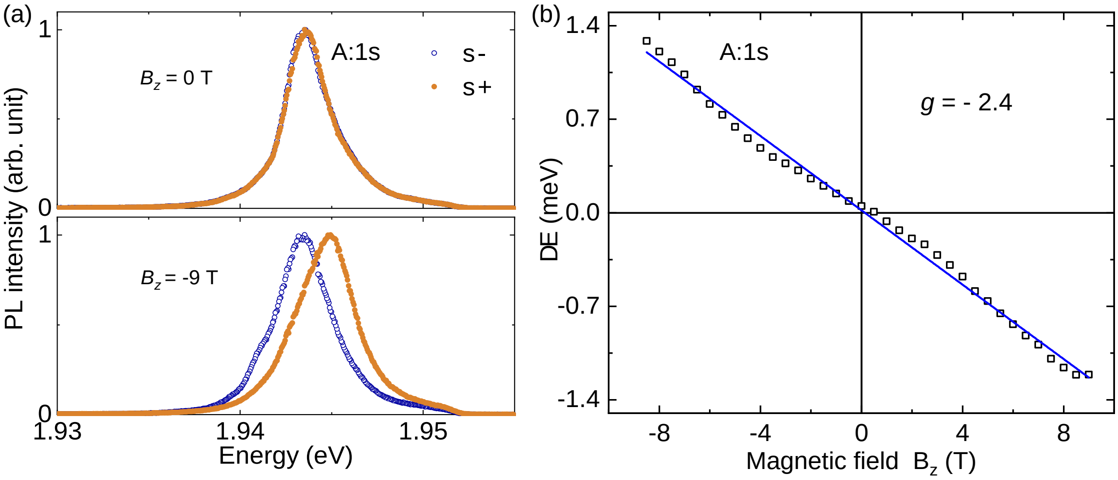

Figure 7.6: **Sample 2.** **(a)** Polarization-resolved photoluminescence emission spectra at $T = 4\ K$ for MoS_2 monolayer in positive and negative magnetic fields ($B_z = 0\ T$ and $B_z = -9\ T$) applied perpendicular to the layer. The orange and blue curves correspond to σ^+ and σ^- polarization. **(b)** Energy difference between the two circular polarizations for the A:1s excitons at different magnetic fields B_z. The Landé g-factor of the neutral excitons is extracted from linear fit.

annihilation [270, 271], but this is beyond the laser power range investigated here.

The high quality sample 2 is further confirmed in studies using polarized light in excitation and detection. Studies of optically controlled valley polarization and valley coherence are one of the main motivations for the quest of cleaner TMD materials with narrower linewidth [272]. We first investigate exciton spin-valley polarization based on the chiral optical selection rules [26, 33].

In our experiment the MoS_2 ML is excited by a circularly polarized (σ^+) continuous wave He-Ne laser (1.96 eV) with power density $5\mu W/\mu m^2$. We define the circular PL polarization degree as $P_c = \frac{I_{\sigma+} - I_{\sigma-}}{I_{\sigma+} + I_{\sigma-}}$, where $I_{\sigma+}(I_{\sigma-})$ are the intensity of the right (σ^+) and left (σ^-) circularly polarized emission as detailed in Chapter 1 and Chapter 3. We find $P_c \approx 50\%$ for the emission in Fig. 7.4 (c), comparable to previously reported values in exfoliated MoS_2 ML samples [35, 37, 51, 273].

A coherent superposition of valley states, valley coherence, can be generated using linearly polarized excitation [41, 274]. The MoS_2 ML is excited by a linearly polarized (X) laser and we detect the emitted light in both polarization directions X and Y. The linear PL polarization degree P_{lin} is defined as $P_{lin} = \frac{I_X - I_Y}{I_X + I_Y}$, where $I_X(I_Y)$ denotes the intensity of the X and Y linearly polarized emission, respectively. In our experiment we find sizeable P_{lin} of about 26% for the emission in Fig. 7.4 (d). Please note that the exact values of P_c and P_{lin} critically depend on the laser excitation energy [20], which was not varied here. The results in Fig. 7.4 (c) and (d) show that we can generate exciton valley polarization and valley coherence optically, making these large area CVD-grown films highly useful for future the studies of valley and spin physics in monolayer MoS_2. Optical generation of spin-valley polarization in TMDs is interesting for hybrid devices that rely on subsequent spin transfer to graphene for effective spin transport [275, 276].

The narrow PL linewidth in CVD-grown monolayer now allows us to distinguish spectrally the emisssion from non-identical valleys K^+ and K^- and to study the valley Zeeman effect. Fig. 7.6 (a) shows the polarization-resolved PL spectra at $T = 4$ K in applied magnetic field. We discuss the change in the PL emission energy when applying a magnetic field B_z perpendicular to the monolayer plane (Faraday geometry). Comparing the top panel of Fig. 7.6 (a) at $B_z = 0$ T and bottom panel of Fig. 7.6 (a) at $B_z = -9$ T we observe the σ^+ polarized emission is shifted to higher energy compared to the σ^- polarized component. In Fig. 7.6 (b) we plot the full magnetic field dependence of the energy splitting in magnetic field $B_z = -9$ T to $+9$ T showing good agreement with time-reversal symmetry.

$$\Delta Z = E_{\sigma^+}^{PL} - E_{\sigma^-}^{PL} = g\mu_B B_z$$

Here, g is the effective g-factor and μ_B is the Bohr magneton. The Zeeman splitting is extracted by fitting the A:1s emission spectra with Lorentzians as discussed in the section 6.2 of Chapter 6. We observe a clear linear dependence of the A:1s splitting on the applied fields and the extracted Landé g-factor = -2.4 close to the value obtained in capped MoS_2 monolayers [51]. Some literatures reported the experimental values for the exciton g-factor on MoS_2 MLs between -4 and -4.5 [231, 277], obtained with magneto-reflectivity measurements on CVD-grown MoS_2 monolayers. Variations in the measured neutral exciton g-factor can be due different strain in CVD monolayers. Our measurements show the Zeeman effect of excitons can be studied in CVD-grown monolayers even in small continuous magnetic fields, so far this was only possible in pulsed magnetic fields of the order of 50 T.

7.3 Discussion and Conclusions.

The first optical spectroscopy reports for emission in ML MoS_2 exfoliated on SiO_2/Si substrates have given PL linewidth of the order of 50 meV, even at low temperature [6, 36, 71, 273, 278]. Now in exfoliated and hBN encapsulated samples we approach the radiatively broadened, homogeneous limit with linewidth of 1 meV [51, 235, 262]. This research field has made impressive progress as the impact of disorder in the ML environment on the measured optical properties of the ML is better understood [79, 84]. In this chapter I have shown with our collaborators that CVD-grown monolayers, picked-up from the growth substrate and encapsulated in exfoliated hBN flakes show high optical quality and allow detailed spectroscopic and valley polarization studies. An important aspect of our work is that the initial growth is performed on SiO_2, a commonly available substrate material of industrial grade.

Other hybrid approaches with CVD growth and exfoliated flakes have also shown promising results using different substrates. In general, the detrimental effects of the substrate material can be studied for monolayers that are lifted of the substrate after growth, for instance, Yu et al [261] reported strongly enhanced PL emission for suspended MoS_2 and WS_2 monolayers. Recent experiments on $MoSe_2$ monolayers encapsulated in hBN and suspended over a micro trench do not only show extremely narrow linewidth close to the homogeneous limit, but also display very little variation of the emission energy in a spatial scan of the suspended region [108]. Better optical quality for CVD-grown WS_2 removed from the substrate has also been reported by Hoshi et al [259] and for CVD-grown WSe_2 by Delhomme et al [279], confirming this trend.

Direct growth not on SiO_2 but directly on hBN is another way to achieve high quality material, demonstrated for both WS_2 and MoS_2 monolayers [280]. A combination of CVD-grown hBN and CVD-grown MoS_2 that can be stacked on top of each other has also been reported, where these stack showed superior optical quality to as-grown MoS_2 on SiO_2 [281]. Also molecular beam epitaxy (MBE) is making progress for large scale growth of layered materials [27]. Here for example large area films of MBE-grown hBN can be used as a substrate to transfer TMD monolayer flakes. This heterostructure also showed overall spectrally narrow emission of the TMD ML [282]. MBE growth of $MoSe_2$ on hBN flakes also resulted in MLs with high optical quality and uniformity [283].

As substrate and encapsulation techniques progress, ultimately the TMD material quality itself will need to be improved. Bulk materials for exfoliation, the flux growth techniques is reported to generate MLs material with very low defect density [246]. Here further improvement in the structural quality of CVD-grown layers needs to be investigated in the future. Additional decrease of the defect density in TMD samples grown by CVD can be achieved by optimization of the multiple thermodynamic and kinetic growth parameters including temperature, partial pressure of the components and their flow rates, as well as the TMD monolayer/substrate interaction. Moreover, the application of the gaseous precursors for transition metals and chalcogens in combination with the appropriate catalysts may provide an additional degree of freedom for optimizing the crystalline growth in the future. A specific aspect that can be improved at the LPCNO is the pick-up process for the CVD layers, as will be detailed in the next chapter. This will allow us to use high quality CVD layers as building blocks for van der Waals structures with controlled interlayer coupling.

Chapter 8

Controlling interlayer excitons in MoS_2 layers grown by chemical vapor deposition

Combining MoS_2 monolayers to form multilayers allows to access new functionalities. Deterministic assembly of large area van der Waals structures requires concrete indicators of successful interlayer coupling in bilayers grown by chemical vapor deposition (CVD). In this chapter, I examine the correlation between the stacking order and the interlayer coupling of valence states in both as-grown MoS_2 homobilayer samples and in artificially stacked bilayers from monolayers, all grown by CVD. We experimentally demonstrate that hole delocalization over the bilayer is only allowed in *2H* stacking and results in strong interlayer exciton absorption and also in a larger A-B exciton transition separation as compared to *3R* bilayers. Comparing *2H* and *3R* reflectivity spectra allows to extract an interlayer coupling energy of about $t_\perp = 49$ meV, so far only estimated from model calculations. Beyond DFT calculations performed by Iann Gerber (LPCNO) including excitonic effects confirm signatures of efficient interlayer coupling for *2H* stacking in agreement with our experiments. The results reported in this chapter are published in [284].

8.1 Introduction

Transition metal dichalcogenides (TMDs) with the form MX_2 (M = Mo, W, Ti, etc and X = S, Se, Te) have tunable electronic properties from metallic to semiconducting depending on the crystal symmetry, composition and number of layers [139, 185, 207, 285, 272]. The bandstructure of TMD semiconductors is drastically modified by changing for instance, the combination of two different monolayer materials such as $MoSe_2$-WSe_2 into a heterobilayer results in type II band alignment and opens new research perspectives on periodic moiré potentials for carriers in the different layers and the resulting interlayer excitons [150, 286, 287, 288, 289]. Twisted homobilayers of graphene, WSe_2 and $MoSe_2$ allow accessing new superconducting phases and correlated insulating states [117, 290]. In Chapters 5 and 6, we studied naturally occurring bilayers of *2H* MoS_2. To access the new functionalities provided by *assembling* monolayers to form multilayers it is necessary to identify physical parameters that strongly depend on interlayer coupling and to experimentally control them. One approach is to compare CVD-grown MoS_2 bilayers with artificially stacked bilayers made from CVD monolayers with *2H* (180° twist angle) and *3R* (0° twist angle) stacking. Studying these two precise alignments is also relevant for samples initially assembled with other twist angles as reconstruction results also in these experiments in the formation of μm wide *2H* and *3R* areas [115, 291], which are energetically most stable. To artificially stack large area CVD layers and control interlayer coupling through stacking (*i.e.* 0° or 180° twist angle) is technologically relevant for 2D materials optoelectronics [289], as CVD substrates are covered by a large number of monolayers and are very practical to stack (twist) due to their symmetric triangular shape and well characterized edge termination.

In this chapter, I show thanks to a fruitful collaboration between experiment and theory (from Iann Gerber, LPCNO) that the valence states for *2H* bilayers are strongly impacted by interlayer coupling as the hole is delocalized over the 2 layers [60, 212, 67]. This leads to important changes in the optical spectra governed by $K-K$ transitions as we observe strong absorption from interlayer excitons and a clear change in separation between A- to B-exciton transition in differential white light reflection at $T = 4\ K$. These observations are made possible due to the drastically improved optical quality of CVD samples removed from the growth substrate and encapsulated in hBN [80], as described in the previous Chapter 7. We show that both indicators for interlayer coupling are absent in the measured *3R* bilayer spectra as hole hopping between the layers is symmetry forbidden [211]. Comparing for *3R* (no interlayer coupling) and for *2H*, the A-B exciton absorption spectra allows us to extract an experimental value of the perpendicular hopping (coupling) term of $t_\perp \approx 49$ meV, important for moiré superlattices [292] and so far only roughly estimated from theory [211].

In addition to our optical spectroscopy experiments, I compare our results with density functional theory (DFT) calculations, as well as by applying GW-type approaches. The calculations show that the valence band (VB) splitting for *2H* differs from *3R* due to interlayer coupling. In the calculated absorption spectra, including excitonic effects by solving the Bethe-Salpeter-Equation (BSE) on top of GW calculations, for *2H* stacking we show strong interlayer exciton absorption, absent for *3R* stacking. Note that the similar results are obtained using different computational setting shown in Chapter 5.

8.2 Experimental Results

8.2.1 Interlayer excitons in as-grown CVD MoS_2 homobilayers.

The thermodynamically most stable configurations of TMD homobilayers are the *2H* and the *3R* stacking [60, 226]. In practice, most naturally occurring molybdenite shows *2H*, not *3R* stacking [229]. In this chapter we focus on high quality CVD-grown flakes for several reasons : during CVD growth of MoS_2 both *2H* and *3R* stackings for bilayers can occur [293] and we are therefore able to compare the optical response for samples grown under identical conditions. Secondly, as all

CVD flakes on our substrate show the same edge termination (see Fig. 8.1 (b) and Fig. 8.2 (a)), we can artificially stack two layers in *2H* and *3R* configuration with a precise twist angle to compare with the as-grown samples - see discussion below. Third, many monolayers cover the SiO_2 substrate and can all be picked-up in a single step, which makes fabrication of bilayer structures very efficient. CVD flakes with larger surface area are also more convenient to fabricate devices with electrical contacts.

Before presenting optical spectroscopy results on as-grown *2H* and *3R* bilayers, I give more information on sample fabrication and characterization :

CVD samples growth. MoS_2 crystals were grown in the group of Andrey Turchanin (FSU Jena) on thermally oxidized silicon substrates (Siltronix, oxide thickness 300 nm, roughness < 0.2 nm RMS) by a modified CVD growth method in which a Knudsen-type effusion cell is used for the delivery of sulfur precursor [83]. This is the same set of CVD samples investigated in Chapter 7.

Determination of bilayer stacking. Optical microscope images of as-grown CVD bilayers on SiO_2/Si with *3R* and *2H* stacking (sample 1) are presented in Fig. 8.2 (a). The stacking can be determined already by the relative rotation of the triangular monolayers and was confirmed in second harmonic generation (SHG) experiments [168, 294], which I carried out during my one month stay in Richard Warburton's group at University of Basel (Switzerland) during June 2019 with Nadine Leisgang, see technical details in the section 3.3 of Chapter 3. SHG spectroscopy is a second-order nonlinear process. Broken inversion symmetry and strong light matter interaction in bilayer *3R* MoS_2 enables us to observe higher harmonics generation. In a SHG experiment, two photons of the same frequency are converted into a single photon with twice that frequency :

$$\mathbf{P}_i^{(2)}(2\omega) \propto \chi_{ijk}^{(2)}\mathbf{E}_i(\omega)\mathbf{E}_k(\omega).$$

where, $\mathbf{P}_i$ is the induced polarization and $\mathbf{E}_{i,k}$ the applied electric field vector components. TMD *monolayer* crystal lattices in the *2H* phase belong to the trigonal prismatic (D_{3h}) point group. The second-order nonlinear susceptibility tensor $\chi_{ijk}^{(2)}$ has four non-zero elements with one free parameter $\chi_0^{(2)}$ in this symmetry [168, 294]. The TMD layers are excited with linearly polarized light under normal incidence. We detect the SHG response with a linear polarizer, oriented along the fundamental polarization angle. This results in a six-fold SHG intensity pattern $I_{\text{SHG}}^{\parallel} \propto \cos^2 3(\theta - \theta_0)$ (SHG polarization parallel to the excitation polarization), where the angle θ_0 is the rotation of the armchair direction of the crystal relative to the laboratory axis. Polarization-resolved SHG experiments were performed using a home-built, confocal microscope set-up at room temperature. A Ti:Sapphire laser source with 76 MHz repetition rate at a wavelength of 804 nm was used. The laser (average power 8 mW) with a spot size (~ 1.5 μm) was focused on the sample by a microscope objective lens ($NA = 0.65$) at normal incidence and with a fixed linear polarization. The SHG signal was collected by the same objective and directed through a dichroic beamsplitter to a spectrometer with a 300 grooves/mm grating and a nitrogen cooled silicon charge-coupled device (CCD). The SHG intensity strongly depends on the polarization angle (θ - θ_0) between the

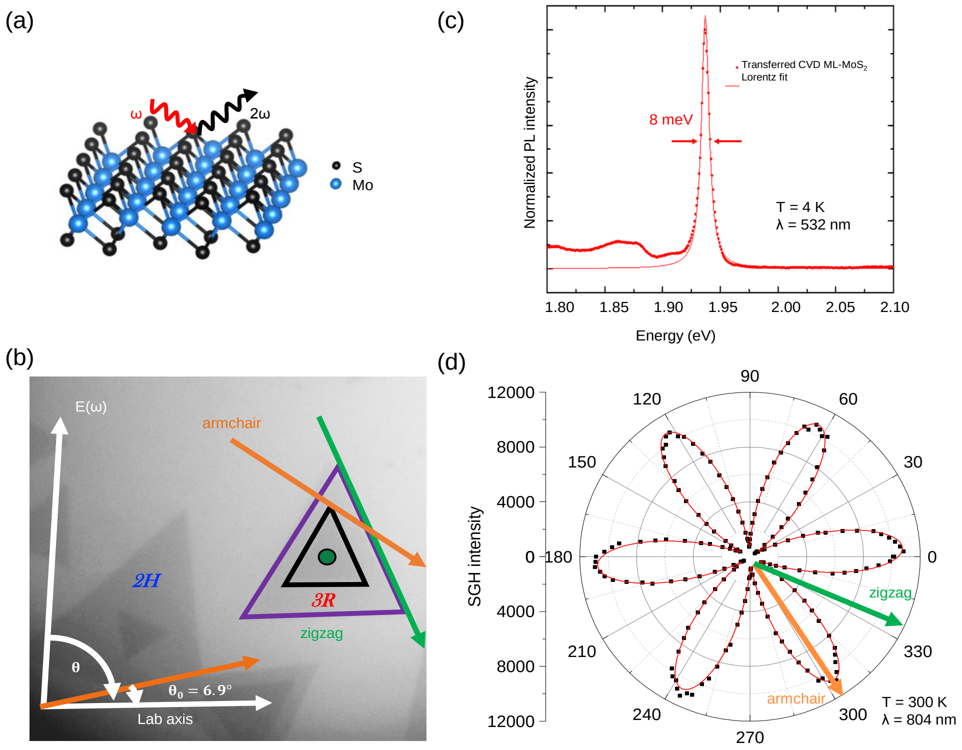

Figure 8.1: SHG characterization of encapsulated *3R* bilayer MoS_2. **(a)** Schematic representation of the crystallographic orientation of MoS_2 monolayer. **(b)** Optical image of the as-grown MoS_2 *3R* and *2H* bilayers before encapsulation. The armchair direction forms an angle θ_0 with respect to the laboratory axis (LAB). The indicated armchair and zigzag edges were determined by polarization-resolved SHG performed on the *3R* bilayer. **(c)** PL spectrum of ML MoS_2 transferred and encapsulated in hBN following the water-assisted transfer method. A laser (532 nm) was used as an excitation source and the spectrum was collected at $T = 4\ K$. **(d)** Polar plot of the polarized SHG signal of CVD grown *3R* MoS_2 bilayer. Fitting the angular dependence to $I^{\parallel}_{\mathrm{SHG}} \propto \cos^2 3(\theta - \theta_0)$ (solid red line), the armchair direction (orange arrow) of the sample is determined as $\theta_0 = 6.9°$. This armchair direction is 30° from the zigzag direction (light green arrow).

laser polarization $E(\omega)$ and the armchair direction of the crystal shown in Fig. 8.1 (b). To perform polarization-resolved SHG, the laser polarization was rotated using a half-wave plate, and the SHG intensity $I^{\parallel}_{\mathrm{SHG}}$ was collected. The polar plot of *3R* MoS_2 bilayer in Fig. 8.1 (d) directly reveals the stacking order and the crystallographic orientation of the bilayer. It is important to note that for the *2H* MoS_2 bilayers no SHG signal could be detected as inversion symmetry is restored, only *3R* bilayers gave an SHG response. SHG spectroscopy therefore allows a clear distinction between *3R* and *2H* stacked bilayers studied in this work.

Sample pick-up and encapsulation. We first identified suitable bilayers on the substrate and picked-up onto PDMS from the substrate to encapsulate them in hBN, the procedure is also mentioned in the section 2.1 in Chapter 2. Here we developed with my colleague Ioannis Paradisanos the following procedure : The

SiO_2/Si substrate for hosting the van der Waals structure was cleaned with a 10 minute ultrasonication bath in acetone and isopropanol followed by oxygen plasma exposure. A clean PDMS stamp was first placed on a glass slide and the SiO_2/Si substrate containing the as-grown CVD MoS_2 monolayers and homobilayers was brought in contact with the PDMS stamp [97]. The substrate was pressed against the PDMS stamp and distilled water droplets were injected at the perimeter of the substrate. Water droplets penetrated into the SiO_2/MoS_2/PDMS interface and after 1 minute the SiO_2/Si substrate was carefully lifted, resulting into the transfer of a large area of CVD-grown MoS_2 triangles onto the PDMS stamp, as shown in Fig. 8.3 (b). During the water-assisted pick-up technique, high-purity ($> 20\ M\Omega$) deionized water was used and the samples were dried with a nitrogen gun. Finally, hBN flakes were exfoliated from high quality bulk crystal [77] onto the target substrate and subsequent deterministic-dry transfer of the CVD-grown MoS_2 triangles from the PDMS stamp on top of the hBN was applied. Thermal annealing at 150 deg. for 30 minutes is performed after each transfer step. The thickness of the top and bottom hBN has been carefully selected to optimize the oscillator strength of the interlayer excitons (IEs) [60]. As a result, using a water assisted pick-up technique [97], the as-grown CVD bilayers have been deterministically transferred and encapsulated in hBN to achieve high optical quality [80], which has recently been shown to be crucial for optical spectroscopy on CVD samples lowering the typical emission linewidth from about 50 meV to below 5 meV at $T = 4\ K$. An example of a photoluminescence spectrum of a CVD MoS_2 *monolayer* used here is shown in Fig. 8.1 (c). I present a typical PL spectrum collected from a hBN-encapsulated ML MoS_2 next to the manually assembled bilayers. The A-exciton emission has a linewidth of 8 meV at the full width at half maximum (FWHM), very close to the recently reported high optical quality encapsulated CVD ML MoS_2 [80] as described in Chapter 7.

Low temperature reflectance measurements. Low temperature reflectance measurements were performed in a home-built micro-spectroscopy set-up assembled around a closed-cycle, low vibration attoDry cryostat with a temperature controller ($T = 4\ K$ to $300\ K$). The white light source for reflectivity is a halogen lamp with a stabilized power supply focused initially on a pin-hole that is imaged on the sample. The excitation/detection spot diameter is $\approx 1\ \mu$m, i.e. smaller than the typical size of the homobilayers. The imaginary part of the optical susceptibility $\mathrm{Im}(\chi)$, a measure of the absorption, were deduced from the differential reflectivity signal, using the Kramers-Kronig relation [247].

In Fig. 8.2 (c), the absorption spectra for as-grown CVD *2H* and *3R* MoS_2 bilayers (sample 1) can be compared. There are two striking differences between the *2H* and *3R* bilayer spectra : **(i)** While A and B intralayer excitons are identified for both configurations, a pronounced feature at ≈ 2 eV appears exclusively in the *2H* bilayer. This feature is assigned to an interlayer state, its energy being in good agreement with the very recently identified IEs in high quality and hBN encapsulated, *exfoliated* MoS_2 bilayers with *2H* stacking [60, 236, 67], in contrast to *CVD-grown* samples studied here. This observation of IEs was made possible by our specific CVD sample preparation for the optical spectroscopy experiment [80] also as explained in Chapter 7. IE absorption was not detectable in very detailed earlier

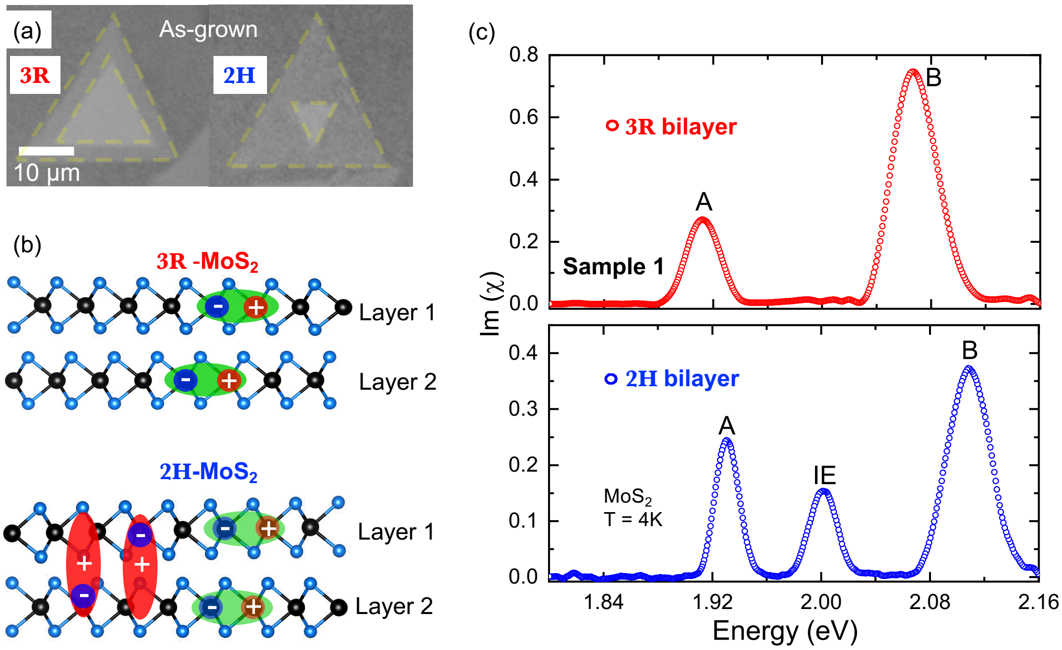

Figure 8.2: **(a)** Optical microscope images of as-grown *3R* (left) and *2H* CVD MoS$_2$ bilayers (right) on SiO$_2$/Si before pick-up. **(b)** Schematic of *3R* stacked bilayer with intralayer excitons (top) compared to *2H* stacked bilayer where in addition interlayer excitons are observed as in panel **(b)**. **(c)** Typical absorption spectra for sample 1 with as-grown *2H*-bilayer (blue) and as-grown *3R*-bilayer (red), are recorded at $T = 4\ K$, both bilayers are encapsulated in high quality hBN for optical spectroscopy [77].

works due to considerably larger optical linewidth or detection of emission and not absorption [166, 295, 296]. In contrast to *2H* stacking, in the *3R* configuration no additional states are detected between the A- and B-excitons, thus indicating that delocalization of holes is not allowed in this particular stacking order [60], see below for a more detailed discussion. **(ii)** The separation between the A- and B-exciton transitions is considerably larger in the *2H* bilayers (about 185 meV) as compared to the *3R* bilayer (about 150 meV, mainly given by the spin-orbit splitting in the VBs). This is a second indication for efficient interlayer coupling of A-B valence states for *2H* stacking, as the separation of the valence states mainly governs the A-B exciton separation [12, 211, 67].

8.2.2 Controlling interlayer coupling through stacking.

In Fig. 8.2 we show that *as-grown* CVD MoS$_2$ bilayers experience interlayer coupling resulting in interlayer exciton formation, here observed for a non-contaminated interface between the top and bottom layer. Contamination from secondary transfer processes could potentially suppress the coupling between the layers and hence IE formation. By choosing *2H* or *3R* orientation *manually* when stacking CVD-grown monolayers to form bilayers one can allow hole tunneling between the layers or not. This requires to pick-up the CVD-grown monolayers from their growth

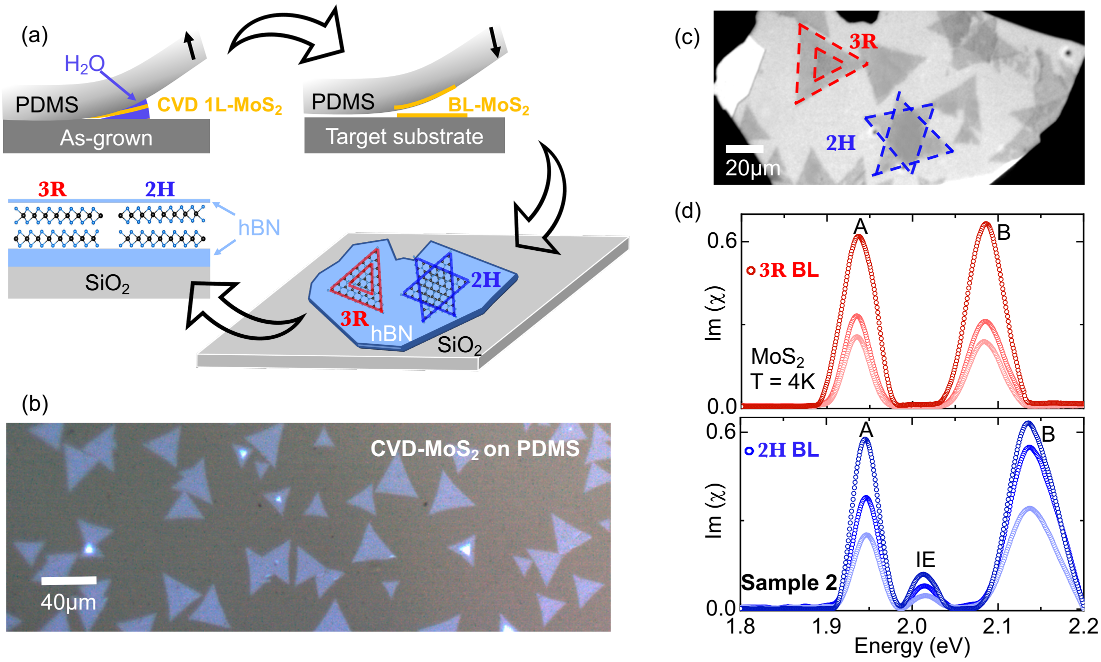

Figure 8.3: **(a)** Schematic of sample pick-up, bilayer assembly and encapsulation for optics. **(b)** Optical micrograph of CVD-grown MoS$_2$ monolayers and a few homobilayers, transferred to the PDMS stamp following water assisted pick-up [97] from the growth substrate. **(c)** Optical micrograph of artificially-assembled *3R* and *2H* MoS$_2$ homobilayers encapsulated in hBN (sample 2), fabricated by an all-dry deterministic transfer process. **(d)** Absorption spectra of sample 2 are collected from different areas of the artificially stacked *3R* (red) and *2H* (blue) MoS$_2$ homobilayers.

substrate while maintaining their structural integrity, optical quality and a sufficiently clean interface after transfer. Furthermore, fine control of the twist angle between the top and bottom layer is needed, since the IE formation is allowed only in a precise stacking order, see sample preparation schematic in Fig. 8.3 (a). Here we use water assisted deterministic transfer that allows the ability to controllably assemble CVD bilayers with a desired twist angle [97]. First, CVD-grown monolayers have been carefully picked-up from the growth substrate and transferred to PDMS [97, 72]. The structural integrity of the CVD-grown monolayers is preserved in this case. Then we stack manually *2H* and *3R* bilayers and encapsulate them in hBN as shown in Fig. 8.3 (c). Small deviations from 0° or 180° twist angle are expected but natural reconstruction of the bilayer will again favor the lowest energy arrangement, *3R* and *2H*, respectively [115, 291], as detailed in Chapter 3.

Absorption spectra have been collected from ten different areas of the assembled *2H* and *3R* bilayers sample. In Fig. 8.3 (d), typical examples of the assembled *2H* and *3R* absorption spectra are presented. The spectra show a striking resemblance with the as-grown bilayer spectra discussed before in Fig. 8.2 (c). So also for the assembled *2H* bilayers we identify clear interlayer exciton absorption and an increased separation between the A- and B-excitons. It is important to note that the IE transition was clearly observed over the whole surface area of the manually constructed *2H* bilayer. We take it as a strong indication of efficient interlayer

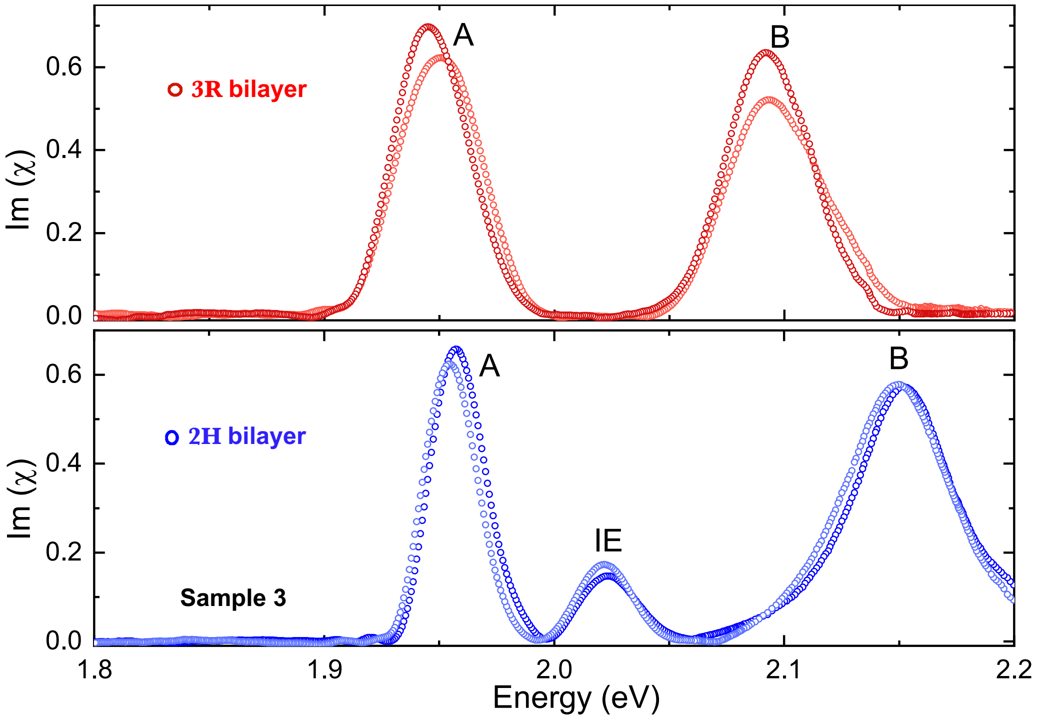

Figure 8.4: Absorption spectra collected at $T = 4\ K$ from two different areas of the artificially stacked *3R* (red) and *2H* (blue) MoS_2 homobilayers, from a different sample as compared to Fig. 8.3 (d).

coupling and possibly efficient reconstruction/self-rotation to the *2H* configuration. We therefore further confirm the formation of IEs exclusively in the *2H* stacking. By manually choosing the stacking configuration i.e. twist angle, it is possible to tune the VB splitting and the formation of interlayer excitons in large area, high quality CVD samples. An important step is to show reproducibility of the results obtained through manual stacking. I have fabricated another set of *2H* and *3R* stacked bilayers and have clearly confirmed the results on interlayer coupling, see Fig. 8.4. Please note that difference in the overall spectral shape can arise from small variations in the top and bottom hBN layer thickness.

8.3 Beyond-DFT band structure calculations including GW+BSE.

In order compare our optical spectroscopy analysis with theory, our colleague Iann Gerber at the LPCNO performed beyond DFT calculations to study the striking differences between *2H* and *3R* MoS_2 bilayers, see [284] for the computational details. Please note that the GW+BSE calculations are performed for MoS_2 bilayers in vacuum for simplicity and not in hBN. The general target of our calculations is to understand the microscopic origin of the optical transitions and to reproduce the energetic order qualitatively.

In GW calculations we compare bandstructures corrected by screening effects,

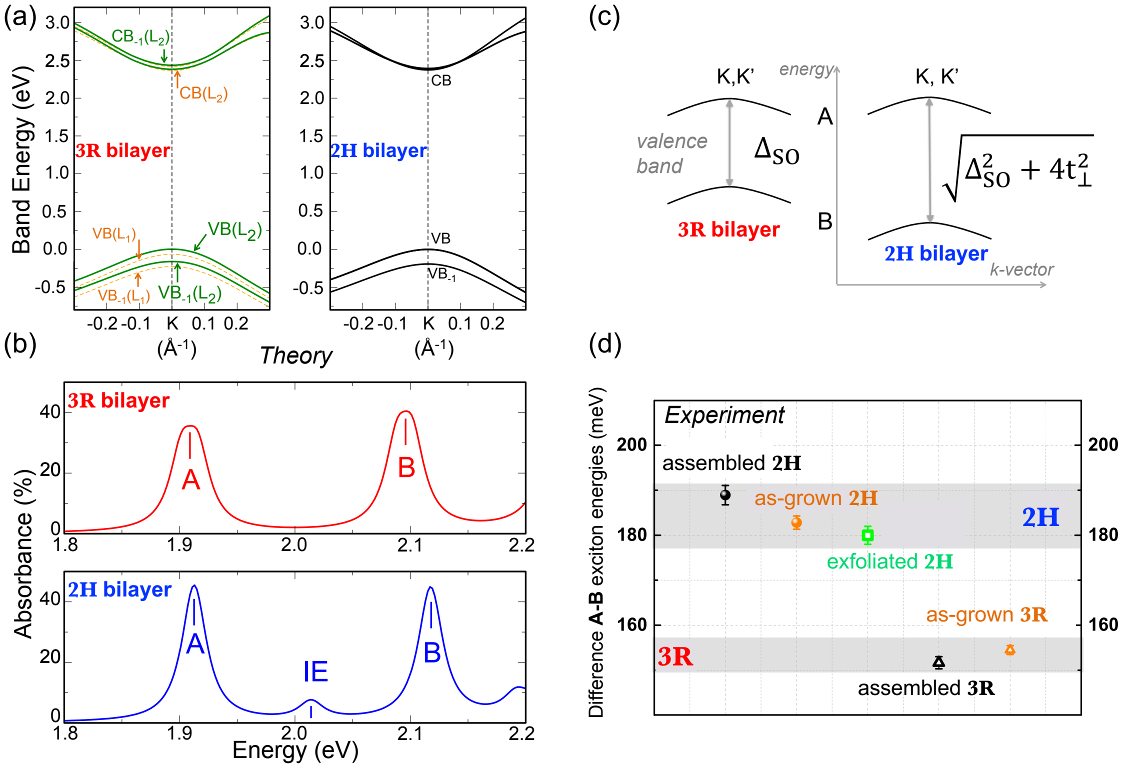

Figure 8.5: **(a)** Valence and conduction bands around K-point calculated at the G_0W_0 level for *2H* and *3R* stacking, with the energy value of the VB set to 0 in K. **(b)** Calculated absorption using G_0W_0+BSE approach for both stackings. **(c)** Schematic of the A- and B-valence bands for *3R* bilayers (left) and *2H* bilayers (right) as a function of the spin-orbit splitting Δ_{SO} and the interlayer coupling parameter $t_\perp$. **(d)** Energy difference between B- and A-exciton for the as-grown (orange), as well as artificially-assembled (black) *2H* and *3R* MoS_2 homobilayers. The error bars represent the standard deviation extracted over 10 different spectra in each case. Grey shaded are is a guide to the eye to underline clear differences between *3R* and *2H* bilayers.

the exciton description being added later. In the vicinity of the K-point of the Brillouin zone, see Fig. 8.5 (a) and schematic in Fig. 8.5 (c), differences between *2H* and *3R* stacking in VB, VB$_{-1}$ states are clear. We find a VB splitting between A- and B-exciton states in the *2H* bilayer that is 19 meV larger than in the 3R bilayer. By solving the BSE we obtain the absorption for the *2H* and *3R* bilayers shown in Fig. 8.3 (b). **The main characteristics are : (i) The presence of a strong interlayer exciton peak in *2H* and (ii) A larger A-B exciton separation for *2H* than for *3R* configuration, exactly as found in the experiments** shown in Figs. 8.2 and 8.3. Interestingly, in *3R* stacking, there is a minor departure from degeneracy that splits VB and VB$_{-1}$ states from distinct layers when they remain degenerate in *2H* configuration. As a consequence, two distinct A-type excitons separated by only 14 meV constitute the A-peak of the *3R*-bilayer absorption spectrum in our calculation, explaining its larger width compared to the *2H* case, see Fig. 8.5 (c). The origin of this splitting, that keeps

	Monolayer	3R-bilayer	2H-bilayer	$t_\perp$
VB splitting	178 (189)	175 (189)	194 (203)	57 (42)
S	185	186	205	43

Table 8.1: Valence band splittings, A-B transition energy differences (S) extracted from GW and GW+BSE calculations and the corresponding interlayer coupling parameters. Values extracted for standard DFT calculations are in parentheses. All values are given in meV.

VB(L_1) and VB(L_2) states to be of the same spin-states, is the lack of symmetry inversion combined with different atomic environments for Mo atoms [297]. This is especially true for the VBs since the atomic orbitals that constitute those states are particularly sensitive to crystal field splitting.

8.4 Discussion

To summarize the main experimental findings, first we observe strong interlayer exciton absorption between the main A- and B-exciton transitions for CVD-grown (Fig. 8.2 (b)) and artificially stacked (Fig. 8.3 (d) and 8.4) *2H* bilayers, whereas this interlayer transition is absent for *3R* stacking as hole tunnelling is symmetry forbidden and only intralayer exciton transitions are observed. A second striking observation is that stacking of the layers also affects the energy difference between A- and B-exciton transitions. This is demonstrated in Fig. 8.5 (d), where the A-B exciton energy difference is compared between as-grown and assembled *2H* and *3R* bilayers. It is apparent that *2H* bilayers exhibit a significantly larger energy difference between the A- and B-exciton states, compared to *3R* bilayers.

Our next target is to experimentally extract the interlayer hopping term, $t_\perp$ based on a k . p model of bilayers in the vicinity of K- points [211, 67, 292] and compared it to post-DFT estimates. As indicated in Fig. 8.5 (c), for *3R* stacking the measured A- to B-exciton splitting S_{3R} is roughly given by the spin-orbit splitting as $S_{3R} = \Delta_{SO}$. For *2H*-stacking the A-B splitting in the valence band depends on the coupling energy $t_\perp$ as $S_{2H} = \sqrt{\Delta_{SO}^2 + 4t_\perp^2}$ and hence

$$t_\perp = \sqrt{\frac{S_{2H}^2 - \Delta_{SO}^2}{4}}, \tag{8.1}$$

where S_{2H} is the measured A-B exciton splitting of the as-grown *2H* MoS_2 bilayer and as a value for Δ_{SO} we take the measured A-B separation in the *3R* sample. For $S_{2H} = 183$ meV and $\Delta_{SO} = 155$ meV, we obtain $t_\perp \approx 49$ meV. This value can be compared to the ones extracted from our standard DFT calculations as previously done [211], or from more advanced GW and GW+BSE calculations. Table 8.1 summarizes calculated valence band splittings and A-B energy differences for monolayer, *2H* and *3R* stacking as well as the corresponding coupling strength, directly extracted from the VB splitting as in [292] or Eq. 8.1. The agreement between theoretical, including previous rough estimates [211], and experimental results is good as we reproduce the larger A-B splitting for the *2H* bilayers as compared to *3R*. Although we measure exciton transitions and not directly the VB splitting in the *2H* bilayer, the agreement between theory and experiment strongly supports our interpretation for the reason behind the different A-B exciton splitting. It should be noted that for *3R* bilayers, $t_\perp = 0$ since interlayer hopping is not allowed in this case. This short numerical analysis highlights that the efficiency of this interlayer coupling will depend on the ratio of $t_\perp$ versus the spin-orbit VB splitting [66], which is much smaller in MoS_2 ($\Delta_{SO} \approx 150$ meV) as compared to WSe_2 ($\Delta_{SO} \approx 430$ meV). This leads in principle to tunable interlayer coupling for MoS_2 [61] and so called spin-layer-locking for WSe_2 bilayers [298].

Larger A-B exciton splitting in bulk MoS_2 for *2H* compared to *3R* stacking has also been demonstrated in early experiments using optical transmission spectroscopy [299, 300] and more recently in angle resolved electron emission spectroscopy [301]. The A-B exciton splitting in MoS_2 bilayers has been previously studied by several groups [166, 302, 303]. In these reports, the spin-orbit coupling and interlayer coupling have been discussed, but neither interlayer exciton formation nor an experimental analysis of the coupling term $t_\perp$. In our study the direct comparison in the same set-up on the same substrate of *2H* and *3R* bilayers with good optical quality due to encapsulation allows to determine the difference in A-B exciton energies precisely, which we ascribe to interlayer coupling, as supported by our quasi-particle GW and absorption spectrum including excitonic effects calculations. From an experimental point of view, our results suggest two practical test criteria for interlayer coupling following artificial stacking : the strong interlayer exciton absorption and the clear difference in A-B exciton transition energies. The physics discussed here for *2H* and *3R* bilayers is also relevant for samples with a twist angle slightly different from 0° or 180° as reconstruction/self-rotation results in artificial stacks typically in large areas of *2H* and *3R* stacking, which will show the optical properties of the samples investigated here. Interestingly interlayer exciton absorption has been reported in bulk *2H*-$MoTe_2$ and bulk *2H*-$MoSe_2$ [68, 114]. Please note that the interlayer coupling for CVD-grown MoS_2 bilayers is also studied in a very recent report [304].

8.5 Conclusions

In this chapter we have discussed the fabrication methods for *2H* and *3R* MoS_2 bilayers from CVD as-grown homobilayers and artificially assembled bilayers from monolayers. The stacking order can be identified by SHG spectroscopy as only *3R* stacked bilayers show SHG signal, no SHG signal can be obtained from *2H* stacked bilayers because of restored inversion symmetry. We have demonstrated experimentally and theoretically the interlayer coupling of the valence states in as-grown MoS_2 homobilayer sample and manually stacked bilayers. The hole delocalization is forbidden in *3R* and is only allowed in *2H* stacking. There are two main difference in *3R* and *2H* bilayers : First *2H* bilayer exhibits a larger A-B separation as compared to *3R* stacking. Another clear difference is that the interlayer exciton transition is absent in *3R* bilayers as hole tunneling is forbidden due to symmetry. In addition, we have extracted experimentally the interlayer coupling energy of about 49 meV which is very close to the value extracted from GW+BSE calculations.

Chapter 9

Conclusions and prospective

In this chapter I will summarize the main results presented in this PhD thesis manuscript and introduce some ideas for future research directions for fundamental optical properties of 2D materials and future applications.

In the beginning of this PhD thesis we have presented experimental observations of the exciton-phonon interaction in $MoSe_2$ monolayers encapsulated in hexagonal boron nitride (hBN), which has an important impact on both optical absorption and emission processes. The exciton transition linewidth down to 1 meV at low temperatures makes it possible to observe high-energy tails in absorption and emission extending over several meV, not masked by inhomogeneous broadening. Our combined experimental and theoretical study sheds light on the strong impact of the exciton-acoustic phonon interaction in TMD monolayers on exciton formation and recombination. We interpret the observed strong absorption above the exciton resonance in terms of phonon-assisted exciton formation. Asymmetric lineshapes with high-energy tails both in emission and absorption are due to deformation potential exciton-acoustic phonon coupling and can be fitted by our simplified analytical theory. Our developed analysis shows that exciton-phonon interaction is quite strong in TMD MLs as compared with conventional GaAs-based quantum wells. In 2D crystals, the excitons interact with phonons that have a 2D density of states. In contrast, in GaAs quantum wells, the 2D exciton will interact with 3D phonons in the crystal. The strength of the exciton-phonon interaction in GaAs quantum wells is smaller than in $MoSe_2$ despite higher values of deformation potential. Qualitatively, the enhanced exciton-phonon interaction in atom-thin crystals is due to the fact that for small wavevectors, the phonon density of states is larger for 2D phonons than for 3D phonons.

In Chapter 5, I have investigated new optical transitions at the K-point of homobilayer and trilayer MoS_2 in absorption. These transitions correspond to interlayer excitons that are mixed with intralayer B-excitons due to hole delocalization over two individual layers that results strong oscillator strength. The optical signatures of interlayer excitons are visible up to room temperature in optical absorption measurements on both bilayer and trilayer MoS_2. The microscopic origin of these transitions is uncovered in post-DFT calculations performed by Iann Gerber (LPCNO). An experimental way to identify intralayer and interlayer transitions and tuning transition energy of interlayer exciton in magnetic field is discussed in Chapter 6. There are two criteria which identify intra/interlayer exciton character by performing magneto-optics : (i) The interlayer excitions transition shows larger Zeeman splitting compared to intralayer excitons and (ii) The Landé g-factors of interlayer and intralayer excitons are opposite in sign. We further demonstrated interlayer excitons character in externally applied electric fields. The transition energy of interlayer excitons with the large in-built electric dipole in bilayer MoS_2 can be tuned to A:1s and B:1s resonances. These energy shifts are due to the quantum confined Stark effect. The interlayer excitons split into two transitions and both shifts in energy under external electric fields. We have observed strong coupling of the blue-shifted interlayer exciton with the intralayer B-exciton. In contrast, the interaction of the red-shifted interlayer exciton with the intralayer A-exciton shows only a weak coupling. From our experimental observation we conclude that the interlayer exciton has a strong B-exciton component in its wave function but a much smaller A-exciton component. Our observations are supported by beyond-standard density functional theory calculations including excitonic effects. We expect that at even higher applied electric fields than those in these experiments, the interlayer exciton will lie lower in energy than the A-exciton and will recover its absorption strength once it is sufficiently red-detuned from the A-exciton. This will represent an advantageous scenario for applications : the ground-state exciton is long-lived and possesses both a large in-built electric dipole moment and a strong absorption. For optoelectronics, the highly tunable excitons with an in-built dipole found here in MoS_2 bilayers are promising for exploring coupling to optical cavity modes, where excitons and photons can couple to form polaritons.

In MoS_2 trilayers, we uncover different interlayer excitons with very distinct Stark shifts : Similar to the bilayer, one interlayer exciton splits into two resonances and shifts with electric field, indicating a large dipole. In contrast, a second interlayer exciton at lower energy shows a negligible Stark shift. According to our calculations, this second exciton shows a spatially symmetric charge distribution with respect to the middle layer and, hence, a negligible in-built dipole. In principle, the interlayer exciton with large oscillator strength and a large static dipole moment in bilayer and trilayer MoS_2 structures offer desirable configurations for coupling quantum tunneling with cavity photons, previously reported at cryogenic temperatures in III-V semiconductor nano-structures.

Thanks to hBN encapsulation of CVD-grown monolayers we are able to largely suppress the detrimental impact of disorder in the ML environments. This leads to improved optical quality as a result the PL emission linewidth for our CVD grown samples is decreased by one order of magnitude. This allows detailed optical spectroscopy and valley polarization studies described in Chapter 7. Our result shows that the optical quality not only depends on the intrinsic crystal quality but in addition is impacted by the local environment which the monolayer interacts with. We show that CVD-grown crystals can be used for investing excitonic physics for fundamental research and hold great promise for wafer-scale applications. For future device applications we can further improve the optical quality of CVD-grown crystals by lowering its defect density and also choosing a suitable substrate. Direct growth not on SiO_2 but directly on hBN is another way to achieve high optical quality.

The improvement in our transfer approach for the CVD-grown layers at LPCNO allows us to use high quality CVD layers as building blocks for van der Waals structures with controlled interlayer coupling which are discussed in Chapter 8. The interlayer coupling for hole states in the valence bands is governed by symmetry and also the spin-orbit splitting. DFT band structure and absorption calculations show hole delocalization is forbidden due to symmetry in *3R* stacking and is allowed in *2H*. Therefore *2H* MoS_2 bilayers show favourable conditions to observe interlayer excitons in absorption, as hole hybridization is symmetry allowed and the valence band spin-orbit splitting is comparatively small compared to WSe_2 for example. By manually stacking the *2H* and *3R* MoS_2 bilayers using CVD-grown monolayers we experimentally investigate the interlayer coupling of the valence states. We experimentally demonstrated that hole delocalization is forbidden in *3R* and is only allowed in *2H* stacking. Our results are supported by GW+BSE calculations. The interlayer coupling in assembled bilayer clearly reveals clean interface and high structural integrity which are important requirements for device assembly.

The progress in high optical quality of CVD-grown monolayers using encapsulation in hBN combined with our stacking approach will be useful for study of van der Waals heterostructure for examples layer dependent studies or exploring twisted homo- and heterobilayers and multilayer structures.

The large number of layered materials which are stable in ambient conditions opens up many possibilities of combining mono- and few-layer crystals. The number of the resulting combinations and the possible functionalities are of great interest for research. In this framework very interesting studies are currently being done by combining semiconducting TMDs with ferromagnetic layered materials such as CrI_3 and $CrBr_3$. We can use for example CVD-grown TMD layer on magnetic layered materials. The presence of a local magnetic field could lift the valley degeneracy of a TMDs monolayer without the need of an external magnetic field. The idea is to induce a valley Zeeman splitting in TMD monolayer already at zero applied magnetic field due to proximity effects. Another pathway of modifying the light-matter interaction in TMD monolayers for example is to couple the exciton resonance to optical nanoresonators. In a collaboration with the group of CEMES, I am working on enhancing light emission of exciton resonances by coupling WSe_2 and $MoSe_2$ monolayers to nanoresonators where the TMD monolayer active region is simply exfoliated on the top of the Si-based nanoresonator.

In the very end I would like to present the list of published papers to which I gave my contribution during my three year PhD. Most of them are extensively covered in writing this manuscript while some are on different topics (such as GaAs quantum dots, TMD monolayers on nanoantennas) are left out.

Here is the list :

- J. Poumirol, I. Paradisanos, **S. Shree**, G. Agez, X. Marie, C. Robert, N. Mallet, P. R. Wiecha, G. Larrieu, V. Larrey, F. Fournel, K. Watanabe, T. Taniguchi, Au. Cuche, V. Paillard, B. Urbaszek, "Unveiling the optical emission channels of monolayer semiconductors coupled to silicon nanoantennas ", ACS Photonics (2020).

- **S. Shree**, I. Paradisanos, X. Marie, C. Robert, and B. Urbaszek, "Guide to optical spectroscopy of layered semiconductors",
  An invited article Nature Review Physics (2020).

- N. Leisgang*, **S. Shree***, I. Paradisanos*, L. Sponfeldner*, C. Robert, D. Lagarde, A. Balocchi, K. Watanabe, T. Taniguchi, X. Marie, R. J. Warburton, I. C. Gerber, and B. Urbaszek, "Giant Stark splitting of an exciton in bilayer MoS_2",
  Nature Nanotechnology, 63, 1375 (2020), ***joint first author**.

- I. Paradisanos*, **S. Shree***, A. George, N. Leisgang, C. Robert, K. Watanabe, T. Taniguchi, R. J. Warburton, A. Turchanin, X. Marie, I. C. Gerber and B. Urbaszek, "Controlling interlayer excitons in MoS_2 layers grown by chemical vapor deposition",
  Nature Communications, 11, 2391 (2020), ***joint first author**.

- **S. Shree**, A. George, T. Lehnert, C. Neumann, M. Benelajla, C. Robert, X. Marie, K. Watanabe,T. Taniguchi, U. Kaiser, B. Urbaszek and A. Turchanin, "High optical quality of MoS_2 monolayers grown by chemical vapor deposition",
  2D Materials, 7, 015011 (2019).

- M. Goryca, J.Li, A.V. Stier, T. Taniguchi, K.Watanabe, E. Courtade, **S. Shree**, C. Robert, B. Urbaszek, X. Marie and S.A. Crooker, "Revealing exciton masses and dielectric properties of monolayer semiconductors with high magnetic fields",
  Nature Communications, 10, 4172 (2019).

- I. C. Gerber, E. Courtade, **S. Shree**, C. Robert, T. Taniguchi, K. Watanabe, A. Balocchi, P. Renucci, D. Lagarde, X. Marie, and B. Urbaszek, "Interlayer excitons in bilayer MoS_2 with strong oscillator strength up to room temperature",
  Physical Review B, 99, 035443 (2019).

- **S. Shree**, M. Semina, C. Robert, B Han, T. Amand, A. Balocchiet, M. Manca, E. Courtade, X. Marie, T. Taniguchi, K.Watanabe, M. M. Glazov and B. Urbaszek, “Observation of exciton-phonon coupling in $MoSe_2$ monolayers”,
  Physical Review B, 98, 035302 (2018).

- B. Han, C. Robert, E. Courtade, M. Manca, **S. Shree**, T. Amand, P. Renucci, T. Taniguchi, K. Watanabe, X. Marie, L. E. Golub, M. M. Glazov, and B. Urbaszek, “Exciton states in monolayer $MoSe_2$ and $MoTe_2$ probed by upconversion spectroscopy",
Physical Review X, 8, 031073 (2018).

- M. Manca, G.Wang, T. Kuroda, **S. Shree**, A. Balocchi, P. Renucci, X. Marie, M. V. Durnev, M. M. Glazov, K. Sakoda, T. Mano, T. Amand, and B. Urbaszek, “Electrically tunable dynamic nuclear spin polarization in GaAs quantum dots at zero magnetic field",
Applied Physics. Letter, 112, 142103 (2018).

Symposium, Conference, and Workshop Participation

1. **Oral presentation** on " Interlayer excitons in bilayer MoS_2", **2020 MRS Fall Meeting & Exhibit, Boston, USA**, 27 November - 04 December 2020.

2. **Oral presentation** on "Controlling interlayer exciton in MoS_2 layers", **Graphene 2020, Grenoble, France**, 19 - 23 October 2020.

3. **Oral presentation** on "High optical quality of MoS_2 monolayers grown by chemical vapor deposition", **2019 MRS Fall Meeting & Exhibit, Boston, USA**, 1 - 6 December 2019.

4. **Oral presentation** on "Exciton - phonon interaction and upconversion spectroscopy in monolayer $MoSe_2$”, **2018 MRS Fall Meeting & Exhibit Boston, USA**, 25 - 30 November, 2018.

In addition several oral and poster presentations within the ***European union 4PHOTON network*** *and outside the network.*

Summary in French

Chapter 1: Introduction aux dichalcogénures de métaux de transition

L'étude des monocouches atomiques remonte en fait à plusieurs décennies, mais c'est seulement avec l'isolement d'une seule couche de graphite que les recherches sur les matériaux lamellaires ont évolué dans un domaine très actif. Parmi les matériaux actuellement étudiés récemment environ 1800 matériaux ont été prédits pour être exfoliables, stables sous forme de monocouche. Ces matériaux sont disponibles avec diverses fonctionnalités comme le montre la Fig. 9.1 avec une large plage d'énergie de la bande interdite qui offre des possibilités d'utilisation de ces matériaux pour une large gamme d'applications. Leur finesse ultime donne accès à de nouveaux degrés de liberté du système électronique comme l'indice de vallée ou les interactions entre quasi-particules comme les excitons (paires électron-trou liées à Coulomb). Des fonctionnalités supplémentaires émergent lorsque ces matériaux sont empilés dans des hétérostructures van der Waals.

Les TMD massifs et à quelques couches présentent une bande interdite indirecte cependant, les monocouches TMD montrent une bande interdite directe donnant lieu à une forte émission et entraînant également une grande absorption accordable comme le montre la Fig. 9.3 (a). Les propriétés optiques des TMD sont dominées par des excitons, c'est-à-dire les paires électron-trou. Ceci donne lieu à des maxima d'absorption bien définis en énergies en dessous de la bande interdite des porteurs libres. Les monocouches de TMD consistent d'une couche d'atomes de métal de transition coordonnée de manière hexagonale prise en sandwich entre les couches de chalcogène supérieure et inférieure, conduisant à une structure cristalline prismatique trigonale, voir Fig. 9.2. La symétrie du cristal est donnée par l'ordre d'empilement, qui joue un rôle important dans l'interaction lumière-matière, conduisant à une réponse optique qui dépend du nombre de couches et de l'angle de torsion (twist angle) entre les couches.

Les excitons dans les monocouches TMD ont des énergies de liaison remarquablement élevées de l'ordre de plusieurs centaines de meV. Cela est dû aux grandes masses effectives d'électrons et de trous aux points K de la zone de Brillouin, à l'écrantage diélectrique réduit et au confinement idéal 2D des porteurs dans le plan monocouche. Par conséquent, dans les monocouches TMD, les résonances excitoniques dominent au-delà de la température ambiante. Un fort clivage spin-orbite d'environ 200 meV (pour Mo) et 400 meV (pour W) apparaît dans les bandes de valence au point K. En conséquence, deux transitions optiques interbandes distinctes sont observées en absorption, nommées A (transition de la bande de valence

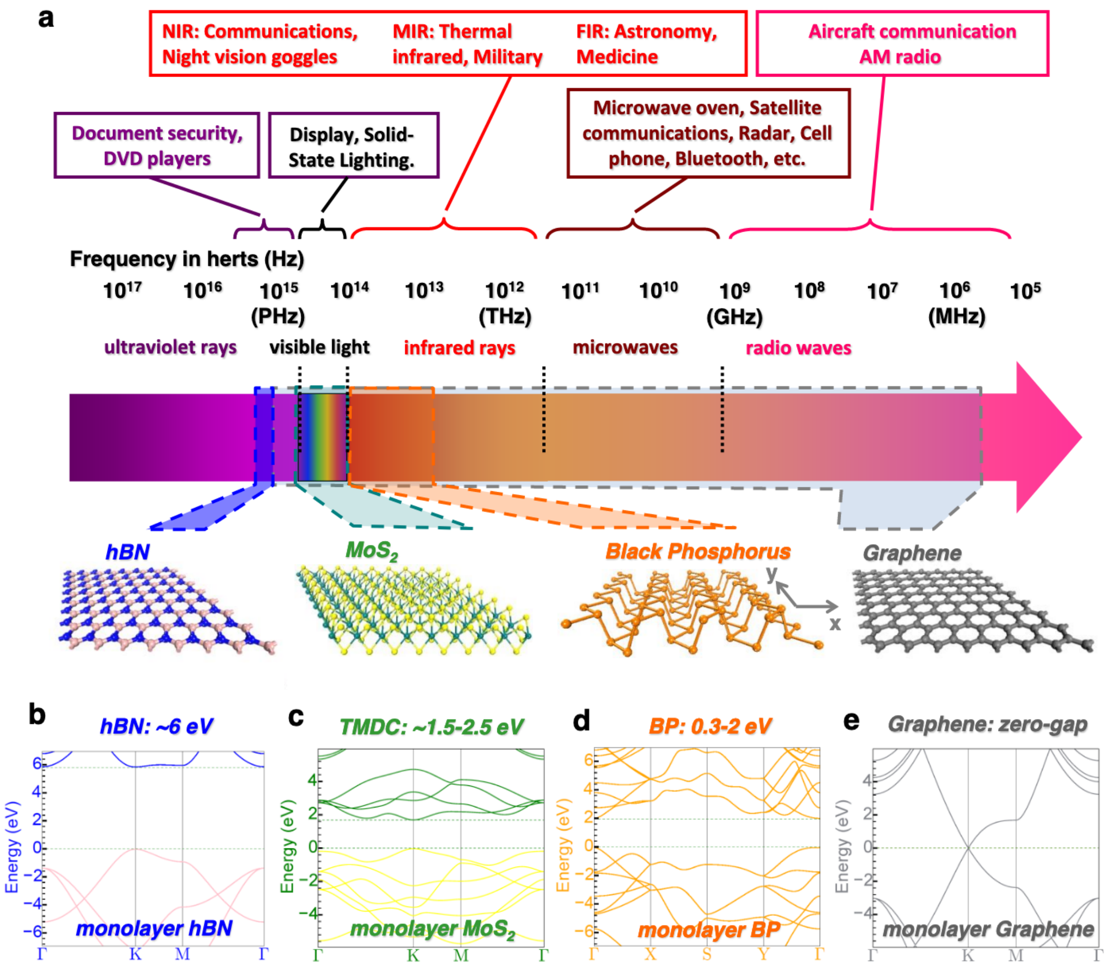

Figure 9.1: (a) Gamme de longueurs d'onde et bande interdite d'énergie textbf (b) - (e) couverte par différents matériaux 2D. La figure est reproduite à partir de [3].

supérieure) et B (transition de la bande de valence inférieure).

Les transitions optiques qui sont permises par le dipôle, l'impulsion et le spin sont appelées excitons brillants. Dans les matériaux lamellaires, des excitons avec différentes orientations spatiales du dipôle optique, soit dans le plan soit hors du plan de couche, participent aux transitions optiques. Ces deux types d'excitons peuvent être sondés optiquement en raison de règles de sélection optique sélectives de vallée. Les transitions interbandes dans les matériaux monocouches tels que MoS_2 ou WSe_2 sont régies par des règles de sélection chirale car les transitions optiques dans la vallée K^+ (K^-) sont σ^+ (σ^-) polarisé, voir Fig. 9.3 (b) - (c). Par conséquent, un matériau TMD est un système idéal pour étudier le degré de liberté de la vallée d'électrons dans le cadre de ce que l'on appelle la valleytronics.

D'une part dans les hétérobilayers TMD, des excitons intercouches peuvent se former en raison de l'alignement de bande de type II (ou décalé) avec les électrons photoexcités et trous résidants dans différentes couches comme indiqué sur la Fig. 9.4. Ces excitons sont appelés indirects dans l'espace réel. D'autre part, dans les homobilayers, l'exciton intercouche se forme lorsqu'un trou est délocalisé sur les deux couches alors qu'un électron est dans une couche. Dans ce cas, l'exciton

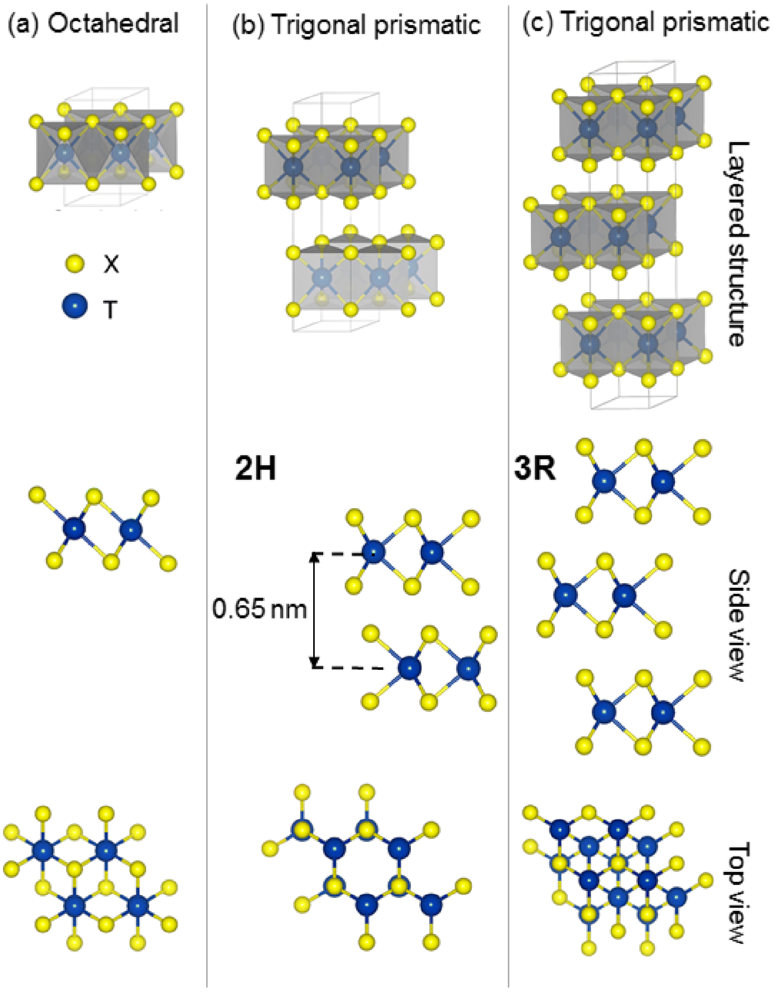

Figure 9.2: Représentation structurelle des différentes phases du polytype TMD ((**a**) octaédrique, (**b**) - (**c**) trigonal prismatique) et leur coordination des atomes métalliques correspondants. Des séquences d'empilage dissemblables de couches simples prismatiques trigonales avec un angle de rotation différent des couches correspondant les unes aux autres peuvent donner un empilement différent: symétrie hexagonale (*2H*) et symétrie rhomboédrique (*3R*). Le schema est tiré de [3]

intercouche a une contribution de l'exciton intralayer (également appelé exciton intercouche mixte). Ces excitons intercouches possèdent une forte force d'oscillateur et peuvent être sondés jusqu'à la température ambiante en absorption, pas en photoluminescence, car ce n'est pas la configuration d'exciton la plus basse énergie.

Chapter 2: Techniques expérimentales

Exfoliation

Les méthodes répandues pour fabriquer des échantillons 2D sont l'exfoliation mécanique à partir de cristaux massifs et la croissance directe par dépôt chimique en phase vapeur (CVD) d'échantillons monocouches sur des substrats tels que SiO_2 / Si.

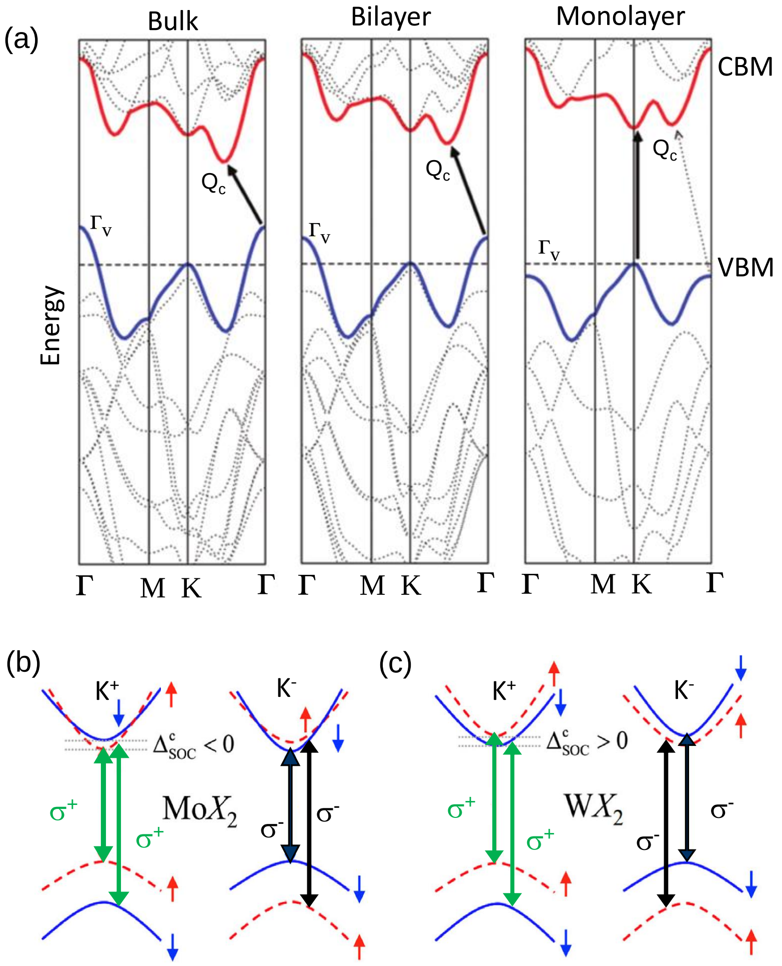

Figure 9.3: **(a)** Structure de bande calculée de MoS$_2$ massif, bicouche et monocouche. Les trois panneaux montrent la transition du semi-conducteur à bande interdite indirecte au semi-conducteur direct. La figure est tirée de la référence [6]. **(b) - (c)** Le schéma montre que les bandes de conduction sont opposées dans les monocouches MoX$_2$ et WX$_2$. La flèche représente la transition A-exciton autorisée en terme de conservation de spin en respectant les règles de sélection optique.

Les forces de van der Waals intercouches sont considérablement plus faibles que la liaison covalente intra-couche, ce qui rend un très grand nombre de cristaux exfoliables. Les cristaux TMD exfoliés à partir d'un crystal de haute qualité présentent une densité de défauts comparativement faible jusqu'à moins de 10^{11} cm^{-2}) et une meilleure réponse optique par rapport aux cristaux élaborés par CVD [84]. L'exfoliation est la méthode la plus utilisée en raison de la haute qualité des échantillons, de la simplicité de la manipulation et de la rentabilité. Cependant, il existe plusieurs limitations qui empêchent l'exfoliation d'être viable au-delà des applications en recherche: (a) l'emplacement d'une seule monocouche sur le tampon / substrat est aléatoire, (b) la recherche d'une monocouche parmi des flocons d'épaisseur variable prend du temps (c) les monocouches sont relativement petites avec une dimension latérale moyenne de quelques dizaines de micromètres, et (d) le rendement pour trouver une monocouche par unité de surface est très faible.

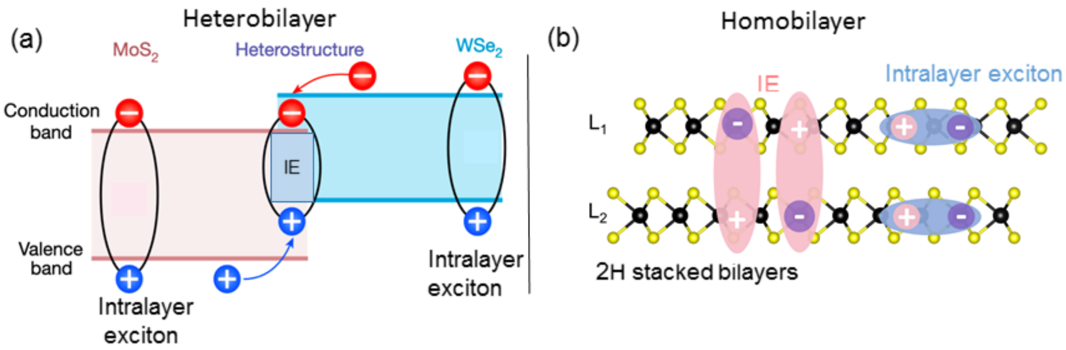

Figure 9.4: **(a)** Schéma de l'alignement des bandes de type II dans l'hétérostructure WSe_2 - MoS_2 avec des excitons intralayer (A: 1s) et intercouche (IE). Les zones rouge et bleu représentent les bandes correspondantes dans les deux matériaux individuels et l'hétérobilayer. Les trous et les électrons sont représentés respectivement par des symboles positifs et négatifs. La figure est tirée de [53]. **(b)** Formation d'excitons inter-couches pendant qu'un trou est délocalisé sur les deux couches représentées en rouge et un exciton intra-couche peut être créé lorsque l'électron et le trou sont situés dans une couche.

Comme alternative à l'exfoliation, CVD est simple, rentable et permet une croissance directe de matériau monocouche sur une grande surface [83, 259]. Détacher des monocouches élaborés par CVD du substrat de croissance pour fabriquer des hétérostructures est possible en utilisant, par exemple, un processus assistée par vapeur d'eau [97, 284]. Pour de nombreuses études de spectroscopie optique d'échantillons élaborés par CVD et également d'échantillons exfoliés, la qualité intrinsèque des monocouches n'était pas le facteur limitant de la qualité optique (c'est-à-dire l'émission de défauts et un large élargissement inhomogène ont été observés), mais l'impact néfaste de l'environnement diélectrique local comme le substrat. Cela a été démontré en comparant des couches de TMD directement élaborés ou exfoliées sur SiO_2 avec des couches de TMD prises en sandwich entre des couches épaisses (jusqu'à plusieurs dizaines de nm) de hBN supérieur et inférieur. [51, 79, 80]. La réponse optique est encore améliorée en sélectionnant une épaisseur optimisée de hBN pour l'hétérostructure de van der waals [81, 82].

Des couches individuelles de cristaux massif de haute qualité peuvent être assemblées dans l'hétérostructure van der Waals en utilisant l'estampage à sec déterministe [72] ou le prélèvement direct. Cela permet un transfert contrôlé des couches à des emplacements précis sur un substrat.

Chapter 3: Techniques de spectroscopie optique

Dans ce chapitre, nous donnons une introduction à la spectroscopie optique pour les matériaux lamellaires en tant qu'outil puissant et non invasif pour accéder aux détails de la structure de bande électronique et de la qualité du cristal. Les applications potentielles en photonique et en optoélectronique sont basées sur notre compréhension de l'interaction lumière-matière à l'échelle d'une monocouche atomique. Les TMD atomiquement minces, tels que MoS_2 et WSe_2, sont des systèmes modèles pour les semi-conducteurs en couches avec une bande interdite dans la région visible du spectre optique. Ils peuvent être assemblés pour former des hétérostructures et combiner les propriétés uniques des monocouches constituantes. Nous décrivons les principes de fonctionnement de la spectroscopie de micro-photoluminescence et des expériences d'absorption optique. Nous discutons de l'origine physique des principales caractéristiques d'absorption et d'émission dans les spectres optiques et comment elles peuvent être accordées. Nous expliquons les aspects clés des configurations pratiques pour effectuer des expériences dans différentes conditions telles que des températures variables ou dans des champs magnétiques appliqués et comment des paramètres tels que la taille du faisceau de détection et la longueur d'onde du laser d'excitation impactent les spectres optiques, voir Fig. 9.5 . Nous décrivons l'influence importante de l'environnement de l'échantillon direct, tels que les substrats et les couches d'encapsulation, sur les mécanismes d'émission et d'absorption illustrés dans la Fig. 9.5. Un aperçu des techniques optiques qui sondent le couplage entre les couches et analysent la dynamique de polarisation des porteurs pour la spintronique et la valléetronique est fourni. Le travail correspondant à ce chapitre est va apparaitre dans un article de revue [98] que j'ai rédigé pendant ma thèse.

Chapter 4: Observation du couplage exciton-phonon dans des monocouches $MoSe_2$

Dans ce chapitre, nous étudions expérimentalement et théoriquement dans les monocouches $MoSe_2$ encapsulées dans hBN l'interaction exciton-phonon, qui a un impact important sur les processus d'absorption optique et d'émission. La largeur de la raie de transition d'exciton jusqu'à 1 meV à basses températures permet d'observer des queues de haute énergie en absorption et en émission s'étendant sur plusieurs meV, non masquées par un élargissement inhomogène. Pour adapter et interpréter nos spectres, nos collaborateurs Marina Semina et Mikhail Glazov (Ioffe Institute, Saint-Pétersbourg, Russie) ont développé une théorie analytique de l'interaction exciton-phonon tenant compte du potentiel de déformation induit par les phonons acoustiques longitudinaux, qui joue un rôle important dans la formation des excitons. Leur théorie permet d'ajuster les spectres d'absorption et d'émission que j'ai mesurés et d'estimer le potentiel de déformation dans les monocouches $MoSe_2$, voir Fig. 9.6. Nous soulignons les raisons pour lesquelles le couplage exciton-phonon est beaucoup plus fort dans les TMD bidimensionnels par rapport aux structures de puits quantiques classiques. L'importance des interactions exciton-phonon est en outre mise en évidence par l'observation d'une multitude de caractéristiques Raman dans les expériences d'excitation de photoluminescence. Les travaux correspondant à ce chapitre sont publiés sous le titre Shree et al. [124].

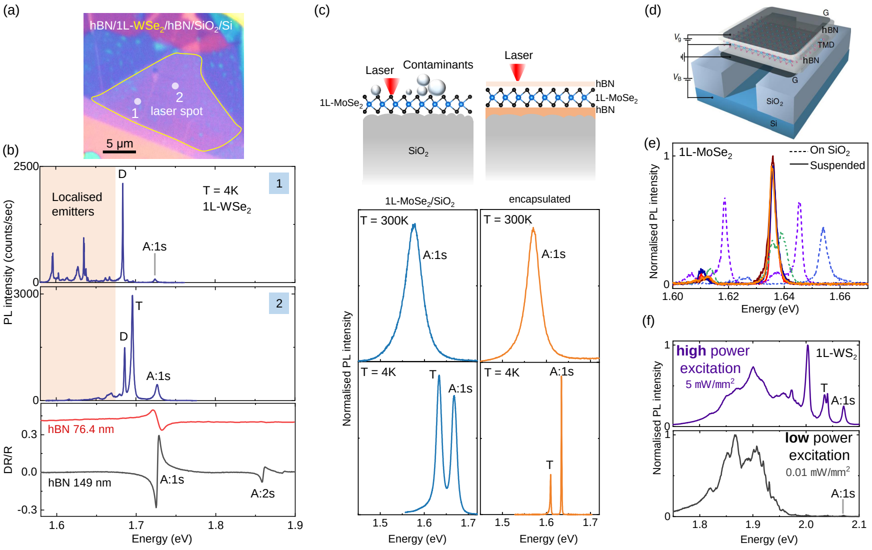

Figure 9.5: **Variation de la réponse de photoluminescence (PL) pour différentes conditions expérimentales**. **(a)** Une micrographie optique d'un échantillon d'hétérostructure van der Waals typique contenant une monocouche WSe $_2$ entre la couche d'encapsulation hBN supérieure et inférieure, l'homogénéité de l'échantillon et les imperfections de l'échantillon (bulles et rides) peuvent être vus. Les régions homogènes et non homogènes de l'échantillon sont marquées 1 et 2 en blanc, respectivement. **(b)** Spectres PL typiques à $T = 4\ K$ enregistrés à deux emplacements différents 1 et 2 de l'échantillon montré dans **(a)**. Les principales transitions d'excitons (excitons neutres (A: 1s), excitons chargés (T) et exciton noir (dark) à spin interdit (D) sont désactivées et des émetteurs localisés apparaissent lorsque PL est enregistré sur les bulles ou sur les rides. Cependant, une forte émission de PL correspondant aux principaux excitons des monocouches WSe$_2$ est enregistré sur la région plate de l'échantillon. **(c)** Esquisse de structures d'échantillon monocouche MoSe$_2$ dans différents environnements diélectriques. Le panneau de gauche est la structure d'échantillon d'une monocouche TMD non encapsulée sur SiO $_2$ et la monocouche TMD encapsulée dans hBN est sur le panneau de droite. Les spectres PL typiques enregistrés à $T = 300\ K$ et $4\ K$ sur l'échantillon encapsulé et non encapsulé. La largeur spectrale diminue considérablement pour l'échantillon encapsulé à $T = 4\ K$ par rapport à l'échantillon non encapsulé. **(d)** couche MoSe$_2$ encapsulée par hBN suspendue au-dessus d'une tranchée [108] et les spectres correspondants sont affichés dans **(e)**. L'énergie d'émission PL reste constante sur les échantillons en suspension à différents endroits sur la monocouche montrant l'homogénéité de l'échantillon [108]. **(f)** WS$_2$ monocouche encapsulée en hBN sur un substrat SiO$_2$ / Si, couche WS$_2$ traitée au plasma pour générer des défauts optiquement actifs. Spectres d'émission PL typiques pour une excitation laser CW (532 nm) à 0,01 μ W et 5 μ W à $T = 4\ K$. L'intensité d'émission PL des excitons principaux est clairement visible à haute densité de puissance, alors que ces caractéristiques ne sont presque pas détectables à faible densité de puissance laser. Les spectres PL à faible densité de puissance laser révèlent que les porteurs peuvent être piégés efficacement par les sites de défauts et se recombiner en émettant des photons à une énergie plus faible. Par conséquent, à faible puissance laser, l'émission de défauts PL est considérablement plus forte que l'émission d'exciton libre.

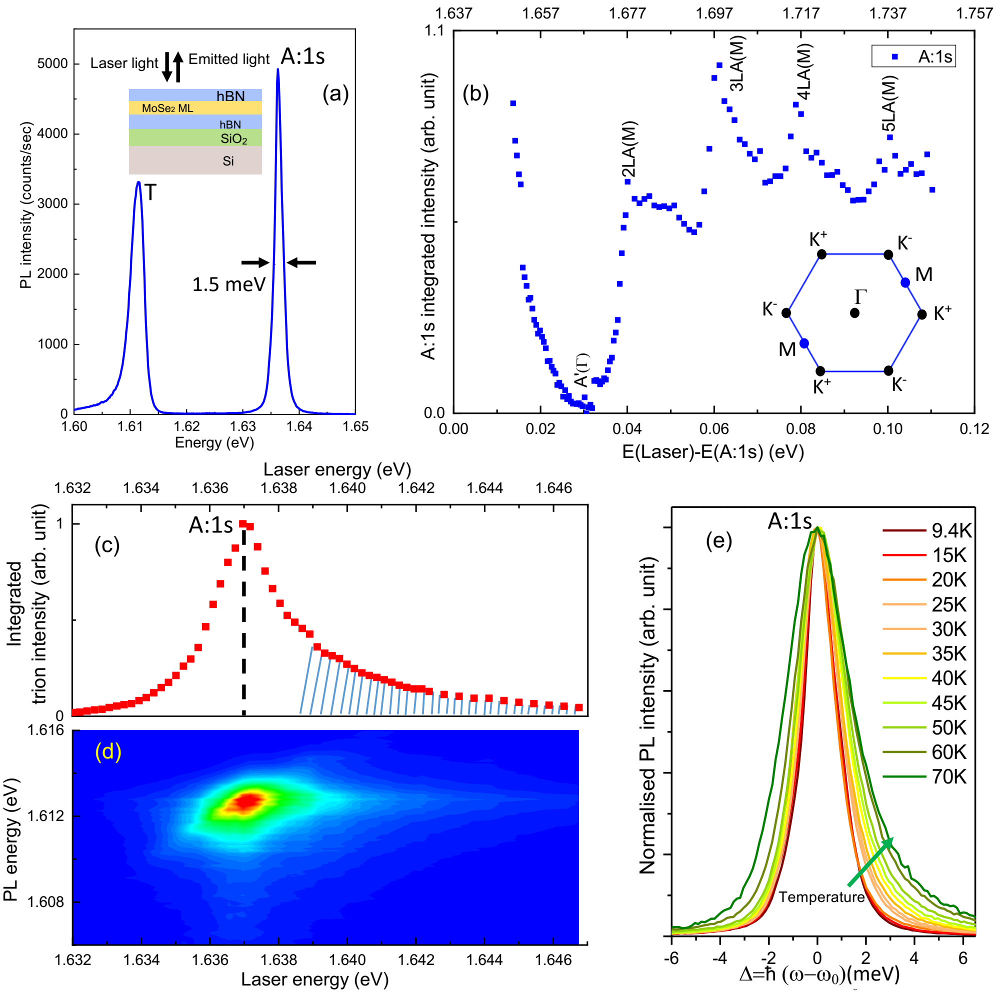

Figure 9.6: **Résultats de la spectroscopie optique. ML MoSe $_2$ encapsulé dans hBN - Exemple 1** **(a)** Spectre d'émission PL typique à $T = 4\ K$. Les pics d'émission à l'énergie 1,613 eV et 1,637 eV sont dus à l'exciton A: 1 chargé (T) et neutre. Encart du panneau **(a)**: Schémas de la structure de l'échantillon: $MoSe_2$ ML encapsulé dans hBN, la couche inférieure de hBN a une épaisseur de (140 ±5 nm) comme déterminé par l'AFM, la couche SiO $_2$ a une épaisseur de 80 nm. **(b)** Expériences PLE: Intensité PL intégrée A: 1s tracée en termes d'énergie excédentaire (axe inférieur), définie comme la différence entre l'énergie laser (axe supérieur) et la résonance A: 1s. La période d'oscillation moyenne correspond au phonon acoustique longitudinal LA (M) du point M. Encart du panneau **(b)**: Schémas de la zone de Brillouin 2D avec points K, M et Γ. **(c)** Intensité trion PL intégrée en fonction du laser à balayage d'énergie d'excitation à travers la résonance A: 1s. **(d)** Courbe de contour du laser à balayage d'intensité trion PL à travers une résonance A: 1s à $T = 4\ K$. **(e)** Emission PL dépendante de la température à la résonance A: 1s. Pour une meilleure comparaison de la forme d'émission, l'intensité A: 1s PL est normalisée à la valeur maximale et l'énergie décalée pour compenser l'évolution de la température de la bande interdite.

Chapter 5: Excitons intercouches dans des bicouches de MoS_2 avec une forte force d'oscillateur jusqu'à température ambiante

Les paires électron-trou liées par l'interaction de Coulomb, les excitons, régissent les propriétés optiques des dichalcogénures de métaux de transition semi-conducteurs comme MoS_2 et WSe_2. Dans ce chapitre, nous étudions les transitions optiques au point K pour *2H* homobilayer MoS_2 dans les mesures de réflectivité dans des échantillons de haute qualité encapsulés dans du nitrite de bore hexagonal (hBN) et comparons avec les calculs de la théorie fonctionnelle de la densité (DFT) réalisé par Iann Gerber (LPCNO) avec effets excitoniques (GW-BSE). Dans les spectres calculés et mesurés, nous trouvons une forte transition d'exciton intercouche en énergie entre les excitons intra-couches A et B, observable pour $T = 4 - 300\ K$, alors qu'aucune transition de ce type n'est observée pour la monocouche dans la même structure dans cette gamme d'énergie, voir Fig. 9.8. Les excitons intercouches consistent en un électron localisé dans une couche et un état de trou délocalisé sur la bicouche, ce qui se traduit par la combinaison inhabituelle d'une force d'oscillateur élevée et d'un moment dipolaire statique, voir Fig. 9.7. Nous trouvons également des signatures d'excitons intercouches impliquant la deuxième bande de valence la plus élevée (VB) et comparons les calculs d'absorption pour différents empilements bicouches. Pour l'homotrilayer MoS $_2$, nous observons également des excitons intercouches et une division d'énergie entre différents A-excitons intra-couches provenant respectivement des couches moyenne et externe. Le travail décrit dans ce chapitre correspond à la publication [60].

Effet Stark des excitons intercouches en MoS_2 bicouche et tricouche

Dans les monocouches TMD, l'absorption optique est forte, mais l'énergie de transition n'est pas accordable car l'exciton neutre n'a pratiquement pas de dipôle électrique hors plan. En revanche, les transitions d'exciton entre les couches dans les hétérocouches sont largement accordables dans les champs électriques appliqués, mais leur couplage à la lumière est considérablement réduit. Dans ce chapitre, nous montrons l'accord de plus de 120 meV d'excitons intercouches avec une forte force d'oscillateur dans des bicouches MoS_2, comme le montre la figure 9.9. Ces décalages sont dus à l'effet Stark à confinement quantique, ici l'électron est localisé dans l'une des couches mais le trou est délocalisé sur la bicouche. Nous sondons optiquement l'interaction entre les excitons intra et inter-couches car ils sont énergétiquement accordés en résonance, voir Fig. 9.10. Nos observations expérimentales sont étayées par des calculs au-delà de la théorie fonctionnelle de densité DFT par Iann Gerber (LPCNO), y compris les effets excitoniques (GW-BSE). Dans les trilayers MoS_2, nos expériences mettent en évidence deux types d'excitons intercouches avec et sans dipôles électriques intégrés. Les transitions excitoniques hautement accordables, avec une grande force d'oscillateur et des dipôles intégrés, qui conduisent à des interactions exciton-exciton considérables, sont très prometteuses pour l'optique

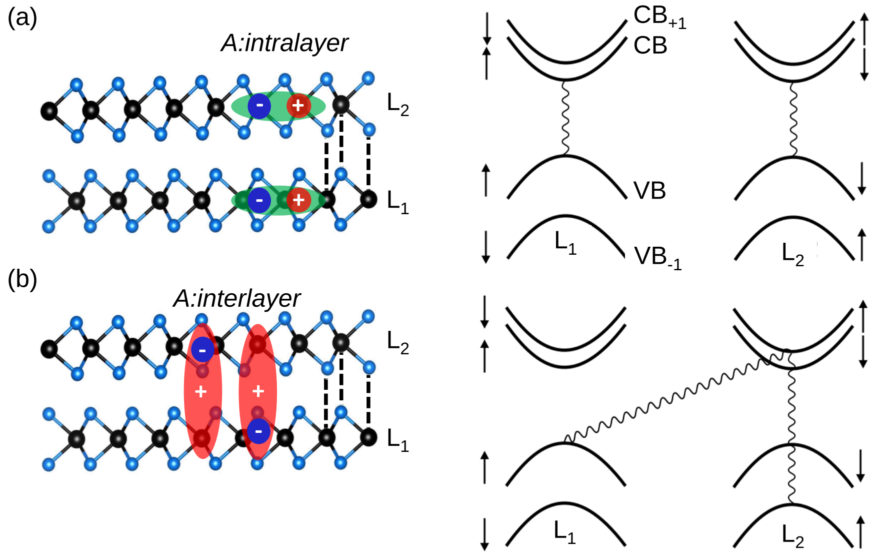

Figure 9.7: **Schéma des excitons intralayer et interlayer dans *2H* MoS_2 homobilayers.** **(a)** Les excitons intra-couche consistent en un électron (rouge) et un trou (bleu) dans la même couche alors que dans **(b)** un électron localisé sur une couche interagit avec un état de trou hybridé pour former un exciton intercouche. Les règles de sélection optique, représentées par des lignes ondulées, pour les transitions entre couches et entre couches dans l'espace k sont également données pour les points K, respectant la conservation du spin. Pour plus de clarté, seule un exciton intercouche (spin up) est représentée, il y a aussi l'état spin down avec la même énergie.

non linéaire avec polaritons (en microcavité). Les résultats décrits dans ce chapitre sont basés sur la publication [106] également grâce à une collaboration fructueuse avec le groupe de Richard Warburton à l'Université de Bâle (Suisse).

Chapter 7: Haute qualité optique des monocouches MoS_2 élaborés par dépôt chimique en phase vapeur

Dans les chapitres précédents, nous avons discuté des transitions excitatrices dans les monocouches $MoSe_2$ et les monocouches et multicouches MoS_2. Toutes les données présentées proviennent d'échantillons qui ont été exfoliés à l'aide de cristaux massifs de haute qualité et encapsulés dans du hBN. Tant la recherche fondamentale que les applications potentielles des couches TMD reposent sur des échantillons de haute qualité. Le dépôt chimique en phase vapeur (CVD) permet de cultiver des TMD sur de grandes surfaces sur des substrats peu coûteux.

Dans ce chapitre, nous montrons que la croissance CVD réalisée dans le groupe de nos collaborateurs Andrey Turchanin et Antony George (FSU Jena, Allemagne) donne des monocouches de MoS_2 de haute qualité optique. Nous déterminons une concentration de défauts de 10^{13} cm $^{-2}$ pour nos échantillons par HRTEM, comparable aux concentrations de défauts pour les ML exfoliées de la masse naturelle

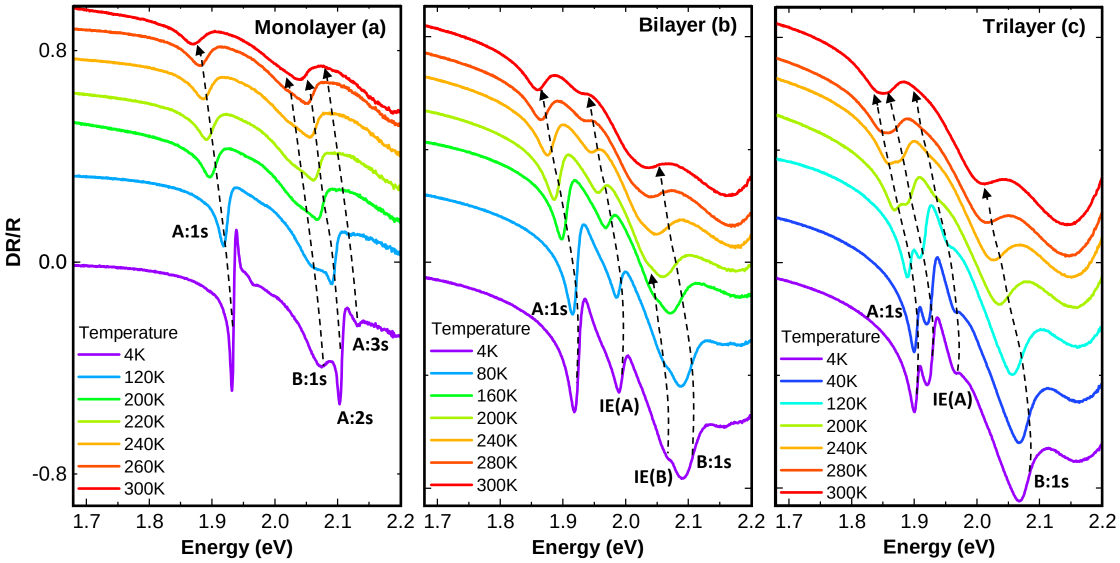

Figure 9.8: **Résultats de la spectroscopie optique:** Spectres de réflectivité différentielle en fonction de la température pour les monocouches **(a)**, les bicouches **(b)** et les tricouches **(c)**. MoS_2 encapsulé dans le hBN. Réflectivité différentielle des trois épaisseurs différentes (ML, BL et TL) à une température d'échantillon de $T = 4\ K$ jusqu'à 300 K. Les spectres ont été décalés pour plus de clarté. Les excitons intralayer A et B (A:1s, A:2s, A:3s et B:1s) et les deux résonances interlayer IE(A) et IE(B) sont étiquetés.

signalées par plusieurs groupes dans la littérature [257, 258, 84]. Pour avoir accès à la qualité optique intrinsèque des ML, j'ai retiré les ML du substrat de croissance SiO_2 et les ai encapsulés dans des flocons de hBN à faible densité de défauts, afin de réduire l'impact nuisible du désordre diélectrique. Nous montrons une largeur de raie de transition optique de 5 meV à basse température $T = 4\ K$ pour les excitons libres en émission et en absorption. Ceci est comparable au meilleur échantillon de ML obtenu par exfoliation mécanique d'un matériau en vrac. La photoluminescence de MoS_2 ML produite par CVD est dominée par les excitons libres et ne présente pas de défauts même à basse température. La qualité optique élevée de l'échantillon est confirmée par l'observation des états d'excitation de la série de Rydberg. Nous générons optiquement la cohérence et la polarisation de la vallée dans nos couches de MoS_2 produites par CVD, ce qui montre la possibilité d'étudier la physique du spin et de la vallée dans les échantillons CVD de grande surface comme le montre. Les résultats présentés dans ce chapitre sont basés sur la publication Shree. et al [80].

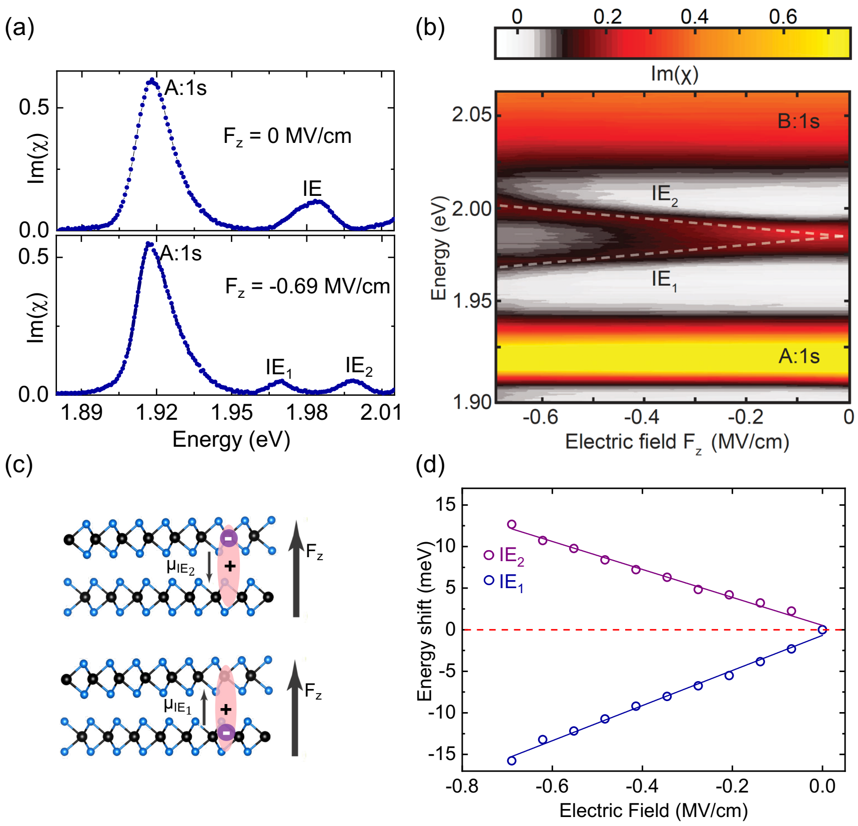

Figure 9.9: Bicouches MoS_2 dans heterostructure de van der Waals (vdWH) sous champ électrique appliqué ($T = 4\ K$). **(a)** Spectres d'absorption typiques enregistrés sans ($F_z = 0$ MV/cm) et avec ($F_z = -0,69$ MV/cm) un champ électrique appliqué, extraits de **(b)**. **(b)**. Carte de couleurs des spectres d'absorption de la bicouche MoS_2 vdWH (dispositif 1). Décalage brutal des excitons intercouches aux petits champs électriques. Les excitons intralayer A et B (A:1s et B:1s) et les deux branches des résonances interlayer A (IE_1 et IE_2) sont étiquetés. **(c)** Schéma des excitons intercalaires dans les homo bicouches de MoS_2. Un électron localisé dans une couche interagit avec un état de trou hybridé pour former un exciton intercouche. La direction du moment dipolaire dépend de la localisation de l'électron, soit dans la couche inférieure (μ_{IE1}), soit dans la couche supérieure (μ_{IE2}). **(d)** Décalage des excitons de la couche A en fonction de F_z, extrait des spectres du panneau **(b)**. Les lignes bleues et violettes continues sont des ajustements linéaires aux points de données expérimentales aux champs électriques faibles/modérés ($F_z = 0$ MV/cm à $F_z = -0,69$ MV/cm).

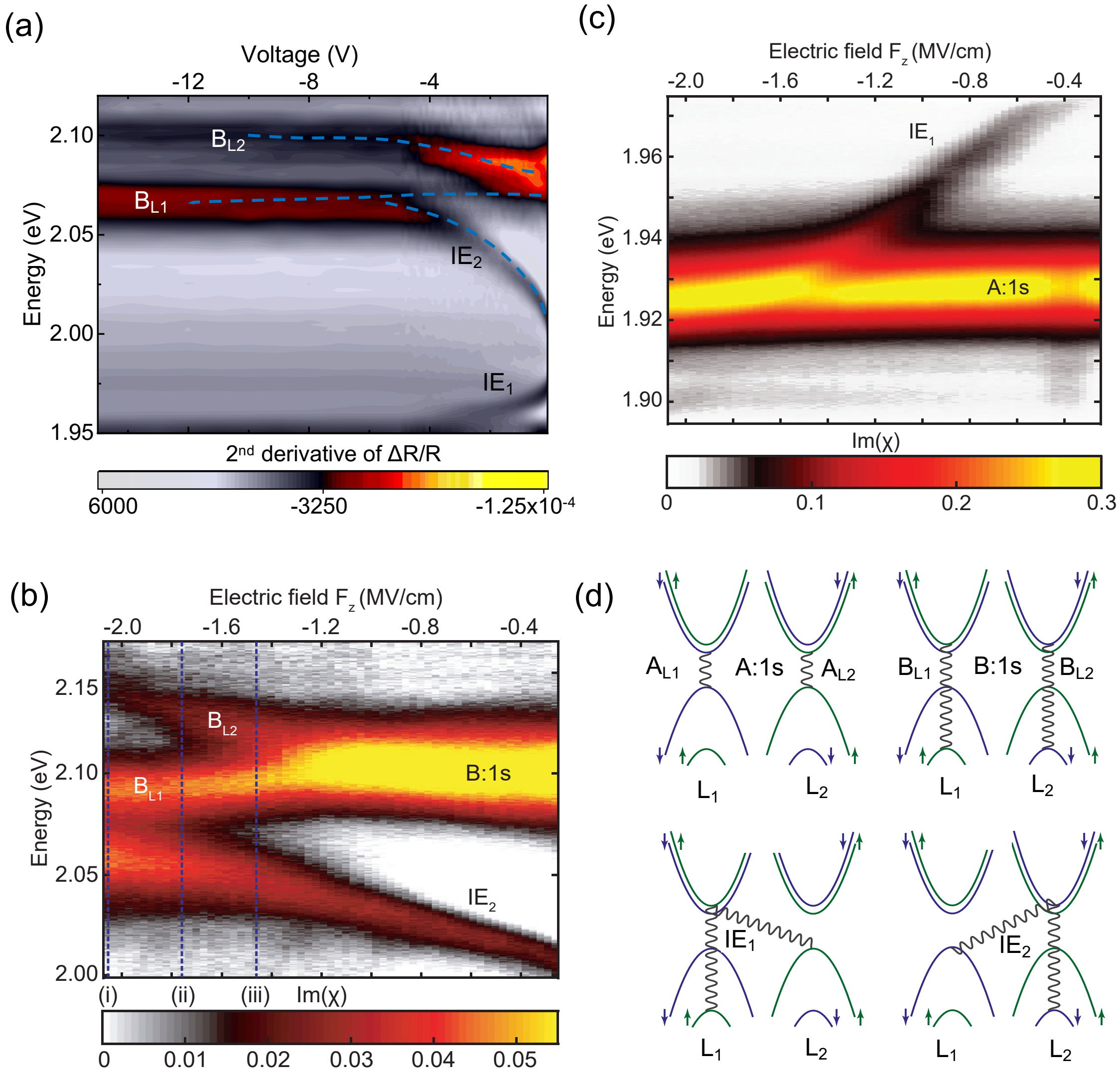

Figure 9.10: **Dépendance en fonction du champs électriques (a)** Carte de couleurs des spectres de la dérivée 2^{nd} du contraste de réflectivité ($\Delta R/R$) centrée autour de l'exciton B de la couche interne pour un seul dispositif à grille 1. **(b)** Carte de couleurs des spectres d'absorption centrés autour de l'exciton B de la couche interne. B_{L1} et B_{L2} sont les excitons de la couche interne résidant dans la couche 1 (L_1) et 2 (L_2), respectivement pour un dispositif à double porte, voir [106] pour une configuration détaillée. Les lignes verticales en pointillés montrent un déplacement de l'énergie de résonance. **(c)** Carte de couleurs des spectres d'absorption (σ^+-polarisation) centrée autour de l'exciton de la couche A, montrant un très petit croisement évité avec IE_1. Les données concernent le même dispositif que dans **(b)**. **(d)** Diagramme de bande et schémas des excitons intralayer et interlayer dans les bicouches de MoS_2 au point K. Les résonances intralayer dans le panneau supérieur A:1s et B:1s correspondent à des excitons où l'électron et le trou résident dans la même couche. Des excitations intra-couche peuvent se former dans chacune des deux couches, désignées par l'indice L_1 (L_2) pour la couche 1 (couche 2). Les excitons inter-couches dans le panneau inférieur IE_1 et IE_2 consistent en un électron confiné dans une couche et un trou délocalisé sur les deux couches. Des lignes ondulées relient les états impliqués pour la formation des différents complexes excitoniques au point K.

Chapter 8: Contrôle des excitons intercouches dans les couches MoS_2 cultivées par dépôt chimique en phase vapeur

La combinaison de monocouches MoS_2 pour former des multicouches permet d'accéder à de nouvelles fonctionnalités. L'assemblage déterministe de structures de van der Waals de grande surface nécessite des indicateurs concrets de la réussite du couplage entre les couches dans les bicouches produites par dépôt chimique en phase vapeur. Dans ce chapitre, j'examine la corrélation entre l'ordre d'empilement et le couplage entre les couches des états de valence dans des échantillons de monocouches de MoS_2 tels qu'ils ont été cultivés et dans des bicouches artificiellement empilées à partir de monocouches, toutes cultivées par dépôt chimique en phase vapeur. Nous démontrons expérimentalement que la délocalisation des trous sur la bicouche n'est autorisée que dans l'empilement *2H* et qu'elle entraîne une forte absorption d'exciton entre les couches ainsi qu'une plus grande séparation de transition d'exciton A-B par rapport aux bicouches *3R*. Au-delà des calculs de TFD effectués par Iann Gerber (LPCNO) incluant les effets excitoniques, les signatures de couplage efficace entre les couches pour l'empilement *2H* sont confirmées en accord avec nos expériences. Les résultats présentés dans ce chapitre sont publiés dans [284].

Bibliography

[1] Feynman, R. There's plenty of room at the bottom. In *Feynman and computation*, 63–76 (CRC Press, 2018).

[2] Dong, Z. *et al.* Raman characterization on two-dimensional materials-based thermoelectricity. *Molecules* **24**, 88 (2019).

[3] Xia, F., Wang, H., Xiao, D., Dubey, M. & Ramasubramaniam, A. Two-dimensional material nanophotonics. *Nature Photonics* **8**, 899 (2014).

[4] Zhu, Z., Murtaza, I., Meng, H. & Huang, W. Thin film transistors based on two dimensional graphene and graphene/semiconductor heterojunctions. *Royal Society of Chemistry Advances* **7**, 17387–17397 (2017).

[5] Song, S. *et al.* Room temperature semiconductor–metal transition of $MoTe_2$ thin films engineered by strain. *Nano Letters* **16**, 188–193 (2016).

[6] Splendiani, A. *et al.* Emerging photoluminescence in monolayer MoS_2. *Nano Letters* **10**, 1271 (2010).

[7] Yun, W. S., Han, S. W., Hong, S. C., Kim, I. G. & Lee, J. D. Thickness and strain effects on electronic structures of transition metal dichalcogenides: 2H-MX_2 semiconductors (M = Mo, W; X = S, Se, Te). *Physical Review B* **85**, 033305 (2012).

[8] Zhao, W. *et al.* Origin of indirect optical transitions in few-layer MoS_2, WS_2, and WSe_2. *Nano Letters* **13**, 5627–5634 (2013).

[9] Liu, G.-B., Xiao, D., Yao, Y., Xu, X. & Yao, W. Electronic structures and theoretical modelling of two-dimensional group-vib transition metal dichalcogenides. *Chemical Society Reviews* **44**, 2643–2663 (2015).

[10] Li, T., & Galli, G. Electronic properties of MoS_2 nanoparticles. *The Journal of Physical Chemistry C* **111**, 16192–16196 (2007).

[11] Zhu, Z. Y., Cheng, Y. C. & Schwingenschlögl, U. Giant spin-orbit-induced spin splitting in two-dimensional transition-metal dichalcogenide semiconductors. *Physical Review B* **84**, 153402 (2011).

[12] Kormanyos, A. *et al.* k.p theory for two-dimensional transition metal dichalcogenide semiconductors. *2D Materials* **2**, 022001 (2015).

[13] Wang, G. *et al.* Colloquium: Excitons in atomically thin transition metal dichalcogenides. *Reviews of Modern Physics* **90**, 021001 (2018).

[14] Klingshirn, C. F. *Semiconductor optics* (Springer Science & Business Media, 2012).

[15] Shinada, M. & Sugano, S. Interband optical transitions in extremely anisotropic semiconductors. i. bound and unbound exciton absorption. *Journal of the Physical Society of Japan* **21**, 1936–1946 (1966).

[16] Cheiwchanchamnangij, T. & Lambrecht, W. R. L. Quasiparticle band structure calculation of monolayer, bilayer, and bulk MoS_2. *Physical Review B* **85**, 205302 (2012).

[17] Ramasubramaniam, A. Large excitonic effects in monolayers of molybdenum and tungsten dichalcogenides. *Physical Review B* **86**, 115409 (2012).

[18] Qiu, D. Y., da Jornada, F. H. & Louie, S. G. Optical spectrum of MoS_2: Many-body effects and diversity of exciton states. *Physical Review Letter* **111**, 216805 (2013).

[19] Chernikov, A. *et al.* Exciton binding energy and nonhydrogenic Rydberg series in monolayer WS_2. *Physical Review Letters* **113**, 076802 (2014).

[20] Wang, G. *et al.* Giant enhancement of the optical second-harmonic emission of WSe_2 monolayers by laser excitation at exciton resonances. *Physical Review Letters* **114**, 097403 (2015).

[21] Raja, A. *et al.* Coulomb engineering of the bandgap and excitons in two-dimensional materials. *Nature Communications* **8**, 15251 (2017).

[22] Rytova, N. S. Screened potential of a point charge in a thin film. *Proceedings MSU, Physics, Astronomy* **3**, 30 (1967).

[23] Keldysh, L. Coulomb interaction in thin semiconductor and semimetal films. *Soviet Journal of Experimental and Theoretical Physics Letters* **29**, 658 (1979).

[24] Cudazzo, P., Tokatly, I. V. & Rubio, A. Dielectric screening in two-dimensional insulators: Implications for excitonic and impurity states in graphane. *Physical Review B* **84**, 085406 (2011).

[25] Goryca, M. *et al.* Revealing exciton masses and dielectric properties of monolayer semiconductors with high magnetic fields. *Nature Communications* **10**, 1–12 (2019).

[26] Xiao, D., Liu, G.-B., Feng, W., Xu, X. & Yao, W. Coupled spin and valley physics in monolayers of MoS_2 and other group-VI dichalcogenides. *Physical Review Letters* **108**, 196802 (2012).

[27] Zhang, Y. *et al.* Direct observation of the transition from indirect to direct bandgap in atomically thin epitaxial $MoSe_2$. *Nature Nanotechnology* **9**, 111–115 (2014).

[28] Miwa, J. A. *et al.* Electronic structure of epitaxial single-layer MoS_2. *Physical Review Letters* **114**, 046802 (2015).

[29] Kosmider, K., González, J. W. & Fernández-Rossier, J. Large spin splitting in the conduction band of transition metal dichalcogenide monolayers. *Physical Review B* **88**, 245436 (2013).

[30] Molina-Sánchez, A., Sangalli, D., Hummer, K., Marini, A. & Wirtz, L. Effect of spin-orbit interaction on the optical spectra of single-layer, double-layer, and bulk MoS_2. *Physical Review B* **88**, 045412 (2013).

[31] Liu, G.-B., Shan, W.-Y., Yao, Y., Yao, W. & Xiao, D. Three-band tight-binding model for monolayers of group-VIB transition metal dichalcogenides. *Physical Review B* **88**, 085433 (2013).

[32] Kormányos, A., Zólyomi, V., Drummond, N. D. & Burkard, G. Spin-orbit coupling, quantum dots, and qubits in monolayer transition metal dichalcogenides. *Physical Review X* **4**, 011034 (2014).

[33] Cao, T. *et al.* Valley-selective circular dichroism in MoS_2. *Nature Communications* **3**, 887 (2012).

[34] Yao, W., Xiao, D. & Niu, Q. Valley-dependent optoelectronics from inversion symmetry breaking. *Physical Review B* **77**, 235406 (2008).

[35] Mak, K. F., He, K., Shan, J. & Heinz, T. F. Control of valley polarization in monolayer MoS_2 by optical helicity. *Nature Nanotechnology* **7**, 494 (2012).

[36] Sallen, G. *et al.* Robust optical emission polarization in MoS_2 monolayers through selective valley excitation. *Physical Review B* **86**, 081301 (2012).

[37] Zeng, H., Dai, J., Yao, W., Xiao, D. & Cui, X. Valley polarization in MoS_2 monolayers by optical pumping. *Nature Nanotechnology* **7**, 490 (2012).

[38] Zhu, C. *et al.* Strain tuning of optical emission energy and polarization in monolayer and bilayer MoS_2. *Physical Review B* **88**, 121301 (2013).

[39] Lagarde, D. *et al.* Carrier and polarization dynamics in monolayer MoS_2. *Physical Review Letters* **112**, 047401 (2014).

[40] Glazov, M. *et al.* Exciton fine structure and spin decoherence in monolayers of transition metal dichalcogenides. *Physical Review B* **89**, 201302 (2014).

[41] Jones, A. M. *et al.* Optical generation of excitonic valley coherence in monolayer WSe_2. *Nature Nanotechnology* **8**, 634 (2013).

[42] Echeverry, J., Urbaszek, B., Amand, T., Marie, X. & Gerber, I. Splitting between bright and dark excitons in transition metal dichalcogenide monolayers. *Physical Review B* **93**, 121107 (2016).

[43] Wang, G. *et al.* In-plane propagation of light in transition metal dichalcogenide monolayers: optical selection rules. *Physical Review Letters* **119**, 047401 (2017).

[44] Robert, C. *et al.* Exciton radiative lifetime in transition metal dichalcogenide monolayers. *Physical Review B* **93**, 205423 (2016).

[45] Robert, C. *et al.* Fine structure and lifetime of dark excitons in transition metal dichalcogenide monolayers. *Physical Review B* **96**, 155423 (2017).

[46] Wang, G. *et al.* Spin-orbit engineering in transition metal dichalcogenide alloy monolayers. *Nature Communications* **6**, 1–7 (2015).

[47] Zhang, X.-X., You, Y., Zhao, S. Y. F. & Heinz, T. F. Experimental evidence for dark excitons in monolayer WSe_2. *Physical Review Letters* **115**, 257403 (2015).

[48] Arora, A. *et al.* Excitonic resonances in thin films of WSe_2: from monolayer to bulk material. *Nanoscale* **7**, 10421–10429 (2015).

[49] Withers, F. *et al.* WSe_2 light-emitting tunneling transistors with enhanced brightness at room temperature. *Nano Letters* **15**, 8223–8228 (2015).

[50] Kormányos, A. *et al.* k· p theory for two-dimensional transition metal dichalcogenide semiconductors. *2D Materials* **2**, 022001 (2015).

[51] Cadiz, F. *et al.* Excitonic linewidth approaching the homogeneous limit in MoS_2-based van der Waals heterostructures. *Physical Review X* **7**, 021026 (2017).

[52] Robert, C. *et al.* Measurement of the spin-forbidden dark excitons in MoS_2 and $MoSe_2$ monolayers. *Nature Communications* **11**, 4037 (2020).

[53] Unuchek, D. *et al.* Room-temperature electrical control of exciton flux in a van der Waals heterostructure. *Nature* **560**, 340–344 (2018).

[54] Srivastava, A. *et al.* Optically active quantum dots in monolayer WSe_2. *Nature Nanotechnology* **10**, 491 (2015).

[55] He, Y.-M. *et al.* Single quantum emitters in monolayer semiconductors. *Nature Nanotechnology* **10**, 497–502 (2015).

[56] Chakraborty, C., Kinnischtzke, L., Goodfellow, K. M., Beams, R. & Vamivakas, A. N. Voltage-controlled quantum light from an atomically thin semiconductor. *Nature Nanotechnology* **10**, 507 (2015).

[57] You, Y. *et al.* Observation of biexcitons in monolayer WSe_2. *Nature Physics* **11**, 477–481 (2015).

[58] Courtade, E. *et al.* Charged excitons in monolayer WSe_2: Experiment and theory. *Physical Review B* **96**, 085302 (2017).

[59] Chen, S.-Y., Goldstein, T., Taniguchi, T., Watanabe, K. & Yan, J. Coulomb-bound four-and five-particle intervalley states in an atomically-thin semiconductor. *Nature Communications* **9**, 1–8 (2018).

[60] Gerber, I. C. *et al.* Interlayer excitons in bilayer MoS_2 with strong oscillator strength up to room temperature. *Physical Review B* **99**, 035443 (2019).

[61] Wu, S. *et al.* Electrical tuning of valley magnetic moment through symmetry control in bilayer MoS_2. *Nature Physics* **9**, 149 (2013).

[62] Lee, J., Mak, K. F. & Shan, J. Electrical control of the valley hall effect in bilayer MoS_2 transistors. *Nature Nanotechnology* **11**, 421 (2016).

[63] Rivera, P. *et al.* Observation of long-lived interlayer excitons in monolayer $MoSe_2$-WSe_2 heterostructures. *Nature Communications* **6**, 6242 (2015).

[64] Chen, H. *et al.* Ultrafast formation of interlayer hot excitons in atomically thin MoS_2/WS_2 heterostructures. *Nature Communications* **7**, 1–8 (2016).

[65] Kunstmann, J. *et al.* Momentum-space indirect interlayer excitons in transition-metal dichalcogenide van der Waals heterostructures. *Nature Physics* **14**, 801–805 (2018).

[66] Horng, J. *et al.* Observation of interlayer excitons in $\mathrm{MoSe_2}$ single crystals. *Physical Review B* **97**, 241404 (2018).

[67] Slobodeniuk, A. *et al.* Fine structure of k-excitons in multilayers of transition metal dichalcogenides. *2D Materials* **6**, 025026 (2019).

[68] Arora, A. *et al.* Interlayer excitons in a bulk van der Waals semiconductor. *Nature Communications* **8**, 639 (2017).

[69] Heo, H. *et al.* Interlayer orientation-dependent light absorption and emission in monolayer semiconductor stacks. *Nature Communications* **6**, 1–7 (2015).

[70] Radisavljevic, B., Radenovic, A., Brivio, J., Giacometti, i. V. & Kis, A. Single-layer $\mathrm{MoS_2}$ transistors. *Nature Nanotechnology* **6**, 147 (2011).

[71] Mak, K. F., Lee, C., Hone, J., Shan, J. & Heinz, T. F. Atomically thin $\mathrm{MoS_2}$: a new direct-gap semiconductor. *Physical Review Letters* **105**, 136805 (2010).

[72] Castellanos-Gomez, A. *et al.* Deterministic transfer of two-dimensional materials by all-dry viscoelastic stamping. *2D Materials* **1**, 011002 (2014).

[73] Tonndorf, P. *et al.* Photoluminescence emission and raman response of monolayer $\mathrm{MoS_2}$, $\mathrm{MoSe_2}$, and $\mathrm{WSe_2}$. *Optics Express* **21**, 4908–4916 (2013).

[74] Duan, X. *et al.* Lateral epitaxial growth of two-dimensional layered semiconductor heterojunctions. *Nature Nanotechnology* **9**, 1024 (2014).

[75] Geim, A. K. & Grigorieva, I. V. Van der Waals heterostructures. *Nature* **499**, 419—425 (2013).

[76] El Kazzi, S. *et al.* $\mathrm{MoS_2}$ synthesis by gas source mbe for transition metal dichalcogenides integration on large scale substrates. *Journal of Applied Physics* **123**, 135702 (2018).

[77] Taniguchi, T. & Watanabe, K. Synthesis of high-purity boron nitride single crystals under high pressure by using Ba-BN solvent. *Journal of Crystal Growth* **303**, 525 – 529 (2007).

[78] Cadiz, F. *et al.* Ultra-low power threshold for laser induced changes in optical properties of 2D molybdenum dichalcogenides. *2D Materials* **3**, 045008 (2016).

[79] Raja, A. *et al.* Dielectric disorder in two-dimensional materials. *Nature Nanotechnology* **14**, 832–837 (2019).

[80] Shree, S. *et al.* High optical quality of $\mathrm{MoS_2}$ monolayers grown by chemical vapor deposition. *2D Materials* **7**, 015011 (2019).

[81] Robert, C. *et al.* Optical spectroscopy of excited exciton states in $\mathrm{MoS_2}$ monolayers in van der Waals heterostructures. *Physical Review Materials* **2**, 011001 (2018).

[82] Fang, H. *et al.* Control of the exciton radiative lifetime in van der Waals heterostructures. *Physical Review Letters* **123**, 067401 (2019).

[83] George, A. *et al.* Controlled growth of transition metal dichalcogenide monolayers using knudsen-type effusion cells for the precursors. *Journal of Physics: Materials* **2**, 016001 (2019).

[84] Rhodes, D., Chae, S. H., Ribeiro-Palau, R. & Hone, J. Disorder in van der Waals heterostructures of 2D materials. *Nature Materials* **18**, 541 (2019).

[85] Li, X. *et al.* Large-area synthesis of high-quality and uniform graphene films on copper foils. *Science* **324**, 1312–1314 (2009).

[86] Yu, Q. *et al.* Control and characterization of individual grains and grain boundaries in graphene grown by chemical vapour deposition. *Nature Materials* **10**, 443–449 (2011).

[87] Lee, Y.-H. *et al.* Synthesis of large-area $\mathrm{MoS_2}$ atomic layers with chemical vapor deposition. *Advanced materials* **24**, 2320–2325 (2012).

[88] Kobayashi, Y. *et al.* Growth and optical properties of high-quality monolayer $\mathrm{WS_2}$ on graphite. *ACS Nano* **9**, 4056–4063 (2015).

[89] Rhyee, J.-S. *et al.* High-mobility transistors based on large-area and highly crystalline CVD-grown $\mathrm{MoSe_2}$ films on insulating substrates. *Advanced Materials* **28**, 2316–2321 (2016).

[90] Naylor, C. H. *et al.* Monolayer single-crystal 1T-$\mathrm{MoTe_2}$ grown by chemical vapor deposition exhibits weak antilocalization effect. *Nano Letters* **16**, 4297–4304 (2016).

[91] Najmaei, S. *et al.* Vapour phase growth and grain boundary structure of molybdenum disulphide atomic layers. *Nature Materials* **12**, 754–759 (2013).

[92] Van Der Zande, A. M. *et al.* Grains and grain boundaries in highly crystalline monolayer molybdenum disulphide. *Nature Materials* **12**, 554–561 (2013).

[93] Cong, C. *et al.* Synthesis and optical properties of large-area single-crystalline 2D semiconductor WS_2 monolayer from chemical vapor deposition. *Advanced Optical Materials* **2**, 131–136 (2014).

[94] Benameur, M. M. *et al.* Visibility of dichalcogenide nanolayers. *Nanotechnology* **22**, 125706 (2011).

[95] Zande, A. M. v. d. *et al.* Large-scale arrays of single-layer graphene resonators. *Nano Letters* **10**, 4869–4873 (2010).

[96] Suk, J. W. *et al.* Transfer of CVD-grown monolayer graphene onto arbitrary substrates. *ACS Nano* **5**, 6916–6924 (2011).

[97] Jia, H. *et al.* Large-scale arrays of single-and few-layer MoS_2 nanomechanical resonators. *Nanoscale* **8**, 10677–10685 (2016).

[98] Shree, S., Paradisanos, I., Marie, X., Robert, C. & Urbaszek, B. Guide to optical spectroscopy of layered semiconductors. *arXiv preprint arXiv:2006.16872* (2020).

[99] Bermudez, V. M. & McClure, D. S. Spectroscopic studies of the two-dimensional magnetic insulators chromium trichloride and chromium tribromide - I. *Journal of Physics and Chemistry of Solids* **40**, 129–147 (1979).

[100] Molina-Sánchez, A., Catarina, G., Sangalli, D. & Fernandez-Rossier, J. Magneto-optical response of chromium trihalide monolayers: chemical trends. *Journal of Materials Chemistry C* (2020).

[101] Karni, O. *et al.* Infrared interlayer exciton emission in MoS_2/WSe_2 heterostructures. *Physical Review Letters* **123**, 247402 (2019).

[102] Ling, X., Wang, H., Huang, S., Xia, F. & Dresselhaus, M. S. The renaissance of black phosphorus. *Proceedings of the National Academy of Sciences* **112**, 4523–4530 (2015).

[103] Ansari, L. *et al.* Quantum confinement-induced semimetal-to-semiconductor evolution in large-area ultra-thin $PtSe_2$ films grown at 400 deg C. *npj 2D Materials and Applications* **3**, 1–8 (2019).

[104] Pawley, J. *Handbook of biological confocal microscopy*, vol. 236 (Springer Science & Business Media, 2006).

[105] Hecht, E. *et al.* *Optics*, vol. 4 (Addison Wesley San Francisco, 2002).

[106] Leisgang, N. *et al.* Giant Stark splitting of an exciton in bilayer MoS_2. *Nature Nanotechnology* (2020).

[107] Zhang, X.-X. *et al.* Magnetic brightening and control of dark excitons in monolayer WSe_2. *Nature Nanotechnology* **12**, 883 (2017).

[108] Zhou, Y. *et al.* Controlling excitons in an atomically thin membrane with a mirror. *Physical Review Letters* **124**, 027401 (2020).

[109] Waldecker, L. *et al.* Rigid band shifts in two-dimensional semiconductors through external dielectric screening. *Physical Review Letters* **123**, 206403 (2019).

[110] Scuri, G. *et al.* Large excitonic reflectivity of monolayer $MoSe_2$ encapsulated in hexagonal boron nitride. *Physical Review Letters* **120**, 037402 (2018).

[111] Ho, C., Huang, Y., Tiong, K. & Liao, P. Absorption-edge anisotropy in ReS_2 and $ReSe_2$ layered semiconductors. *Physical Review B* **58**, 16130 (1998).

[112] Zhang, E. *et al.* Tunable ambipolar polarization-sensitive photodetectors based on high-anisotropy $ReSe_2$ nanosheets. *ACS Nano* **10**, 8067–8077 (2016).

[113] Wilson, J. A. & Yoffe, A. The transition metal dichalcogenides discussion and interpretation of the observed optical, electrical and structural properties. *Advances in Physics* **18**, 193–335 (1969).

[114] Arora, A. *et al.* Valley-contrasting optics of interlayer excitons in Mo-and W-based bulk transition metal dichalcogenides. *Nanoscale* **10**, 15571–15577 (2018).

[115] Sung, J. *et al.* Broken mirror symmetry in excitonic response of reconstructed domains in twisted $MoSe_2/MoSe_2$ bilayers. *Nature Nanotechnology* (2020).

[116] Yu, H., Liu, G.-B., Tang, J., Xu, X. & Yao, W. Moiré excitons: From programmable quantum emitter arrays to spin-orbit–coupled artificial lattices. *Science Advances* **3**, e1701696 (2017).

[117] Shimazaki, Y. *et al.* Strongly correlated electrons and hybrid excitons in a moiré heterostructure. *Nature* 1–6 (2020).

[118] Sushko, A. *et al.* High resolution imaging of reconstructed domains and moire patterns in functional van der Waals heterostructure devices. *arXiv preprint arXiv:1912.07446* (2019).

[119] Ciarrocchi, A. *et al.* Polarization switching and electrical control of interlayer excitons in two-dimensional van der Waals heterostructures. *Nature Photonics* **13**, 131–136 (2019).

[120] Nagler, P. *et al.* Giant magnetic splitting inducing near-unity valley polarization in van der Waals heterostructures. *Nature Communications* **8**, 1551 (2017).

[121] Pelant, I. & Valenta, J. *Luminescence spectroscopy of semiconductors* (Oxford University Press, 2012).

[122] Haunschild, J. *et al.* Quality control of as-cut multicrystalline silicon wafers using photoluminescence imaging for solar cell production. *Solar Energy Materials and Solar Cells* **94**, 2007–2012 (2010).

[123] Moody, G. *et al.* Intrinsic homogeneous linewidth and broadening mechanisms of excitons in monolayer transition metal dichalcogenides. *Nature Communications* **6**, 8315 (2015).

[124] Shree, S. *et al.* Observation of exciton-phonon coupling in $MoSe_2$ monolayers. *Physical Review B* **98**, 035302 (2018).

[125] Barbone, M. *et al.* Charge-tuneable biexciton complexes in monolayer WSe_2. *Nature Communications* **9**, 1–6 (2018).

[126] Paradisanos, I. *et al.* Room temperature observation of biexcitons in exfoliated WS_2 monolayers. *Applied Physics Letters* **110**, 193102 (2017).

[127] Sigl, L. *et al.* Condensation signatures of photogenerated interlayer excitons in a van der Waals heterostack. *arXiv preprint arXiv:2001.07567* (2020).

[128] Jakubczyk, T. *et al.* Radiatively limited dephasing and exciton dynamics in $MoSe_2$ monolayers revealed with four-wave mixing microscopy. *Nano Letters* **16**, 5333–5339 (2016).

[129] Cassabois, G., Valvin, P. & Gil, B. Hexagonal boron nitride is an indirect bandgap semiconductor. *Nature Photonics* **10**, 262 (2016).

[130] Ai, N., Walden-Newman, W., Song, Q., Kalliakos, S. & Strauf, S. Suppression of blinking and enhanced exciton emission from individual carbon nanotubes. *ACS nano* **5**, 2664–2670 (2011).

[131] Raynaud, C. *et al.* Superlocalization of excitons in carbon nanotubes at cryogenic temperature. *Nano Letters* **19**, 7210–7216 (2019).

[132] Blancon, J.-C. *et al.* Scaling law for excitons in 2D perovskite quantum wells. *Nature Communications* **9**, 1–10 (2018).

[133] Lien, D.-H. *et al.* Engineering light outcoupling in 2D materials. *Nano Letters* **15**, 1356–1361 (2015).

[134] Zhang, H. *et al.* Interference effect on optical signals of monolayer MoS_2. *Applied Physics Letters* **107**, 101904 (2015).

[135] Roddaro, S., Pingue, P., Piazza, V., Pellegrini, V. & Beltram, F. The optical visibility of graphene: interference colors of ultrathin graphite on SiO_2. *Nano Letters* **7**, 2707–2710 (2007).

[136] Bandurin, D. A. *et al.* High electron mobility, quantum hall effect and anomalous optical response in atomically thin InSe. *Nature Nanotechnology* **12**, 223 (2017).

[137] Luo, Y., Liu, N., Kim, B., Hone, J. & Strauf, S. Exciton dipole orientation of strain-induced quantum emitters in WSe_2. *Nano Letters* (2020).

[138] Rivera, P. *et al.* Interlayer valley excitons in heterobilayers of transition metal dichalcogenides. *Nature Nanotechnology* **13**, 1004–1015 (2018).

[139] Hong, X. *et al.* Ultrafast charge transfer in atomically thin MoS_2/WS_2 heterostructures. *Nature Nanotechnology* **9**, 682 (2014).

[140] Hill, H. M. *et al.* Observation of excitonic Rydberg states in monolayer MoS_2 and WS_2 by photoluminescence excitation spectroscopy. *Nano Letters* **15**, 2992–2997 (2015).

[141] Srivastava, A. & Imamoğlu, A. Signatures of bloch-band geometry on excitons: nonhydrogenic spectra in transition-metal dichalcogenides. *Physical Review Letters* **115**, 166802 (2015).

[142] Glazov, M. *et al.* Intrinsic exciton-state mixing and nonlinear optical properties in transition metal dichalcogenide monolayers. *Physical Review B* **95**, 035311 (2017).

[143] Wang, G. *et al.* Exciton states in monolayer $MoSe_2$: impact on interband transitions. *2D Materials* **2**, 045005 (2015).

[144] Chow, C. M. *et al.* Phonon-assisted oscillatory exciton dynamics in monolayer $MoSe_2$. *npj 2D Materials and Applications* **1**, 33 (2017).

[145] Dyakonov, M. I. *Spin physics in semiconductors*, vol. 1 (Springer, 2017).

[146] Tornatzky, H., Kaulitz, A.-M. & Maultzsch, J. Resonance profiles of valley polarization in single-layer MoS_2 and $MoSe_2$. *Physical Review Letters* **121**, 167401 (2018).

[147] Dufferwiel, S. *et al.* Valley coherent exciton-polaritons in a monolayer semiconductor. *Nature Communications* **9**, 1–7 (2018).

[148] Dey, P. *et al.* Gate-controlled spin-valley locking of resident carriers in WSe_2 monolayers. *Physical Review Letters* **119**, 137401 (2017).

[149] Mak, K. F., Shan, J. & Ralph, D. C. Probing and controlling magnetic states in 2D layered magnetic materials. *Nature Reviews Physics* **1**, 646–661 (2019).

[150] Seyler, K. L. *et al.* Signatures of moiré-trapped valley excitons in $MoSe_2/WSe_2$ heterobilayers. *Nature* **567**, 66–70 (2019).

[151] Yu, H., Liu, G.-B. & Yao, W. Brightened spin-triplet interlayer excitons and optical selection rules in van der Waals heterobilayers. *2D Materials* **5**, 035021 (2018).

[152] Andersen, T. I. *et al.* Moiré excitons correlated with superlattice structure in twisted WSe_2/WSe_2 homobilayers. *arXiv preprint arXiv:1912.06955* (2019).

[153] Rivera, P. *et al.* Valley-polarized exciton dynamics in a 2D semiconductor heterostructure. *Science* **351**, 688–691 (2016).

[154] Unuchek, D. *et al.* Valley-polarized exciton currents in a van der Waals heterostructure. *Nature Nanotechnology* **14**, 1104–1109 (2019).

[155] Srivastava, A. *et al.* Valley zeeman effect in elementary optical excitations of monolayer WSe_2. *Nature Physics* **11**, 141–147 (2015).

[156] Back, P. *et al.* Giant paramagnetism-induced valley polarization of electrons in charge-tunable monolayer $MoSe_2$. *Physical Review Letters* **118**, 237404 (2017).

[157] Carvalho, B. R., Malard, L. M., Alves, J. M., Fantini, C. & Pimenta, M. A. Symmetry-dependent exciton-phonon coupling in 2D and bulk MoS_2 observed by resonance raman scattering. *Physical Review Letters* **114**, 136403 (2015).

[158] Scheuschner, N., Gillen, R., Staiger, M. & Maultzsch, J. Interlayer resonant raman modes in few-layer MoS_2. *Physical Review B* **91**, 235409 (2015).

[159] Oliver, S. M. *et al.* The structural phases and vibrational properties of $Mo_{1-x}W_xTe_2$ alloys. *2D Materials* **4**, 045008 (2017).

[160] Ubrig, N. *et al.* Low-temperature monoclinic layer stacking in atomically thin CrI_3 crystals. *2D Materials* **7**, 015007 (2019).

[161] Wolverson, D., Crampin, S., Kazemi, A. S., Ilie, A. & Bending, S. J. Raman spectra of monolayer, few-layer, and bulk $ReSe_2$: an anisotropic layered semiconductor. *ACS Nano* **8**, 11154–11164 (2014).

[162] Chakraborty, B. *et al.* Symmetry-dependent phonon renormalization in monolayer MoS_2 transistor. *Physical Review B* **85**, 161403 (2012).

[163] Conley, H. J. *et al.* Bandgap engineering of strained monolayer and bilayer MoS_2. *Nano Letters* **13**, 3626–3630 (2013).

[164] Zhang, X. *et al.* Raman spectroscopy of shear and layer breathing modes in multilayer MoS_2. *Physical Review B* **87**, 115413 (2013).

[165] Holler, J. *et al.* Low-frequency raman scattering in WSe_2 - $MoSe_2$ heterobilayers: Evidence for atomic reconstruction. *Applied Physics Letters* **117**, 013104 (2020).

[166] Shinde, S. M. *et al.* Stacking-controllable interlayer coupling and symmetric configuration of multilayered MoS_2. *NPG Asia Materials* **10**, e468 (2018).

[167] Psilodimitrakopoulos, S. *et al.* Ultrahigh-resolution nonlinear optical imaging of the armchair orientation in 2D transition metal dichalcogenides. *Light: Science & Applications* **7**, 18005–18005 (2018).

[168] Mennel, L., Paur, M. & Mueller, T. Second harmonic generation in strained transition metal dichalcogenide monolayers: MoS_2, $MoSe_2$, WS_2, and WSe_2. *APL Photonics* **4**, 034404 (2019).

[169] Seyler, K. L. *et al.* Electrical control of second-harmonic generation in a WSe_2 monolayer transistor. *Nature Nanotechnology* **10**, 407–411 (2015).

[170] Sun, Z. *et al.* Giant nonreciprocal second-harmonic generation from antiferromagnetic bilayer CrI_3. *Nature* **572**, 497–501 (2019).

[171] Molina-Sánchez, A. & Wirtz, L. Phonons in single-layer and few-layer MoS_2 and WS_2. *Physical Review B* **84**, 155413 (2011).

[172] Horzum, S. *et al.* Phonon softening and direct to indirect band gap crossover in strained single-layer $MoSe_2$. *Physical Review B* **87**, 125415 (2013).

[173] Sekine, T., Izumi, M., Nakashizu, T., Uchinokura, K. & Matsuura, E. Raman scattering and infrared reflectance in 2H-$MoSe_2$. *Journal of the Physical Society of Japan* **49**, 1069–1077 (1980).

[174] Jakubczyk, T. *et al.* Impact of environment on dynamics of exciton complexes in a WS_2 monolayer. *2D Materials* (2018).

[175] Hameau, S. *et al.* Strong electron-phonon coupling regime in quantum dots: evidence for everlasting resonant polarons. *Physical Review Letters* **83**, 4152 (1999).

[176] Lee, J., Koteles, E. S. & Vassell, M. Luminescence linewidths of excitons in GaAs quantum wells below 150 K. *Physical Review B* **33**, 5512 (1986).

[177] Borri, P. *et al.* Ultralong dephasing time in InGaAs quantum dots. *Physical Review Letters* **87**, 157401 (2001).

[178] Amand, T. *et al.* Exciton formation and hole-spin relaxation in intrinsic quantum wells. *Physical Review B* **50**, 11624–11628 (1994).

[179] Szczytko, J. *et al.* Determination of the exciton formation in quantum wells from time-resolved interband luminescence. *Physical Review Letters* **93**, 137401 (2004).

[180] Thilagam, A. Exciton formation assisted by longitudinal optical phonons in monolayer transition metal dichalcogenides. *Journal of Applied Physics* **120**, 124306 (2016).

[181] Wang, G. *et al.* Double resonant raman scattering and valley coherence generation in monolayer WSe_2. *Physical Review Letters* **115**, 117401 (2015).

[182] Chow, C. M. E. *et al.* Unusual exciton-phonon interactions at van der Waals engineered interfaces. *Nano Letters* (2017).

[183] Soubelet, P., Bruchhausen, A. E., Fainstein, A., Nogajewski, K. & Faugeras, C. Resonance effects in the raman scattering of monolayer and few-layer $MoSe_2$. *Physical Review B* **93**, 155407 (2016).

[184] Christiansen, D. *et al.* Phonon sidebands in monolayer transition metal dichalcogenides. *Physical Review Letters* **119**, 187402 (2017).

[185] Koperski, M. *et al.* Optical properties of atomically thin transition metal dichalcogenides: observations and puzzles. *Nanophotonics* **6**, 1289–1308 (2017).

[186] Dery, H. & Song, Y. Polarization analysis of excitons in monolayer and bilayer transition-metal dichalcogenides. *Physical Review B* **92**, 125431 (2015).

[187] Dery, H. Theory of intervalley coulomb interactions in monolayer transition-metal dichalcogenides. *Physical Review B* **94**, 075421 (2016).

[188] Plechinger, G. *et al.* Control of biaxial strain in single-layer molybdenite using local thermal expansion of the substrate. *2D Materials* **2**, 015006 (2015).

[189] Schmidt, R. *et al.* Reversible uniaxial strain tuning in atomically thin WSe_2. *2D Materials* **3**, 021011 (2016).

[190] Manca, M. *et al.* Enabling valley selective exciton scattering in monolayer WSe_2 through upconversion. *Nature Communications* **8**, 14927 (2017).

[191] Lindlau, J. *et al.* Identifying optical signatures of momentum-dark excitons in transition metal dichalcogenide monolayers. *arXiv preprint arXiv:1710.00988* (2017).

[192] Han, B. *et al.* Exciton states in monolayer $MoSe_2$ and $MoTe_2$ probed by upconversion spectroscopy. *Physical Review X* **8**, 031073 (2018).

[193] Gantmakher, V. & Levinson, Y. *Carrier Scattering in Metals and Semiconductors* (North-Holland Publishing Company, 1987).

[194] Peter Y. Yu and Manuel Cardona, *Fundamentals of Semiconductors* (Springer-Verlag, Berlin, Germany) 2010. Ch.7.

[195] Danovich, M., Aleiner, I. L., Drummond, N. D. & Fal'ko, V. I. Fast relaxation of photo-excited carriers in 2-D transition metal dichalcogenides. *IEEE Journal of Selected Topics in Quantum Electronics* **23**, 1–5 (2017).

[196] Li, X. *et al.* Intrinsic electrical transport properties of monolayer silicene and MoS_2 from first principles. *Physical Review B* **87**, 115418 (2013).

[197] Kaasbjerg, K., Thygesen, K. S. & Jacobsen, K. W. Phonon-limited mobility in n-type single-layer MoS_2 from first principles. *Physical Review B* **85**, 115317 (2012).

[198] Selig, M. *et al.* Excitonic linewidth and coherence lifetime in monolayer transition metal dichalcogenides. *Nature Communications* **7**, 13279 (2016).

[199] Dey, P. *et al.* Optical coherence in atomic-monolayer transition-metal dichalcogenides limited by electron-phonon interactions. *Physical Review Letters* **116**, 127402 (2016).

[200] Jin, Z., Li, X., Mullen, J. T. & Kim, K. W. Intrinsic transport properties of electrons and holes in monolayer transition-metal dichalcogenides. *Physical Review B* **90**, 045422 (2014).

[201] Ivchenko, E. L. *Optical spectroscopy of semiconductor nanostructures* (Alpha Science, Harrow UK, 2005).

[202] Ando, T. & Uemura, Y. Theory of quantum transport in a two-dimensional electron system under magnetic fields. i. characteristics of level broadening and transport under strong fields. *Journal of the Physical Society of Japan* **36**, 959–967 (1974).

[203] Deych, L. I., Erementchouk, M. V., Lisyansky, A. A., Ivchenko, E. L. & Voronov, M. M. Exciton luminescence in one-dimensional resonant photonic crystals: A phenomenological approach. *Physical Review B* **76**, 075350 (2007).

[204] Piermarocchi, C., Tassone, F., Savona, V., Quattropani, A. & Schwendimann, P. Nonequilibrium dynamics of free quantum-well excitons in time-resolved photoluminescence. *Physical Review B* **53**, 15834–15841 (1996).

[205] Pöllmann, C. *et al.* Resonant internal quantum transitions and femtosecond radiative decay of excitons in monolayer WSe_2. *Nature Materials* **14**, 889–893 (2015).

[206] Jusserand, B., Poddubny, A. N., Poshakinskiy, A. V., Fainstein, A. & Lemaitre, A. Polariton resonances for ultrastrong coupling cavity optomechanics in GaAs/AlAs multiple quantum wells. *Physical Review Letters* **115**, 267402 (2015).

[207] Novoselov, K. S., Mishchenko, A., Carvalho, A. & Castro Neto, A. H. 2D materials and van der Waals heterostructures. *Science* **353** (2016).

[208] Zhang, Y. *et al.* Direct observation of a widely tunable bandgap in bilayer graphene. *Nature* **459**, 820 (2009).

[209] Bastard, G., Mendez, E., Chang, L. & Esaki, L. Exciton binding energy in quantum wells. *Physical Review B* **26**, 1974 (1982).

[210] He, K. *et al.* Tightly bound excitons in monolayer WSe_2. *Physical Review Letters* **113**, 026803 (2014).

[211] Gong, Z. *et al.* Magnetoelectric effects and valley-controlled spin quantum gates in transition metal dichalcogenide bilayers. *Nature Communications* **4**, 2053 (2013).

[212] Deilmann, T. & Thygesen, K. S. Interlayer excitons with large optical amplitudes in layered van der Waals materials. *Nano Letters* **18**, 2984–2989 (2018).

[213] Kang, J., Tongay, S., Zhou, J., Li, J. & Wu, J. Band offsets and heterostructures of two-dimensional semiconductors. *Applied Physics Letters* **102**, 012111 (2013).

[214] Molas, M. R. *et al.* The optical response of monolayer, few-layer and bulk tungsten disulfide. *Nanoscale* **9**, 13128–13141 (2017).

[215] Beal, A. R. & Liang, W. Y. Excitons in 2H-WSe_2 and 3R-WS_2. *Journal of Physics C: Solid State Physics* **9**, 2459 (1976).

[216] Calman, E. *et al.* Indirect excitons in van der Waals heterostructures at room temperature. *Nature Communications* **9**, 1895 (2018).

[217] Zhang, C. *et al.* Interlayer couplings, moiré patterns, and 2D electronic superlattices in MoS_2/WSe_2 hetero-bilayers. *Science Advances* **3**, e1601459 (2017).

[218] Akashi, R. *et al.* Two-dimensional valley electrons and excitons in noncentrosymmetric 3R-MoS_2. *Physical Review Applied* **4**, 014002 (2015).

[219] Fogler, M., Butov, L. & Novoselov, K. High-temperature superfluidity with indirect excitons in van der Waals heterostructures. *Nature Communications* **5**, 1–5 (2014).

[220] Schneider, C., Glazov, M. M., Korn, T., Höfling, S. & Urbaszek, B. Two-dimensional semiconductors in the regime of strong light-matter coupling. *Nature Communications* **3**, 2695 (2018).

[221] Low, T. *et al.* Polaritons in layered two-dimensional materials. *Nature Materials* **16**, 182 (2017).

[222] Liu, X. *et al.* Strong light–matter coupling in two-dimensional atomic crystals. *Nature Photonics* **9**, 30–34 (2015).

[223] Dufferwiel, S. *et al.* Exciton–polaritons in van der Waals heterostructures embedded in tunable microcavities. *Nature Communications* **6**, 8579 (2015).

[224] Lindlau, J. *et al.* The role of momentum-dark excitons in the elementary optical response of bilayer WSe_2. *Nature Communications* **9**, 2586 (2018).

[225] Wang, Z., Chiu, Y.-H., Honz, K., Mak, K. F. & Shan, J. Electrical tuning of interlayer exciton gases in WSe_2 bilayers. *Nano Letters* **18**, 137–143 (2017).

[226] Grimme, S., Antony, J., Ehrlich, S. & Krieg, H. A consistent and accurate ab initio parametrization of density functional dispersion correction (DFT-D) for the 94 elements H-Pu. *The Journal of Chemical Physics* **132**, 154104–19 (2010).

[227] He, J., Hummer, K. & Franchini, C. Stacking effects on the electronic and optical properties of bilayer transition metal dichalcogenides MoS_2, $MoSe_2$, WS_2 and WSe_2. *Physical Review B* **89**, 075409 (2014).

[228] Liu, K. *et al.* Evolution of interlayer coupling in twisted molybdenum disulfide bilayers. *Nature Communications* **5**, 4966 (2014).

[229] Frondel, J. W. & Wickman, F. E. Molybdenite polytypes in theory and occurrence. II. some naturally-occurring polytypes of molybdenite. *American Mineralogist: Journal of Earth and Planetary Materials* **55**, 1857–1875 (1970).

[230] Qiu, D. Y., Cao, T. & Louie, S. G. Nonanalyticity, valley quantum phases, and lightlike exciton dispersion in monolayer transition metal dichalcogenides: Theory and first-principles calculations. *Physical Review Letter* **115**, 176801 (2015).

[231] Stier, A. V., McCreary, K. M., Jonker, B. T., Kono, J. & Crooker, S. A. Exciton diamagnetic shifts and valley zeeman effects in monolayer WS_2 and MoS_2 to 65 Tesla. *Nature Communications* **7**, 1–8 (2016).

[232] Gerber, I. C. & Marie, X. Dependence of band structure and exciton properties of encapsulated WSe_2 monolayers on the hbn-layer thickness. *Physical Review B* **98**, 245126

(2018).

[233] Wang, H. *et al.* Integrated circuits based on bilayer MoS_2 transistors. *Nano Letters* **12**, 4674–4680 (2012).

[234] Jiang, T. *et al.* Valley and band structure engineering of folded MoS_2 bilayers. *Nature Nanotechnology* **9**, 825 (2014).

[235] Ajayi, O. A. *et al.* Approaching the intrinsic photoluminescence linewidth in transition metal dichalcogenide monolayers. *2D Materials* **4**, 031011 (2017).

[236] Niehues, I., Blob, A., Stiehm, T., de Vasconcellos, S. M. & Bratschitsch, R. Interlayer excitons in bilayer MoS_2 under uniaxial tensile strain. *Nanoscale* **11**, 12788–12792 (2019).

[237] Carrascoso, F., Lin, D.-Y., Frisenda, R. & Castellanos-Gomez, A. Biaxial strain tuning of interlayer excitons in bilayer MoS_2. *Journal of Physics: Materials* **3**, 015003 (2019).

[238] Kormányos, A. *et al.* Monolayer mos: Trigonal warping, the γ valley, and spin-orbit coupling effects. *Physical Review B* **88**, 045416 (2013).

[239] Pisoni, R. *et al.* Interactions and magnetotransport through spin-valley coupled Landau levels in monolayer MoS_2. *Physical Review Letters* **121**, 247701 (2018).

[240] Molas, M. *et al.* Brightening of dark excitons in monolayers of semiconducting transition metal dichalcogenides. *2D Materials* **4**, 021003 (2017).

[241] Cristofolini, P. *et al.* Coupling quantum tunneling with cavity photons. *Science* **336**, 704–707 (2012).

[242] Back, P., Zeytinoglu, S., Ijaz, A., Kroner, M. & Imamoğlu, A. Realization of an electrically tunable narrow-bandwidth atomically thin mirror using monolayer $MoSe_2$. *Physical Review Letters* **120**, 037401 (2018).

[243] Joe, A. Y. *et al.* Electrically controlled emission from triplet charged excitons in atomically thin heterostructures. *arXiv preprint arXiv:1912.07678* (2019).

[244] Pisoni, R. *et al.* Absence of interlayer tunnel coupling of K-valley electrons in bilayer MoS_2. *Physical Review Letters* **123**, 117702 (2019).

[245] Roch, J. G. *et al.* Quantum-confined Stark effect in a MoS_2 monolayer van der Waals heterostructure. *Nano Letters* **18**, 1070–1074 (2018).

[246] Verzhbitskiy, I., Vella, D., Watanabe, K., Taniguchi, T. & Eda, G. Suppressed out-of-plane polarizability of free excitons in monolayer WSe_2. *ACS Nano* (2019).

[247] Roch, J. G. *et al.* Spin-polarized electrons in monolayer MoS_2. *Nature Nanotechnology* **14**, 432–436 (2019).

[248] Miller, D. A. *et al.* Band-edge electroabsorption in quantum well structures: The quantum-confined Stark effect. *Physical Review Letters* **53**, 2173 (1984).

[249] Amani, M. *et al.* Near-unity photoluminescence quantum yield in MoS_2. *Science* **350**, 1065–1068 (2015).

[250] Edelberg, D. *et al.* Approaching the intrinsic limit in transition metal diselenides via point defect control. *Nano Letters* **19**, 4371–4379 (2019).

[251] Dean, C. R. *et al.* Boron nitride substrates for high-quality graphene electronics. *Nature Nanotechnology* **5**, 722 (2010).

[252] Jin, C. *et al.* Interlayer electron–phonon coupling in WSe_2/hBN heterostructures. *Nature Physics* **13**, 127 (2017).

[253] Stier, A. V. *et al.* Magnetooptics of exciton Rydberg states in a monolayer semiconductor. *Physical Review Letters* **120**, 057405 (2018).

[254] Tongay, S. *et al.* Tuning interlayer coupling in large-area heterostructures with CVD-grown MoS_2 and WS_2 monolayers. *Nano Letters* **14**, 3185–3190 (2014).

[255] Yang, L. *et al.* Spin coherence and dephasing of localized electrons in monolayer MoS_2. *Nano Letters* **15**, 8250–8254 (2015).

[256] Neumann, A. *et al.* Opto-valleytronic imaging of atomically thin semiconductors. *Nature Nanotechnology* **12**, 329 (2017).

[257] Zhou, W. *et al.* Intrinsic structural defects in monolayer molybdenum disulfide. *Nano Letters* **13**, 2615–2622 (2013).

[258] Hong, J. *et al.* Exploring atomic defects in molybdenum disulphide monolayers. *Nature Communications* **6**, 6293 (2015).

[259] Hoshi, Y. *et al.* Effect of a pick-and-drop process on optical properties of a CVD-grown monolayer tungsten disulfide. *Physical Review Materials* **2**, 064003 (2018).

[260] Plechinger, G. *et al.* A direct comparison of CVD-grown and exfoliated MoS_2 using optical spectroscopy. *Semiconductor Science and Technology* **29**, 064008 (2014).

[261] Yu, Y. *et al.* Engineering substrate interactions for high luminescence efficiency of transition-metal dichalcogenide monolayers. *Advanced Functional Materials* **26**, 4733–4739 (2016).

[262] Wierzbowski, J. *et al.* Direct exciton emission from atomically thin transition metal dichalcogenide heterostructures near the lifetime limit. *Scientific Reports* **7**, 12383 (2017).

[263] Vancsó, P. *et al.* The intrinsic defect structure of exfoliated MoS_2 single layers revealed by scanning tunneling microscopy. *Scientific Reports* **6**, 29726 (2016).

[264] Lehnert, T., Lehtinen, O., Algara–Siller, G. & Kaiser, U. Electron radiation damage mechanisms in 2D $MoSe_2$. *Applied Physics Letters* **110**, 033106 (2017).

[265] Komsa, H.-P. *et al.* Two-dimensional transition metal dichalcogenides under electron irradiation: Defect production and doping. *Physical Review Letters* **109**, 035503 (2012).

[266] McDonnell, S., Addou, R., Buie, C., Wallace, R. M. & Hinkle, C. L. Defect-dominated doping and contact resistance in MoS_2. *ACS Nano* **8**, 2880–2888 (2014).

[267] Chuang, H.-J. *et al.* Low-resistance 2D/2D ohmic contacts: A universal approach to high-performance WSe_2, MoS_2, and $MoSe_2$ transistors. *Nano Letters* **16**, 1896–1902 (2016).

[268] Mak, K. F. *et al.* Tightly bound trions in monolayer MoS_2. *Nature Materials* **12**, 207 (2013).

[269] ODonnell, K. & Chen, X. Temperature dependence of semiconductor band gaps. *Applied Physics Letters* **58**, 2924–2926 (1991).

[270] Kumar, N. *et al.* Exciton-exciton annihilation in $MoSe_2$ monolayers. *Physical Review B* **89**, 125427 (2014).

[271] Mouri, S. *et al.* Nonlinear photoluminescence in atomically thin layered WSe_2 arising from diffusion-assisted exciton-exciton annihilation. *Physical Review B* **90**, 155449 (2014).

[272] Schaibley, J. R. *et al.* Valley depolarization dynamics and valley hall effect of excitons in monolayer and bilayer MoS_2. *Nature Reviews Materials* **1**, 16055 (2016).

[273] Kioseoglou, G. *et al.* Valley polarization and intervalley scattering in monolayer MoS_2. *Applied Physics Letters* **101**, 221907 (2012).

[274] Wang, G. *et al.* Control of exciton valley coherence in transition metal dichalcogenide monolayers. *Physical Review Letters* **117**, 187401 (2016).

[275] Luo, Y. K. *et al.* Opto-valleytronic spin injection in monolayer MoS_2/few-layer graphene hybrid spin valves. *Nano Letters* **17**, 3877–3883 (2017).

[276] Avsar, A. *et al.* Optospintronics in graphene via proximity coupling. *ACS Nano* **11**, 11678–11686 (2017).

[277] Mitioglu, A. *et al.* Magnetoexcitons in large area CVD-grown monolayer MoS_2 and $MoSe_2$ on sapphire. *Physical Review B* **93**, 165412 (2016).

[278] Korn, T., Heydrich, S., Hirmer, M., Schmutzler, J. & Schüller, C. Low-temperature photocarrier dynamics in monolayer MoS_2. *Applied Physics Letters* **99**, 102109 (2011).

[279] Delhomme, A. *et al.* Magneto-spectroscopy of exciton Rydberg states in a CVD grown WSe_2 monolayer. *Applied Physics Letters* **114**, 232104 (2019).

[280] Cong, C. *et al.* Intrinsic excitonic emission and valley zeeman splitting in epitaxial MS_2 (M= Mo and W) monolayers on hexagonal boron nitride. *Nano Research* **11**, 6227–6236 (2018).

[281] Wang, S., Wang, X. & Warner, J. H. All chemical vapor deposition growth of MoS_2: h-BN vertical van der Waals heterostructures. *ACS Nano* **9**, 5246–5254 (2015).

[282] Courtade, E. *et al.* Spectrally narrow exciton luminescence from monolayer MoS_2 and $MoSe_2$ exfoliated onto epitaxially grown hexagonal BN. *Applied Physics Letters* **113**, 032106 (2018).

[283] Pacuski, W. *et al.* Narrow excitonic lines and large-scale homogeneity of transition-metal dichalcogenide monolayers grown by molecular beam epitaxy on hexagonal boron nitride. *Nano Letters* (2020).

[284] Paradisanos, I. *et al.* Controlling interlayer excitons in MoS_2 layers grown by chemical vapor deposition. *Nature Communications* **11**, 1–7 (2020).

[285] Mak, K. F. & Shan, J. Photonics and optoelectronics of 2D semiconductor transition metal dichalcogenides. *Nature Photonics* **10**, 216–226 (2016).

[286] Zhang, N. *et al.* Moiré intralayer excitons in a $MoSe_2/MoS_2$ heterostructure. *Nano Letters* **18**, 7651–7657 (2018).

[287] Tran, K. *et al.* Evidence for moiré excitons in van der Waals heterostructures. *Nature* **567**, 71 (2019).

[288] Jin, C. *et al.* Observation of moiré excitons in WSe_2/WS_2 heterostructure superlattices. *Nature* **567**, 76 (2019).

[289] Alexeev, E. M. *et al.* Resonantly hybridized excitons in moiré superlattices in van der Waals heterostructures. *Nature* **567**, 81 (2019).

[290] Cao, Y. *et al.* Unconventional superconductivity in magic-angle graphene superlattices. *Nature* **556**, 43 (2018).

[291] Weston, A. *et al.* Atomic reconstruction in twisted bilayers of transition metal dichalcogenides. *Nature Nanotechnology* 1–6 (2020).

[292] Tong, Q. *et al.* Topological mosaics in moiré superlattices of van der Waals heterobilayers. *Nature Physics* **13**, 356–362 (2016).

[293] Xia, M. *et al.* Spectroscopic signatures of AA' and AB stacking of chemical vapor deposited bilayer MoS_2. *ACS Nano* **9**, 12246–12254 (2015).

[294] Leisgang, N. *et al.* Optical second harmonic generation in encapsulated single-layer InSe. *AIP Advances* **8**, 105120 (2018).

[295] Huang, S. *et al.* Probing the interlayer coupling of twisted bilayer MoS_2 using photoluminescence spectroscopy. *Nano Letters* **14**, 5500–5508 (2014).

[296] van Der Zande, A. M. *et al.* Tailoring the electronic structure in bilayer molybdenum disulfide via interlayer twist. *Nano Letters* **14**, 3869–3875 (2014).

[297] Kormányos, A., Zólyomi, V., Fal'ko, V. I. & Burkard, G. Tunable berry curvature and valley and spin hall effect in bilayer MoS_2. *Physical Review B* **98**, 035408 (2018).

[298] Jones, A. M. *et al.* Spin–layer locking effects in optical orientation of exciton spin in bilayer WSe_2. *Nature Physics* **10**, 130–134 (2014).

[299] Clark, A. & Williams, R. The optical absorption properties of synthetic MoS_2. *Journal of Physics D: Applied Physics* **1**, 1222 (1968).

[300] Roxlo, C., Chianelli, R., Deckman, H., Ruppert, A. & Wong, P. Bulk and surface optical absorption in molybdenum disulfide. *Journal of Vacuum Science & Technology A: Vacuum, Surfaces, and Films* **5**, 555–557 (1987).

[301] Suzuki, R. *et al.* Valley-dependent spin polarization in bulk MoS_2 with broken inversion symmetry. *Nature Nanotechnology* **9**, 611 (2014).

[302] Zhang, Y. *et al.* On valence-band splitting in layered MoS_2. *ACS Nano* **9**, 8514–8519 (2015).

[303] Jin, W. *et al.* Direct measurement of the thickness-dependent electronic band structure of MoS_2 using angle-resolved photoemission spectroscopy. *Physical Review Letters* **111**, 106801 (2013).

[304] Hsu, W.-T. *et al.* Tailoring excitonic states of van der Waals bilayers through stacking configuration, band alignment, and valley spin. *Science Advances* **5**, eaax7407 (2019).